frontiers | Research Topics

Terahertz technologies for biosensing and biomedical analysis

Edited by
Yiming Zhu, Olga P. Cherkasova and Junhong Lü

Published in
Frontiers in Bioengineering and Biotechnology

ISSN 1664-8714
ISBN 978-2-8325-3420-5
DOI 10.3389/978-2-8325-3420-5

About Frontiers

Frontiers is more than just an open access publisher of scholarly articles: it is a pioneering approach to the world of academia, radically improving the way scholarly research is managed. The grand vision of Frontiers is a world where all people have an equal opportunity to seek, share and generate knowledge. Frontiers provides immediate and permanent online open access to all its publications, but this alone is not enough to realize our grand goals.

Frontiers journal series

The Frontiers journal series is a multi-tier and interdisciplinary set of open-access, online journals, promising a paradigm shift from the current review, selection and dissemination processes in academic publishing. All Frontiers journals are driven by researchers for researchers; therefore, they constitute a service to the scholarly community. At the same time, the *Frontiers journal series* operates on a revolutionary invention, the tiered publishing system, initially addressing specific communities of scholars, and gradually climbing up to broader public understanding, thus serving the interests of the lay society, too.

Dedication to quality

Each Frontiers article is a landmark of the highest quality, thanks to genuinely collaborative interactions between authors and review editors, who include some of the world's best academicians. Research must be certified by peers before entering a stream of knowledge that may eventually reach the public - and shape society; therefore, Frontiers only applies the most rigorous and unbiased reviews. Frontiers revolutionizes research publishing by freely delivering the most outstanding research, evaluated with no bias from both the academic and social point of view. By applying the most advanced information technologies, Frontiers is catapulting scholarly publishing into a new generation.

What are Frontiers Research Topics?

Frontiers Research Topics are very popular trademarks of the *Frontiers journals series*: they are collections of at least ten articles, all centered on a particular subject. With their unique mix of varied contributions from Original Research to Review Articles, Frontiers Research Topics unify the most influential researchers, the latest key findings and historical advances in a hot research area.

Find out more on how to host your own Frontiers Research Topic or contribute to one as an author by contacting the Frontiers editorial office: frontiersin.org/about/contact

Terahertz technologies for biosensing and biomedical analysis

Topic editors

Yiming Zhu — University of Shanghai for Science and Technology, China
Olga P. Cherkasova — Institute of Laser Physics (RAS), Russia
Junhong Lü — Shanghai Advanced Research Institute, Chinese Academy of Sciences (CAS), China

Citation

Zhu, Y., Cherkasova, O. P., Lü, J., eds. (2023). *Terahertz technologies for biosensing and biomedical analysis*. Lausanne: Frontiers Media SA.
doi: 10.3389/978-2-8325-3420-5

Table of contents

frontiers | Frontiers in Bioengineering and Biotechnology

TYPE Editorial
PUBLISHED 21 August 2023
DOI 10.3389/fbioe.2023.1268427

OPEN ACCESS

EDITED AND REVIEWED BY
Gianni Ciofani,
Italian Institute of Technology (IIT), Italy

*CORRESPONDENCE
Yiming Zhu,
ymzhu@usst.edu.cn

RECEIVED 28 July 2023
ACCEPTED 07 August 2023
PUBLISHED 21 August 2023

CITATION
Zhu Y (2023), Editorial: Terahertz technologies for biosensing and biomedical analysis.
Front. Bioeng. Biotechnol. 11:1268427.
doi: 10.3389/fbioe.2023.1268427

Editorial: Terahertz technologies for biosensing and biomedical analysis

Yiming Zhu*

Terahertz Technology Innovation Research Institute, Terahertz Spectrum and Imaging Technology Cooperative Innovation Center, Shanghai Key Lab of Modern Optical System, University of Shanghai for Science and Technology, Shanghai, China

KEYWORDS

terahertz technology, biomedicine, detection, neuroscience, spectral database, instrumentation

Editorial on the Research Topic
Terahertz technologies for biosensing and biomedical analysis

Terahertz technology mainly refers to electromagnetic radiation technology with a frequency between 0.1 and 10 THz, which is in the transition region between macro electronics and micro photonics. This frequency band contains important information such as spatial conformation, which directly represents the function of biological macromolecules, which cannot be detected in other electromagnetic wave segments. In the field of biomedicine microcosmic, terahertz technology will provide revolutionary scientific methods for revealing the material laws of interaction between biological macromolecules and cells, presenting the physical characteristics of these effects and activities, and finally explaining various life phenomena. At the macro level of biomedicine, it will bring revolutionary changes to the diagnosis, treatment, evaluation, monitoring and early warning of diseases and subsequent drug design, research and development, production and evaluation.

First, terahertz technology is used to study biomolecules and cells. Zhang et al. the myristoylphosphatidycholine in water (DMPC) bilayer of atomic and molecular dynamics simulation on carefully layered molecular numerical calculation and calibration of optical dielectric constant, The spatially resolved (subnanometer) dielectric spectra of phospholipid bilayers over a wide range from terahertz to mid-infrared have been demonstrated for the first time. Zhang et al. used terahertz spectroscopy to obtain refractive indices of three cell types, *E. coli*, stem cells and cancer cells, and their states under stress. Terahertz spectroscopy also has potential applications for detecting protein concentrations in urine samples. Xue et al. were able to distinguish proteins of different molecular weights by analyzing terahertz spectral absorption in the 0.5–1.2 terahertz band. At the same concentration, the terahertz absorption of high molecular weight protein is greater than that of low molecular weight protein. It is found that terahertz time-domain spectroscopy technology utilizes the vibration and interaction between electromagnetic waves and substances in the terahertz frequency range, and obtains the spectral information of samples by measuring the propagation time and amplitude of light waves, so as to realize substance analysis and detection.

Second, terahertz waves are useful in medicine for the detection and diagnosis of diseases. For example, Shi et al. using a high-resolution terahertz imaging system, can scan non-tumor adjacent tissue and gastric cancer tissue sections by observing the difference in transmittance between different tissue layers in the terahertz image, i.e., the submucosa has

lower transmittance than the mucosal and muscle layers of non-tumor adjacent tissue. It can realize the identification of non-tumor tissue and tumor tissue. Li et al. identified and confirmed the types of gout stones in a timely manner by combining Raman spectroscopy and terahertz spectroscopy techniques to reduce pain and inflammation in patients and prevent complications associated with gout stones. Then, terahertz waves are widely used in the field of neuroscience, and research has simulated and experimented with the terahertz interactions of nerve fibers and neurons to explore their electromagnetic and transport properties. Guo et al. investigated the electromagnetic properties of nerve fibers at THz-FIR band. Firstly, the electromagnetic transmission model of nerve fibers is established and theoretical research is carried out. Secondly, a pattern matching algorithm named RNMMA is proposed to calculate the transmission characteristics of terahertz FIR waves at Ranvier nodes. By comparing with the results of electromagnetic simulation software, the scattering matrix obtained by this algorithm is in good agreement with the actual situation. The study reveals how terahertz FIR signals can be transmitted forward through Ranvier nodes with low losses. Then, Shaoqing et al. established a propagation and thermal effect model of the interaction between 0.3 and 3 THz waves and neurons, and took field intensity and temperature changes as evaluation criteria. The effect of cumulative radiation of terahertz waves on neuronal structure was investigated experimentally. The results show that the frequency and power of terahertz waves are the main factors affecting the neuronal field intensity and temperature, and there is a positive correlation between them.

In addition, Huang et al. introduced the research achievements of terahertz time-domain spectroscopy in the analysis of chemical drugs, traditional Chinese medicine and biological drugs in recent 10 years. The scientific feasibility of terahertz time-domain spectroscopy in drug detection is also revealed. The problems existing in the practical application of terahertz time-domain spectroscopy and its further development prospects in drug analysis are discussed. It shows that terahertz technology is widely used in the analysis of chemical drugs, traditional Chinese medicine and biological drugs, and can be used to study the structure and interaction of drugs, identify the authenticity of drugs, whether the deterioration.

Finally, the combination of terahertz technology and other technologies can be used for biomedical database construction, instrument development, etc., which promotes its development in the biomedical field. Li et al. established a spectral database of gout stones and urinary stones by combining Raman spectroscopy and terahertz spectroscopy techniques. The database will provide accurate and comprehensive technical support for the rapid diagnosis of clinical gout. Biosensing is developed through the combination of terahertz spectroscopy and microfluidic technology, which can be used for biological sample detection. On the one hand, Zhang et al. constructed an automated, high-throughput sample preparation and detection system for inquiring biological cell phenotypes to measure the refractive index of living cells in near-physiological environments, which is suitable for cell health assessment and drug discovery. On the other hand, Fu et al. investigated the structure of a polydimethylsiloxane microfluidic chip (M-chip) suitable for measuring water-based samples, in particular the effect of the cavity depth of the M-chip on the terahertz spectrum. When the depth is less than 210 μm, the Fresnel formula of the two-interface model should be used for the analysis of the terahertz spectral data, and when the depth is not less than 210 μm, the Fresnel formula of the single-interface model can be used. Terahertz wave construction practical instrument. Wang et al. built a terahertz attenuated total reflection spectrometer with a signal-to-noise ratio (SNR) of 40–60 dB. The device can be used to detect liquid biological samples with high sensitivity, such as the identification and quantitative analysis of lactose aqueous solution.

In short, terahertz technology has a wide range of application prospects in all aspects of the biomedical field, although there are still some technical challenges and problems to overcome, but with the continuous development of technology and in-depth research, terahertz technology will play a greater role in the future.

Author contributions

YZ: Writing–original draft.

Conflict of interest

The author declares that the research was conducted in the absence of any commercial or financial relationships that could be construed as a potential conflict of interest.

Publisher's note

frontiers | Frontiers in Bioengineering and Biotechnology

TYPE Original Research
PUBLISHED 31 August 2022
DOI 10.3389/fbioe.2022.984880

OPEN ACCESS

EDITED BY
Junhong Lü,
Shanghai Advanced Research Institute (CAS), China

REVIEWED BY
Yubin Gong,
University of Electronic Science and Technology of China, China
Xiao-Yu Peng,
Chongqing Institute of Green and Intelligent Technology (CAS), China

*CORRESPONDENCE
Chao Chang,
changc@xjtu.edu.cn

†These authors have contributed equally to this work

SPECIALTY SECTION
This article was submitted to Nanobiotechnology, a section of the journal Frontiers in Bioengineering and Biotechnology

RECEIVED 02 July 2022
ACCEPTED 08 August 2022
PUBLISHED 31 August 2022

CITATION
Zhang Z, Li Y, Xiang Z, Huang Y, Wang R and Chang C (2022), Dielectric dispersion characteristics of the phospholipid bilayer with subnanometer resolution from terahertz to mid-infrared. *Front. Bioeng. Biotechnol.* 10:984880. doi: 10.3389/fbioe.2022.984880

Dielectric dispersion characteristics of the phospholipid bilayer with subnanometer resolution from terahertz to mid-infrared

Ziyi Zhang[1†], Yangmei Li[1†], Zuoxian Xiang[1], Yindong Huang[1], Ruixing Wang[1] and Chao Chang[1,2*]

[1]Innovation Laboratory of Terahertz Biophysics, National Innovation Institute of Defense Technology, Beijing, China, [2]School of Physics, Peking University, Beijing, China

There is growing interest in whether the myelinated nerve fiber acts as a dielectric waveguide to propagate terahertz to mid-infrared electromagnetic waves, which are presumed stable signal carrier for neurotransmission. The myelin sheath is formed as a multilamellar biomembrane structure, hence insights into the dielectric properties of the phospholipid bilayer is essential for a complete understanding of the myelinated fiber functioning. In this work, by means of atomistic molecular dynamics simulations of the dimyristoylphosphatidylcholine (DMPC) bilayer in water and numerical calculations of carefully layered molecules along with calibration of optical dielectric constants, we for the first time demonstrate the spatially resolved (in sub-nm) dielectric spectrum of the phospholipid bilayer in a remarkably wide range from terahertz to mid-infrared. More specifically, the membrane head regions exhibit both larger real and imaginary permittivities than that of the tail counterparts in the majority of the 1–100 THz band. In addition, the spatial variation of dielectric properties suggests advantageous propagation characteristics of the phospholipid bilayer in a relatively wide band of 55–85 THz, where the electromagnetic waves are well confined within the head regions.

KEYWORDS

myelinated nerve fiber, phospholipid bilayer, terahertz/mid-infrared, optical/dielectric constants, subnanometer resolution

Introduction

The electromagnetic spectrum from terahertz to mid-infrared region is vital to living organisms since the collective vibrations of most biomacromolecules (e.g., DNA and protein) fall within this frequency range, where many significant physiological phenomena and biomedical applications have been reported (Barone et al., 2005; Kitagawa et al., 2006; Rodrigo et al., 2015; Cheon et al., 2016; Turker-Kaya and Huck,

2017; Mittal et al., 2018; Zhu et al., 2021; Zhang et al., 2021; Li et al., 2021; Li et al., 2022; Sun et al., 2022). In addition, the spectra of the optical constant (refractive index and extinction coefficient), and the dielectric constant (real and imaginary parts of the permittivity) of all biomaterials contain the inherent information of their internal molecules, atoms and chemical bonds, and hence could be utilized as the functional biosignatures (Pethig and Kell, 1987; Parthasarathy et al., 2005; Davidov et al., 2021). A recent experimental study finds that the frog sciatic nerve shows distinct refractive indexes measured at different spots in the terahertz to mid-infrared band, suggesting that the myelinated nerve fiber might act as a decent dielectric waveguide (Liu et al., 2019). Although this finding is a major step forward in supporting that terahertz/mid-infrared electromagnetic waves might be information carriers for neural signal propagation, a question is still left unanswered: what is the specific frequency band for the best information propagation? Intuitively, this band should possess the following features:

1) The band should be continuous and broad. In other words, the frequencies of the electromagnetic waves for the neural signal propagation cannot be a single frequency or some isolated frequencies. This feature contributes to provide a stable and robust communication capability.
2) The refractive index, or the real part of the permittivity, of the myelin sheath should be obviously higher than that of the axon and the extracellular fluid. This feature guarantees that the electromagnetic waves cannot spread to the extracellular fluid and propagate primarily through the myelin sheath rather than the axon.
3) The extinction coefficient, or the imaginary part of the permittivity, of the myelin sheath should be small enough. This feature manifests that the electromagnetic waves can propagate through a considerable long myelin sheath without getting weaker.

In order to answer the above questions, the optical/dielectric properties of the myeline sheath and the axon in the frequency range from terahertz to mid-infrared must be investigated primarily. Researchers have attempted to directly measure the optical/dielectric properties of the myelinated nerve fiber by experiments. Antonov *et al.* carried out the first *in vivo* measurement of the refractive index of a peripheral nerve fiber of the sciatic nerve in *Rana temporaria* using holographic interference microscopy, and the constant refractive indexes of the myelin sheath and the axon in the visible were obtained (Antonov et al., 1983). Rahman *et al.* measured the frequency-dependent refractive index and extinction coefficient of the sciatic nerve of *Xenopus laevis in vitro* for the first time based on a spectrophotometer working in the wavelength range of 860–2,250 nm (Rahman et al., 2018). Tayebi *et al.* analyzed the refractive index dispersion of an individual nerve fiber in striatal medium spiny neurons using a triple-wavelength diffraction phase interferometer (473, 589 and 685 nm) (Tayebi et al., 2019). We find that the related experimental studies are extremely rare due to the limitation of the existing practical techniques and measuring instruments. Currently, to the best of our knowledge, there is no ready-to-use and abundant measured data which could reveal the optical/dielectric properties of the myeline sheath and the axon in the terahertz to mid-infrared spectrum.

It is well known that the myelin sheath and the axon mainly consist of the biomembrane and the intracellular fluid, respectively (Kolb and Whishaw, 1980; Rinholm and Bergersen, 2012; Fields, 2014). As the phospholipid bilayer and the water are respectively the major constituents of the biomembrane and the intracellular fluid, the optical/dielectric properties of the phospholipid bilayer and the water are thus reasonable indicators of those of the myeline sheath and the axon, respectively. The optical/dielectric constants of the water over a wide frequency range from direct current to ultraviolet at various temperature have been thoroughly investigated, and plenty of theoretical and experimental data can be acquired from the available literature (Hale and Querry, 1973; Segelstein 1981; Buchner et al., 1999; Praprotnik and Janežič, 2005; Heyden et al., 2010; Midi et al., 2014; Rowe et al., 2020; Krishnamoorthy et al., 2021). The studies on the biomembrane or phospholipid bilayer also have been started for long. Zhou et al. applied the linear response theory to estimate the susceptibilities across a dilauroylphosphatidylethanolamine (DLPE) bilayer (Zhou and Schulten, 1995). Stern et al. established a rigorous expression to calculate the permittivity of a dipalmitoylphosphatidylcholine (DPPC) by combining statistical mechanics and continuum electrostatics (Stern and Feller, 2003). Tanizaki et al. proposed a three-layered model with different dielectric constants as hydrocarbon, ester group and water based on the generalized Born formalism (Tanizaki and Feig, 2005). Hishida et al. focused on the hydration state of the lipid membrane with techniques of terahertz time-domain spectroscopy and small-angle X-ray scattering, and the dielectric constants of dimyristoylphosphatidylcholine (DMPC) solutions in the frequency range of 0.5–2.6 THz were measured (Hishida and Tanaka, 2011). Hielscher et al. measured the absorbance spectra of six different types of phospholipids in the far-infrared region from 600 to 50 cm^{-1} using Fourier transform infrared spectroscopy (Hielscher and Hellwig, 2012). Siddiquee et al. imaged dioleoylphosphatidylcholine (DOPC) and DPPC membranes based on the local absorption coefficients measured by a scanning near-field optical microscopy system with 640 nm laser beam (Siddiquee et al., 2019). In summary, although previous studies have made great contributions to the frequency-dependent optical/dielectric constants of the phospholipid bilayer, however, the dispersion profiles obtained by both theoretical and experiment methods are

almost narrowband spectra. In addition, it can be found that the studies of the subnanometer resolution optical/dielectric properties of the phospholipid bilayer are only focused on the static permittivity. The broadband optical/dielectric properties of the phospholipid bilayer in the frequency range from terahertz to mid-infrared with subnanometer resolution are still unclear.

To verify whether the myelinated nerve fiber is an applicable candidate for terahertz/mid-infrared electromagnetic propagation, herein, we theoretically investigate the spatially resolved dielectric properties of the phospholipid bilayer broadly ranging from 1 to 100 THz *via* molecular dynamics (MD) simulations for the first time. A membrane-water system based on DMPC molecules is constructed, and the space-frequency distribution of the dielectric properties in terms of the equilibrated membrane-water system is computed. The optimal band for electromagnetic propagation through the myelinated nerve fiber is discussed, and the real and imaginary permittivities across the equilibrated membrane-water system in this band are presented.

Materials and methods

Material characteristics

For any homogeneous, linear and isotropic biomaterial, its optical constant $\tilde{n}$ and dielectric constant $\tilde{\varepsilon}$ are frequency-dependent and can be expressed as follows:

$$\tilde{n} = n(\omega) + i\kappa(\omega) \tag{1}$$

$$\tilde{\varepsilon} = \varepsilon'(\omega) + i\varepsilon''(\omega) \tag{2}$$

where $n(\omega)$ and $\kappa(\omega)$ are respectively the refractive index and the extinction coefficient at angular frequency ω, $\varepsilon'(\omega)$ and $\varepsilon''(\omega)$ are respectively the real and imaginary parts of the permittivity at angular frequency ω, and i is the imaginary unit. If the magnetic properties of the biomaterial can be neglected, according to the physical definitions of the optical and dielectric constants, the following relation can be easily derived

$$\tilde{n}^2 = \tilde{\varepsilon} \tag{3}$$

Substituting Eq. 1 and Eq. 2 into Eq. 3, we can obtain that

$$\varepsilon'(\omega) = n^2(\omega) - \kappa^2(\omega) \tag{4}$$

$$\varepsilon''(\omega) = 2n(\omega)\kappa(\omega) \tag{5}$$

Eq. 4 and Eq. 5 give rigorous mathematical relations between the optical constant and the dielectric constant. The values of $\varepsilon'(\omega)$ and $\varepsilon''(\omega)$ can be determined by the values of $n(\omega)$ and $\kappa(\omega)$, and vice versa. Therefore, if we have obtained the frequency-dependent dielectric properties of the biomaterial, its frequency-dependent optical properties are also known to us. Moreover, the values of $\varepsilon'(\omega)$ and $\varepsilon''(\omega)$, or $n(\omega)$ and $\kappa(\omega)$, are interrelated as well. In the case of $\varepsilon'(\omega)$ and $\varepsilon''(\omega)$, Kramers–Kronig relations establish their relations as follows (Bertie and Zhang, 1992):

$$\varepsilon'(\omega) = \varepsilon_\infty + \frac{2}{\pi} P \int_0^\infty \frac{\omega' \varepsilon''(\omega')}{(\omega')^2 - \omega^2} d\omega' \tag{6}$$

$$\varepsilon''(\omega) = -\frac{2}{\pi} P \int_0^\infty \frac{\omega \varepsilon'(\omega')}{(\omega')^2 - \omega^2} d\omega' \tag{7}$$

where ε_∞ is the optical dielectric constant equal to the real part of the permittivity at infinite frequency and the symbol P denotes the Cauchy principal value which indicates that the integration range is cut open at the point where the integrand is singular. The relations of $n(\omega)$ and $\kappa(\omega)$ show the similar expressions as Eq. 6 and Eq. 7 and will not be listed here.

Phospholipids, the main components in biological membranes, are a sort of important biomaterial. A phospholipid molecule is basically composed of carbon, hydrogen, oxygen, nitrogen and phosphorus, and should be divided into two parts according to the different chemical characteristics: the hydrophilic head and the hydrophobic tail. The hydrophilic head includes the polar phosphatidylcholine while the hydrophobic tail includes the non-polar aliphatic chain. For this reason, under liquid condition phospholipids exist in the form of the double layer structure with their hydrophilic heads outside and hydrophobic tails inside, which is known as the phospholipid bilayer. Related studies have confirmed that biological membranes often in the liquid crystalline state in order to maximize their functional roles (Molugu et al., 2017; Paracini et al., 2018). Most naturally occurring phospholipids (such as DMPC, DPPC, etc.) behave slight differences in the length of the hydrophobic tails (Guo et al., 2014), and thus their optical and dielectric properties should vary little. Herein, we use DMPC for our study as the mammalian membranes contain abundant amounts of this type of phospholipid (Jurczak et al., 2021). It should be noted that the DMPC membrane has a phase transition temperature about 23–24°C, meaning that the membrane is in the gel (liquid crystalline) state exhibiting immobile (fluidic) feature below (above) this temperature (Kučerka et al., 2011).

Model and MD simulation

MD simulation is a powerful technique to understand the physical basis of the structure as well as the function of biomacromolecules (Karplus and McCammon, 2002). It is applicable to simulating the dynamic motions of a number of biological systems at atomic or near-atomic level of detail (Brandman et al., 2012; Zhao et al., 2013). Herein, we perform the MD simulation with GROMACS, which is one of the most widely used MD package (Abraham et al., 2015). As illustrated in Figure 1, we place a single DMPC molecule along

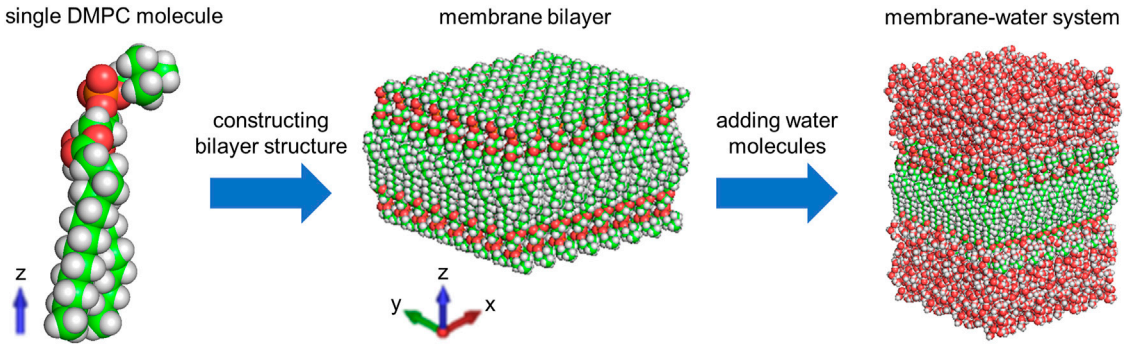

FIGURE 1
Model of the membrane-water system based on DMPC molecules for the MD simulation.

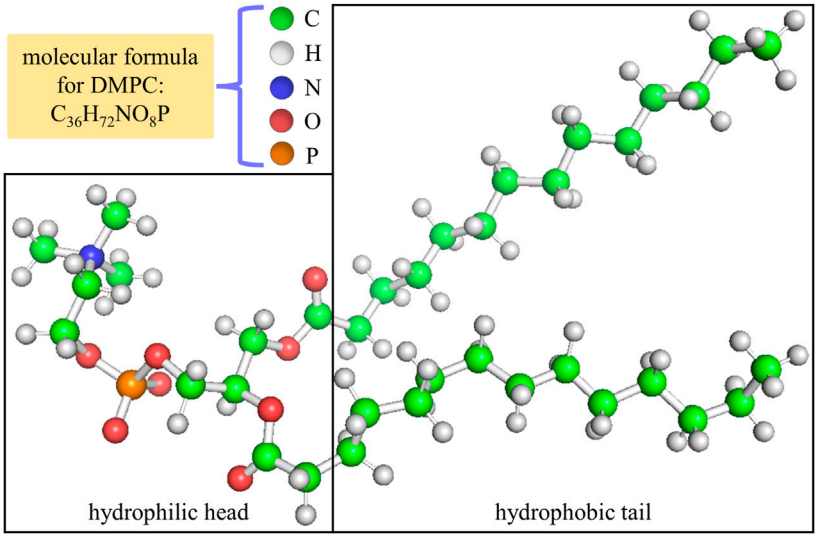

FIGURE 2
Position of the dividing line between the hydrophilic head and the hydrophobic tail in a DMPC molecule.

TABLE 1 Chemical units used for the hydrophilic head of a DMPC molecule.

Chemical unit	Number	*R* (468.3 nm)	*R* (589.3 nm)	*R* (653.3 nm)
CH_3	3	5.719	5.653	5.636
CH_2	5	4.695	4.647	4.624
COO	2	6.261	6.200	6.173
C	1	2.601	2.591	2.572
H	1	1.043	1.028	1.026
PO_4	1	10.821	10.769	10.733
N	1	2.820	2.744	2.698

TABLE 2 Chemical units used for the hydrophobic tail of a DMPC molecule.

Chemical unit	Number	R (468.3 nm)	R (589.3 nm)	R (653.3 nm)
CH_3	2	5.719	5.653	5.636
CH_2	23	4.695	4.647	4.624

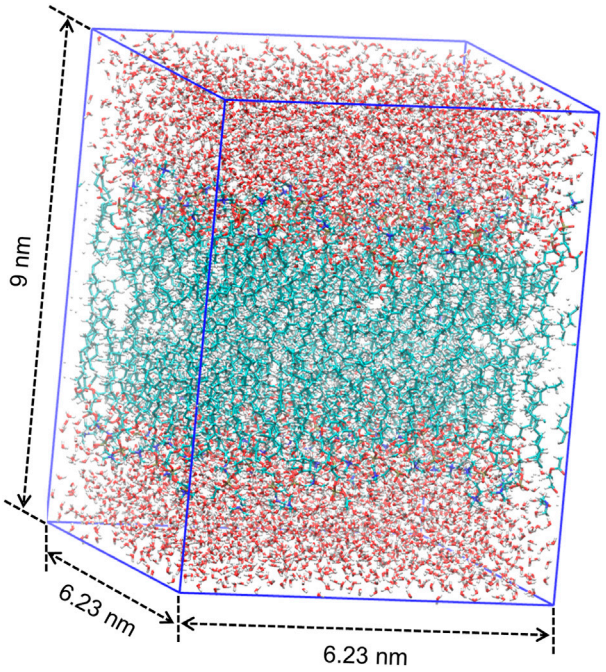

FIGURE 3
Final structure of the equilibrated membrane-water system.

the z direction and use it as the smallest unit. A membrane bilayer is then built by replicating this smallest unit in both x and y directions and inverting in the z direction. The completed membrane bilayer is composed of 128 DMPC molecules with 64 per leaflet, orienting parallel to the x-y plane with the normal in the z direction. The equivalent area per DMPC molecule is 0.606 nm, which is consistent with the experimental values (Wohlert and Edholm, 2006). The distance between two phosphorus atoms which are inverted relative to each other is 3.3 nm. Finally, a membrane-water system is constructed by adding 6,968 water molecules on both sides of the membrane bilayer to well hydrate it, which satisfies the actual state of biological membranes (Park et al., 2020). The dimension of the membrane-water system is approximately 6.23 nm × 6.23 nm × 9 nm.

Before conducting the MD simulation, it is worth noting that the periodic boundary condition is used to avoid edge effects owing to the finite size of the constructed membrane-water system. In addition, the all-atom CHARMM36 force field and the TIP3P water model are used to achieve high-accuracy computation, and the Particle Mesh Ewald method is used for high-efficiency computation of the long-range electrostatic interactions. We keep the simulation temperature at 310 K which is above the phase transition temperature of the DMPC membrane by applying Nosé-Hoover thermostat algorithm. After energy minimization, NVT and NPT ensembles, an equilibrium system can be established and its equilibrated data of the atoms such as charges, velocities and positions can be collected for post-processing.

The frequency range of the spectrum computed by GROMACS is determined based on the sampling theorem as

$$\frac{2}{T} \ll f \ll \frac{1}{2\mathrm{d}t} \tag{8}$$

where $f = \omega/2\pi$ is the frequency, T is the length of the simulation time and $\mathrm{d}t$ is the timestep. It can be inferred from Eq. 8 that the frequency resolution of the computed spectrum should be $2/T$. Theoretically, a longer simulation time can result in a more accurate spectrum. However, as the simulation time increases the computational burden should be aggravated dramatically, and hence a compromise between the simulation accuracy and cost is inevitable. Herein, we set the values of T and $\mathrm{d}t$ to be respectively 1 ns and 1.5 fs in our simulation to investigate terahertz to mid-infrared dielectric spectra of the phospholipid bilayer.

Subnanometer-scale dielectric spectra computation

We attempt to slice the equilibrium system along the z direction into multi-layered structures with subnanometer resolution and compute the dielectric spectra for each layer which can be treated as a homogeneous, linear and isotropic material. Based on the linear response theory (Iftimie and Tuckerman, 2005), the following relation can be derived for each layer

$$n(\omega)\alpha(\omega) = \frac{1}{6c\varepsilon_0 V k_B T}\int_{-\infty}^{\infty} \mathrm{d}t e^{-\mathrm{i}\omega t}\frac{\mathrm{dM}(0)}{\mathrm{d}t}\cdot\frac{\mathrm{dM}(t)}{\mathrm{d}t} \tag{9}$$

where $\alpha(\omega)$ is the absorption coefficient at angular frequency ω which is equal to $2\kappa(\omega)\omega/c$, c is the velocity of light, ε_0 is the vacuum permittivity, V is the volume, k_B is Boltzmann constant and T is the temperature. The angular brackets represent an ensemble average taken over all time origins and $\mathrm{dM}(0)/\mathrm{d}t$ and

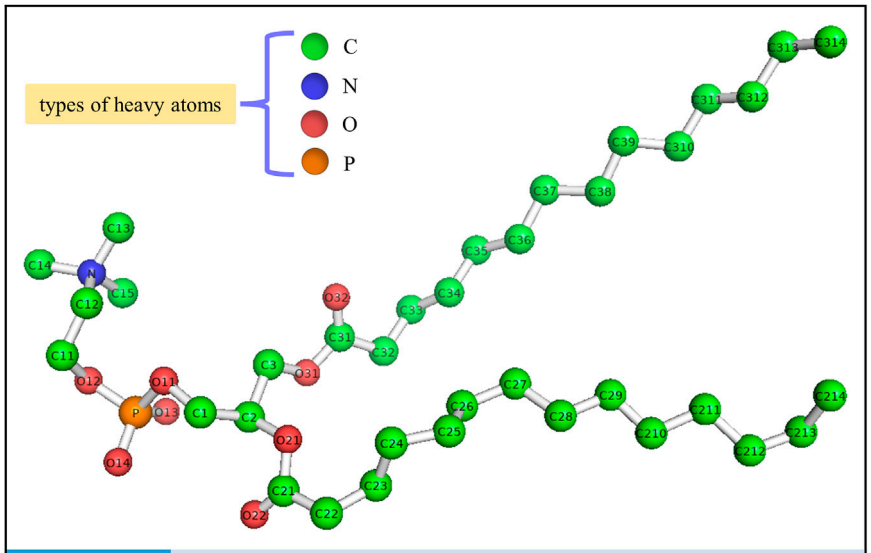

label	N	C13	C14	C15	C12	C11	P	O13	O14	O11
ordinal number	1	2	3	4	5	6	7	8	9	10
label	O12	C1	C2	O21	C21	O22	C22	C3	O31	C31
ordinal number	11	12	13	14	15	16	17	18	19	20
label	O32	C32	C23	C24	C25	C26	C27	C28	C29	C210
ordinal number	21	22	23	24	25	26	27	28	29	30
label	C211	C212	C213	C214	C33	C34	C35	C36	C37	C38
ordinal number	31	32	33	34	35	36	37	38	39	40
label	C39	C310	C311	C312	C313	C314				
ordinal number	41	42	43	44	45	46				

FIGURE 4
Label and the corresponding ordinal number for each heavy atom in a DMPC molecule.

$\mathrm{dM}(t)/\mathrm{d}t$ are respectively the time derivatives of the total dipole moment at times 0 and t. According to the physical definition of the dipole moment, it can be easily derived that

$$\frac{\mathrm{dM}(0)}{\mathrm{d}t}\cdot\frac{\mathrm{dM}(t)}{\mathrm{d}t}=\sum_{j=1}^{N}\mathrm{q}_j\boldsymbol{v}_j(0)\cdot\sum_{k=1}^{N}\mathrm{q}_k\boldsymbol{v}_k(t) \tag{10}$$

where N is the number of all atoms, q_j is the charge of jth atom, q_k is the charge of kth atom, $\mathrm{v}_j(0)$ is the velocity of jth atom at time 0 and $\mathbf{v}_k(t)$ is the velocity of kth atom at time t. We note that the right-hand side of this equation represents the electrical flux-flux correlation function, which can be directly computed using the equilibrated data generated by the MD simulation. Substituting Eq. 5 and Eq. 10 into Eq. 9, we can obtain that

$$\varepsilon''(\omega)=\frac{1}{6\varepsilon_0 VkTw}\int_{-\infty}^{\infty}\mathrm{d}te^{-\mathrm{i}\omega t}\sum_{j=1}^{N}\mathrm{q}_j\boldsymbol{v}_j(0)\cdot\sum_{k=1}^{N}\mathrm{q}_k\boldsymbol{v}_k(t) \tag{11}$$

After the imaginary part of the frequency-dependent permittivity for each layer is computed, the real part $\varepsilon'(\omega)$ can be obtained by using Eq. 6 and then the subnanometer

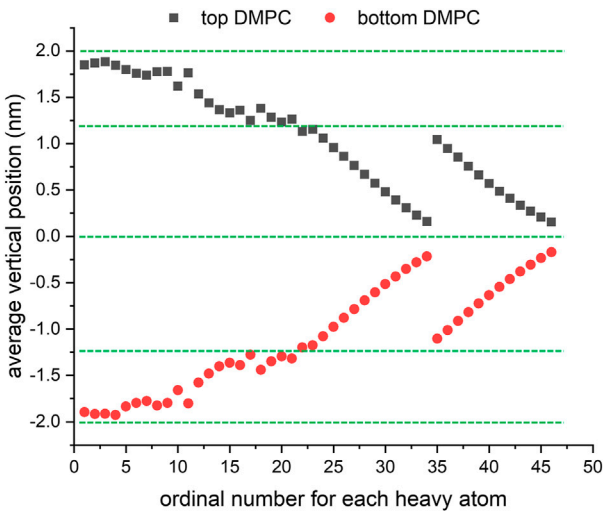

FIGURE 5
Average vertical position versus ordinal number for each heavy atom in the equilibrated DMPC bilayer.

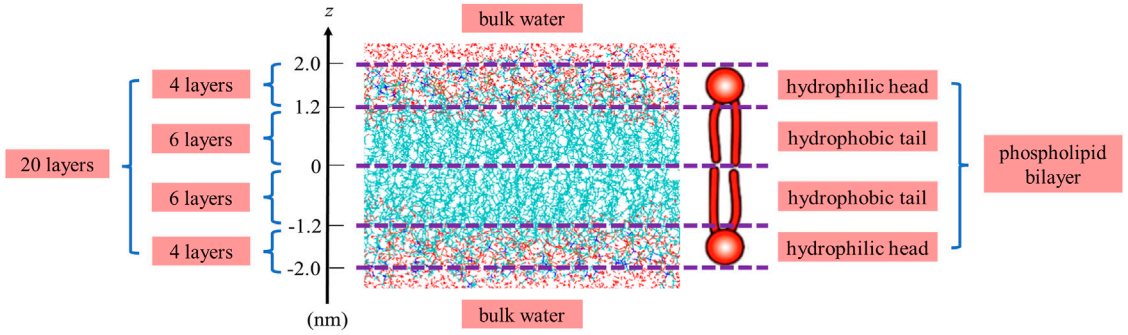

FIGURE 6
Details of layering for the equilibrium system.

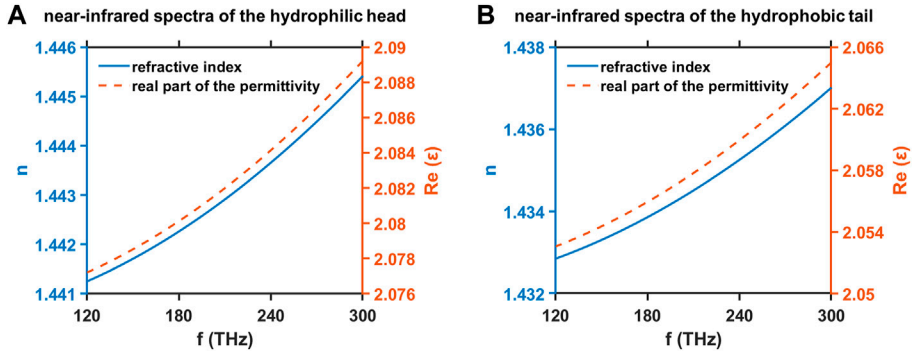

FIGURE 7
Refractive index n and real part of the permittivity ε' at near-infrared frequency f for the hydrophilic head **(A)** and the hydrophobic tail **(B)** of a DMPC molecule through the Cauchy dispersion model and the Vogel method.

resolution dielectric spectra of the phospholipid bilayer are determined.

Optical dielectric constant estimation

We can see from Kramers–Kronig relations that it is enough to know $\varepsilon'(\omega)$ to determine $\varepsilon''(\omega)$ while insufficient to compute $\varepsilon'(\omega)$ just by $\varepsilon''(\omega)$ due to the existence of the unknown optical dielectric constant ε_∞. Actually, for transparent materials such as the phospholipid molecule their vibrational and electronic absorptions are both very weak in the range from near-infrared to near-ultraviolet, and consequently no optical absorption can be seen in their extinction coefficient spectra and the corresponding refractive index spectra demonstrate a feature of the normal dispersion. In this frequency range, the refractive index varies little and can be used to estimate the value of ε_∞. Based on Cauchy dispersion model (Cauchy 1830), the optical constant of a phospholipid molecule from near-infrared to near-ultraviolet region can be well described as

$$n(\lambda) = A + \frac{B}{\lambda^2} + \frac{C}{\lambda^4} \tag{12}$$

$$\kappa(\lambda) = 0 \tag{13}$$

where $n(\lambda)$ and $\kappa(\lambda)$ are the refractive index and the extinction coefficient at wavelength λ, respectively. The parameters A, B and C are fit coefficients. It can be found that A is dimensionless and mainly contributes to the near-infrared region of the refractive index spectrum. Theoretically, $n(\lambda)$ tends to be A when λ approaches infinity. The units of B and C are nm^2 and nm^4, respectively. These two parameters contribute to the visible and near-ultraviolet regions of the refractive index spectrum, respectively.

In order to determine Cauchy dispersion model of the phospholipid molecule, we need to know the values of its fit coefficients. It can be easily solved if we know three pairs of values of wavelength and refractive index. Herein, we use Vogel method

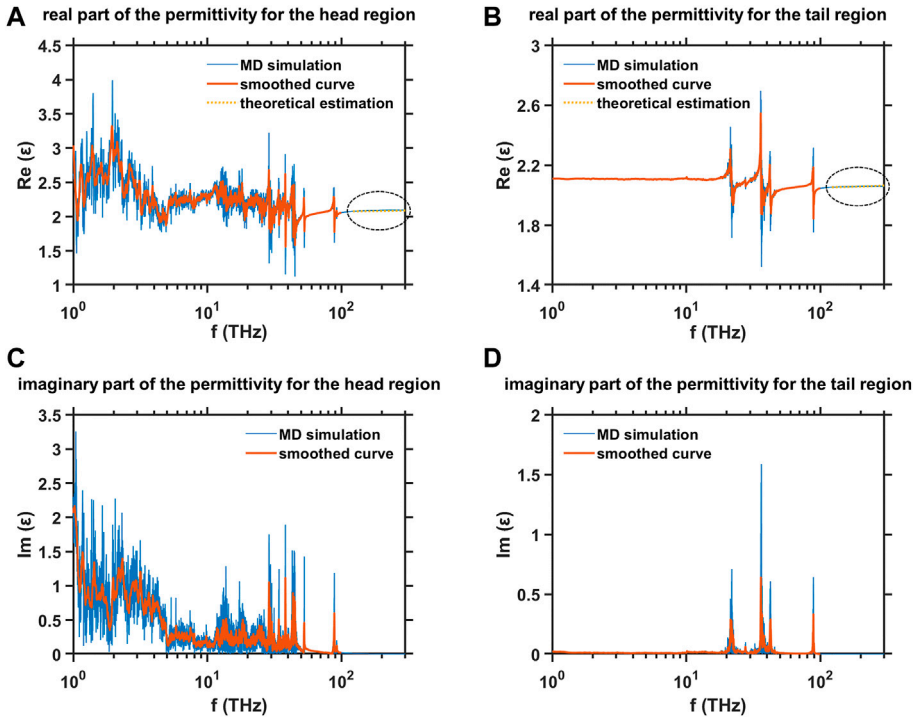

FIGURE 8
MD simulation results of the dielectric spectra in the frequency range from terahertz to mid-infrared for two regions of hydrophilic head and the hydrophobic tail in the equilibrated DMPC monolayer **(A)** Real part of the permittivity for the head region, **(B)** real part of the permittivity for the tail region, **(C)** imaginary part of the permittivity for the head region, and **(D)** imaginary part of the permittivity for the tail region.

and Lorentz-Lorenz equation to achieve this (Vogel 1948; Cao et al., 2009). Based on Vogel method, a molecule under investigation is divided into many chemical units (atoms, structures and groups) with known molar refractions at 468.3, 589.3 and 653.3 nm. By adding up the molar refractions of all the chemical units, the molar refractions of a molecule at these three wavelengths are obtained, and the corresponding refractive indexes are calculated using Lorentz-Lorenz equation:

$$n(\lambda) = \sqrt{\frac{M + 2\rho \cdot R(\lambda)}{M - \rho \cdot R(\lambda)}} \tag{14}$$

where $R(\lambda)$ is the molar refraction at wavelength λ, M is the molecular weight and ρ is the density. At this point we have known three pairs of values of wavelength and refractive index, and substituting these values into Eq. 12 we can compute the values of the fit coefficients in Cauchy dispersion model.

Generally speaking, it is expected that the dielectric properties for the hydrophilic head and the hydrophobic tail of a phospholipid molecule should behave differently owing to their obvious difference in chemical constituent. Therefore, we separately calculate the optical dielectric constants of the hydrophilic head and the hydrophobic tail and use them as reference values for the optical dielectric constants of all sublayers in the hydrophilic head and the hydrophobic tail. For a DMPC molecule, the dividing line between its hydrophilic head and hydrophobic tail is demonstrated in Figure 2. The chemical units used for the hydrophilic head and the hydrophobic tail are listed in Tables 1, 2.

Results and discussion

The final structure of the equilibrated membrane-water system is displayed in Figure 3, where we can find that the hydrophobic tails of all phospholipid molecules are contracted as well as disordered. Herein, the equilibrium system is layered based on the average vertical position of each heavy atom (non-hydrogen atom) in the phospholipid bilayer. In total, there are 46 heavy atoms in a DMPC molecule. We label these atoms as shown in Figure 4, and then assign each label a specific ordinal number. Figure 5 gives the result of the average vertical position versus ordinal number for each heavy atom in the equilibrated DMPC bilayer. It is noted that for the pair of heavy atoms with the same ordinal number which are respectively located at the top and bottom DMPC molecules, their average vertical positions are substantially symmetric about the plane of $z = 0$. The thickness of the DMPC monolayer is approximately 2 nm, with 0.8 nm for the

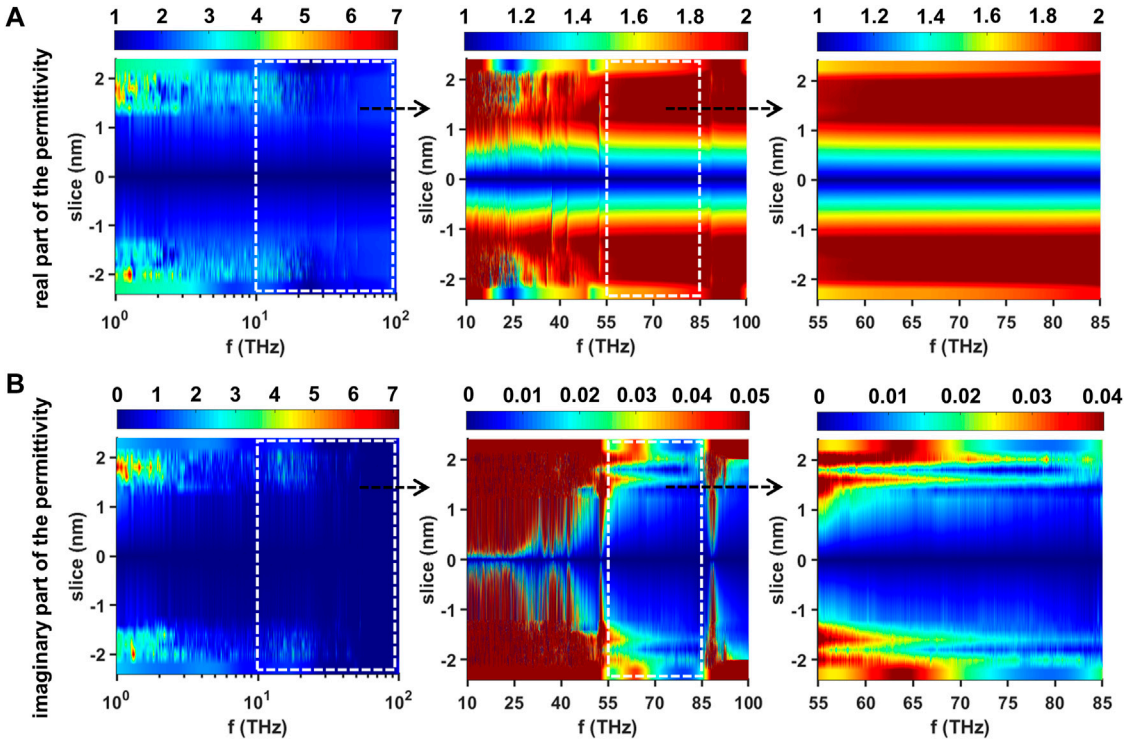

FIGURE 9
Dielectric spectra of the equilibrated membrane-water system in the range of 1–100 THz **(A)** Real part of the permittivity in the range of 1–100 THz (left), 10–100 THz (middle) and 55–85 THz (right) and **(B)** imaginary part of the permittivity in the range of 1–100 THz (left), 10–100 THz (middle) and 55–85 THz (right). The dashed rectangles are used to outline the regions we are interested. Each region is further enlarged and redrawn in its right adjacent subfigure.

hydrophilic head and 1.2 nm for the hydrophobic tail. In order to study the subnanometer resolution dielectric properties of the biomembrane, we use 0.2 nm thickness as spacing of layers and finally slice the phospholipid bilayer into 20 layers, as shown in Figure 6.

We conduct the theoretical estimation of the refractive index n (real part of the permittivity ε') for the hydrophilic head and the hydrophobic tail of a DMPC molecule through Cauchy dispersion model as well as Vogel method, and the corresponding near-infrared spectra are shown in Figure 7. For both the hydrophilic head and the hydrophobic tail, their n and ε' vary little in the near-infrared region, and the hydrophilic head has higher amplitudes than the hydrophobic tail. Herein, the values of ε' at 300 THz for the hydrophilic head and the hydrophobic tail are adopt as the optical dielectric constants of all sublayers in the hydrophilic head and the hydrophobic tail, respectively.

The dielectric spectra in the frequency range from terahertz to mid-infrared for two regions of the hydrophilic head and the hydrophobic tail in the equilibrated DMPC monolayer are studied by MD simulation, and the results are shown in Figure 8. The original data is smoothed based on the moving average window to offer the readers a clearer view of the variation trends of the dielectric spectra. The imaginary parts of the permittivity ε'' for the head and tail regions are first computed, and the real parts ε' are then obtained through Kramers–Kronig relations. It should be noted that the near-infrared data are also included in the spectra which agree well with the results of theoretical estimation, indicating the validity of MD simulation. In most cases, both the values of ε' and ε'' for the head region are higher than those for the tail region, and only at some limited frequencies the head region shows lower amplitudes. This is mainly caused by the high polarity of the head region. In addition, it can be seen that there are many characteristic peaks in the spectra, which is due to the effects of the chemical bond vibration such as C-H stretching and COO stretching.

Results of the subnanometer resolution dielectric spectra in the frequency range from terahertz to mid-infrared (1–100 THz) in terms of the equilibrated membrane-water system are shown in Figure 9. The layered data have been further interpolated to get a smooth dielectric spectrum landscape. We can obviously see that the dielectric properties of the equilibrated phospholipid

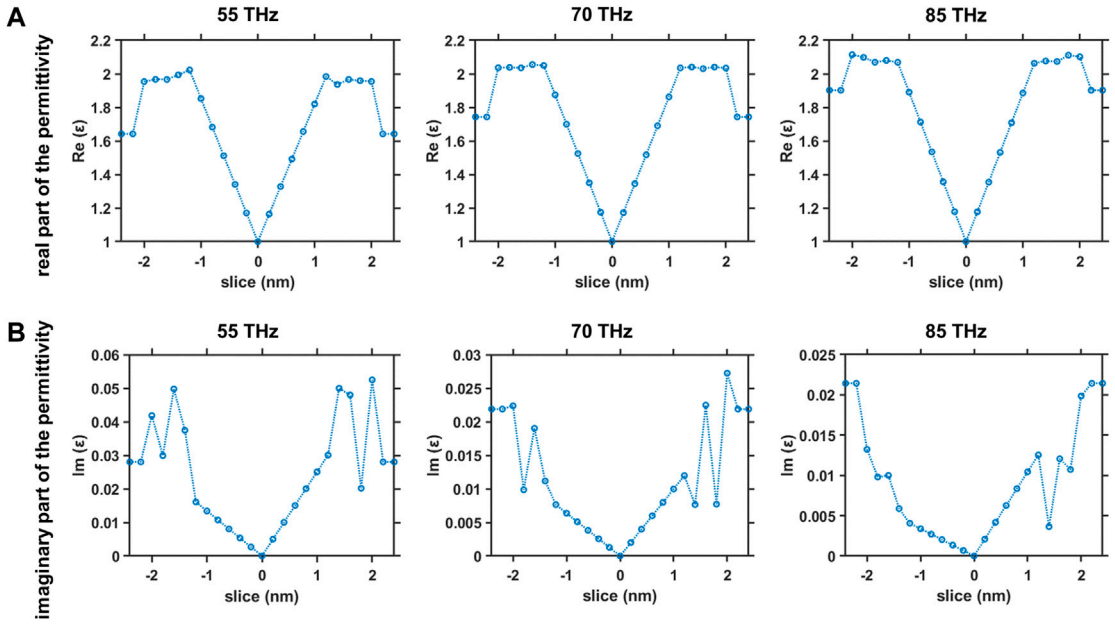

FIGURE 10
Dielectric properties across the equilibrated membrane-water system at frequencies in the range of 55–85 THz **(A)** Real part of the permittivity versus slice position at 55 THz (left), 70 THz (middle) and 85 THz (right) and **(B)** imaginary part of the permittivity versus slice position at 55 THz (left), 70 THz (middle) and 85 THz (right).

bilayer are also substantially symmetric about the plane in which the vertical position of the slice is 0. In the range of 1–10 THz, the values of ε' of the head region can be up to about 7 at some specific slice positions and frequencies, while in these cases the corresponding values of ε'' are also very large. Furthermore, the characteristic peaks of the head and tail region can be found to be mainly concentrated in the range of 1–55 THz. Overall, the frequency range of 1–55 THz might not be an ideal band for electromagnetic propagation through the myelinated nerve fiber. This band not only cannot meet the requirements of continuity and width for robust electromagnetic propagation, but also cannot support the long-distance electromagnetic propagation due to the severe attenuation caused by the large values of ε''. In addition, when the frequency is below 20 THz or above 85 THz, the values of ε' of the head region can be lower than those of the water region, which can lead to the electromagnetic waves spreading to the region outside the myelinated nerve fiber. Actually, the band of 55–85 THz can be a good frequency window in which all the conditions for electromagnetic propagation within the myelin sheath are satisfied. Figure 10 shows the dielectric properties across the equilibrated membrane-water system at different frequencies chosen from the range of 55–85 THz. We can clearly see that the values of ε' at the head layers are larger than those at the tail and water layers, and the values of ε'' at both the head and tail layers are trivial. Therefore, it can be inferred that the electromagnetic waves working at this band mainly propagate along the head regions of the phospholipid bilayer of the myelinated nerve fiber.

Conclusion

In this work, to explore the possibilities of the myelinated nerve fiber acting as a terahertz/mid-infrared dielectric waveguide, we for the first time construct the spatially sub-nm resolved dielectric spectrum in a frequency band widely ranging from 1 to 100 THz regarding a membrane-water system, where the phospholipid bilayer is the major constituent of the myelin sheath. According to calculations on roughly divided head and tail regions of the bilayer, we find that the head region shows higher values of ε' and ε'' compared with the tail region in the majority of the band. After a fine layering, the membrane-water system is further analyzed in terms of the space-frequency dielectric distribution. Clearly, the head layers possess larger ε' values than those of the tail and water layers in 55–85 THz, while the ε'' values at both the head and tail layers are trivial. This suggests a long-distance electromagnetic propagation within the myelin sheath especially the head regions of the phospholipid bilayer in this specific band. Our finding could be a theoretical evidence that the mid-infrared electromagnetic waves could serve as a type of highly stable information carrier for neural signal propagation.

Data availability statement

The original contributions presented in the study are included in the article/Supplementary Material, further inquiries can be directed to the corresponding author.

Author contributions

CC designed the research and revised the manuscript. ZZ and YL conducted the research and wrote the manuscript. ZX, YH, and RW validated the data and helped revise the manuscript.

Funding

This work is supported by the National Natural Science Foundation of China (Grant Nos T2241002, 12174449, and 61905286).

Conflict of interest

The authors declare that the research was conducted in the absence of any commercial or financial relationships that could be construed as a potential conflict of interest.

The handling editor JL declared a past collaboration with the author CC.

Publisher's note

References

Abraham, M. J., Murtola, T., Schulz, R., Páll, S., Smith, J. C., Hess, B., et al. (2015). GROMACS: High Performance Molecular Simulations through Multi-Level Parallelism from Laptops to Supercomputers. *SoftwareX* 1–2, 19–25. doi:10.1016/j.softx.2015.06.001

Antonov, I. P., Goroshkov, A. V., Kalyunov, V. N., Markhvida, I. V., Rubanov, A. S., and Tanin, L. V. (1983). Measurement of the Radial Distribution of the Refractive Index of the Schwann's Sheath and the Axon of a Myelinated Nerve Fiber *In Vivo*. *J. Appl. Spectrosc.* 39, 822–824. doi:10.1007/BF00662830

Barone, P. W., Baik, S., Heller, D. A., and Strano, M. S. (2005). Near-Infrared Optical Sensors Based on Single-Walled Carbon Nanotubes. *Nat. Mat.* 4, 86–92. doi:10.1038/nmat1276

Bertie, J. E., and Zhang, S. L. (1992). Infrared Intensities of Liquids. IX. The Kramers-Kronig Transform, and its Approximation by the Finite Hilbert Transform via Fast Fourier Transforms. *Can. J. Chem.* 70 (2), 520–531. doi:10.1139/v92-074

Brandman, R., Brandman, Y., and Pande, V. S. (2012). A-site Residues Move Independently from P-Site Residues in All-Atom Molecular Dynamics Simulations of the 70S Bacterial Ribosome. *PLoS One* 7 (1), e29377. doi:10.1371/journal.pone.0029377

Buchner, R., Barthel, J., and Stauber, J. (1999). The Dielectric Relaxation of Water between 0°C and 35°C. *Chem. Phys. Lett.* 306 (1–2), 57–63. doi:10.1016/S0009-2614(99)00455-8

Cao, X., Hancock, B. C., Leyva, N., Becker, J., Yu, W., and Masterson, V. M. (2009). Estimating the Refractive Index of Pharmaceutical Solids Using Predictive Methods. *Int. J. Pharm. X.* 368 (1–2), 16–23. doi:10.1016/j.ijpharm.2008.09.044

Cauchy, A. L. (1830). Sur la réfraction et la réflexion de la lumière. *Bull. Des. Sc. Math.* 14, 6–10.

Cheon, H., Yang, H.-J., Lee, S.-H., Kim, Y. A., and Son, J.-H. (2016). Terahertz Molecular Resonance of Cancer DNA. *Sci. Rep.* 6, 37103. doi:10.1038/srep37103

Davidov, D., Shemesh, D., Einstein, O., and Abookasis, D. (2021). Parametric Handheld Optical Probe (HOPE) for Biological Tissue Characterization in the Near-Infrared Spectral Range. *Opt. Commun.* 495, 127076. doi:10.1016/j.optcom.2021.127076

Fields, R. D. (2014). Myelin--More Than Insulation. *Science* 344 (6168), 264–266. doi:10.1126/science.1253851

Guo, Y., Pogodin, S., and Baulin, V. A. (2014). General Model of Phospholipid Bilayers in Fluid Phase within the Single Chain Mean Field Theory. *J. Chem. Phys.* 140 (17), 174903. doi:10.1063/1.4873586

Hale, G. M., and Querry, M. R. (1973). Optical Constants of Water in the 200-nm to 200-µm Wavelength Region. *Appl. Opt.* 12 (3), 555–563. doi:10.1364/AO.12.000555

Heyden, M., Sun, J., Funkner, S., Mathias, G., Forbert, H., Havenith, M., et al. (2010). Dissecting the THz Spectrum of Liquid Water from First Principles via Correlations in Time and Space. *Proc. Natl. Acad. Sci. U. S. A.* 107 (27), 12068–12073. doi:10.1073/pnas.0914885107

Hielscher, R., and Hellwig, P. (2012). Specific Far Infrared Spectroscopic Properties of Phospholipids. *Spectrosc. Int. J.* 27 (5–6), 525–532. doi:10.1155/2012/279650

Hishida, M., and Tanaka, K. (2011). Long-Range Hydration Effect of Lipid Membrane Studied by Terahertz Time-Domain Spectroscopy. *Phys. Rev. Lett.* 106 (15), 158102. doi:10.1103/PhysRevLett.106.158102

Iftimie, R., and Tuckerman, M. E. (2005). Decomposing Total IR Spectra of Aqueous Systems into Solute and Solvent Contributions: A Computational Approach Using Maximally Localized Wannier Orbitals. *J. Chem. Phys.* 122 (21), 214508. doi:10.1063/1.1908950

Jurczak, P., Szutkowski, K., Lach, S., Jurga, S., Czaplewska, P., Szymanska, A., et al. (2021). DMPC Phospholipid Bilayer as a Potential Interface for Human Cystatin C Oligomerization: Analysis of Protein-Liposome Interactions Using NMR Spectroscopy. *Membranes* 11 (1), 13. doi:10.3390/membranes11010013

Karplus, M., and McCammon, J. A. (2002). Molecular Dynamics Simulations of Biomolecules. *Nat. Struct. Biol.* 9 (9), 646–652. doi:10.1038/nsb0902-646

Kitagawa, J., Ohkubo, T., Onuma, M., and Kadoya, Y. (2006). THz Spectroscopic Characterization of Biomolecule/Water Systems by Compact Sensor Chips. *Appl. Phys. Lett.* 89 (4), 041114. doi:10.1063/1.2236295

Kolb, B., and Whishaw, I. Q. (1980). *Fundamentals of Human Neuropsychology*. San Francisco: W.H. Freeman & Company.

Krishnamoorthy, A., Nomura, K., Baradwaj, N., Shimamura, K., Rajak, P., Mishra, A., et al. (2021). Dielectric Constant of Liquid Water Determined with Neural Network Quantum Molecular Dynamics. *Phys. Rev. Lett.* 126 (21), 216403. doi:10.1103/PhysRevLett.126.216403

Kučerka, N., Nieh, M.-P., and Katsaras, J. (2011). Fluid Phase Lipid Areas and Bilayer Thicknesses of Commonly Used Phosphatidylcholines as a Function of Temperature. *Biochimica Biophysica Acta - Biomembr.* 1808 (11), 2761–2771. doi:10.1016/j.bbamem.2011.07.022

Li, Y., Chang, C., Zhu, Z., Sun, L., and Fan, C. (2021). Terahertz Wave Enhances Permeability of the Voltage-Gated Calcium Channel. *J. Am. Chem. Soc.* 143 (11), 4311–4318. doi:10.1021/jacs.0c09401

Li, Y., Zhu, Z., Sun, L., Fan, C., and Chang, C. (2022). Physicochemical Insights on Terahertz Wave Diminished Side Effects of Drugs from Slow Dissociation. *ACS Nano* 16 (5), 8419–8426. doi:10.1021/acsnano.2c02952

Liu, G., Chang, C., Qiao, Z., Wu, K., Zhu, Z., Cui, G., et al. (2019). Myelin Sheath as a Dielectric Waveguide for Signal Propagation in the Mid-infrared to Terahertz Spectral Range. *Adv. Funct. Mat.* 29 (7), 1807862. doi:10.1002/adfm.201807862

Midi, N. S., Ohyama, K., Sasaki, R.-i., and Shinyashiki, N. (2014). Broadband Complex Dielectric Constants of Water and Sodium Chloride Aqueous Solutions

with Different DC Conductivities. *IEEJ Trans. Elec. Electron. Eng.* 9 (S1), S8–S12. doi:10.1002/tee.22036

Mittal, S., Yeh, K., Leslie, L. S., Kenkel, S., Kajdacsy-Balla, A., and Bhargava, R. (2018). Simultaneous Cancer and Tumor Microenvironment Subtyping Using Confocal Infrared Microscopy for All-Digital Molecular Histopathology. *Proc. Natl. Acad. Sci. U. S. A.* 115 (25), E5651–E5660. doi:10.1073/pnas.1719551115

Molugu, T. R., Lee, S., and Brown, M. F. (2017). Concepts and Methods of Solid-State NMR Spectroscopy Applied to Biomembranes. *Chem. Rev.* 117 (19), 12087–12132. doi:10.1021/acs.chemrev.6b00619

Paracini, N., Clifton, L. A., Skoda, M. W. A., and Lakey, J. H. (2018). Liquid Crystalline Bacterial Outer Membranes Are Critical for Antibiotic Susceptibility. *Proc. Natl. Acad. Sci. U. S. A.* 115 (32), E7587–E7594. doi:10.1073/pnas.1803975115

Park, S. H., Wu, J., Yao, Y., Singh, C., Tian, Y., Marassi, F. M., et al. (2020). Membrane Proteins in Magnetically Aligned Phospholipid Polymer Discs for Solid-State NMR Spectroscopy. *Biochimica Biophysica Acta - Biomembr.* 1862 (9), 183333. doi:10.1016/j.bbamem.2020.183333

Parthasarathy, R., Globus, T., Khromova, T., Swami, N., and Woolard, D. (2005). Dielectric Properties of Biological Molecules in the Terahertz Gap. *Appl. Phys. Lett.* 87 (11), 113901. doi:10.1063/1.2046730

Pethig, R., and Kell, D. B. (1987). The Passive Electrical Properties of Biological Systems: Their Significance in Physiology, Biophysics and Biotechnology. *Phys. Med. Biol.* 32 (8), 933–970. doi:10.1088/0031-9155/32/8/001

Praprotnik, M., and Janežič, D. (2005). Molecular Dynamics Integration and Molecular Vibrational Theory. III. The Infrared Spectrum of Water. *J. Chem. Phys.* 122 (17), 174103. doi:10.1063/1.1884609

Rahman, E., Powner, M. B., Kyriacou, P. A., and Triantis, I. F. (2018). Assessment of the Complex Refractive Indices of Xenopus Laevis Sciatic Nerve for the Optimization of Optical (NIR) Neurostimulation. *IEEE Trans. Neural Syst. Rehabil. Eng.* 26 (12), 2306–2314. doi:10.1109/TNSRE.2018.2878107

Rinholm, J. E., and Bergersen, L. H. (2012). The Wrap that Feeds Neurons. *Nature* 487 (7408), 435–436. doi:10.1038/487435a

Rodrigo, D., Limaj, O., Janner, D., Etezadi, D., de Abajo, F. J. G., Pruneri, V., et al. (2015). Mid-Infrared Plasmonic Biosensing with Graphene. *Science* 349 (6244), 165–168. doi:10.1126/science.aab2051

Rowe, P. M., Fergoda, M., and Neshyba, S. (2020). Temperature-Dependent Optical Properties of Liquid Water from 240 to 298 K. *J. Geophys. Res. Atmos.* 125 (17), e2020JD032624. doi:10.1029/2020JD032624

Segelstein, D. J. (1981). *The Complex Refractive Index of Water*. Kansas City: University of Missouri-Kansas City.

Siddiquee, A. M., Hasan, I. Y., Wei, S. B., Langley, D., Balaur, E., Liu, C., et al. (2019). Visualization and Measurement of the Local Absorption Coefficients of Single Bilayer Phospholipid Membranes Using Scanning Near-Field Optical Microscopy. *Biomed. Opt. Express* 10 (12), 6569–6579. doi:10.1364/BOE.10.006569

Stern, H. A., and Feller, S. E. (2003). Calculation of the Dielectric Permittivity Profile for a Nonuniform System: Application to a Lipid Bilayer Simulation. *J. Chem. Phys.* 118 (7), 3401–3412. doi:10.1063/1.1537244

Sun, L., Li, Y., Yu, Y., Wang, P., Zhu, S., Wu, K., et al. (2022). Inhibition of Cancer Cell Migration and Glycolysis by Terahertz Wave Modulation *via* Altered Chromatin Accessibility. Research. 2022, 9860679. doi:10.34133/2022/9860679

Tanizaki, S., and Feig, M. (2005). A Generalized Born Formalism for Heterogeneous Dielectric Environments: Application to the Implicit Modeling of Biological Membranes. *J. Chem. Phys.* 122 (12), 124706. doi:10.1063/1.1865992

Tayebi, B., Kim, W., Sharif, F., Yoon, B. J., and Han, J. H. (2019). Single-Shot and Label-free Refractive Index Dispersion of Single Nerve Fiber by Triple-Wavelength Diffraction Phase Microscopy. *IEEE J. Sel. Top. Quantum Electron.* 25 (1), 1–8. doi:10.1109/JSTQE.2018.2814740

Turker-Kaya, S., and Huck, C. W. (2017). A Review of Mid-infrared and Near-Infrared Imaging: Principles, Concepts and Applications in Plant Tissue Analysis. *Molecules* 22 (1), 168. doi:10.3390/molecules22010168

Vogel, A. I. (1948). Physical Properties and Chemical Constitution. Part XXIII. Miscellaneous Compounds. Investigation of the So-Called Co-ordinate or Dative Link in Esters of Oxy-Acids and in Nitro-Paraffins by Molecular Refractivity Determinations. Atomic, Structural, and Group Parachors and Refractivities. *J. Chem. Soc.*, 1833–1855. doi:10.1039/JR9480001833

Wohlert, J., and Edholm, O. (2006). Dynamics in Atomistic Simulations of Phospholipid Membranes: Nuclear Magnetic Resonance Relaxation Rates and Lateral Diffusion. *J. Chem. Phys.* 125 (20), 204703. doi:10.1063/1.2393240

Zhang, J., He, Y., Liang, S., Liao, X., Li, T., Qiao, Z., et al. (2021). Non-Invasive, Opsin-free Mid-infrared Modulation Activates Cortical Neurons and Accelerates Associative Learning. *Nat. Commun.* 12, 2730. doi:10.1038/s41467-021-23025-y

Zhao, G., Perilla, J. R., Yufenyuy, E. L., Meng, X., Chen, B., Ning, J., et al. (2013). Mature HIV-1 Capsid Structure by Cryo-Electron Microscopy and All-Atom Molecular Dynamics. *Nature* 497, 643–646. doi:10.1038/nature12162

Zhou, F., and Schulten, K. (1995). Molecular Dynamics Study of a Membrane-Water Interface. *J. Phys. Chem.* 99 (7), 2194–2207. doi:10.1021/j100007a059

Zhu, J., Wang, R., Liu, Q., Luo, Z., Tian, B., and Zhu, L.-G. (2021). Mid-Infrared Multispectral Confocal Microscope Using off-Axis Parabolic Mirrors to Study Epiretinal Membranes. *Appl. Opt.* 60 (27), 8616–8623. doi:10.1364/AO.436257

frontiers | Frontiers in Bioengineering and Biotechnology

TYPE Original Research
PUBLISHED 10 November 2022
DOI 10.3389/fbioe.2022.1055232

OPEN ACCESS

EDITED BY
Junhong Lü,
Shanghai Advanced Research Institute (CAS), China

REVIEWED BY
Chaohai Du,
Peking University, China
Xiaojun Wu,
Beihang University, China

*CORRESPONDENCE
Shaomeng Wang,
wangsm@uestc.edu.cn
Yubin Gong,
ybgong@uestc.edu.cn

SPECIALTY SECTION
This article was submitted to Nanobiotechnology, a section of the journal Frontiers in Bioengineering and Biotechnology

RECEIVED 27 September 2022
ACCEPTED 14 October 2022
PUBLISHED 10 November 2022

CITATION
Guo L, Xu D, Wang K, Sun Y, Zhang Q, Ning H, Lu C, Wang S and Gong Y (2022), Electromagnetic characteristics of in vivo nerve fibers at the terahertz-far-infrared band.
Front. Bioeng. Biotechnol. 10:1055232.
doi: 10.3389/fbioe.2022.1055232

Electromagnetic characteristics of *in vivo* nerve fibers at the terahertz-far-infrared band

Lianghao Guo[1], Duo Xu[1], Kaicheng Wang[1], Yuankun Sun[1], Qin Zhang[1], Hui Ning[1], Chang Lu[2], Shaomeng Wang[1,3]* and Yubin Gong[1,3]*

[1]School of Electronic Science and Engineering, University of Electronic Science and Technology of China, Chengdu, Sichuan, China, [2]Department of Electronic Communication and Technology, Shenzhen Institute of Information Technology, Shenzhen, China, [3]National Key Lab on Vacuum Electronics, Medico-Engineering Cooperation on Applied Medicine Research Center, School of Electronic Science and Engineering, University of Electronic Science and Technology of China, Chengdu, China

How terahertz signals perform in the neural system has attracted widespread interest in the life sciences community. Relevant experimental reveals that in animal nerve cells, the myelin sheath of the nerve axon has a higher refractive index than the intracellular and extracellular fluids in the Terahertz-far-infrared (THz-FIR) frequency band. This makes THz-FIR wave transmission possible in nerve fibers. Based on this premise, this article carries out the following work from the theoretical level to investigate the electromagnetic (EM) characteristics of *in vivo* nerve fibers at the THz-FIR band. First, the EM transmission model of the nerve fibers is established and studied theoretically. The dispersion curves of THz-FIR wave modals transmission in nerve fibers are calculated, which predict that nerve fibers can act as dielectric waveguides for transmitting THz-FIR waves and the THz-FIR waves can transmit at speeds up to 10^8 m/s. Second, a mode matching algorithm is proposed, which is named RNMMA, to calculate the transmission characteristics of THz-FIR waves at the nodes of Ranvier. The scattering matrix obtained from the proposed algorithm is in good agreement with the results from EM simulation software, which reveals how THz-FIR signals are transmitted forward through the nodes of Ranvier with low loss.

KEYWORDS

THz-FIR, myelin sheath, nodes of Ranvier, transmission, mode matching algorithm

Introduction

As a complex physical system, the human brain has often been a popular topic in life science research, especially in the study of neural information generation and transmission in neurobiology (Adolphs, 2015; Liu, 2018). Electrochemical theory played a leading role in the early studies, although it could not perfectly explain many underlying problems, such as the generation and origin of consciousness (Tononi, 2004; Tegmark, 2015). Meanwhile, action potential signaling mainly relies on the transmembrane transport of ions to cause the potential difference between the excitatory site and the non-excited site, thereby forming a local current. However, traditional electrochemical theories cannot explain the transmission mechanism of

high-frequency signals in living organisms, such as how THz and FIR signals that are generated by various redox reactions in biological cells are transmitted. In this context, research of the physical mechanisms that coexist with existing electrochemical theories may reveal new prospects for explaining high-level signal transduction mechanisms, including whether there are more efficient physical ways to transmit and store information in the nervous system. Neuro-electromagnetics provides a new way to study the mechanism of the high-level communication and rapid response of the nervous system. However, it also has many problems, such as how to generate and transmit signals efficiently.

Recently, studies on THz-FIR spectroscopy have confirmed that many oxidative metabolic processes in biological cells produce a large number of biological photons, covering the spectrum range of THz-FIR. Many of the biological macromolecules that play an important role in life activities, such as proteins and phospholipids, also have vibration frequencies in the THz-FIR range (Wetzel and LeVine, 1999; Laman et al., 2008; Miller and Dumas, 2010). The ion channels on the surface of the nerve membrane are not only related to action potential activity but also show that the process of ion transport across the membrane generates THz-FIR radiation (Li et al., 2021; Liu et al., 2021; Guo et al., 2022; Hu et al., 2022; Wang et al., 2022). These are several potential sources for the THz-FIR signals transmitting on the nerve fibers. The THz-FIR signals can also affect the activity of the proteins in the cells (Chao et al., 2021), DNA molecular unhelix (Wu et al., 2020), and the selective transmission of ion channels (Li et al., 2021). As information carrier candidates, THz biophotons may become high-speed signal carriers that connect intracellular organelles and cells independently of electrical and chemical transmissions (Xiang et al., 2020).

Some nerve fibers in the vertebrate nervous system are a kind of EM waveguide structure (i.e., wrapped by high resistance and the low capacitance of nerve myelin sheath). This structure can accelerate the conduction of action potential. Meanwhile, in the FIR range, it supports biological photon signal transmission between cells (Kumar et al., 2016; Zangari et al., 2018; Liu et al., 2019). This natural waveguide structure enables signal transmission at a speed of up to 10^8 m/s, which is far higher than the conduction speed of the action potential. The nerve myelin sheath with a dense membrane structure can isolate the polar water environment on both sides of the membrane and greatly reduce the attenuation of the THz-FIR wave due to polarization loss in the transmission process.

Our current work is focused on how THz-FIR waves behave in nerve fibers, and how the THz-FIR waves hop and exchange energy with periodic nodes of Ranvier structures. In view of this hypothesis, we build a transmission model of nerve fibers and nodes of Ranvier (as shown in Figure 1). The myelinated nerve axon can be regarded as a fiber transmission line that is loaded with layered annular media (i.e., nerve cell fluid, myelin sheath, and extracellular fluid). In contrast to optical fiber, the energies of THz-FIR waves concentrate in the myelin sheath area rather than the fiber core area because of its high dielectric constant; while the physical environment of the nerve fibers are polarity solutions, and there is no obvious boundary. Meanwhile, the node of Ranvier is a periodic structure that is formed by the discontinuity of the myelin sheath, which will inevitably produce energy changes. The main work and innovations of this article are as follows: 1) the field equations and dispersion curves of THz-FIR wave transmission in both myelinated and unmyelinated bare nerve fibers are obtained; 2) the transmission efficiencies of THz-FIR electromagnetic waves in different modes are quantitatively analyzed; and 3) a new mode matching algorithm is proposed that can quickly calculate the scattering parameters and energy exchange of THz-FIR wave transmission at the nodes of Ranvier.

Methods

THz-FIR transmission modes in myelin-sheathed nerve fibers

As shown in Figure 1, the nerve fiber is structurally composed of three regions, and the dielectric constants are represented by ε_1, ε_2, and ε_3, respectively. Compared with the intracellular fluid and extracellular fluid of nerve cells (i.e., water as the solvent and have strong absorption characteristics in the THz-FIR band), the myelin sheath is a tight membrane structure with a high dielectric constant and low loss in the THz-FIR band (Liu et al., 2019). The relationship of the dielectric constant of the three-layer media can be expressed as $\varepsilon_3 < \varepsilon_1 < \varepsilon_2$ (Friede and Bischhausen, 1982; Kumar et al., 2016; Liu et al., 2019).

From the completeness of the EM field, it can be known that the THz-FIR transmission modes on the nerve fiber are composed of the guided modes of the finite mode and the integral of the radiation modes over their continuum spectra. Hence, we decompose the fields on the nerve fiber into two parts,

$$\boldsymbol{E}(r,\varphi,z,t) = \sum_{n=1}^{N} C_n \boldsymbol{E}_n(r,\varphi) e^{j(\omega t - \beta_{z,n} z)} + \int C_\xi \boldsymbol{E}_\xi(r,\varphi) e^{j(\omega t - \beta_{z,\xi} z)} d\xi \tag{1–1}$$

$$\boldsymbol{H}(r,\varphi,z,t) = \sum_{n=1}^{N} D_n \boldsymbol{H}_n(r,\varphi) e^{j(\omega t - \beta_{z,n} z)} + \int D_\xi \boldsymbol{H}_\xi(r,\varphi) e^{j(\omega t - \beta_{z,\xi} z)} d\xi \tag{1–2}$$

where the first terms with the subscript n represent the guided modes at a certain frequency and the second terms with continuous subscript ξ denote the integral over the radiation modes. Here, the integration variable ξ represents the radial wavenumbers of the radiation modes. N is the total number of the guided modes on the nerve fiber at a certain frequency. C_n is the normalized amplitude, ω is the angular frequency, and $\beta_{z,n}$ and $\beta_{z,\xi}$ are the propagation constants of the nth or ξth mode along the nerve fiber and have the same value in the three regions.

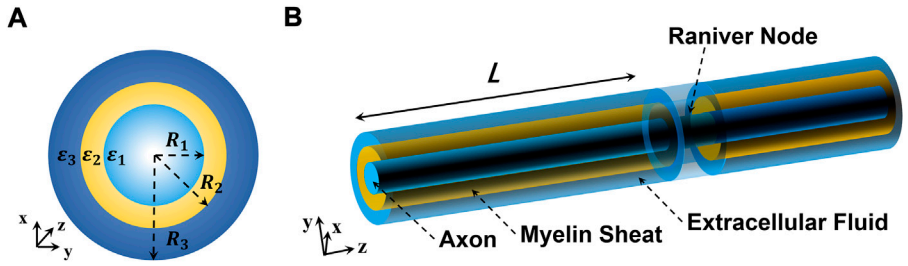

FIGURE 1
Schematic diagram of the nerve fiber structure. **(A)** Cross section of the nerve fiber and **(B)** 3D perspective graphics of the nerve fiber.

$\boldsymbol{E}_n(r,\varphi)$, $\boldsymbol{H}_n(r,\varphi)$ describe the electric and magnetic fields of the nth mode in the cross-sectional area of the nerve fiber, which can be expressed as the superpositions of transverse and longitudinal components,

$$\begin{aligned}\boldsymbol{E}_n(r,\varphi) &= \boldsymbol{E}_{t,n}(r,\varphi) + \boldsymbol{E}_{z,n}(r,\varphi),\ \ \boldsymbol{H}_n(r,\varphi)\\ &= \boldsymbol{H}_{t,n}(r,\varphi) + \boldsymbol{H}_{z,n}(r,\varphi)\end{aligned} \tag{2}$$

The longitudinal components of the electric field $\boldsymbol{E}_{z,n}(r,\varphi)$ and magnetic field $\boldsymbol{H}_{z,n}(r,\varphi)$ satisfy the Helmholtz equation. Thus, we have

$$\begin{aligned}\nabla^2\boldsymbol{E}_z + \omega^2\mu\varepsilon\boldsymbol{E}_{z,n} - j\omega\mu\sigma\boldsymbol{E}_{z,n} = 0,\\ \nabla^2\boldsymbol{H}_z + \omega^2\mu\varepsilon\boldsymbol{H}_{z,n} - j\omega\mu\sigma\boldsymbol{H}_{z,n} = 0\end{aligned} \tag{3}$$

which can be further expressed as,

$$\begin{aligned}\boldsymbol{E}_{\mathrm{iz},n} &= C_{\mathrm{in}}\psi_{\mathrm{in}}(\beta_{\mathrm{in}}r)\begin{pmatrix}\sin n\varphi\\ \cos n\varphi\end{pmatrix}, i = 1,2,3,\\ \boldsymbol{H}_{\mathrm{iz},n} &= D_{\mathrm{in}}\psi_{\mathrm{in}}(\beta_{\mathrm{in}}r)\begin{pmatrix}\sin n\varphi\\ \cos n\varphi\end{pmatrix}, i = 1,2,3\end{aligned} \tag{4}$$

where ψ_{in} represents the Bessel function of order n and has different combinations and representations in different regions. The subscript i represents ith region in Figure 1A. β_{in} represents the transverse propagation constant in the ith region.

Here, we make the approximation $\varepsilon_1 \approx \varepsilon_3$, due to the influence of the high dielectric constant myelin sheaths. However, for the bare nerve axon at the node of Ranvier, the approximation is no longer used because the bare axon is similar to a weakly conducting fiber (which we will discuss in detail later on). For the guided modes in the myelinated axons, the propagation constants β_z satisfy the relations of $k_0\sqrt{\varepsilon_1} < \beta_z < k_0\sqrt{\varepsilon_2}$. The transverse propagation constants of the three regions can be expressed as $\beta_{1n}^2 = \beta_{z,n}^2 - k_0^2\varepsilon_1, \beta_{2n}^2 = k_0^2\varepsilon_2 - \beta_{z,n}^2$, and $\beta_{3n}^2 = \beta_{z,n}^2 - k_0^2\varepsilon_3$, where $k_0 = \omega/c_0$. Accordingly, the Bessel function distribution of the corresponding region satisfies $\psi_{1n} = I_n(\beta_{1n}r)$, $\psi_{2n} = J_n(\beta_{2n}r) + Y_n(\beta_{2n}r)$, and $\psi_{3n} = K_n(\beta_{1n}r)$, respectively, which means that the field decays exponentially at both sides of the myelin sheath region. The transverse field components are expressed in terms of the longitudinal field components,

$$\begin{aligned}\boldsymbol{E}_t &= \frac{j}{\omega^2\mu_0\varepsilon_0\varepsilon_i - \beta_z^2}\left(-\beta_z\nabla_t\boldsymbol{H}_z + \omega\mu_0\boldsymbol{e}_z\times\nabla_t\boldsymbol{H}_z\right),\\ \boldsymbol{H}_t &= \frac{j}{\omega^2\mu_0\varepsilon_0\varepsilon_i - \beta_z^2}\left(-\beta_z\nabla_t\boldsymbol{E}_z + \omega\varepsilon_0\varepsilon_i\boldsymbol{e}_z\times\nabla_t\boldsymbol{E}_z\right)\end{aligned} \tag{5}$$

Furthermore, we can obtain the guided mode expressions of 12 field components in the three regions, as follows:

$$\begin{bmatrix}\boldsymbol{E}_{1r}\\ \boldsymbol{E}_{1\varphi}\\ \boldsymbol{H}_{1r}\\ \boldsymbol{H}_{1\varphi}\end{bmatrix} = j\begin{bmatrix}\frac{\beta_{z,n}}{\beta_{1n}}I_n'(\beta_{1n}r)\sin n\varphi & -\frac{\omega\mu n}{\beta_{1}^2 r}I_n(\beta_{1n}r)\sin n\varphi\\ \frac{\beta_{z,n}n}{\beta_{1n}^2 r}I_n(\beta_{1n}r)\cos n\varphi & -\frac{\omega\mu}{\beta_{1n}}I_n'(\beta_{1n}r)\cos n\varphi\\ -\frac{\omega\varepsilon_0\varepsilon_1 n}{\beta_{1n}^2 r}I_n(\beta_{1n}r)\cos n\varphi & \frac{\beta_{z,n}}{\beta_{1n}}I_n'(\beta_{1n}r)\cos n\varphi\\ \frac{\omega\varepsilon_0\varepsilon_1}{\beta_{1n}}I_n'(\beta_1 r)\sin n\varphi & -\frac{\beta_z n}{\beta_{1n}^2 r}I_n(\beta_{1n}r)\sin n\varphi\end{bmatrix}\times\begin{bmatrix}C_1\\ D_1\end{bmatrix} \tag{6a}$$

$$\begin{bmatrix}\boldsymbol{E}_{2r}\\ \boldsymbol{E}_{2\varphi}\\ \boldsymbol{H}_{2r}\\ \boldsymbol{H}_{2\varphi}\end{bmatrix} = j\begin{bmatrix}-\frac{\beta_{z,n}}{\beta_{2n}}J_n'(\beta_{2n}r)\sin n\varphi & -\frac{\beta_{z,n}}{\beta_{2n}}Y_n'(\beta_{2n}r)\sin n\varphi & \frac{\omega\mu n}{\beta_{2n}^2 r}J_n(\beta_{2n}r)\sin n\varphi & \frac{\omega\mu n}{\beta_{2n}^2 r}Y_n(\beta_{2n}r)\sin n\varphi\\ -\frac{\beta_{z,n}n}{\beta_{2n}^2 r}J_n(\beta_{2n}r)\cos n\varphi & -\frac{\beta_{z,n}n}{\beta_{2n}^2 r}Y_n(\beta_{2n}r)\cos n\varphi & \frac{\omega\mu}{\beta_{2n}}J_n'(\beta_{2n}r)\cos n\varphi & \frac{\omega\mu}{\beta_{2n}}Y_n'(\beta_{2n}r)\cos n\varphi\\ \frac{\omega\varepsilon_0\varepsilon_2 n}{\beta_{2n}^2 r}J_n(\beta_{2n}r)\cos n\varphi & \frac{\omega\varepsilon_0\varepsilon_2 n}{\beta_{2n}^2 r}Y_n(\beta_{2n}r)\cos n\varphi & -\frac{\beta_{z,n}}{\beta_{2n}}J_n'(\beta_{2n}r)\cos n\varphi & -\frac{\beta_{z,n}}{\beta_{2n}}Y_n'(\beta_{2n}r)\cos n\varphi\\ -\frac{\omega\varepsilon_0\varepsilon_2}{\beta_{2n}}J_n'(\beta_{2n}r)\sin n\varphi & -\frac{\omega\varepsilon_0\varepsilon_2}{\beta_{2n}}Y_n'(\beta_{2n}r)\sin n\varphi & \frac{\beta_{z,n}n}{\beta_{2n}^2 r}J_n(\beta_{2n}r)\sin n\varphi & \frac{\beta_{z,n}n}{\beta_{2n}^2 r}Y_n(\beta_{2n}r)\sin n\varphi\end{bmatrix}\times\begin{bmatrix}C_{21}\\ C_{22}\\ D_{21}\\ D_{22}\end{bmatrix} \tag{6b}$$

$$\begin{bmatrix} \boldsymbol{E}_{3r} \\ \boldsymbol{E}_{3\varphi} \\ \boldsymbol{H}_{3r} \\ \boldsymbol{H}_{3\varphi} \end{bmatrix} = j \begin{bmatrix} \frac{\beta_{z,n}}{\beta_{3n}} K_n'(\beta_{3n} r)\sin n\varphi & -\frac{\omega\mu n}{\beta_{3n}^2 r} K_n(\beta_{3n} r)\sin n\varphi \\ \frac{\beta_{z,n} n}{\beta_{3n}^2 r} K_n(\beta_{3n} r)\cos n\varphi & -\frac{\omega\mu}{\beta_{3n}} K_n'(\beta_{3n} r)\cos n\varphi \\ -\frac{\omega\varepsilon_0\varepsilon_3 n}{\beta_{3n}^2 r} K_n(\beta_{3n} r)\cos n\varphi & \frac{\beta_{z,n}}{\beta_{3n}} K_n'(\beta_{3n} r)\cos n\varphi \\ \frac{\omega\varepsilon_0\varepsilon_3}{\beta_{3n}} K_n'(\beta_1 r)\sin n\varphi & -\frac{\beta_{z,n} n}{\beta_{3n}^2 r} K_n(\beta_{3n} r)\sin n\varphi \end{bmatrix} \times \begin{bmatrix} C_3 \\ D_3 \end{bmatrix} \tag{6c}$$

The dispersion curves of THz-FIR wave transmitting in nerve fibers can be obtained by using the tangential continuous boundary conditions for the electric and magnetic fields on $r = R_1$ and $r = R_2$, and the dispersion equation of nth HEM mixing mode is as follows:

$$\begin{vmatrix} I_n(\beta_{1n}R_1) & 0 & -I_n(\beta_{2n}R_1) & -Y_n(\beta_{2n}R_1) & 0 & 0 & 0 & 0 \\ 0 & I_n(\beta_{1n}R_1) & 0 & 0 & -J_n(\beta_{2n}R_1) & -Y_n(\beta_{2n}R_1) & 0 & 0 \\ \frac{\beta_{1}n}{\beta_{1n}^2R_1}I_n(\beta_{1n}R_1) & -\frac{\omega\mu}{\beta_{1n}}I_n'(\beta_{1n}R_1) & \frac{\beta_{2}n}{\beta_{2n}^2R_1}J_n(\beta_{1n}R_1) & \frac{\beta_{2}n}{\beta_{2n}^2R_1}Y_n(\beta_{2n}R_1) & -\frac{\omega\mu}{\beta_{2n}}J_n'(\beta_{2n}R_1) & -\frac{\omega\mu}{\beta_{2n}}Y_n'(\beta_{2n}R_1) & 0 & 0 \\ \frac{\omega\varepsilon_0\varepsilon_1}{\beta_{1n}}I_n'(\beta_1R_1) & -\frac{\beta_{1}n}{\beta_{1n}^2R_1}I_n(\beta_{1n}R_1) & \frac{\omega\varepsilon_0\varepsilon_2}{\beta_{2n}}J_n'(\beta_{2n}R_1) & \frac{\omega\varepsilon_0\varepsilon_2}{\beta_{2n}}Y_n'(\beta_{2n}R_1) & -\frac{\beta_{1}n}{\beta_{2n}^2R_1}J_n(\beta_{2n}R_1) & -\frac{\beta_{1}n}{\beta_{2n}^2R_1}Y_n(\beta_{2n}R_1) & 0 & 0 \\ 0 & 0 & J_n(\beta_{2n}R_2) & Y_n(\beta_{2n}R_2) & 0 & 0 & -K_n(\beta_{3n}R_2) & 0 \\ 0 & 0 & 0 & 0 & J_n(\beta_{2n}R_2) & Y_n(\beta_{2n}R_2) & 0 & -K_n(\beta_{3n}R_2) \\ 0 & 0 & -\frac{\beta_{1}n}{\beta_{2n}^2R_2}J_n(\beta_{2n}R_2) & -\frac{\beta_{1}n}{\beta_{2n}^2R_2}Y_n(\beta_{2n}R_2) & \frac{\omega\mu}{\beta_{2n}}J_n(\beta_{2n}R_2) & \frac{\omega\mu}{\beta_{2n}}Y_n'(\beta_{2n}R_2) & -\frac{\beta_{3}n}{\beta_{3n}^2R_2}K_n(\beta_{3n}R_2) & \frac{\omega\mu}{\beta_{3n}}K_n'(\beta_{3n}R_2) \\ 0 & 0 & -\frac{\omega\varepsilon_0\varepsilon_2}{\beta_{2n}}J_n'(\beta_{2n}R_2) & -\frac{\omega\varepsilon_0\varepsilon_2}{\beta_{2n}}Y_n'(\beta_{2n}R_2) & \frac{\beta_{1}n}{\beta_{2n}^2R_2}J_n(\beta_{2n}R_2) & \frac{\beta_{1}n}{\beta_{2n}^2R_2}Y_n(\beta_{2n}R_2) & -\frac{\omega\varepsilon_3}{\beta_{3n}}K_n'(\beta_1R_2) & \frac{\beta_{3}n}{\beta_{3n}^2R_2}K_n(\beta_{3n}R_2) \end{vmatrix} = 0 \tag{7}$$

It is worth noting that when $n \neq 0$, the aforementioned equation has non-zero solutions, indicating that the THz-FIR waves on the nerve fibers are transmitting in mixed modes. When n=0, the THz-FIR waves will no longer transmit in the mixed modes but are decomposed into independent TE and TM modes, and the field components satisfy $\boldsymbol{E}_z = \boldsymbol{E}_\varphi = \boldsymbol{H}_r = 0$ or $\boldsymbol{H}_z = \boldsymbol{H}_\varphi = \boldsymbol{E}_r = 0$. Therefore, in the case of n = 0, the left-hand determinant can be rewritten as a 4×4 order determinant.

For the radiation modes, it is used to describe the radiation fields outside and inside of the myelin sheath, which are necessary supplements to the guided modes to provide a completely orthogonal set of modes. The fields of the radiation modes will not decay exponentially for increasing values of r outside of the nerve fiber (i.e., extend to infinity). Because there is no need to limit the function describing the radiation modes to those decaying exponentially for large r, a combination of Bessel and Neumann functions is used to describe the radiation modes. It is worth noting that the radiation modes also satisfy the boundary conditions and the fields remain finite on-axis at $r = 0$. The propagation constants of radiation modes satisfy $\beta_z < k_0\sqrt{e_1}$, and the transverse propagation constants can be expressed as $\beta_{1n}^2 = k_0^2\varepsilon_1 - \beta_{z,n}^2, \beta_{2n}^2 = k_0^2\varepsilon_2 - \beta_{z,n}^2$, and $\beta_{3n}^2 = k_0^2\varepsilon_3 - \beta_{z,n}^2$ in three regions. Accordingly, the Bessel function ψ_{in} in Eq. 4 can be written as $\psi_{1n} = J_n(\beta_{1n}r)$, $\psi_{2n} = J_n(\beta_{2n}r) + Y_n(\beta_{2n}r)$, and $\psi_{3n} = J_n(\beta_{3n}r) + Y_n(\beta_{3n}r)$. Unfortunately, in the general field solution of the radiation mode, there are 10 unknowns and only eight boundary conditions. Therefore, the propagation constants of the radiation modes can theoretically take continuous values (Dietrich and Marcuse, 1970; Marcuse, 1973).

Here, we ignore the evanescent radiation modes of the nerve fiber, which are the modes with imaginary values of the propagation constants β_z and do not propagate in the z-direction. However, omitting evanescent radiation modes keeps the set of orthogonal modes from being complete.

Nodes of Ranvier mode matching algorithm

In the vertebrate nervous system, nerve fibers are not completely enclosed by myelin sheaths, which periodically disintegrate to form structures called the node of Ranvier. The membranes of the axon that are exposed at the narrow node of Ranvier contain large numbers of ion channels, which enable the action potential to jump over the nodes. A schematic diagram of the structure is shown in Figure 2. The calculations of the electric and magnetic fields at the node of Ranvier are very complicated because of the discontinuity of the longitudinal section of the THz-FIR wave in the transmission direction. To analyze the THz-FIR wave transmission and field mode transformation at the nodes of Ranvier, we propose the nodes of Ranvier pattern matching algorithm (RNMMA), which theoretically consists of three steps: 1) the RNMMA begins by expanding the tangential components of the electric and magnetic fields at the node in terms of the normal modes in each region; 2) the scattering matrices on the boundaries of III and IV are obtained by using mode orthogonality and power normalization; and 3) the total scattering matrix of one node of Ranvier can be obtained from the matrix cascade, and then the distributions and mode characteristics of the electric and magnetic fields at the nodes of Ranvier can be solved. To simplify the analysis, we made the boundaries of III and IV perpendicular to the z-direction, while the boundaries are not strictly perpendicular physiologically.

As shown in Figure 2, the structure of the node of Ranvier (④ and ⑤ regions) can be regarded as an unmyelinated neural axon, whose structure is similar to an optical fiber. The permittivity of the extracellular fluid in ⑤ region is the same as that in ③ region, and the permittivity in ④ region is the same as that in ① region. The field components can also be described by Eqs 1–5. The Bessel function in ④ and ⑤ regions can be expressed as $\psi_{4n} = J_n(\beta_{4n}r)$ and $\psi_{5n} = K_n(\beta_{5n}r)$ for guided modes, which can ensure that the field propagates in region ④ and decays exponentially in the r-direction in region ⑤. The propagation constants satisfy $k_0\sqrt{\varepsilon_5} < \beta_{z,n} < k_0\sqrt{\varepsilon_3}$, and the transverse propagation constants can be expressed $\beta_{4n}^2 = k_0^2\varepsilon_4 - \beta_{z,n}^2$ and $\beta_{5n}^2 = \beta_{z,n}^2 - k_0^2\varepsilon_5$. When $\beta_{z,n} < k_0\sqrt{\varepsilon_5}$, the transmission modes of the THz-FIR wave generated by the node of Ranvier are radiation modes. The transverse propagation constants can be expressed as $\beta_n^2 = k_0^2\varepsilon_4 - \beta_{z,n}^2$ and $\beta_{5n}^2 = k_0^2\varepsilon_5 - \beta_{z,n}^2$. The field components in

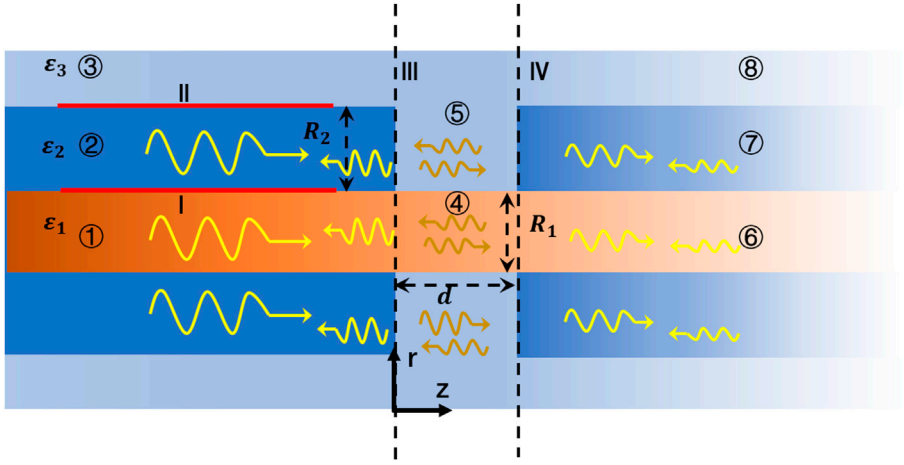

FIGURE 2
Schematic diagram of one node of Ranvier structure, and electromagnetic wave transmissions and reflections.

the r-direction can be described by a combination of Bessel and Neumann functions, $\psi_{4n} = J_n(\beta_{4n}r)$ and $\psi_{5n} = J_n(\beta_{5n}r) + Y_n(\beta_{5n}r)$.

The tangential components of electric and magnetic fields at the boundary can be expressed in terms of each normal mode:

$$\boldsymbol{E}_t = \sum_{N,p} C_N^p \boldsymbol{E}_{t,N}^p(r,\varphi)e^{-jp\beta_{zN}z} \tag{8}$$

$$\boldsymbol{H}_t = \sum_{N,p} C_N^p \boldsymbol{H}_{t,N}^p(r,\varphi)e^{-jp\beta_{zN}z} \tag{9}$$

where p ($p = +, -$) represents the propagation direction of the wave, N indicates the mode number, A_N^p is the amplitude coefficient of each mode, and $\boldsymbol{E}_{t,N}^p(r,\varphi)$ and $\boldsymbol{H}_{t,N}^p(r,\varphi)$ are the transverse electric field and magnetic field of each mode in different regions. The pattern functions of different regions all satisfy the orthogonality theorem of patterns,

$$\oint_S \boldsymbol{e}_z \cdot \left(\boldsymbol{E}_{t,m}^q \times \boldsymbol{H}_{t,n}^{p^*} + \boldsymbol{E}_{t,n}^{p^*} \times \boldsymbol{H}_{t,m}^q\right) \mathrm{ds} = 4\delta_{mn} S_0(p,q) P_n \tag{10}$$

where δ_{mn} is the Kronecker delta. When m = n, $\delta_{\mathrm{mn}} = 1$, otherwise $\delta_{\mathrm{mn}} = 0$, which means the different modes are orthogonal to each other. Meanwhile, p and q represent the propagation directions of the modes. When p and q are both positive, $S = 1$; when p and q are both negative, $S = -1$; otherwise, $S = 0$. This means the same modes of forwarding and backward transmissions are also orthogonal to each other. The scattering matrix (SM) is the premise of analyzing the THz-FIR wave propagation mode at the node of Ranvier, the core of which is establishing the coupling matrix (CM). N and M modes are, respectively, considered in the axon and node of Ranvier regions on both sides of the III boundary. By applying the continuity conditions ($\boldsymbol{E}_{t,\mathrm{axon}} = \boldsymbol{E}_{t,\mathrm{NR}}$ and $\boldsymbol{H}_{t,\mathrm{axon}} = \boldsymbol{H}_{t,\mathrm{NR}}$) at the junction (z = 0), we obtain the equation for the electric field as

$$\left.\begin{aligned} 0 \le r < R_1 \quad & \sum_{n=1}^{N}\left(C_{1,n}^+ \pm C_{1,n}^-\right)\psi_{1t,n}(r,\varphi) \\ R_1 \le r < R_2 \quad & \sum_{n=1}^{N}\left(C_{2,n}^+ \pm C_{2,n}^-\right)\psi_{2t,n}(r,\varphi) \\ R_2 \le r \quad & \sum_{n=1}^{N}\left(C_{3,n}^+ \pm C_{3,n}^-\right)\psi_{3t,n}(r,\varphi) \end{aligned}\right\} = \begin{cases} \sum_{m=1}^{M}\left(D_{4,m}^+ \pm D_{4,m}^+\right)\psi_{t,m}(r,\varphi) & 0 \le r < R_1 \\ \sum_{m=1}^{M}\left(D_{5,m}^+ \pm D_{5,m}^+\right)\psi_{5t,m}(r,\varphi) & R_1 \le r \end{cases} \tag{11}$$

where $\psi_{\mathrm{it},n}(r,\varphi)$ represents tangential electric field (E) and tangential magnetic field (H). By making use of the property of mode orthogonality, we can derive a set of an equation involving the unknown coefficients. To this end, the aforementioned equation is multiplied $\psi_{\mathrm{it},n}(r,\varphi)$ in the different regions and integrated with the whole interface. We can get

$$\sum_{i=1,2,3}\sum_{n=1}^{N} F_{i,n}\left(C_{i,n}^+ + C_{i,n}^-\right) = \sum_{j=1,2,3}\sum_{i=4,5}\sum_{m=1}^{M} f_{ij,nm}\left(D_{i,m}^+ + D_{i,m}^+\right) \tag{12}$$

$$\sum_{i=1,2,3}\sum_{n=1}^{N} F_{i,n}^h\left(C_{i,n}^+ - C_{i,n}^-\right) = \sum_{j=1,2,3}\sum_{i=4,5}\sum_{m=1}^{M} f_{ij,nm}^h\left(D_{i,m}^+ - D_{i,m}^+\right) \tag{13}$$

where $F_{i,n}$ and $f_{\mathrm{ij,nm}}$ are the CM, and their representations are as follows:

$$F_{i,n} = \int_0^{2\pi} \int_{R_{i-1}}^{R_i} \psi^e_{it,n} \psi^e_{it,n} r dr d\theta, \mathrm{i} = 1, 2, 3 \quad (14\text{–}1)$$

$$f_{\mathrm{ji,nm}} = \int_0^{2\pi} \int_{R_{j-1}}^{R_j} \psi^e_{jt,m} \psi^e_{it,n} r dr d\theta, j = 4, 5 \text{ and } \mathrm{i} = 1, 2, 3 \quad (14\text{–}2)$$

$$F^h_{i,n} = \int_0^{2\pi} \int_{R_{i-1}}^{R_i} \psi^h_{it,n} \psi^h_{it,n} r dr d\theta, \mathrm{i} = 1, 2, 3 \quad (14\text{–}3)$$

$$f^h_{\mathrm{ji,nm}} = \int_0^{2\pi} \int_{R_{j-1}}^{R_j} \psi^h_{jt,n} \psi^h_{it,m} r dr d\theta, \ j = 4, 5 \text{ and } i = 1, 2, 3 \quad (14\text{–}4)$$

where $\psi^e_{\mathrm{it},n}$ represents the transverse electric field component of the nth mode in the ith region of the axon region. $\psi^h_{\mathrm{it},n}$ represents the transverse magnetic field component of the nth mode in the ith region of the axon region. Meanwhile, $\psi^e_{\mathrm{jt},m}$ represents the transverse electric field component of the mth mode in the jth region of the NR region. Finally, $\psi^h_{\mathrm{jt},m}$ represents the transverse magnetic field component of the mth mode in the jth region of the NR region.

Therefore, the SM at the Node of Ranvier can be obtained by using the method in Ref. (Itoh, 1989), as follows:

$$\boldsymbol{S}_{22\_\mathrm{III}} = \left(\boldsymbol{I} + \boldsymbol{M}^t_{y\_\mathrm{III}} \boldsymbol{M}_{x\_\mathrm{III}}\right)^{-1} \left(\boldsymbol{I} - \boldsymbol{M}^t_{y\_\mathrm{III}} \boldsymbol{M}_{x\_\mathrm{III}}\right) \quad (15 - 1)$$

$$\boldsymbol{S}_{21\_\mathrm{III}} = 2\left(\boldsymbol{I} + \boldsymbol{M}^t_{y\_\mathrm{III}} \boldsymbol{M}_{x\_\mathrm{III}}\right)^{-1} \boldsymbol{M}^t_{y\_\mathrm{III}} \boldsymbol{M}_{x\_\mathrm{III}} \quad (15 - 2)$$

$$\boldsymbol{S}_{12\_\mathrm{III}} = \boldsymbol{M}_{x\_\mathrm{III}} \left(\boldsymbol{I} + \boldsymbol{S}_{22\_\mathrm{III}}\right) \quad (15 - 3)$$

$$\boldsymbol{S}_{11\_\mathrm{III}} = \boldsymbol{M}_{x\_\mathrm{III}} \boldsymbol{S}_{21\_\mathrm{III}} - \boldsymbol{I} \quad (15 - 4)$$

where

$$\boldsymbol{M}_{x\_\mathrm{III}} = \left(\boldsymbol{Z}^2_{axon} \boldsymbol{F}_{axon}\right)^{-1} \left(\boldsymbol{f}_{NR} \boldsymbol{Z}_{axon} \boldsymbol{Z}_{NR}\right) \quad (16 - 1)$$

$$\boldsymbol{M}_{y\_\mathrm{III}} = \left(\boldsymbol{Z}^2_{axon} \boldsymbol{F}^h_{axon}\right)^{-1} \left(f^h_{NR} \boldsymbol{Z}_{axon} \boldsymbol{Z}_{NR}\right) \quad (16 - 2)$$

and I is the unit matrix. Each term in the CM is given by Eq. 14, and its matrix expression is as follows:

$$\boldsymbol{F}_{\mathrm{axon}} = \begin{bmatrix} F_{1,1}+F_{2,1}+F_{3,1} & \cdots & 0 \\ \vdots & \ddots & \vdots \\ 0 & \cdots & F_{1,N}+F_{2,N}+F_{3,N} \end{bmatrix}_{(N\times N)} \quad (17 - 1)$$

$$\boldsymbol{F}^h_{\mathrm{axon}} = \begin{bmatrix} F^h_{1,1}+F^h_{2,1}+F^h_{3,1} & \cdots & 0 \\ \vdots & \ddots & \vdots \\ 0 & \cdots & F^h_{1,N}+F^h_{2,N}+F^h_{3,N} \end{bmatrix}_{(N\times N)} \quad (17 - 2)$$

$$\boldsymbol{f}_{\mathrm{NR}} = \begin{bmatrix} f_{41,11}+f_{52,11}+f_{53,11} & \cdots & f_{41,1M}+f_{52,1M}+f_{53,1M} \\ \vdots & \ddots & \vdots \\ f_{41,N1}+f_{52,N1}+f_{53,N1} & \cdots & f_{41,NM}+f_{52,NM}+f_{53,NM} \end{bmatrix}_{(N\times M)} \quad (17 - 3)$$

$$\boldsymbol{f}^h_{\mathrm{NR}} = \begin{bmatrix} f^h_{41,11}+f^h_{52,11}+f^h_{53,11} & \cdots & f^h_{41,1M}+f^h_{52,1M}+f^h_{53,1M} \\ \vdots & \ddots & \vdots \\ f^h_{41,N1}+f^h_{52,N1}+f^h_{53,N1} & \cdots & f^h_{41,NM}+f^h_{52,NM}+f^h_{53,NM} \end{bmatrix}_{(N\times M)} \quad (17 - 4)$$

$$\boldsymbol{Z}_{\mathrm{axon}} = \begin{bmatrix} P^{-0.5}_{1,axon} & \cdots & 0 \\ \vdots & \ddots & \vdots \\ 0 & \cdots & P^{-0.5}_{N,axon} \end{bmatrix} \quad (17 - 5)$$

$$\boldsymbol{Z}_{\mathrm{NR}} = \begin{bmatrix} P^{-0.5}_{1,NR} & \cdots & 0 \\ \vdots & \ddots & \vdots \\ 0 & \cdots & P^{-0.5}_{M,NR} \end{bmatrix} \quad (17 - 6)$$

where $\boldsymbol{Z}_{\mathrm{axon}}$ and $\boldsymbol{Z}_{\mathrm{NR}}$ are the normalized matrices, which can be determined by Eq. 10. The SM of the boundary IV can be solved by the same methods. Then, the SM of the entire NR can be obtained by the cascade formula of two-port networks (Chu and Itoh, 1986).

Results and discussion

Dispersion curves and field distributions of different modes

The dispersion curves of the guided modes in the nerve fiber can be obtained by solving Eq. 7. The results are shown in Figure 3. Here, the radii of the three regions of the model are set at $R_1 = 8\mu$m, $R_2 = 10\mu$m, and $R_3 = 20\mu$m (Kwon et al., 2017). The refractive indexes of the medium in the three regions are set as $n_1 = 2.1$, $n_2 = 3$, and $n_3 = 2$ (Liu et al., 2019), and the dielectric constants can be expressed as $\varepsilon_i = n_i^2$. Meanwhile, we will further investigate the effect of the difference in the dielectric constant between the myelin sheath, and the internal and external fluids on the transmission of the THz-FIR wave.

B is the relative propagation constant, which can be represented as $B = \beta_z/k_0$. k_0 is the vacuum propagation constant and is expressed as $k_{=0} = \omega\sqrt{\varepsilon_0\mu_0}$. As shown in Figure 3, we only show the case of $m = 0$, 1, 2, and 3, but in practice the mode order n can take any value. Because the outer boundary of the nerve fiber is a metal tube wall with incomplete conductance, the tangential electric field on the outer boundary surface is not zero and the transmitted electromagnetic waves will no longer be pure TE mode or TM mode. Similar to the structure of optical fibers, the main transmission mode of terahertz waves in myelinated nerve fibers is mainly HEM mixed mode. According to the dominance of electric and magnetic fields, the modes obtained under the nerve fiber are denoted as the HEmn and EHmn hybrid modes when m > 1 (or TE0n or TM0n modes).

As can be seen from the dispersion curves in Figures 3A, C, both myelinated and unmyelinated nerve fibers transmit independent patterns, and each mode has a different propagation constant and corresponding transverse cutoff wavenumber at a given frequency. Hence, for any given excitation signal, the mode that satisfies the transmission characteristics can be found by the dispersion curve. Meanwhile, axons encased in high-refractive myelin sheaths

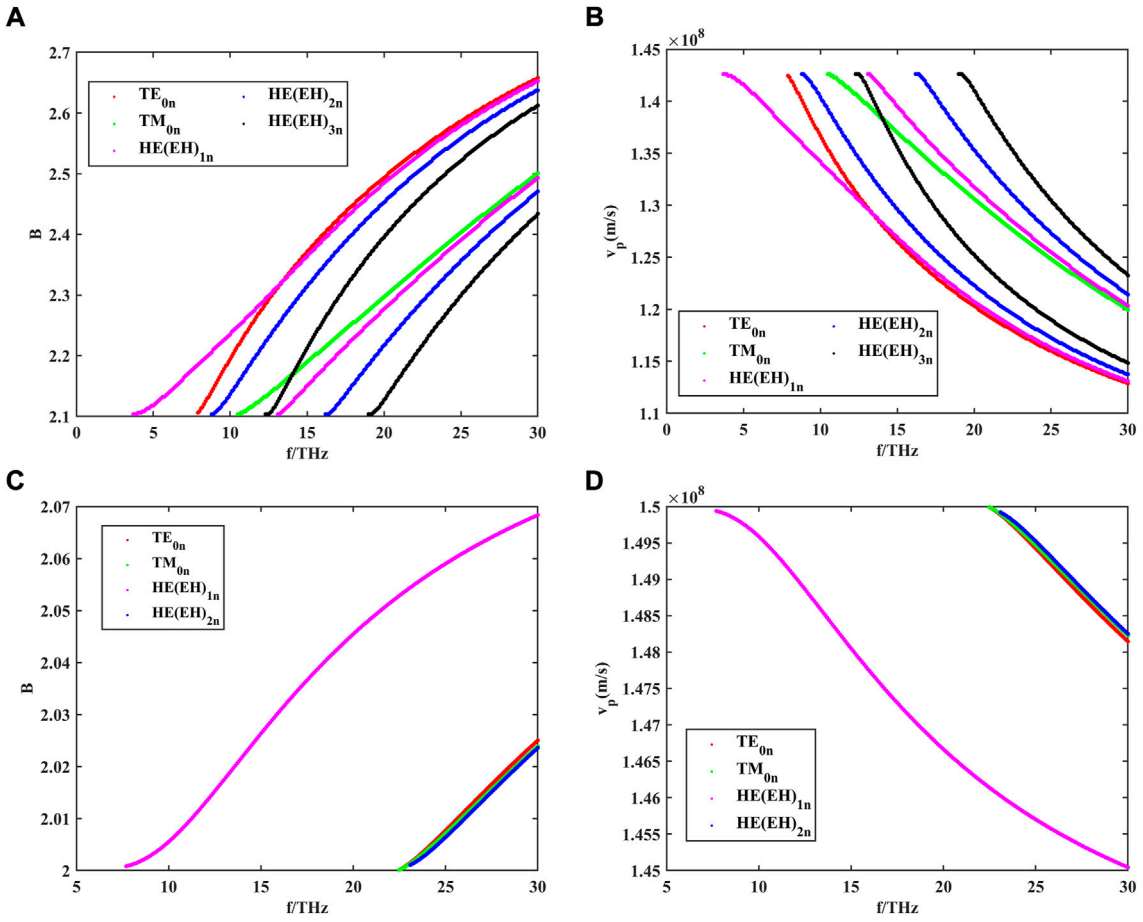

FIGURE 3
(A) Dispersion curves of different guided modes in the myelinated nerve fibers within the frequency range of 0–30 THz, where *m* is the number of angular variations; **(B)** phase velocity of different guided modes in the myelinated nerve fibers within the frequency range of 0–30 THz; **(C)** dispersion curves of different guided modes in the unmyelinated nerve fibers within the frequency range of 0–30 THz; and **(D)** phase velocity of different guided modes in the unmyelinated nerve fibers within the frequency range of 0–30 THz.

greatly increase the number of modes that can be transmitted in nerve fibers compared to bare axons. By using Eq. 18, we further investigated the phase velocities of different modes of propagation in myelin-wrapped and bare axons. The calculated results are shown in Figures 3B, D. The transmission speed of THz waves in nerve fibers can reach 108 m/s, which is much higher than the propagation speed of action potential in myeloid axons (order of magnitude 102 m/s). Therefore, this unique biological structure is more conducive to supporting long-distance and high-speed communication between nerve cells.

$$v_p = \frac{\omega}{\beta_z} \tag{18}$$

To further analyze the number of guided modes that nerve fibers can transmit, we investigate the effect of the difference between the dielectric constant of the myelin sheath and internal fluid on the number of guided modes when f = 30 THz. The results are shown in Figure 4.

The results show that the number of guided modes increases with the increase of the difference between the dielectric constants of the myelin sheath and internal fluid, which indicates that the nerve fiber can transmit THz signals to a greater extent in the frequency band with a higher permittivity of the myelin sheath. In addition, the lateral field distributions of different modes can be obtained by taking the results of Figure 3 into Eq. 6, the results are shown in Figure 5. Here, Figures 5A1–E1 show the electric field intensities and their vector diagrams of the first five modes of THz-FIR wave transmission at the nerve fiber port. Figures 5A2–E2 show the magnetic field intensities and their vector diagrams.

The results show that the energies of electric and magnetic fields are mainly concentrated in the myelin region in both fundamental and higher modes. To compare the influence of

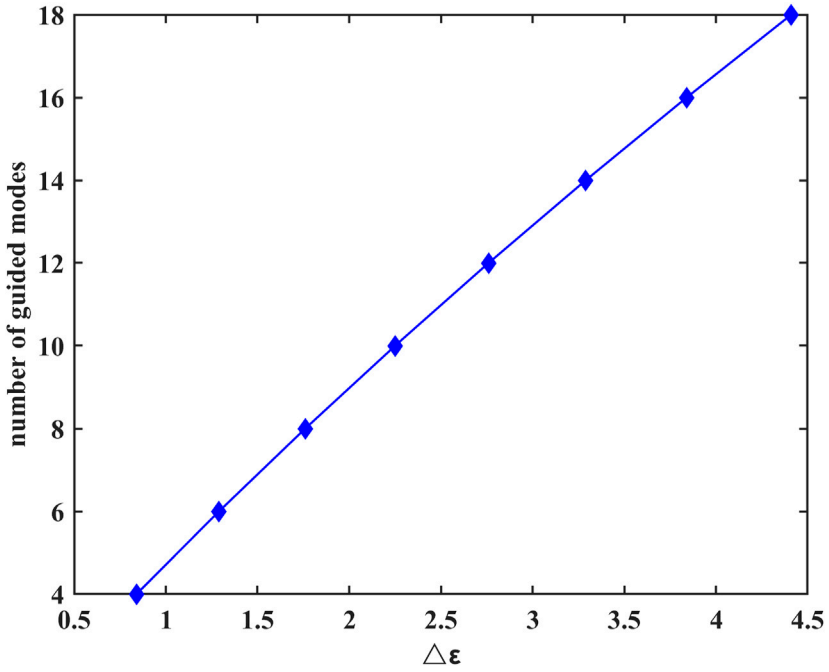

FIGURE 4
Difference between the dielectric constant of the myelin sheath and internal fluid on the number of guided modes at f = 30 THz.

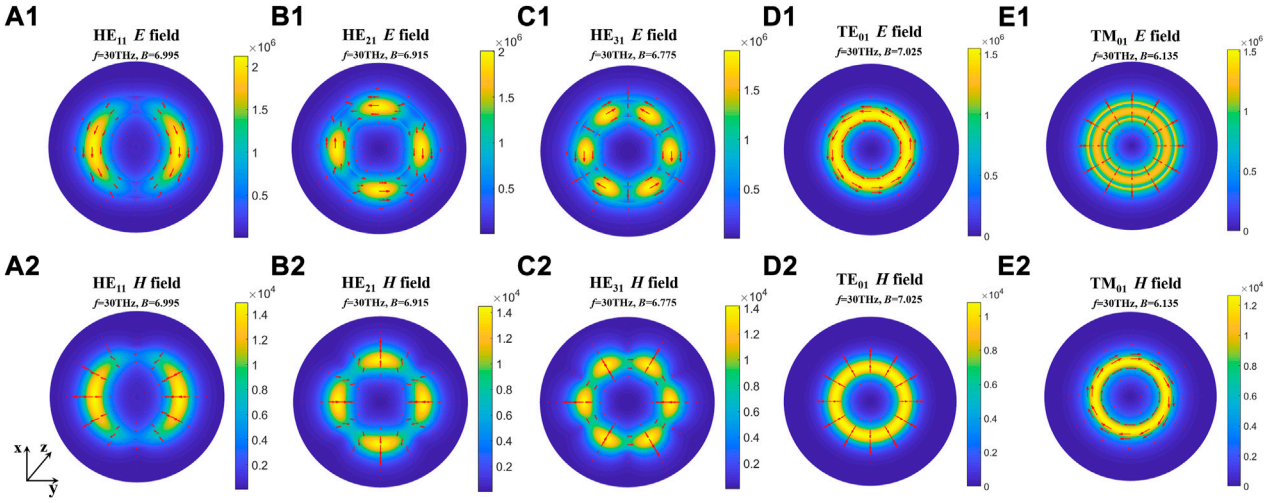

FIGURE 5
The lateral field distributions of different modes. **(A1-E1)** Electric field intensities and their vector diagrams of the first five modes; **(A2-E2)** magnetic field intensities and their vector diagrams of the first five modes.

different myelin dielectric constants and modes on the energy distribution, we conducted the following supplementary studies. The results are shown in Figure 6.

It can be seen from Figure 6 that the energy in the myelinated region increases as the difference in dielectric constants increases. At the same frequency, lower-order modes with high

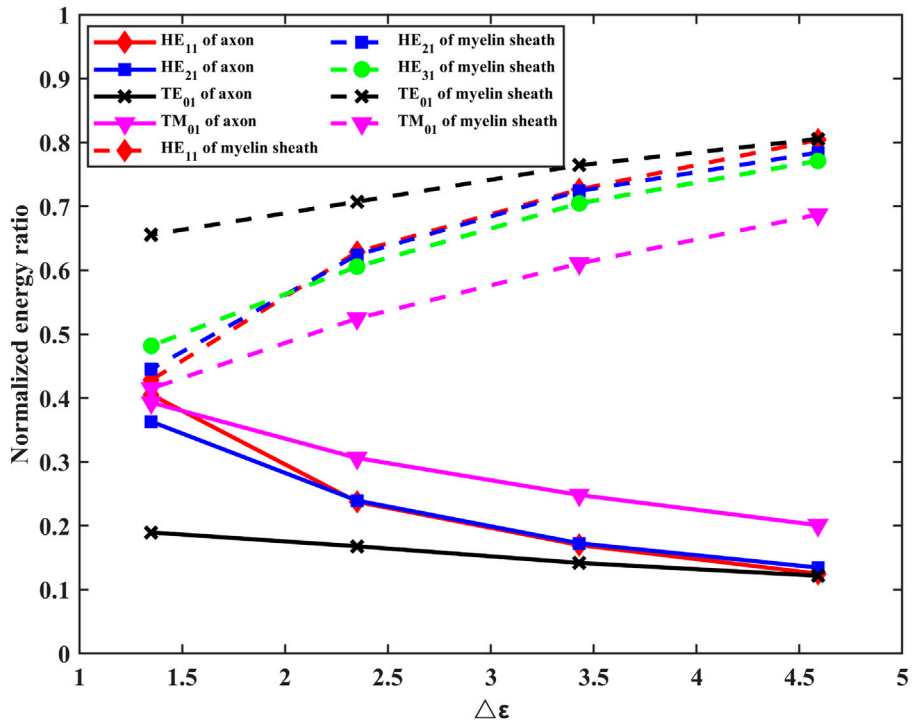

FIGURE 6
Effects of changes in the permittivity of myelin sheaths on energy distribution in axons, myelin sheaths, and fluid regions.

propagation constants concentrate energy more efficiently in the myelin sheath region.

Transmission characteristics of THz-FIR waves in nerve fibers

The complex permittivity of a polar solution can be expressed as:

$$\varepsilon = \varepsilon' - j\left(\varepsilon'' + \frac{\sigma}{\omega}\right) \tag{19}$$

where ε'' is the imaginary part of the permittivity, representing the polarization loss in the nerve fiber. Meanwhile, σ is the electrical conductivity, representing the ohmic loss of the nerve fiber. During the simulation, we take $\varepsilon'' = 0.1$, $\sigma = 30.9$S/m. The normalized Poynting vector of the longitudinal transmission THz-FIR waves in the nerve fibers are shown in Figure 7. It can be seen that myelinated nerve fibers can greatly reduce the loss caused by the absorption of polar liquids, such as water.

We further investigate the effects of different myelin sheath thickness and dielectric constant on THz-FIR wave transmission. The theoretical calculation results of HE11 mode are shown in Figure 8.

Figure 8 shows the relationship between the maximum attenuation of THz-FIR waves traveling along the 100 μm long axon with the difference between the dielectric constants of the myelin sheath and the internal and external fluids, and the thickness of the myelin sheath when the frequency is 30 THz. It can be seen that with the increase of the permittivity and thickness of the myelin sheath, the attenuation of THz-FIR waves is greatly reduced. This indicates that the bearing capacity of the nerve fibers in different positions in the organism for the transmission of the THz-FIR wave is different. Thicker nerve fibers (e.g., squid's spinal nerve) facilitate long-distance transmission of THz-FIR wave.

Transmission characteristics at nodes of Ranvier

As an important physical parameter, the SM can be used to calculate the energy transfer process at the nodes of Ranvier. The calculation process of the SM is shown in Eqs 16 and 17. Here, we set the gap width of the nodes of Ranvier to 2 μm, the thickness of myelin sheath to 2 μm, the length of the axon to 100 μm, and the permittivity of three regions to $\varepsilon_1 = 4$, $\varepsilon_2 = 9$, and $\varepsilon_3 = 4.41$, respectively. We then calculated the S11 curve and S21 curve of the node of Ranvier and compared them with the calculation

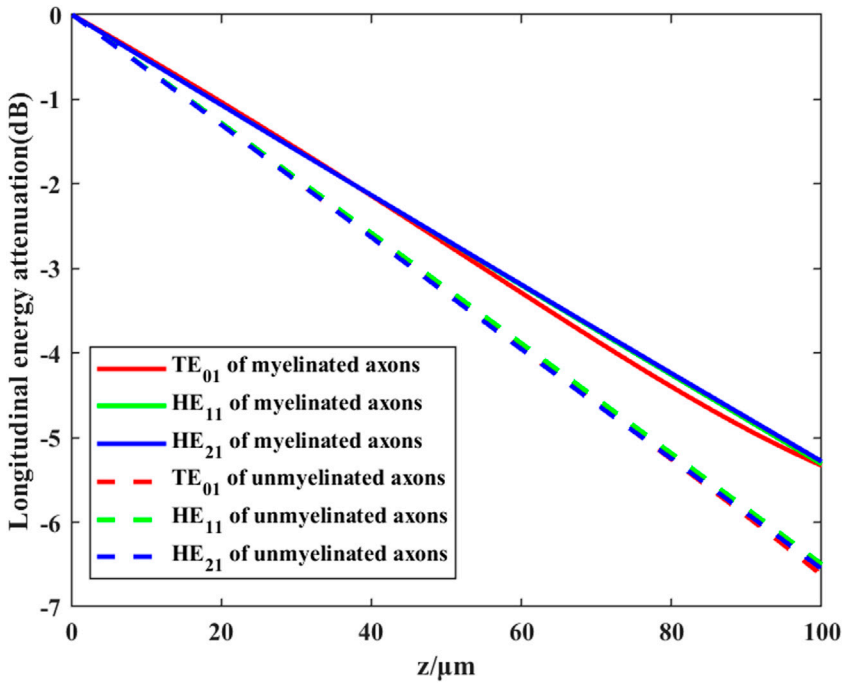

FIGURE 7
Transmission efficiency of different modes of THz-FIR waves in myelinated and unmyelinated nerve fibers at f = 30 THz.

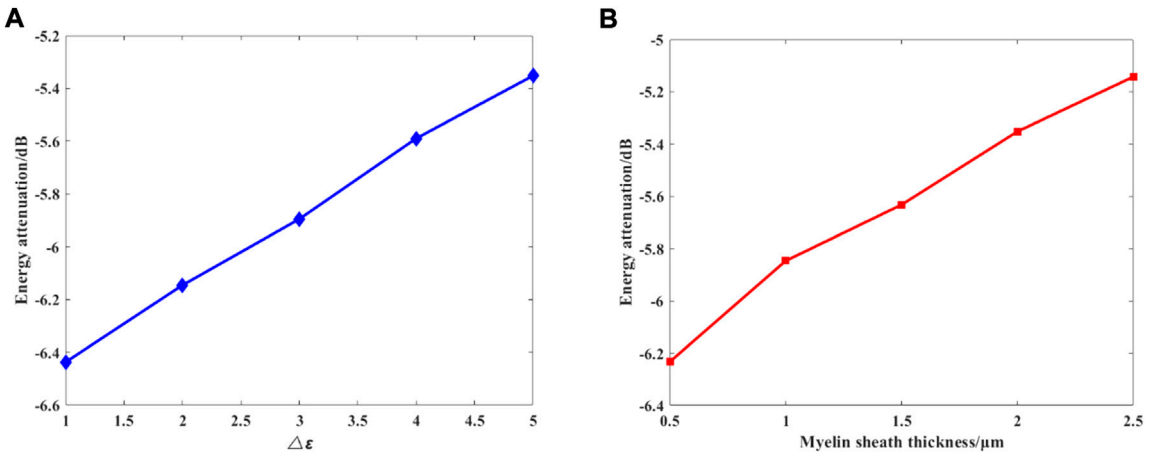

FIGURE 8
(A) Changes in the permittivity of the myelin sheath, and d_{myelin} = 2μm; **(B)** changes in the thickness of myelin sheath, and $\Delta\varepsilon$ = 5.

results of the CST simulation software. The results are shown in Figure 9.

Compared with the result calculated by CST software, the results of the theoretical calculation are consistent with those from CST simulation software, which verifies the accuracy of our method. At f = 12.5 THz, S11 has the minimum value. This indicates that the reflection of THz-FIR transmission is the smallest at this time, which is mainly related to the width of the nodes of Ranvier. At the same time, S21 is greater than −5dB, which indicates that the THz-FIR wave has good transmission

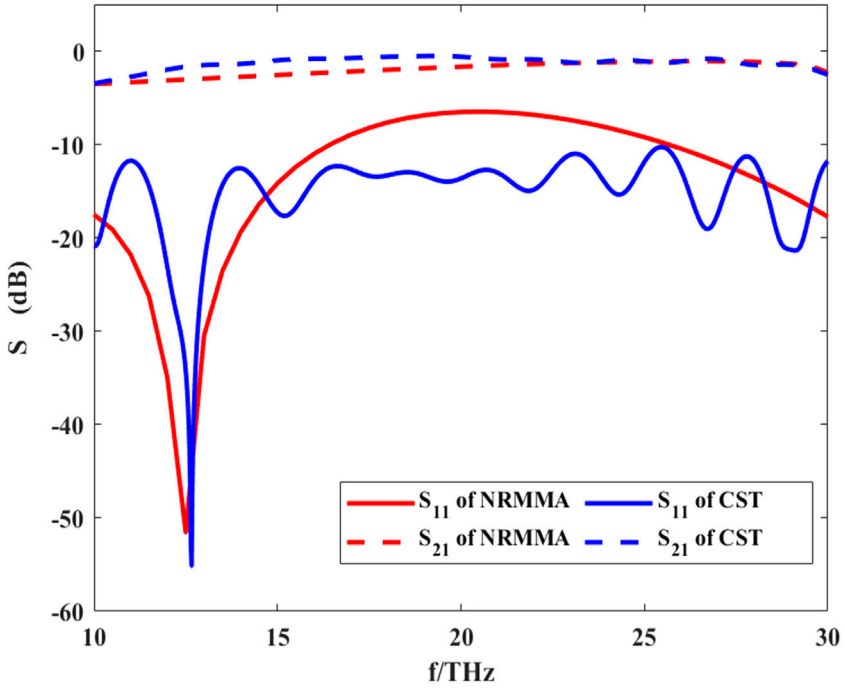

FIGURE 9
S-parameters of THz-FIR wave propagation at the nodes of Ranvier calculated by RNMMA and CST.

performance through the Ranvier junction. Meanwhile, the results also show that the S21 curve maintains a relatively stable value in the range of 10–30 THz and its value is greater than −5dB. This indicates that the node of Ranvier gap width (2 μm) has a weak influence on the transmission of THz waves. This happens because when the periodic gap width is much smaller than the wavelength of the THz-FIR wave, the THz-FIR wave can pass through the structure with minimal loss. This method provides theoretical support for further research on the interaction between THz-FIR waves and ion motion at the nodes of Ranvier.

Conclusion

In this article, we investigated the propagation characteristics of THz-FIR waves at the nerve fibers and the nodes of Ranvier by theoretical analysis. We aimed to study the new physical mechanism of high-frequency signal transmission in the nervous system. First, the exact expressions of the guiding mode and radiation mode in the nerve fiber have been obtained by theoretical analysis and the dispersion curves of the transmission of the THz-FIR wave in the nerve fiber have been obtained by applying proper boundary conditions. Myelinated nerve fibers can support more modes of transmission than unmyelinated bare axons, which greatly enhances the possibility that THz-FIR waves can travel through nerve fibers. It was found from the calculation results of field distributions that the myelinated nerve fibers could concentrate the field energy within the myelin region to a great extent, thus avoiding the strong absorption of THz-FIR waves by the surrounding polar liquids. Meanwhile, the thickness and permittivity of myelin sheath had a considerable influence on the propagation of THz-FIR wave along the nerve fiber. With the increase in the thickness and permittivity of the myelin sheath, the attenuation of the terahertz wave in longitudinal transmission gradually decreases.

We established a pattern-matching algorithm for the first time, named RNMMA, which was used to investigate the electromagnetic wave propagation and reflection characteristics of longitudinal discontinuities at the axon and the nodes of Ranvier. The accuracy of our algorithm has been verified by comparing it with the calculation results of CST.

Data availability statement

The original contributions presented in the study are included in the article/Supplementary Material; further inquiries can be directed to the corresponding authors.

Author contributions

YG and SW designed the research and revised the manuscript. LG and DX conducted the study and wrote the manuscript. KW, YS, QZ, HN, and CL validated the data and helped revise the manuscript.

Funding

This work was supported by the National Natural Science Foundation of China (T224100002, 61921002, and 61988102).

Conflict of interest

The authors declare that the research was conducted in the absence of any commercial or financial relationships that could be construed as a potential conflict of interest.

Publisher's note

All claims expressed in this article are solely those of the authors and do not necessarily represent those of their affiliated organizations, or those of the publisher, the editors, and the reviewers. Any product that may be evaluated in this article, or claim that may be made by its manufacturer, is not guaranteed or endorsed by the publisher.

References

Adolphs, R. (2015). The unsolved problems of neuroscience. *Trends cognitive Sci.* 19, 173–175. doi:10.1016/j.tics.2015.01.007

Chao, T., Guang-Xu, Z., Jun, H., Jun-Hong, L., Wu, K., Ji, W., et al. (2021). Nonthermal and reversible control of neuronal signaling and behavior by midinfrared stimulation. *Proc. Natl. Acad. Sci. U. S. A.* 70, e2015685118. doi:10.1073/pnas.2015685118

Chu, T. S., and Itoh, T. (1986). Generalized scattering matrix method for analysis of cascaded and offset microstrip step discontinuities. *IEEE Trans. Microw. Theory Tech.* 34, 280–284. doi:10.1109/tmtt.1986.1133323

Dietrich and Marcuse (1970). Radiation losses of the dominant mode in round dielectric waveguides. *Bell Syst. Tech. J.* 49, 1665–1693. doi:10.1002/j.1538-7305.1970.tb04284.x

Friede, R. L., and Bischhausen, R. (1982). How are sheath dimensions affected by axon caliber and internode length? *Brain Res.* 235, 335–350. doi:10.1016/0006-8993(82)91012-5

Guo, L., Bo, W., Wang, K., Wang, S., and Gong, Y. (2022). Theoretical investigation on the effect of terahertz wave on Ca2+ transport in the calcium channel. *Iscience* 25, 103561–110042. doi:10.1016/j.isci.2021.103561

Hu, Z.-H., Lv, W.-P., Hui, D.-X., Wang, X.-J., and Wang, Y.-N. (2022). Permeability enhancement of the KcsA channel under radiation of a terahertz wave. *Phys. Rev. E* 105, 024104. doi:10.1103/physreve.105.024104

Itoh, T. (1989). *Numerical techniques for microwave and millimeter wave passive structures*. New Jersey, U.S.: John Wiley & Sons.

Kumar, S., Boone, K., Tuszynski, J., Barclay, P., and Simon, C. (2016). Possible existence of optical communication channels in the brain. *Sci. Rep.* 6, 36508. doi:10.1038/srep36508

Kwon, J., Kim, M., Park, H., Kang, B.-M., Jo, Y., Kim, J.-H., et al. (2017). Label-free nanoscale optical metrology on myelinated axons *in vivo*. *Nat. Commun.* 8, 1832–1839. doi:10.1038/s41467-017-01979-2

Laman, N., Harsha, S. S., Grischkowsky, D., and Melinger, J. S. (2008). High-resolution waveguide THz spectroscopy of biological molecules. *Biophysical J.* 94, 1010–1020. doi:10.1529/biophysj.107.113647

Li, Y., Chang, C., Zhu, Z., Sun, L., and Fan, C. (2021). Terahertz wave enhances permeability of the voltage-gated calcium channel. *J. Am. Chem. Soc.* 143, 4311–4318. doi:10.1021/jacs.0c09401

Liu, G. (2018). The conjectures on physical mechanism of vertebrate nervous system. *Chin. Sci. Bull.* 63, 3864–3865. doi:10.1360/n972018-01143

Liu, G., Chang, C., Qiao, Z., Wu, K., Zhu, Z., Cui, G., et al. (2019). Myelin sheath as a dielectric waveguide for signal propagation in the mid-infrared to terahertz spectral range. *Adv. Funct. Mat.* 29, 1807862. doi:10.1002/adfm.201807862

Liu, X., Qiao, Z., Chai, Y., Zhu, Z., Wu, K., Ji, W., et al. (2021). Nonthermal and reversible control of neuronal signaling and behavior by midinfrared stimulation. *Proc. Natl. Acad. Sci. U. S. A.* 118, e2015685118. doi:10.1073/pnas.2015685118

Marcuse, D. (1973). Coupled mode theory of round optical fibers. *Bell Syst. Tech. J.* 52, 817–842. doi:10.1002/j.1538-7305.1973.tb01992.x

Miller, L. M., and Dumas, P. (2010). From structure to cellular mechanism with infrared microspectroscopy. *Curr. Opin. Struct. Biol.* 20, 649–656. doi:10.1016/j.sbi.2010.07.007

Tegmark, M. (2015). Consciousness as a state of matter. *Chaos, Solit. Fractals* 76, 238–270. doi:10.1016/j.chaos.2015.03.014

Tononi, G. (2004). An information integration theory of consciousness. *BMC Neurosci.* 5, 42–22. doi:10.1186/1471-2202-5-42

Wang, K., Wang, S., Yang, L., Wu, Z., Zeng, B., and Gong, Y. (2022). THz trapped ion model and THz spectroscopy detection of potassium channels. *Nano Res.* 15, 3825–3833. doi:10.1007/s12274-021-3965-z

Wetzel, D. L., and Levine, S. M. (1999). Imaging molecular chemistry with infrared microscopy. *Science* 285, 1224–1225. doi:10.1126/science.285.5431.1224

Wu, K., Qi, C., Zhu, Z., Wang, C., Song, B., and Chang, C. (2020). Terahertz wave accelerates DNA unwinding: A molecular dynamics simulation study. *J. Phys. Chem. Lett.* 11, 7002–7008. doi:10.1021/acs.jpclett.0c01850

Xiang, Z., Tang, C., Yan, L., Chang, C., and Liu, G. (2020). A new viewpoint and model of neural signal generation and transmission: Signal transmission on myelinated neuron. *Chin. Phys. B* 29, 108701. doi:10.1088/1674-1056/abaee9

Zangari, A., Micheli, D., Galeazzi, R., and Tozzi, A. (2018). Node of ranvier as an array of bio-nanoantennas for infrared communication in nerve tissue. *Sci. Rep.* 8, 539. doi:10.1038/s41598-017-18866-x

frontiers | Frontiers in Bioengineering and Biotechnology

TYPE Original Research
PUBLISHED 14 December 2022
DOI 10.3389/fbioe.2022.1052069

OPEN ACCESS

EDITED BY
Junhong Lü,
Shanghai Advanced Research Institute (CAS), China

REVIEWED BY
Qian Xiaoqin,
Jiangsu University Affiliated People's Hospital, China
Guanjun Xu,
East China Normal University, China

*CORRESPONDENCE
Feng Qi,
qifeng@sia.cn
Junhua Zhao,
jhzhao@cmu.edu.cn

†These authors have contributed equally to this work and share first authorship

SPECIALTY SECTION
This article was submitted to Nanobiotechnology, a section of the journal Frontiers in Bioengineering and Biotechnology

RECEIVED 23 September 2022
ACCEPTED 28 November 2022
PUBLISHED 14 December 2022

CITATION
Shi H, Li T, Liu Z, Zhao J and Qi F (2022), Early detection of gastric cancer *via* high-resolution terahertz imaging system.
Front. Bioeng. Biotechnol. 10:1052069.
doi: 10.3389/fbioe.2022.1052069

Early detection of gastric cancer *via* high-resolution terahertz imaging system

Han Shi[1,2,3†], Tenghui Li[2,3†], Zhaoyang Liu[1,4†], Junhua Zhao[2,3*] and Feng Qi[1,4*]

[1]Shenyang Institute of Automation, Chinese Academy of Sciences, Shenyang, China, [2]Department of Surgical Oncology and General Surgery, the First Hospital of China Medical University, Shenyang, China, [3]Key Laboratory of Precision Diagnosis and Treatment of Gastrointestinal Tumors (China Medical University), Ministry of Education, Shenyang, China, [4]Key Laboratory of Terahertz Imaging and Sensing, Liaoning Province, Shenyang, China

Terahertz (THz) wave has demonstrated a good prospect in recent years, but the resolution is still one of the problems that restrict the application of THz technology in medical imaging. Paraffin-embedded samples are mostly used in THz medical imaging studies, which are thicker and significantly different from the current gold standard slice pathological examination in sample preparation. In addition, THz absorption in different layers of normal and cancerous tissues also remains to be further explored. In this study, we constructed a high-resolution THz imaging system to scan non-tumorous adjacent tissue slices and gastric cancer (GC) tissue slices. In this system, a THz quantum cascade laser emitted a pulsed 3 THz signal and the transmitted THz wave was received by a THz detector implemented in a 65 nm CMOS process. The slice thickness was only 20 μm, which was close to that of the medical pathology examination. We successfully found THz transmittance differences between different layers of normal gastric tissues based on THz images, and the resolution could reach 60 μm for the first time. The results indicated that submucosa had a lower THz transmittance than that of mucosa and muscular layer in non-tumorous adjacent tissue. However, in GC tissue, THz transmittance of mucosa and submucosa was similar, caused by the decreased transmittance of mucosa, where the cancer occurs. Therefore, we suppose that the similar terahertz transmittance between gastric mucosa and submucosa may indicate the appearance of cancerization. The images obtained from our THz imaging system were clearer than those observed with naked eyes, and can be directly compared with microscopic images. This is the first application of THz imaging technology to identify non-tumorous adjacent tissue and GC tissue based on the difference in THz wave absorption between different layers in the tissue. Our present work not only demonstrated the potential of THz imaging to promote early diagnosis of GC, but also suggested a new direction for the identification of normal and cancerous tissues by analyzing differences in THz transmittance between different layers of tissue.

KEYWORDS

terahertz, imaging, gastric cancer, H&E staining, high-resolution

1 Introduction

Gastric cancer (GC), as one of the most common cancer worldwide, is the world's major healthcare burden (Joshi and Badgwell, 2021). In recent years, many studies on improving prognosis of patients with GC have been conducted (Alberts et al., 2003; Charalampakis et al., 2018; Salati et al., 2019), and 5-year survival rate can reach 90% in those at early stage (Song et al., 2017). However, the outcome of advanced GC is still poor (Digklia and Wagner, 2016). GC usually infiltrates from the superficial mucosa to the deeper tissue and is frequently diagnosed at advanced stage (Bray et al., 2018). Thus, it is important to improve the diagnostic method of GC.

At present, the imaging diagnosis of cancer mainly depends on computed tomography (CT) and magnetic resonance imaging (MRI). CT as a common technique used to assess tumor invasion, has a short scan time and can image both thorax and abdomen at the same time (Borggreve et al., 2019). MRI is significantly more sensitive to minor lesions and avoids radiation exposure (Brenner et al., 2014; Ohana et al., 2018). However, health concerns may lead to over-testing of patients (Jankauskaite et al., 2022). This phenomenon also occurs in low-income and middle-income countries (Albarqouni et al., 2022). It could be harm to patients and cause unnecessary financial costs. For example, the ionizing radiation from CT scans could cause DNA damage and increase the risk of cancer (Pearce et al., 2012). And the MRI has a high cost and relatively long acquisition times (Bor et al., 2016; Heidkamp et al., 2021). In addition, the sensitivity of CT and MRI in the detection of micro lesions of cancer still needs to be improved (Gai et al., 2021; Liu et al., 2021). As a new type of diagnostic technology, optical imaging has the characteristics of no ionizing radiation exposure and high spatial resolution in cancer diagnosis (Wang et al., 2018). Nevertheless, this technique often requires the use of additional specific probes or dyes, which limits its clinical application. The gold standard for cancer diagnosis is pathological examination. However, it has a long diagnosis period. In addition, compared with examinations based on H&E staining slices, the results of electromagnetic wave detection could be relatively objective. Therefore, there is an urgent need for a technique, which is non-invasive and high-accuracy for cancer diagnosis.

The discovery of new electromagnetic waves often leads to the development of new medical diagnostic and imaging tools (Xiang et al., 2020, Lou et al., 2022). Terahertz (THz) light is a class of electromagnetic waves that the frequency is in the range of 0.1–10 THz (Shumyatsky and Alfano, 2011). Unlike x-rays used in traditional examinations, THz light's frequency is about one-million-time lower. Due to this feature, THz radiation's low-energy photons, which range between 0.4 and 41 millielectronvolts (meV), have no hazard of ionizing radiation (Yang et al., 2016). THz imaging technology has made great achievements in biomedical imaging. It is quite important to extract information from THz images and a sound understanding of interactions between THz waves and tissues will contribute, including absorption, scattering, corresponding path loss *etc.* (Liu et al., 2019). Influence of the effects above can be investigated by MonteCarlo simulations, similar to the work in (Lin et al., 2022). THz imaging system can be divided into different systems according to their structures. Based on terahertz pulsed imaging (TPI) system, researchers have been able to observe the boundary between cancerous and normal tissue in laryngeal cancer, breast cancer, and mouse brain glioma (Oh et al., 2014; Chavez et al., 2018; Vohra et al., 2020; Ke et al., 2022). By using continuous-wave terahertz (CW THz) transmission or reflection scanning imaging system, the difference of THz images between cancerous and normal tissues in colon cancer and mouse brain glioma was detected

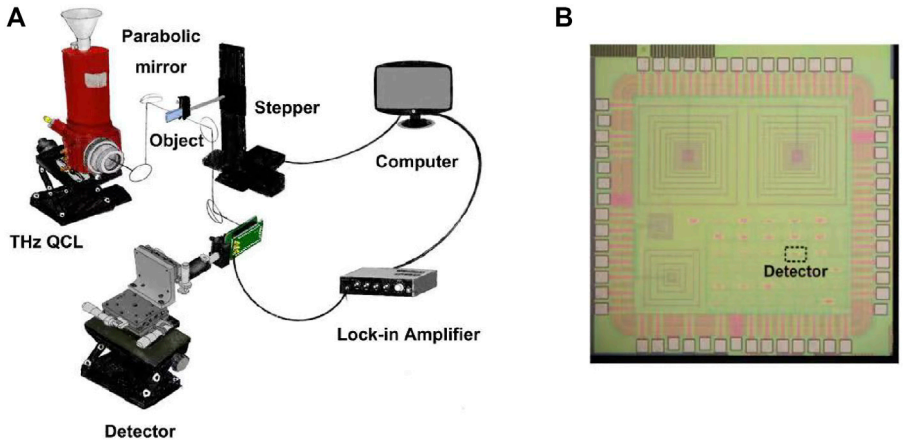

FIGURE 1
(A) Block diagram of the THz imaging system and **(B)** die photo of the THz detector.

TABLE 1 Basic information of patients included.

Patient	Sex	Age	Lesions position	T stage*	Infiltration depth	Histological type	Sample size (mm)
P1	female	42	Gastric antrum	T_3	subserosa	Mucinous adenocarcinoma	14 × 28×0.02
P2	male	52	Gastric antrum	T_4	serosa	Adenocarcinoma	13 × 22×0.02
P3	male	76	Gastric antrum	T_3	subserosa	Papillary tubular adenocarcinoma	70 × 75×0.02
P4	female	64	Gastric antrum	T_2	muscularis propria	Adenocarcinoma	16 × 15×0.02
P5	female	55	Gastric body	T_1	mucosa	Adenocarcinoma	12 × 18×0.02

*The histological depth of tumor invasion.

respectively (Wahaia et al., 2016; Wu et al., 2019). With CW THz near-field microscopy imaging system, researchers successively distinguished cancerous tissues from normal tissues in stomach and colon (Chen et al., 2015; Chen et al., 2022). Based on attenuated total reflection (ATR) imaging system, THz absorption difference between mouse brain glioma and normal mouse brain tissue was observed (Wu et al., 2022). However, previous studies usually focused on the difference in terahertz absorption between cancerous and normal tissues. Further exploration of THz absorption by different fine structures of tissue will promote the application of THz technology in clinical diagnosis. The resolution of THz imaging needs to be improved as well. The use of thinner slices instead of paraffin-embedded samples could also facilitate the observation of fine structure of the tissue. In addition, analysis of normal tissue with THz imaging technology could help explore the difference between normal and cancerous tissue, which may provide a more reliable basis for clinical diagnosis, and study the transformation process of normal tissue into cancerous tissue from the perspective of physics.

In this study, a high-resolution THz imaging system was designed. At 3 THz, the resolution of the scanned image is 60 μm, which is clearer than observation with naked eyes and can be directly compared with microscopic images. With this high-resolution imaging system, we then investigated the THz transmittance of different layers of normal and cancerous tissue by detecting slices of non-tumorous adjacent specimens and GC specimens. The variation of THz transmittance difference between different layers of normal and cancerous tissue reveals the potential of THz in assisting early diagnosis of GC.

2 Materials and methods

2.1 Experimental system setup introduction

The THz imaging system is shown in Figure 1A. A THz quantum cascade laser (QCL) emits a pulsed 3 THz signal with a repetition rate of 5 kHz and a duty cycle of 1%. Two parabolic mirrors are used to focus the THz radiation on an object, which is fixed on a two-dimensional stepper to realize scanning image. The transmitted THz radiation is collimated and focused on a THz detector by two other parabolic mirrors. The output signal of the detector is captured by a lock-in amplifier and then collected by a computer. The detector is shown in Figure 1B, which is a 3 THz detector implemented in a 65 nm CMOS process. The resolution of the imaging system is about 60 μm.

2.2 Human tissue samples

The samples were obtained from patients undergoing surgical resection of GC at the First Hospital of China Medical University during 2016. After surgery, the fresh specimens were fixed in formalin, routinely processed, and embedded in paraffin, then stored as tissue blocks. The samples were sectioned for H&E staining (5 μm) and THz imaging (20 μm), the surrounding paraffin was melted away for THz imaging, and only the relative flat tissues were selected for experiments.

2.3 Ethical approval

This study followed the principles outlined in the Declaration of Helsinki. Required specimens were collected through informed patient consent and in accordance with institutional ethical guidelines. The study protocol was reviewed and approved by the Research Ethics Committee of China Medical University (Shenyang, China).

2.4 H&E staining

The tissue slices (5 μm) were immersed in xylene for deparaffinization and rehydrated in graded ethanol solutions for staining in hematoxylin solution (5 min). They were then dipped in 1% hydrochloric acid ethanol, washed in distilled

10.3389/fbioe.2022.1052069

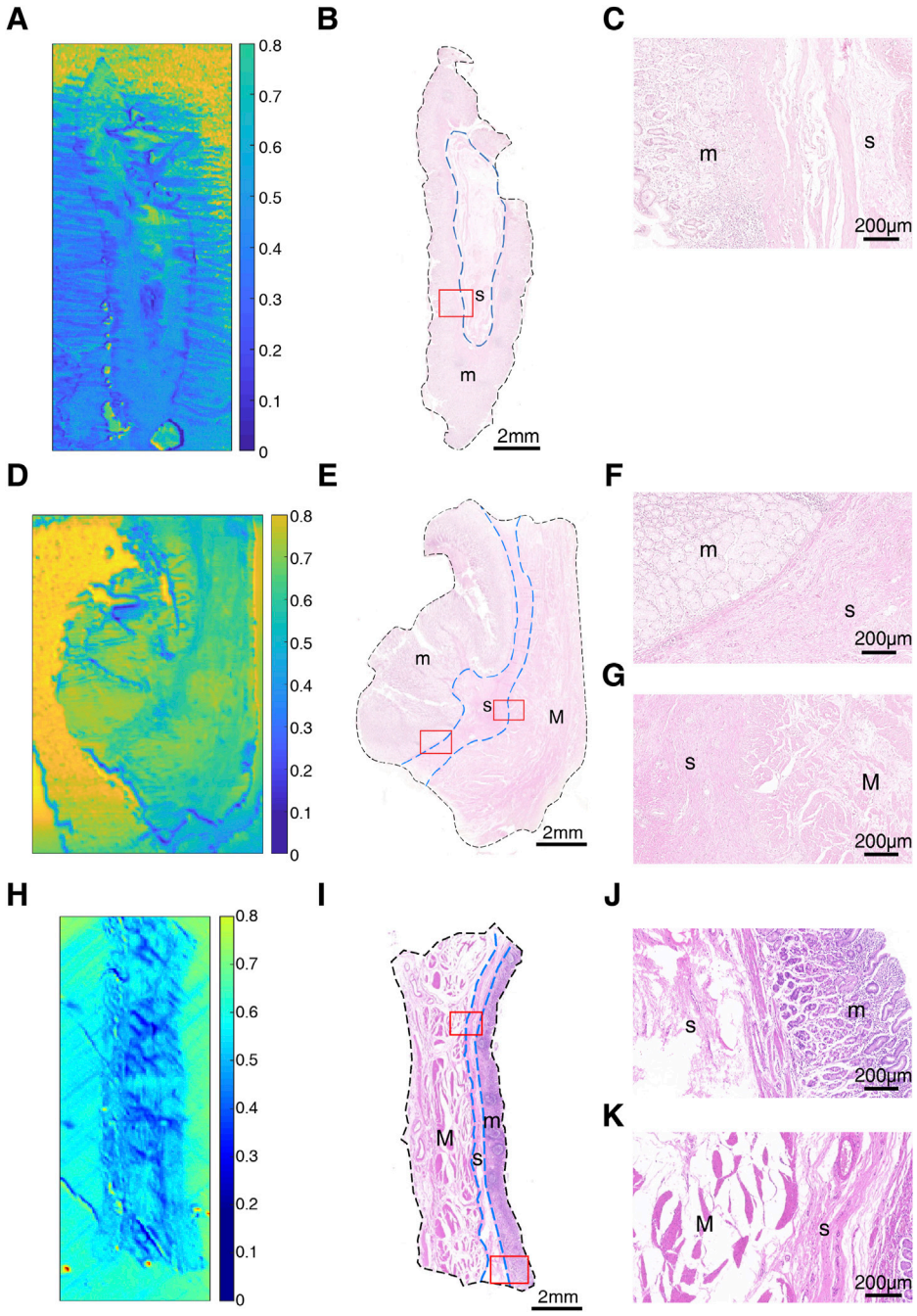

FIGURE 2
Images of non-tumorous adjacent tissue: **(A)** THz image, **(B)** H&E-stained slice, and **(C)** H&E-stained image corresponding to the region indicated by the red square in **(B)** of N1; **(D)** THz image, **(E)** H&E-stained slice, and **(F,G)** H&E-stained images corresponding to the region indicated by the red square in **(E)** of N2; **(H)** THz image, **(I)** H&E-stained slice, and **(J,K)** H&E-stained images corresponding to the region indicated by the red square in **(I)** of N3. In H&E-stained images, "m" indicates "mucosa", "s" indicates "submucosa" and "M" indicates "muscular layer". In **(B,E,I)**, the boundaries of mucosa, submucosa and muscular layer are outlined with dashed blue lines. **(C,F,J)** are boundaries between mucosa and submucosa. **(G,K)** are the boundaries between submucosa and muscular layer.

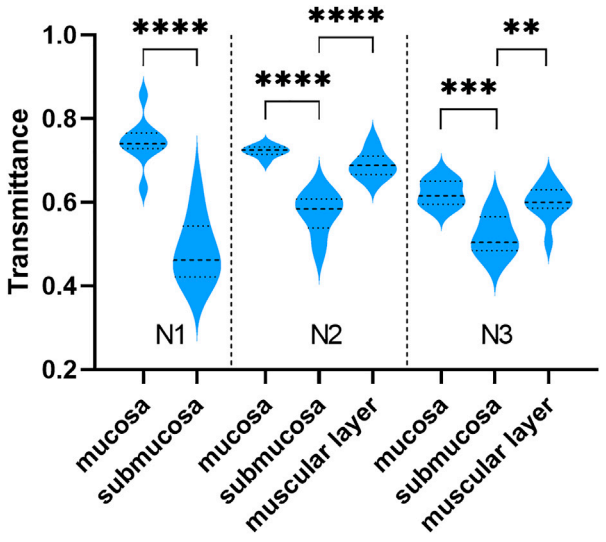

FIGURE 3
The transmittance of different layers in sample N1, N2, and N3. The transmittance of submucosa was lower than that of mucosa and muscular layer. ****: $p < 0.0001$, ***: $p < 0.001$, **: $p < 0.01$.

water, and stained in eosin solution (3 min). Finally, graded alcohol solutions were applied for dehydration and subsequent immersion in xylene. The stained slices were examined by a Leica DM4000B microscope (Leica, Wetzlar, Germany).

2.5 Relative transmittance determination

Combined with histopathological examination, the boundaries of mucosa, submucosa and muscular layer were outlined with dashed blue lines. For each layer of tissue sample in the images, we randomly select nine points in the region with uniform color to calculate the average transmittance as the transmittance of this layer. To quantify transmissivity, we calculated the relative transmittance (RT) to compare the transmittance of different layers in each of the collected samples. RT between mucosa and submucosa was defined as $RT = (T_m\text{-}T_s)/T_m$, where T_m was averaged transmittance of labeled mucosa area in the sample and T_s was averaged transmittance of labeled submucosa area in the same specimen. This was to avoid the influence of tissue variation between different samples on the overall transmittance.

2.6 Statistical analysis

All data comparisons were based on Student's *t*-test and were computed *via* standard software (SPSS v25.0; SPSS Inc., Chicago, IL, United States), by setting significance at $p < 0.05$.

3 Results

3.1 Collected samples

Overall, eight collected tissue samples were tested during the study, which included three non-tumorous adjacent tissues (NATs) (N1, N2, N3) and five primary GC lesions (T1, T2, T3, T4, T5). N1 and T1 were from a 42-year-old woman (P1); N2 and T2 were from a 52-year-old man (P2); T3 was from a 76-year-old man (P3); T4 was from a 64-year-old woman (P4); N3 and T5 were from a 55-year-old woman (P5). Patient characteristics are shown in Table 1. The general shapes of all 8 samples can be distinguished in THz image.

3.2 Difference of THz transmittance between different layers of normal gastric tissue

To explore the transmittance characteristics of normal gastric tissue, we measured and acquired THz images of non-tumorous adjacent tissue N1, N2 and N3 from three GC patients (P1, P2 and P5) (Figure 2). It is shown that THz images had a relative high resolution, corresponding to the position and shape of different tissue layers (mucosa, submucosa, and muscular layer) in H&E examination of these three samples. Figures 2A,D,H were THz images of collected NAT. The boundaries of mucosa, submucosa and muscular layer are outlined with dashed blue lines in H&E-stained slice (Figures 2B,E,I). The magnified H&E-stained images of boundaries between different layers of tissue were also presented in Figures 2C,F,G,J,K. N1 was collected from the NAT from a 42-year-old woman P1 (Figures 2A–C). The T_m and T_s in this sample were 0.745 (±0.057) and 0.485 (±0.077) respectively. The RT of N1 was 0.349. N2 was the slide of the NAT from a 52-year-old man P2 (Figures 2D–G). The T_m, T_s and T_M in this sample were 0.722 (±0.014), 0.574 (±0.048) and 0.690 (±0.031), respectively. The RT of N2 was calculated to be 0.205. N3 was the slide of the NAT from a 55-year-old woman P5 (Figures 2H,K). The T_m, T_s and T_M in this sample were 0.623 (±0.030), 0.519 (±0.047) and 0.599 (±0.042), respectively. The RT of N3 was calculated to be 0.166. RT was defined as the difference in the transmittance of mucosa and submucosa divided by mucosa transmittance. The results showed that the THz transmittance was different between mucosa and submucosa.

Although THz images could not identify tissue morphology of samples alone, it was able to distinguish the region of mucosa, submucosa, and muscular layer in normal gastric tissue through intense color contrast. As shown in Figure 3, the transmittance of submucosa is significantly lower than mucosa in all three samples. Besides, submucosa of sample N2 and N3 also presented a lower transmittance than muscular layer. The THz images of Figure 2 also clearly showed that THz transmittance of submucosa is lower than that of mucosa and muscular layer. That is, the submucosa absorbs more THz waves than mucosa and muscular layer in normal gastric tissue.

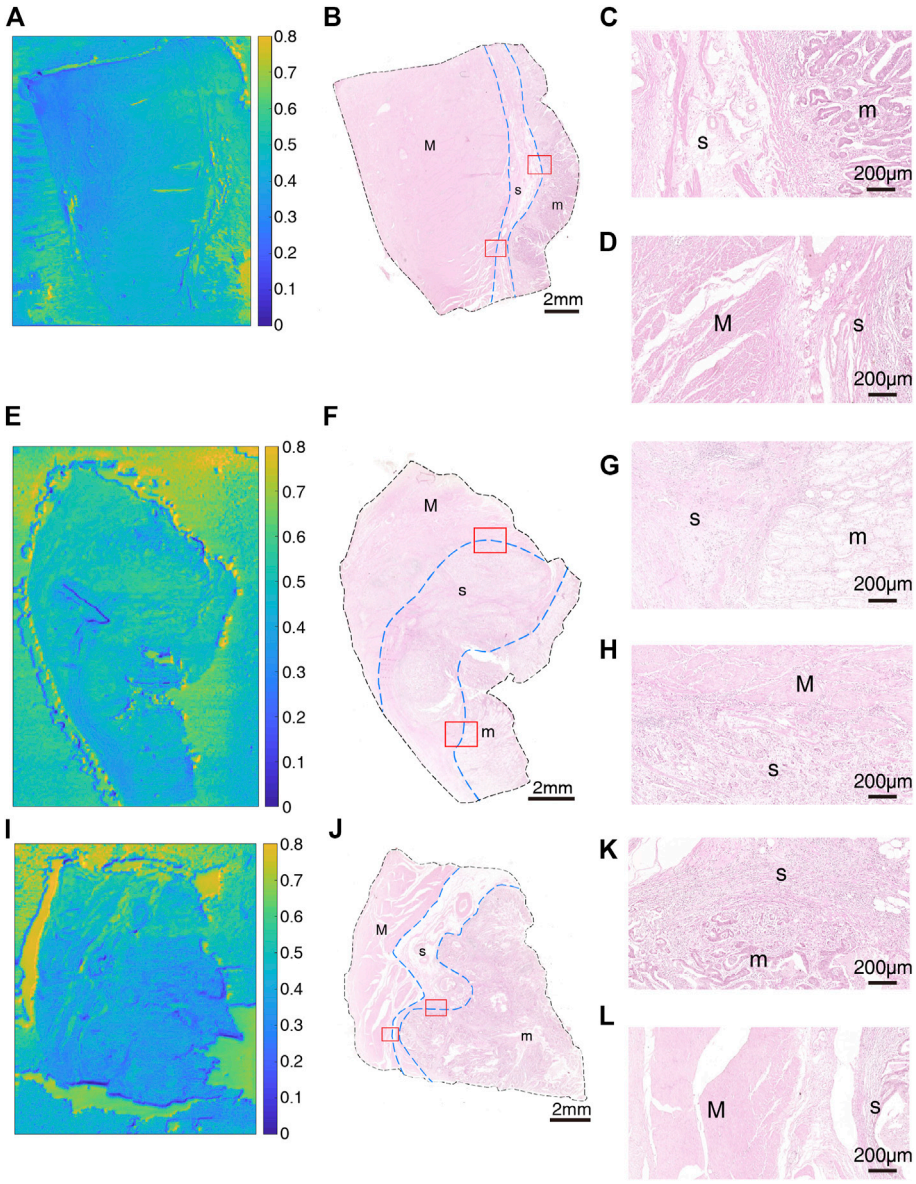

FIGURE 4
Images of GC sample: **(A)** THz image, **(B)** H&E-stained slice, and **(C,D)** H&E-stained images corresponding to the region indicated by the red square in **(B)** of T1; **(E)** THz image, **(F)** H&E-stained slice, and **(G,H)** H&E-stained images corresponding to the region indicated by the red square in **(F)** of T2; **(I)** THz image, **(J)** H&E-stained slice, and **(K,L)** H&E-stained images corresponding to the region indicated by the red square in **(J)** of T3. In H&E-stained images, "m" indicates "mucosa", "s" indicates "submucosa" and "M" indicates "muscular layer". In images **(B,F,J)**, the boundaries of mucosa, submucosa, and muscular layer are outlined with dashed blue lines. **(C,G,K)** are boundaries between mucosa and submucosa. **(D,H,L)** are boundaries between submucosa and muscular layer.

3.3 Variation of difference of THz transmittance between different layers of GC tissue

After that, we obtained THz images of primary cancer lesions T1, T2, T3, T4 and T5 from five GC patients (P1, P2, P3, P4, and P5) to explore whether there were changes in transmittance difference among different layers of GC tissue. Figures 4A,E,I and Figures 5A,E were THz images of collected GC tissues. The boundaries of mucosa, submucosa and muscular layer are outlined with dashed blue lines in H&E-stained slices (Figures 4B,F,J and Figures 5B,F). The magnified H&E-stained images of boundaries between different layers of tissue were also presented in Figures 4C,D,G,H,K,L, and Figures 5C,D,G,H. T1 was collected from the GC tissue from a 42-year-old woman P1 (Figures 4A–D). The T_m, T_s in this sample were

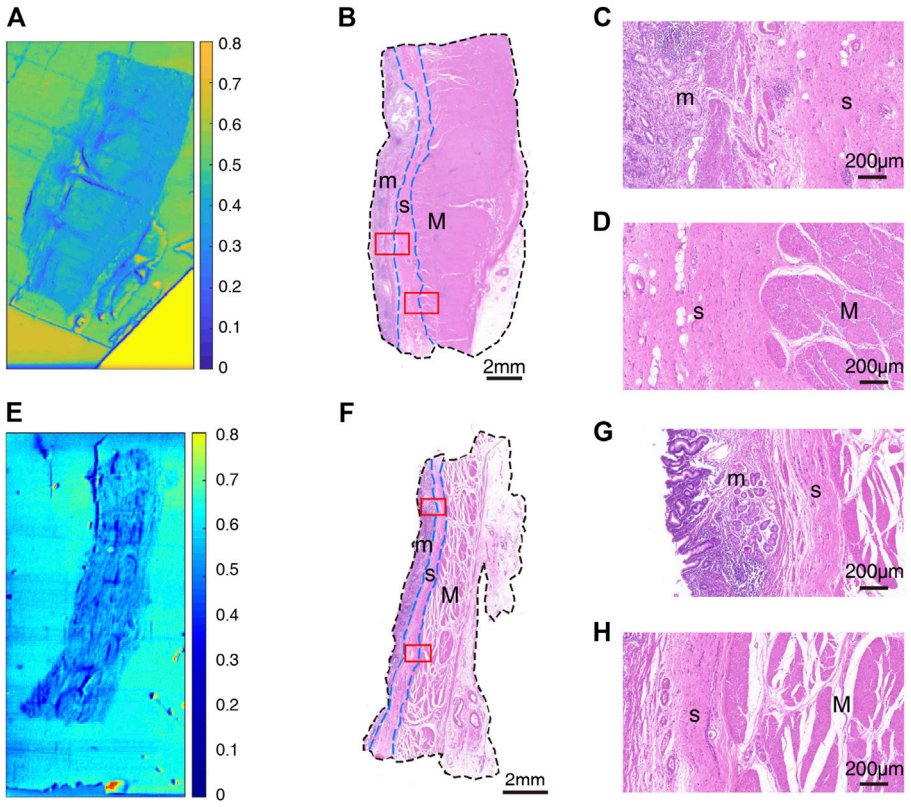

FIGURE 5
Images of GC sample: **(A)** THz image, **(B)** H&E-stained slice, and **(C,D)** H&E-stained images corresponding to the region indicated by the red square in **(B)** of T4; **(E)** THz image, **(F)** H&E-stained slice, and **(G,H)** H&E-stained images corresponding to the region indicated by the red square in **(F)** of T5. In H&E-stained images, "m" indicates "mucosa", "s" indicates "submucosa" and "M" indicates "muscular layer". In images **(B,F)**, the boundaries of mucosa, submucosa, and muscular layer are outlined with dashed blue lines. **(C,G)** are boundaries between mucosa and submucosa. **(D,H)** are boundaries between submucosa and muscular layer.

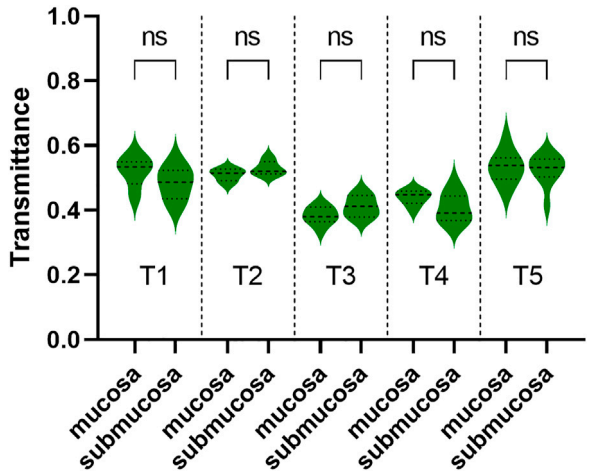

FIGURE 6
The transmittance of mucosa and submucosa in T1, T2, T3, T4, and T5. The transmittance of these two layers was similar in each of the three samples. ns: not significant.

0.520 (±0.045) and 0.483 (±0.050) respectively. The RT was calculated to be 0.071. T2 was from the GC tissue from a 52-year-old man P2 (Figures 4E–H). The T_m, T_s in this sample were 0.509 (±0.019) and 0.530 (±0.021) respectively. The calculated RT was -0.041. T3 was collected from the GC tissue from a 76-year-old man P3 (Figures 4I–L). The T_m, T_s in this sample were 0.382 (±0.027) and 0.411 (±0.032) respectively. The RT was calculated to be −0.076. T4 was from the GC tissue from a 64-year-old woman P4 (Figures 5A–D). The T_m, T_s in this sample were 0.439 (±0.023) and 0.408 (±0.045) respectively. The calculated RT was 0.069. T5 was collected from the GC tissue from a 55-year-old woman P3 (Figures 5E–H). The T_m, T_s in this sample were 0.533 (±0.051) and 0.524 (±0.048) respectively. The RT was calculated to be 0.017. RT was defined as the difference in the transmittance of mucosa and submucosa divided by mucosa transmittance. The results revealed that the THz transmittance between mucosa and submucosa was similar.

Samples' THz images in Figures 4, 5 also showed that the THz transmittance of mucosa is similar to that of submucosa in

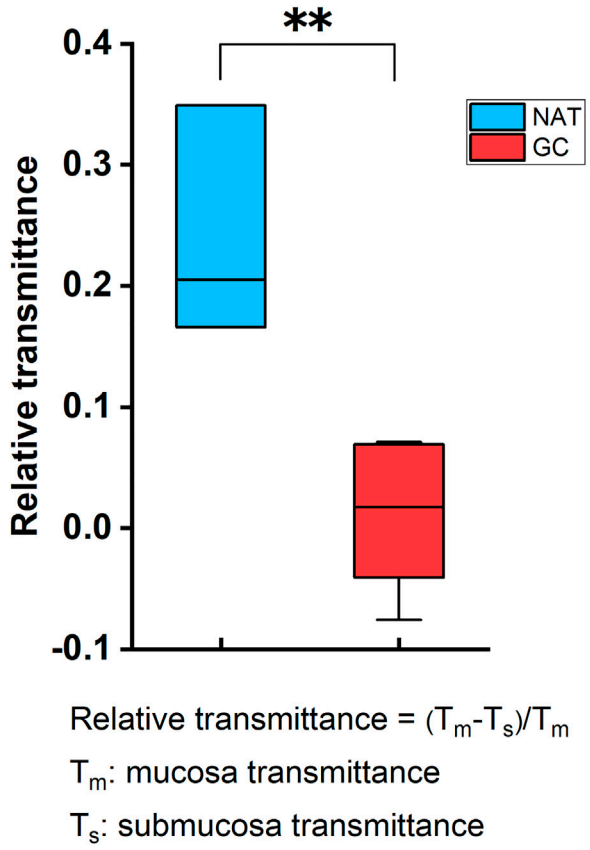

FIGURE 7
The difference of RT between NAT and GC tissue. The transmittance difference between mucosa and submucosa in NAT was significantly higher than that in GC tissue. RT between submucosa and mucosa was defined as RT = $(T_m-T_s)/T_m$, where T_m was averaged transmittance of mucosa and T_s was averaged transmittance of submucosa. **: $p < 0.01$.

sample T1, T2, T3, T4 and T5. Similarly, as Figure 6 presented, there was no significant difference in transmittance between mucosa and submucosa in all five samples. Although the boundaries of mucosa and submucosa in H&E-stained images were still relatively visible, it was difficult to accurately identify the areas of different tissue by color contrast in THz images. This is due to the fact that GC mainly rises from mucosa, which leads to a decrease in THz transmission, so the THz absorption capacity of mucosa is similar to that of submucosa. Based on the findings above, we analyzed RT of three NAT samples and five GC tissue samples to investigate the variation of RT between NAT and GC tissue. The results in Figure 7 revealed a statistical difference of RT between normal and cancerous gastric tissue ($p = 0.006$). The results suggested that our THz imaging technology had the potential to detect cancers by measuring the transmittance difference between different layers of tissue.

4 Discussion

In our study, we designed a high-resolution THz imaging system to scan gastric tissue slides. There was a novel finding that the THz transmittance of mucosa, submucosa and muscular layer were different in normal gastric tissue. The transmittance of submucosa was relatively low, while the transmittance of mucosa and muscular layer were relatively high. It was also found that the transmittance between mucosa and submucosa in GC tissue was similar. We believe this is due to the fact that cancerous tissue mainly arises from the mucosa, resulting in a decrease in THz transmittance.

Considerable progress has been made in the research on the biological application of electromagnetic wave (Zhang et al., 2021; Li et al., 2021). A growing number of studies have shown that THz is a useful approach for identifying cancers because malignant tumors usually contain more water and can absorb large amounts of THz radiation (Reid et al., 2011; Wahaia et al., 2011; Yamaguchi et al., 2016; Wu et al., 2022). The difference in THz transmittance among layers of normal gastric tissue may be due to water content differences as well. CW THz transmission scanning imaging system has shown great potential in the diagnosis of non-melanoma skin cancer, breast cancer and colon cancer (Joseph et al., 2011; Bowman et al., 2016; Wahaia et al., 2016). In addition, the CW THz near-field microscopy imaging system has made some achievements in the identification of cancerous and normal gastric tissues. Nevertheless, these studies have not yet enabled high resolution imaging of the fine structure of tissues. Moreover, current studies on the use of THz imaging to diagnose cancer are usually based on the difference of THz parameters between normal and cancerous tissue (Chen et al., 2022; Ke et al., 2022; Wu et al., 2022). Our study provided a new idea for THz diagnosis of GC. By calculating the difference in transmittance between mucosa and submucosa, the existence of cancerization in tissue sample could be inferred. In addition, we obtained THz images with a resolution of up to 60 μm for the first time, while the thickness of the scanned slice was only 20 μm. Thinner slices are also conducive to further observe of the fine structure of the tissue. Meanwhile, the slices' thickness was close to that of the slices used in clinical pathology examination, facilitating direct comparison of THz images with microscopic images. Our THz transmission imaging system is expected to save time and workload on GC pathology examinations and provide convenience for pathologists.

In the GC tissue we collected, the THz transmittance of the muscular layer was similar to that of the submucosa in some samples (T2, T3, T4, and T5), while different in the other sample (T1). This may be related to different degrees of invasion of cancerous tissue. Our study could assist in the diagnosis of GC by comparing the transmittance difference between mucosa and submucosa. Future studies could further focus on inferring the invasion depth of cancerous tissue by THz imaging to distinguish between early and advanced GC.

In conclusion, we proposed a high-resolution THz imaging system to scan normal and cancerous gastric tissue slides. The resolution is up to 60 μm. With this imaging system, we explored the THz transmittance characteristics of different layers of gastric wall tissue and identify them in THz images for the first time. Moreover, it is impressive that the THz transmittance of submucosa is lower than that of mucosa in NAT slides, but the THz transmittance of submucosa is similar to that of mucosa in GC tissue slides. We hypothesize that similar terahertz transmittance between gastric mucosa and submucosa may be an indication of carcinogenesis. We reported this phenomenon hoping to provide readers with more information. In future studies, we will explore this phenomenon in depth to provide more evidence.

Data availability statement

The raw data supporting the conclusion of this article will be made available by the authors, without undue reservation.

Ethics statement

The studies involving human participants were reviewed and approved by the Research Ethics Committee of China Medical University (Shenyang, China). The patients/participants provided their written informed consent to participate in this study. Written informed consent was obtained from the individual(s) for the publication of any potentially identifiable images or data included in this article.

Author contributions

HS: Investigation, visualization, writing-original draft. TL: Investigation, visualization, writing-original draft. ZL: Investigation, visualization, software. JZ: Conceptualization, resources, writing-review and editing. FQ: Conceptualization, resources, writing-review and editing.

Funding

This research was supported by National Natural Science Foundation of China (61804160, 61801467); The Central Guidance on Local Science and Technology Development Fund of Liaoning Province (No. 2022JH6/100100010); "Xing Liao Ying Cai" Talents of Liaoning Province (XLYC2007074); Applied Basic Research Program of Liaoning Province (2022020284-JH2/1013); Joint Fund for the Cross-Disciplinary in Medicine and Engineering of Science and Technology Program Projects of Liaoning Province (No. 2021-YGJC-04); Shenyang Young and Middle-aged Science and Technology Innovation Talent Support Program (RC200512); Top Young Talents of China Medical University.

Conflict of interest

The authors declare that the research was conducted in the absence of any commercial or financial relationships that could be construed as a potential conflict of interest.

Publisher's note

References

Albarqouni, L., Arab-Zozani, M., Abukmail, E., Greenwood, H., Pathirana, T., Clark, J., et al. (2022). Overdiagnosis and overuse of diagnostic and screening tests in low-income and middle-income countries: A scoping review. *BMJ Glob. Health* 7, e008696. doi:10.1136/bmjgh-2022-008696

Alberts, S. R., Cervantes, A., and van de Velde, C. J. (2003). Gastric cancer: Epidemiology, pathology and treatment. *Ann. Oncol.* 14, ii31–6. doi:10.1093/annonc/mdg726

Bor, R., Fábián, A., and Szepes, Z. (2016). Role of ultrasound in colorectal diseases. *World J. Gastroenterol.* 22, 9477–9487. doi:10.3748/wjg.v22.i43.9477

Borggreve, A. S., Goense, L., Brenkman, H. J. F., Mook, S., Meijer, G. J., Wessels, F. J., et al. (2019). Imaging strategies in the management of gastric cancer: Current role and future potential of MRI. *Br. J. Radiol.* 92, 20181044. doi:10.1259/bjr.20181044

Bowman, T., El-Shenawee, M., and Campbell, L. K. (2016). Terahertz transmission vs reflection imaging and model-based characterization for excised breast carcinomas. *Biomed. Opt. Express* 7, 3756–3783. doi:10.1364/boe.7.003756

Bray, F., Ferlay, J., Soerjomataram, I., Siegel, R. L., Torre, L. A., and Jemal, A. (2018). Global cancer statistics 2018: GLOBOCAN estimates of incidence and mortality worldwide for 36 cancers in 185 countries. *CA A Cancer J. Clin.* 68, 394–424. doi:10.3322/caac.21492

Brenner, H., Kloor, M., and Pox, C. P. (2014). Colorectal cancer. *Lancet* 383, 1490–1502. doi:10.1016/s0140-6736(13)61649-9

Charalampakis, N., Economopoulou, P., Kotsantis, I., Tolia, M., Schizas, D., Liakakos, T., et al. (2018). Medical management of gastric cancer: A 2017 update. *Cancer Med.* 7, 123–133. doi:10.1002/cam4.1274

Chavez, T., Bowman, T., Wu, J., Bailey, K., and El-Shenawee, M. (2018). Assessment of terahertz imaging for excised breast cancer tumors with image morphing. *J. Infrared Millim. Terahertz Waves* 39, 1283–1302. doi:10.1007/s10762-018-0529-8

Chen, H., Han, J., Ma, S., Li, X., Qiu, T., and Chen, X. (2022). Clinical diagnosis of gastric cancer by high-sensitivity THz fiber-based fast-scanning near-field imaging. *Cancers (Basel)* 14, 3932. doi:10.3390/cancers14163932

Chen, H., Ma, S., Wu, X., Yang, W., and Zhao, T. (2015). Diagnose human colonic tissues by terahertz near-field imaging. *J. Biomed. Opt.* 20, 036017. doi:10.1117/1.jbo.20.3.036017

Digklia, A., and Wagner, A. D. (2016). Advanced gastric cancer: Current treatment landscape and future perspectives. *World J. Gastroenterol.* 22, 2403–2414. doi:10.3748/wjg.v22.i8.2403

Gai, Q., Li, X., Li, N., Li, L., Meng, Z., and Chen, A. (2021). Clinical significance of multi-slice spiral CT, MRI combined with gastric contrast-enhanced ultrasonography in the diagnosis of T staging of gastric cancer. *Clin. Transl. Oncol.* 23, 2036–2045. doi:10.1007/s12094-021-02606-9

Heidkamp, J., Scholte, M., Rosman, C., Manohar, S., Fütterer, J. J., and Rovers, M. M. (2021). Novel imaging techniques for intraoperative margin assessment in surgical oncology: A systematic review. *Int. J. Cancer* 149, 635–645. doi:10.1002/ijc.33570

Jankauskaite, L., Grechukha, Y., Kjær, K. A., Mamenko, M., Nakstad, B., Romankevych, I., et al. (2022). Overuse of medical care in paediatrics: A survey from five countries in the European Academy of pediatrics. *Front. Pediatr.* 10, 945540. doi:10.3389/fped.2022.945540

Joseph, C. S., Yaroslavsky, A. N., Neel, V. A., Goyette, T. M., and Giles, R. H. (2011). Continuous wave terahertz transmission imaging of nonmelanoma skin cancers. *Lasers Surg. Med.* 43, 457–462. doi:10.1002/lsm.21078

Joshi, S. S., and Badgwell, B. D. (2021). Current treatment and recent progress in gastric cancer. *Ca. A Cancer J. Clin.* 71, 264–279. doi:10.3322/caac.21657

Ke, J., Jia, L., Hu, Y., Jiang, X., Mo, H., An, X., et al. (2022). Clinical and experimental study of a terahertz time-domain system for the determination of the pathological margins of laryngeal carcinoma. *World J. Surg. Oncol.* 20, 339. doi:10.1186/s12957-022-02788-8

Li, Y., Chang, C., Zhu, Z., Sun, L., and Fan, C. (2021). Terahertz Wave Enhances Permeability of the Voltage-Gated Calcium Channel. *J. Am. Chem. Soc.* 143, 4311–4318. doi:10.1021/jacs.0c09401

Lin, Z., Xu, G., Zhang, Q., and Song, Z. (2022). Average symbol error probability and channel capacity of the underwater wireless optical communication systems over oceanic turbulence with pointing error impairments. *Opt. Express* 30, 15327–15343. doi:10.1364/oe.457043

Liu, G. Z., Chang, C., Qiao, Z., Wu, K. J., Zhu, Z., Cui, G. Q., et al. (2019). Myelin Sheath as a Dielectric Waveguide for Signal Propagation in the Mid-Infrared to Terahertz Spectral Range. *Advanced Functional Materials* 29. doi:10.1002/adfm.201807862

Liu, W., Li, Y., Zhang, X., Li, J., Sun, J., Lv, H., et al. (2021). Preoperative T and N restaging of rectal cancer after neoadjuvant chemoradiotherapy: An accuracy comparison between MSCT and MRI. *Front. Oncol.* 11, 806749. doi:10.3389/fonc.2021.806749

Lou, J., Jiao, Y., Yang, R., Huang, Y., Xu, X., Zhang, L., et al. (2022). Calibration-free, high-precision, and robust terahertz ultrafast metasurfaces for monitoring gastric cancers. *Proceedings of the National Academy of Sciences of the United States of America* 119, e2209218119. doi:10.1073/pnas.2209218119

Oh, S. J., Kim, S. H., Ji, Y. B., Jeong, K., Park, Y., Yang, J., et al. (2014). Study of freshly excised brain tissues using terahertz imaging. *Biomed. Opt. Express* 5, 2837–2842. doi:10.1364/boe.5.002837

Ohana, O., Soffer, S., Zimlichman, E., and Klang, E. (2018). Overuse of CT and MRI in paediatric emergency departments. *Br. J. Radiol.* 91, 20170434. doi:10.1259/bjr.20170434

Pearce, M. S., Salotti, J. A., Little, M. P., McHugh, K., Lee, C., Kim, K. P., et al. (2012). Radiation exposure from CT scans in childhood and subsequent risk of leukaemia and brain tumours: A retrospective cohort study. *Lancet* 380, 499–505. doi:10.1016/s0140-6736(12)60815-0

Reid, C. B., Fitzgerald, A., Reese, G., Goldin, R., Tekkis, P., O'Kelly, P. S., et al. (2011). Terahertz pulsed imaging of freshly excised human colonic tissues. *Phys. Med. Biol.* 56, 4333–4353. doi:10.1088/0031-9155/56/14/008

Salati, M., Orsi, G., Smyth, E., Aprile, G., Beretta, G., De Vita, F., et al. (2019). Gastric cancer: Translating novels concepts into clinical practice. *Cancer Treat. Rev.* 79, 101889. doi:10.1016/j.ctrv.2019.101889

Shumyatsky, P., and Alfano, R. R. (2011). Terahertz sources. *J. Biomed. Opt.* 16, 033001. doi:10.1117/1.3554742

Song, Z., Wu, Y., Yang, J., Yang, D., and Fang, X. (2017). Progress in the treatment of advanced gastric cancer. *Tumour. Biol.* 39, 101042831771462. doi:10.1177/1010428317714626

Vohra, N., Bowman, T., Bailey, K., and El-Shenawee, M. (2020). Terahertz imaging and characterization protocol for freshly excised breast cancer tumors. *J. Vis. Exp.* doi:10.3791/61007

Wahaia, F., Kasalynas, I., Venckevicius, R., Seliuta, D., Valusis, G., Urbanowicz, A., et al. (2016). Terahertz absorption and reflection imaging of carcinoma-affected colon tissues embedded in paraffin. *J. Mol. Struct.* 1107, 214–219. doi:10.1016/j.molstruc.2015.11.048

Wahaia, F., Valusis, G., Bernardo, L. M., Almeida, A., Moreira, J. A., Lopes, P. C., et al. (2011). Detection of colon cancer by terahertz techniques. *J. Mol. Struct.* 1006, 77–82. doi:10.1016/j.molstruc.2011.05.049

Wang, C., Wang, Z., Zhao, T., Li, Y., Huang, G., Sumer, B. D., et al. (2018). Optical molecular imaging for tumor detection and image-guided surgery. *Biomaterials* 157, 62–75. doi:10.1016/j.biomaterials.2017.12.002

Wu, L., Wang, Y., Liao, B., Zhao, L., Chen, K., Ge, M., et al. (2022). Temperature dependent terahertz spectroscopy and imaging of orthotopic brain gliomas in mouse models. *Biomed. Opt. Express* 13, 93–104. doi:10.1364/boe.445597

Wu, L., Xu, D., Wang, Y., Liao, B., Jiang, Z., Zhao, L., et al. (2019). Study of *in vivo* brain glioma in a mouse model using continuous-wave terahertz reflection imaging. *Biomed. Opt. Express* 10, 3953–3962. doi:10.1364/boe.10.003953

Xiang, Z. X., Tang, C. X., Chang, C., Liu, G. Z., et al. (2020). A primary model of THz and far-infrared signal generation and conduction in neuron systems based on the hypothesis of the ordered phase of water molecules on the neuron surface I: signal characteristics. *Science Bulletin* 65, 308–317. doi:10.1016/j.scib.2019.12.004

Yamaguchi, S., Fukushi, Y., Kubota, O., Itsuji, T., Ouchi, T., and Yamamoto, S. (2016). Origin and quantification of differences between normal and tumor tissues observed by terahertz spectroscopy. *Phys. Med. Biol.* 61, 6808–6820. doi:10.1088/0031-9155/61/18/6808

Yang, X., Zhao, X., Yang, K., Liu, Y., Liu, Y., Fu, W., et al. (2016). Biomedical applications of terahertz spectroscopy and imaging. *Trends Biotechnol.* 34, 810–824. doi:10.1016/j.tibtech.2016.04.008

Zhang, J., He, Y., Liang, S., Liao, X., Li, T., Qiao, Z., et al. (2021). Non-invasive, opsin-free mid-infrared modulation activates cortical neurons and accelerates associative learning. *Nat. Commun.* 12, 2730. doi:10.1038/s41467-021-23025-y

frontiers | Frontiers in Bioengineering and Biotechnology

TYPE Original Research
PUBLISHED 10 January 2023
DOI 10.3389/fbioe.2022.1105249

OPEN ACCESS

EDITED BY
Peng-Yuan Wang,
Oujiang Laboratory, China

REVIEWED BY
Chao Chang,
Peking University, China
Yan Peng,
University of Shanghai for Science and Technology, China
Huabin Wang,
Chongqing Institute of Green and Intelligent Technology (CAS), China
Annalisa D'Arco,
National Institute of Nuclear Physics of Rome, Italy

*CORRESPONDENCE
Junhong Lü,
lvjunhong@jnl.ac.cn

SPECIALTY SECTION
This article was submitted to Nanobiotechnology, a section of the journal Frontiers in Bioengineering and Biotechnology

RECEIVED 22 November 2022
ACCEPTED 28 December 2022
PUBLISHED 10 January 2023

CITATION
Zhang G, Wang Y, Qian J, Wang Y, Li X and Lü J (2023), Terahertz refractive phenotype of living cells.
Front. Bioeng. Biotechnol. 10:1105249.
doi: 10.3389/fbioe.2022.1105249

Terahertz refractive phenotype of living cells

Guangxu Zhang[1,2,3], Yadi Wang[2,4], Jiang Qian[1,2,3], Yue Wang[1,2,3], Xueling Li[2,5] and Junhong Lü[1,2,4,5,6]*

[1]Shanghai Institute of Applied Physics, Chinese Academy of Sciences, Shanghai, China, [2]Jinan Microecological Biomedicine Shandong Laboratory, Jinan, China, [3]University of Chinese Academy of Sciences, Beijing, China, [4]School of Pharmacy, Binzhou Medical University, Yantai, China, [5]Shanghai University of Medicine and Health Sciences, Shanghai, China, [6]Shanghai Advanced Research Institute, Chinese Academy of Sciences, Shanghai, China

Cellular refractive index is a vital phenotypic parameter for understanding the cell functional activities. So far, there remains technical challenges to obtain refractive index of viable cells at the terahertz frequency in which contains rich information closely related to their physiological status. Here we introduce a label-free optical platform for interrogating cellular phenotypes to measure the refractive index of living cells in near-physiological environments by using terahertz spectroscopy with the combination of cellular encapsulation in a confined solution droplet. The key technical feature with cells encapsulated in aqueous droplets allows for keeping cellular viability while eliminating the strong adsorption of solvent water to terahertz signal. The obtained high signal-to-noise ratio enables to differentiate different cell types (e.g., *E. coli*, stem cell and cancer cell) and their states under stress conditions. The integrating of terahertz spectroscopy to droplet microfluidic further realizes automated and high-through sample preparation and detection, providing a practical toolkit for potential application in cellular health evaluation and phenotypic drug discovery.

KEYWORDS

terahertz spectroscopy, refractive index, water droplet, living cells, droplet microfluidic

Introduction

Cell refractive index, an important phenotypic parameter that correlates with the biological properties such as internal mass (Gul et al., 2021), has been widely used as marker in the field of cell biology and biomedicine to determine the cell types and investigate cellular activities (Zhuo et al., 2011; Liu et al., 2016). With the rapid development of advanced optical techniques, the measurement of refractive index has been extended to a wider frequency range (Zhuo et al., 2011; Liu et al., 2016). Compared with the visible region, the refractive index in the terahertz (THz) region is non-linear (Baxter and Guglietta, 2011; Tcypkin et al., 2019; Novelli et al., 2020) and reveals the reorientation dynamics of water that hydrates the biomolecules (Tros et al., 2017; Peng et al., 2021), which contains rich information closely related to the cellular activity and physiological status (Yang et al., 2016a; Ball, 2017; Liu et al., 2019; Zhang et al., 2021; Lou et al., 2022). Also intriguing is that THz wave does not cause ionizing damage making its more safe in biological measurements (Olga et al., 2021; Liao et al., 2022). Therefore, a pressing need is to develop a rapid and widely applicable way to measure the THz refractive index of living cell with improved the signal-to-noise ratio.

In principle, the refractive index at THz frequencies of substance can be measured by THz time-domain spectroscopy (THz-TDS) (Baxter and Guglietta, 2011). Several pioneering works have demonstrated the possibility to achieve cellular refractive index by using THz spectroscopy. For example, Yang et al. (2016b) reported that refractive index

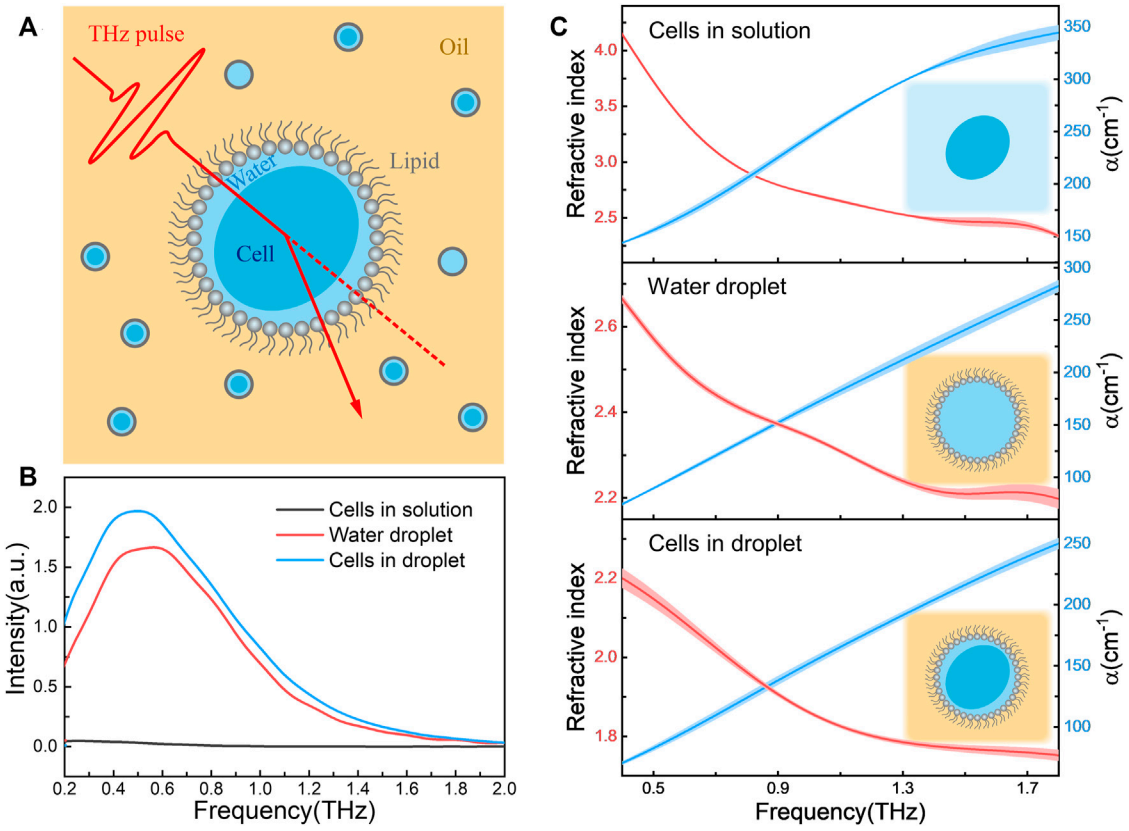

FIGURE 1
(A) Schematic of refractive index measurement platform based on the combination of terahertz spectroscopy and cellular droplet sampling. The cell-containing droplets (water phase) were dispersed in the reagent transparent to THz signals (oil phase), and the phospholipids at the oil-water interface served as surfactants; **(B)** The transmission spectra of *E. coli* in aqueous solution (cells in solution), droplet containing TBS solution alone (water droplet) and *E. coli*-containing droplet (cells in droplet). All *E. coli* samples had the same bacterial concentration of 9.0×10^{10} cfu/mL; **(C)** The refractive index (left axis) and absorption coefficient (α, right axis) spectra of these three samples, where the schematic diagram of the forms of samples are shown in insert. The shaded area indicating the error bars with triplicated measurements.

varied between different species of bacterial colonies. Wang et al. (2019) found that various cells in nervous system had different refractive indices, which would increase after cancerization. Cao et al. (2021) proposed that refractive index could be used to distinguish different cancer cells. However, due to the aqueous medium required for living cells measurement easily produces strong background signal interference (Peng et al., 2020), there remains a big technical challenge for obtaining the refractive index of cells in a viable state.

Herein, we introduce a technical platform for determining the refractive index of cells in an aqueous condition by using the combination of THz-TDS and droplet sampling (Figure 1A). Specifically, the cell samples were encapsulated one by one in aqueous droplets constructed by the self-assemble phospholipids (Yang et al., 2019; Tang et al., 2021; Tang et al., 2022). The cellular encapsulation provides not only a liquid environment for keeping cellular viability (Sart et al., 2022) but also allows for eliminating the strong adsorption of solvent water to THz signal (Weisenstein et al., 2021). Due to the droplets, consisting of the cells and a little confined water around, are surrounded by reagents with high transmittance in THz region, the signal attenuation of the sample mainly attributes to the adsorption of intracellular water. Thus, from the THz signal, we can easily calculate the absorption coefficient (α) and the refractive index of cell samples. Using the optical platform, we have successfully obtained the refractive index of three kinds of cell types, including *E. coli*, stem cell and cancer cell, and their states under stress conditions. We also demonstrated the integrating of this method into a droplet microfluidics chip to acquire an automated and high-through preparation and detection toolkit for the application practicability.

Results and discussion

Refractive index measurement of living cells encapsulated in aqueous droplets

Figure 1B shows the obtained THz signal of samples in three forms, *E. coli* in buffer solution (cells in solution), droplet containing buffer alone (water droplet) and droplet containing *E. coli* (cells in droplet). Due to the strong absorption of solvent water, the transmission THz electric field strength of cells in bulk solution is very weak, almost consistent with the transmission spectrum of buffer itself (Supplementary Figure S3A). In contrast, for samples in droplet forms the signal-to-noise ratio was improved more than an order of magnitude, and the significant

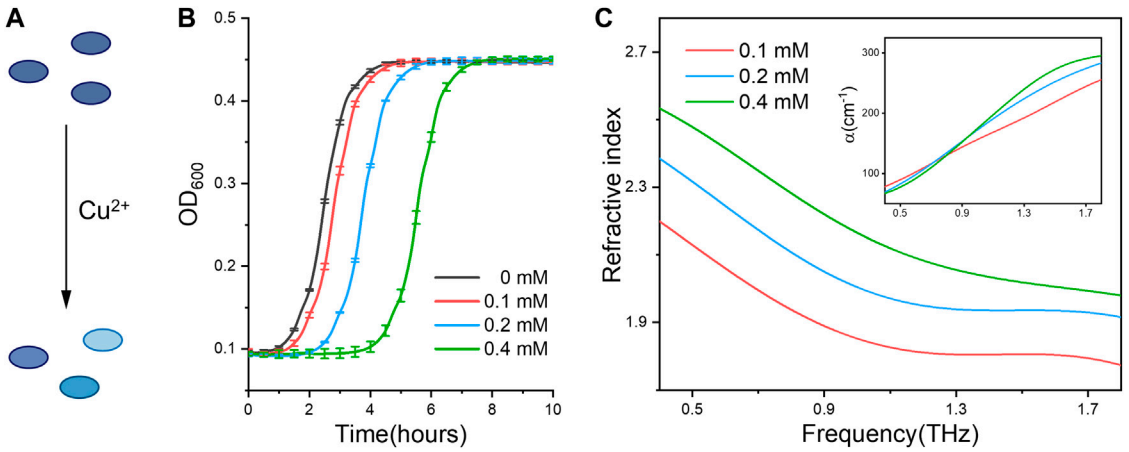

FIGURE 2
(A) Schematic showing Cu^{2+} ions treatment induces distinct activity states of bacterial cells. **(B)** The growth curve of *E. coli* under 0, .1, .2 and .4 mM of Cu^{2+} treatment, respectively. **(C)** Refractive index and absorption coefficient spectra (inset) of *E. coli* cells. All bacterial samples were treated with Cu^{2+} and accounted to the same cell numbers for THz measurement.

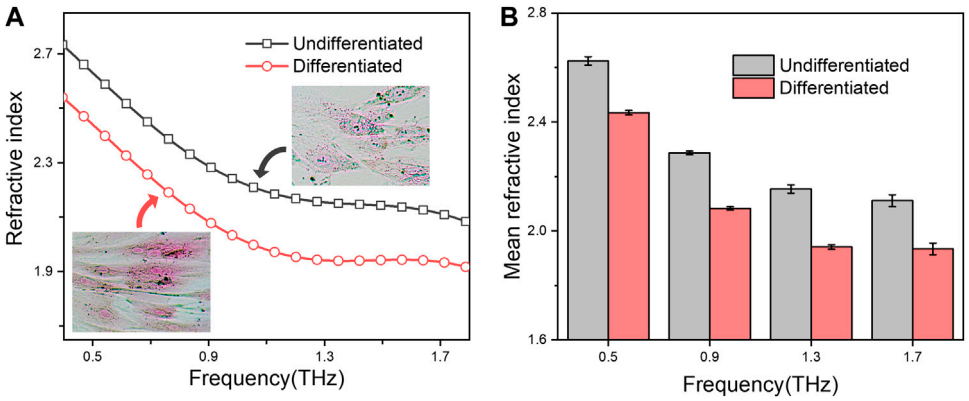

FIGURE 3
(A) Refractive index spectra of undifferentiated or osteogenic differentiated MSCs in droplets. The microscopy photograph of the corresponding cells after alizarin red S staining are shown in insert; **(B)** Mean refractive index at .5, .9, 1.3 and 1.7 THz. All groups were set to the same cell concentration of 1.0 × 10^5 cells/well.

spectral difference was observed between samples with and without cells. The refractive index and absorption coefficient spectra of these three samples were shown in Figure 1C. We found that the optical properties of the cells in solution were nearly same as the buffer alone (Supplementary Figure S3B), suggesting the THz signal are mainly derived from the bulk aqueous solution. However, when the buffer droplets was confined in lipid monolayer, a cell-like environment (Shang and Zhao, 2021), the refractive index significantly decreased comparing to that bulk solution. Interestingly, when the cells were encapsulated in the droplet solutions, the refractive index was further lower down. Since the THz signal of cell-containing droplets might mainly attribute to the intracellular water (Folpini et al., 2017) and little confined water outside the cells, the obtained refractive index is reasonable to describe the physical parameter of living cells themselves.

Terahertz refractive index for cell functional activity assay

Using the established methodology, we ask if the measured refractive index can be used to discriminate the cellular states under different physiological conditions. For this purpose, we firstly compared the bacterial (*E. coli*) cells subjected to metal ions stress. Since trace copper ions are required for keeping the bacterial viability (Giachino and Waldron, 2020), *E. coli* cells under different states were obtained with Cu^{2+} treatment at sublethal concentrations (Figure 2A). From the growth curves (Figure 2B), we can find the bacteria treated under higher Cu^{2+} concentration exhibit longer delayed growth time (lower viability), indicating cellular viable states in an ion concentration dependent manner. Interestingly, bacterial cells with different viable states have distinct physical parameters, including the refractive index and absorption

10.3389/fbioe.2022.1105249

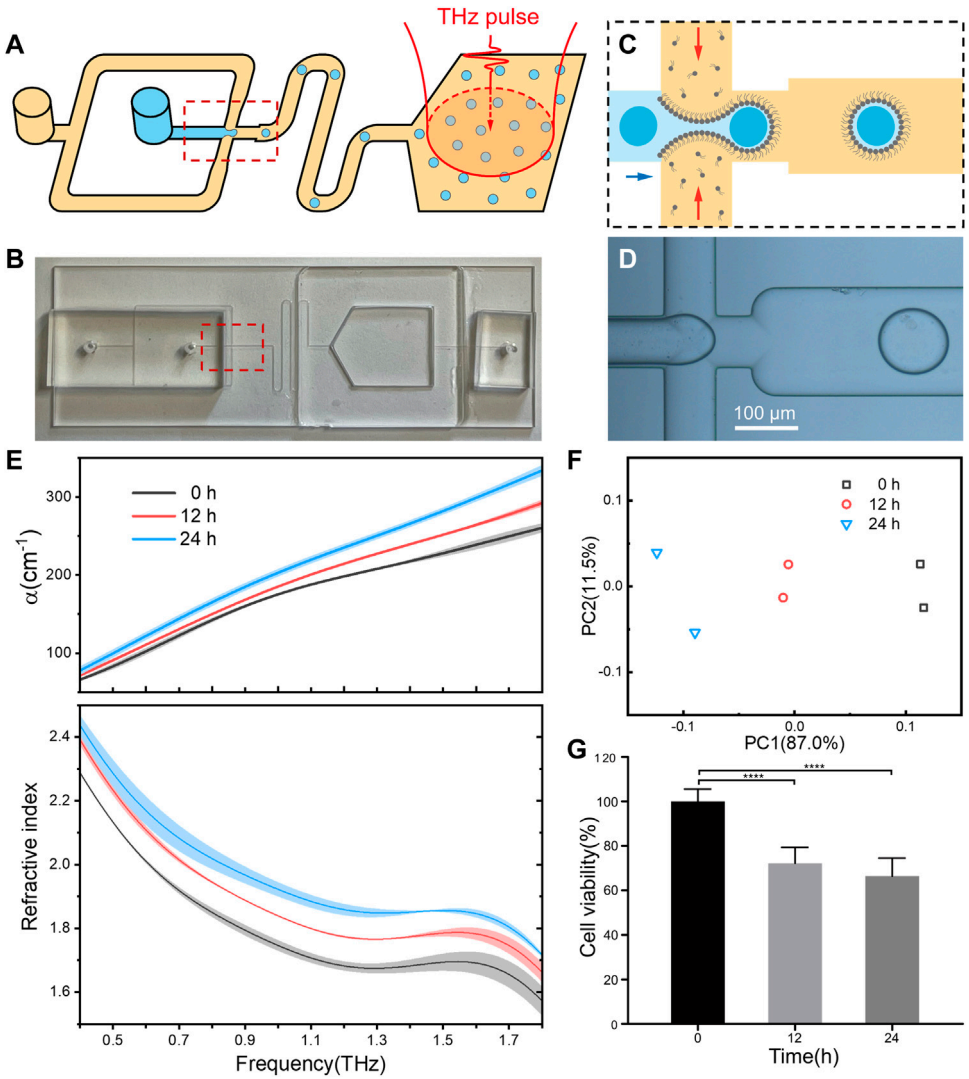

FIGURE 4
The integrating of droplet microfluidics for automated and high-through performance. **(A)** Schematic of the microfluidic device that can generate droplet sample and perform THz-TDS detection. An aqueous phase containing cells was passed through a flow-focusing junction where it met an oil phase containing lipids, leading to the generation of droplets. Red arrows show the position of a cell before and after encapsulation. Droplets were collected in a quartz chamber which severed as the terahertz measurement cuvette. **(B)** The optical image of the microfluidic chip. **(C,D)** The schematic and optical image of the droplet generation process. **(E)** Refractive index spectra of the droplets containing HepG2 cells after treatment by resveratrol for 0, 12 and 24 h. All groups were set to the same cell concentration of 1.4×10^5 cells/well. For each group of cells, the droplets were prepared and measured twice, and the shaded area indicates the error bars. **(F)** Principal component analysis (PCA) plots of the measured refractive index. **(G)** Cell viability of resveratrol treated HepG2 cells.

coefficient spectra shown in Figure 2C. Especially, the cellular refractive index increases with the higher concentration of ions treatment. In other words, the cells with lower viability, either induced by different ion concentrations or treatment times (Supplementary Figure S4), have a bigger refractive index. For example, at the .9 THz frequency, the cellular refractive indexes are 1.89, 2.05 and 2.22 under Cu^{2+} treatments with 0.1 mM, 0.2 mM, 0.4 mM, respectively.

We further test whether the functional stages of eukaryotic cells would be also reflected through these terahertz parameter measurements. To this end, two states of mesenchymal stem cells (MSCs) during osteogenic differentiation were choose for the investigation. The osteogenic differentiation of MSCs led to successively form mineralization of bone matrix (Khezri et al., 2021), showing an intense alizarin red staining (Figure 3A inset; Supplementary Figure S5), in which hydration plays a vital structuring role across the bone hierarchy (Surowiec et al., 2022). As shown in Figure 3, the refractive index of osteogenic differentiated MSCs is smaller than that of undifferentiated ones at the measured terahertz frequency (from .4–1.8 THz). Thus, these results not only indicated that the refractive index changes during the differentiation process of stem cell, but also proved the developed technique is suitable for kinds of cell types.

Taking together, these two experiments clearly demonstrated the feasibility and repeatability of our method to represent the cellular states, either for bacterial cells or eukaryotic cells, by quantitative

measurement of their terahertz refractive indexes, providing a novel label-free technique for evaluating the cellular physiological or pathological activities.

Integrating of microfluidics chip for droplet production and optical detection

Next, we try to integrate droplet formation and terahertz detection into a microfluidics chip for practical applications. In our experiment, a two-module microfluidics device were constructed to generate cell-containing droplets and optical measurements, synchronously (Figures 4A, B). In the cell encapsulation module, an aqueous phase containing living cells was passed through a flow-focusing junction where it met an oil phase containing lipids, leading to the generation of cell-contained droplets (Figures 4C, D). The flow rate and junction geometry were carefully chosen to control the droplet radius for full encapsulation of individual cells inside (Ding et al., 2020). After passing through a flow channel in a sufficient time to get stabilization, the droplets were collected in the detection module, which was fabricated by quartz windows with well-transmission of THz wave. Once enough cells sample were measured, their optical parameters could be achieved.

In a proof-of-concept study, the microfluids chip was applied to analyze the relationship between terahertz refractive index and drug response of living cells. As expected, following with a low-concentration resveratrol treatment, the measured cellular refractive index was increasing accordingly to treatment time (Figure 4E), while the cell viability decreased as indicated in MTT assay (Figure 4G). Principal component analysis (PCA) clearly indicated that the cellular refractive index is high related to the effect of drug treatment (Figure 4F). Although more kinds of drugs and cell lines are still required to setup a universal rule on the relationship of drug effect with cellular refractive index, the integration of terahertz spectroscopy and microfluidic chip paves a brand-new way for drug screening based on cellular refractive phenotypes.

Conclusion

In summary, we have developed a novel strategy and method to measure the refractive index of living cells in near-physiological environment by using terahertz spectroscopy with the combination of cellular encapsulation in a confined solution droplet. The advantage of cell confinement lies on its ability to improving signal-to-noise ratio meanwhile keeping cellular viability. Using this technical platform, we have successfully obtained the refractive index of *E. coli*., mesenchymal stem cell, and liver cancer cell. Importantly, the high sensitivity and good repeatability of this approach enables to discriminate the cellular states and stress responses, such as the stem cells under differentiation conditions, the cancer cells with drug treatment, et al. Furthermore, the technique is easily integrated into a microfluidics chip in which the droplet sampling and optical measurement are simultaneously achieved, demonstrating the key step towards automation and high-through application. This novel technology development not only offers a valuable toolkit to understanding the fundamental role of the intracellular water in cell biology but also provides a label-free optical approach for bioanalytical applications in cellular health evaluation and phenotypic drug discovery.

Materials and methods

Microfluidic device fabrication

The soda-lime glass microfluidic chip was fabricated by conventional photolithography, wet etching and thermal bonding (Baker and Roper, 2010). A glass with chrome layer and AZ-1505 (from AZ technology) were used as a photoresist to create a master. The glass was then etched with a 66:14:20 (v:v:v) mixture of H_2O:HNO_3:HF. After that, access holes of 1 mm diameter were machined using a diamond-tipped drill bit. The chip was cleaned, hydrolyzed and put together under running water for sealing. The chip was then thermal bonding at 500°C.

The two-module microfluidic chip, designed in AutoCAD. The oil phase reagent entered through a wide (200 μm) inlet channel. Cells entered through an inlet channel with a width of 90 μm, then entered a cross-shaped flow-focusing junction (90 μm × 90 μm) where the droplets generated. The droplets then flowed through a meander with 180 μm width and 100 mm total length to sufficiently stabilize the lipid interface. The above microstructures constituted the first module, where the depth of channel was 40 μm. The droplet sample then entered the detection module, a chamber with a height of 1 mm and an area of 1 cm^2, equipped with a waste outlet. In order to ensure the transparency of the cavity in the THz range, laser cutting was used to remove the glass substrates above and below the cavity and quartz plates were glued as substitute substrates. The thickness of the quartz plate is .5 mm, and the distance between them is the same as the height of the cavity (1 mm). To assist the entry/exit of liquid, PDMS pedestals are provided at the inlet and outlet.

Preparation of droplet samples

Reagents for cell culture, including Tris-buffered saline (TBS), culture medium, etc., were purchased from Sinopharm Chemical Reagent (China) unless otherwise specified. DOPC (1,2-dioleoyl-sn-glycero-3-phosphocholine, purchased from Avanti Polar lipids, Inc.) and anhydrous hexadecane (purchased from Sigma-Aldrich) were used as surfactant and oil phase reagent, respectively. Cell suspensions at the indicated concentrations were used as the aqueous phase. For drug-treated cells, they were washed after treatment and transferred to drug-free TBS or culture medium. See Supplementary Material for more details of cell culture procedures.

Chloroform solution of DOPC evaporated under nitrogen gas and dried in vacuum to obtain the thin film of lipids, which was then dissolved in hexadecane to a concentration. The aqueous droplets were fabricated according to the following procedures: the prepared cell suspensions were injected in the phospholipid/hexadecane solutions (45 mg/mL), and the aqueous droplet samples would be obtained by vortex, where the dispersed phase accounted for a volume fraction of 9% for bacteria-containing droplets and 10% for droplets contains other cells. When preparing droplet samples containing eukaryotic cells, vigorous mechanical manipulation should be avoided to prevent cell rupture. When microfluidic chip was used to prepare droplet samples, the oil phase was DOPC dissolved in hexadecane (4 mg/mL) and the water phase was the cell suspension with the pump flow rate at 8 and 1 μL/min, respectively. See Supplementary Material for more details of microfluidic device operation.

THz spectroscopy

The samples were measured using a THz time-domain spectroscopy (THz-TDS) system. See Supplementary Material for the details of the system. In the experiments, samples were placed in a fused quartz cuvette with a thickness of .5 mm (or the quartz detection window of the microfluidic chip with the same thickness), and the sample chamber was controlled at a temperature of 21.0°C ± .5°C and humidity within 1%. Transmission mode was applied for all measurements. The empty cuvette was used first as a reference signal. The absorption coefficient, $\alpha(\nu)$, and the refractive index, $n(\nu)$, were then obtained as follows:

$$\alpha(\nu) = d^{-1}\mathrm{In}\left[I_r(\nu)/I_s(\nu)\right]$$

$$n(\nu) = n_r(\nu) + \frac{c}{2\pi\nu d}\left[\phi_s(\nu) - \phi_r(\nu)\right]$$

Where d is the optical path length of the cuvette, $I_r(\nu)$ and $I_s(\nu)$ are the intensity of reference and sample solutions, $n_r(\nu)$ is the refractive index of the reference, $\Phi_s(\nu)$ and $\Phi_s(\nu)$ are the phase of reference and sample, respectively. The refractive index of the water phase was further obtained by a binary component model, see Supplementary Material for the details. PCA was conducted using R language without any preprocessing of the measured refractive index.

Data availability statement

The original contributions presented in the study are included in the article/Supplementary Material, further inquiries can be directed to the corresponding author.

Author contributions

JL conceived and supervised the study. XL and YdW coordinated the project. GZ, JQ, and YeW performed the experiments. YdW helped figure preparation. XL participated to the manuscript conception. JL and GZ wrote the paper. All authors analyzed data and contributed to writing the manuscript.

Funding

This work was supported by NSAF Joint Fund of National Natural Science Foundation of China (U2230110), Shandong Provincial Natural Science Foundation (ZR2021QC029), the Research Project of Jinan Microecological Biomedicine Shandong Laboratory (JNL-2022021B), Shanghai International Science & Technology Cooperation Program (22490714400), Yantai Region and College Integration Development Project (2021XDRHXMPT28), and the National Defense Science and Technology Innovation Special Zone.

Conflict of interest

JL, GZ, and YdW are coinventors in a provisional application for a Chinese patent on terahertz spectroscopy-based strategies in cellular health evaluation and phenotypic drug discovery.

The remaining authors declare that the research was conducted in the absence of any commercial or financial relationships that could be construed as a potential conflict of interest.

Publisher's note

All claims expressed in this article are solely those of the authors and do not necessarily represent those of their affiliated organizations, or those of the publisher, the editors and the reviewers. Any product that may be evaluated in this article, or claim that may be made by its manufacturer, is not guaranteed or endorsed by the publisher.

Supplementary material

The Supplementary Material for this article can be found online at: https://www.frontiersin.org/articles/10.3389/fbioe.2022.1105249/full#supplementary-material

References

Baker, C. A., and Roper, M. G. (2010). A continuous-flow, microfluidic fraction collection device. *J. Chromatogr. A* 1217, 4743–4748. doi:10.1016/j.chroma.2010.05.023

Ball, P. (2017). Water is an active matrix of life for cell and molecular biology. *Proc. Natl. Acad. Sci.* 114, 13327–13335. doi:10.1073/pnas.1703781114

Baxter, J. B., and Guglietta, G. W. (2011). Terahertz spectroscopy. *Anal. Chem.* 83, 4342–4368. doi:10.1021/ac200907z

Cao, Y., Chen, J., Zhang, G., Fan, S., Ge, W., Hu, W., et al. (2021). Characterization and discrimination of human colorectal cancer cells using terahertz spectroscopy. *Spectrochimica Acta Part A Mol. Biomol. Spectrosc.* 256, 119713. doi:10.1016/j.saa.2021.119713

Ding, Y., Howes, P. D., and deMello, A. J. (2020). Recent advances in droplet microfluidics. *Anal. Chem.* 92, 132–149. doi:10.1021/acs.analchem.9b05047

Folpini, G., Siebert, T., Woerner, M., Abel, S., Laage, D., and Elsaesser, T. (2017). Water librations in the hydration shell of phospholipids. *J. Phys. Chem. Lett.* 8, 4492–4497. doi:10.1021/acs.jpclett.7b01942

Giachino, A., and Waldron, K. J. (2020). Copper tolerance in bacteria requires the activation of multiple accessory pathways. *Mol. Microbiol.* 114, 377–390. doi:10.1111/mmi.14522

Gul, B., Ashraf, S., Khan, S., Nisar, H., and Ahmad, I. (2021). Cell refractive index: Models, insights, applications and future perspectives. *Photodiagnosis Photodyn. Ther.* 33, 102096. doi:10.1016/j.pdpdt.2020.102096

Khezri, K., Maleki Dizaj, S., Rahbar Saadat, Y., Sharifi, S., Shahi, S., Ahmadian, E., et al. (2021). Osteogenic differentiation of mesenchymal stem cells via curcumin-containing nanoscaffolds. *Stem Cells Int.* 2021, 1–9. doi:10.1155/2021/1520052

Liao, Y., Zhang, M., Tang, M., Chen, L., Li, X., Liu, Z., et al. (2022). Label-free study on the effect of a bioactive constituent on glioma cells *in vitro* using terahertz ATR spectroscopy. *Biomed. Opt. Express* 13, 2380–2392. doi:10.1364/boe.452952

Liu, G., Chang, C., Qiao, Z., Wu, K., Zhu, Z., Cui, G., et al. (2019). Myelin sheath as a dielectric waveguide for signal propagation in the mid-infrared to terahertz spectral range. *Adv. Funct. Mater.* 29, 1807862. doi:10.1002/adfm.201807862

Liu, P. Y., Chin, L. K., Ser, W., Chen, H. F., Hsieh, C. M., Lee, C. H., et al. (2016). Cell refractive index for cell biology and disease diagnosis: Past, present and future. *Lab a Chip* 16, 634–644. doi:10.1039/c5lc01445j

Lou, J., Jiao, Y., Yang, R., Huang, Y., Xu, X., Zhang, L., et al. (2022). Calibration-free, high-precision, and robust terahertz ultrafast metasurfaces for monitoring gastric cancers. *Proc. Natl. Acad. Sci.* 119, e2209218119. doi:10.1073/pnas.2209218119

Novelli, F., Ma, C. Y., Adhlakha, N., Adams, E. M., Ockelmann, T., Das Mahanta, D., et al. (2020). Nonlinear terahertz transmission by liquid water at 1 thz. *Appl. Sci.* 10 (15), 102020. doi:10.3390/app10155290

Olga, P. C., Danil, S. S., Eugenia, F. N., Alex, S. R., Anna, S. K., Irina, N. D., et al. (2021). Cellular effects of terahertz waves. *J. Biomed. Opt.* 26, 090902. doi:10.1117/1.JBO.26.9.090902

Peng, Y., Huang, J., Luo, J., Yang, Z., Wang, L., Wu, X., et al. (2021). Three-step one-way model in terahertz biomedical detection. *PhotoniX* 2, 12. doi:10.1186/s43074-021-00034-0

Peng, Y., Shi, C., Zhu, Y., Gu, M., and Zhuang, S. (2020). Terahertz spectroscopy in biomedical field: A review on signal-to-noise ratio improvement. *PhotoniX* 1, 12. doi:10.1186/s43074-020-00011-z

Sart, S., Ronteix, G., Jain, S., Amselem, G., and Baroud, C. N. (2022). Cell culture in microfluidic droplets. *Chem. Rev.* 122, 7061–7096. doi:10.1021/acs.chemrev.1c00666

Shang, L., and Zhao, Y. (2021). Droplet-templated synthetic cells. *Matter* 4, 95–115. doi:10.1016/j.matt.2020.10.003

Surowiec, R. K., Allen, M. R., and Wallace, J. M. (2022). Bone hydration: How we can evaluate it, what can it tell us, and is it an effective therapeutic target? *Bone Rep.* 16, 101161. doi:10.1016/j.bonr.2021.101161

Tang, C., Wang, Y., Cheng, J., Chang, C., Hu, J., and Lü, J. (2022). Probing terahertz dynamics of multidomain protein in cell-like confinement. *Spectrochimica Acta Part A Mol. Biomol. Spectrosc.* 275, 121173. doi:10.1016/j.saa.2022.121173

Tang, C., Yang, J., Wang, Y., Cheng, J., Li, X., Chang, C., et al. (2021). Integrating terahertz metamaterial and water nanodroplets for ultrasensitive detection of amyloid β aggregates in liquids. *Sensors Actuators B Chem.* 329, 129113. doi:10.1016/j.snb.2020.129113

Tcypkin, A. N., Melnik, M. V., Zhukova, M. O., Vorontsova, I. O., Putilin, S. E., Kozlov, S. A., et al. (2019). High Kerr nonlinearity of water in THz spectral range. *Opt. Express* 27, 10419–10425. doi:10.1364/oe.27.010419

Tros, M., Zheng, L., Hunger, J., Bonn, M., Bonn, D., Smits, G. J., et al. (2017). Picosecond orientational dynamics of water in living cells. *Nat. Commun.* 8, 904. doi:10.1038/s41467-017-00858-0

Wang, Y., Jiang, Z., Xu, D., Chen, T., Chen, B., Wang, S., et al. (2019). Study of the dielectric characteristics of living glial-like cells using terahertz ATR spectroscopy. *Biomed. Opt. Express* 10, 5351–5361. doi:10.1364/boe.10.005351

Weisenstein, C., Wigger, A. K., Richter, M., Sczech, R., Bosserhoff, A. K., and Bolívar, P. H. (2021). THz detection of biomolecules in aqueous environments—status and perspectives for analysis under physiological conditions and clinical use. *J. Infrared, Millim. Terahertz Waves* 42, 607–646. doi:10.1007/s10762-021-00792-9

Yang, J., Tang, C., Wang, Y., Chang, C., Zhang, J., Hu, J., et al. (2019). The terahertz dynamics interfaces to ion–lipid interaction confined in phospholipid reverse micelles. *Chem. Commun.* 55, 15141–15144. doi:10.1039/c9cc07598d

Yang, X., Wei, D., Yan, S., Liu, Y., Yu, S., Zhang, M., et al. (2016). Rapid and label-free detection and assessment of bacteria by terahertz time-domain spectroscopy. *J. Biophot.* 9, 1050–1058. doi:10.1002/jbio.201500270

Yang, X., Zhao, X., Yang, K., Liu, Y., Liu, Y., Fu, W., et al. (2016). Biomedical applications of terahertz spectroscopy and imaging. *Trends Biotechnol.* 34, 810–824. doi:10.1016/j.tibtech.2016.04.008

Zhang, J., He, Y., Liang, S., Liao, X., Li, T., Qiao, Z., et al. (2021). Non-invasive, opsin-free mid-infrared modulation activates cortical neurons and accelerates associative learning. *Nat. Commun.* 12, 2730. doi:10.1038/s41467-021-23025-y

Zhuo, W., Gabriel, P., Krishnarao, V. T., and Andre, B. (2011). Tissue refractive index as marker of disease. *J. Biomed. Opt.* 16, 1–8. doi:10.1117/1.3656732

frontiers | Frontiers in Bioengineering and Biotechnology

TYPE Original Research
PUBLISHED 17 February 2023
DOI 10.3389/fbioe.2023.1119694

OPEN ACCESS

EDITED BY
Junhong Lü,
Shanghai Advanced Research Institute (CAS), China

REVIEWED BY
Ali Passian,
Oak Ridge National Laboratory (DOE), United States
Olga Korostynska,
Oslo Metropolitan University, Norway

*CORRESPONDENCE
Chunyan Yao,
yao_yao24@yahoo.com

SPECIALTY SECTION
This article was submitted to Nanobiotechnology, a section of the journal Frontiers in Bioengineering and Biotechnology

RECEIVED 09 December 2022
ACCEPTED 10 February 2023
PUBLISHED 17 February 2023

CITATION
Xue Z, Mao P, Peng P, Yan S, Zang Z and Yao C (2023), Terahertz spectra of proteinuria and non-proteinuria. *Front. Bioeng. Biotechnol.* 11:1119694. doi: 10.3389/fbioe.2023.1119694

Terahertz spectra of proteinuria and non-proteinuria

Zhenrui Xue[1], Ping Mao[1,2], Ping Peng[1], Shihan Yan[3,4], Ziyi Zang[3] and Chunyan Yao[1]*

[1]Department of Transfusion Medicine, Southwest Hospital, Third Military Medical University (Army Medical University), Chongqing, China, [2]Department of Clinical Laboratory, Sichuan Provincial Crops Hospital of Chinese People's Armed Police Forces, Leshan, Sichuan, China, [3]Chongqing Institute of Green and Intelligent Technology, Chinese Academy of Sciences, Chongqing, China, [4]Chongqing School, University of Chinese Academy of Sciences (UCAS Chongqing), Chongqing, China

In clinical practice, proteinuria detection is of great significance in the diagnosis of kidney diseases. Dipstick analysis is used in most outpatient settings to semi-quantitatively measure the urine protein concentration. However, this method has limitations for protein detection, and alkaline urine or hematuria will cause false positive results. Recently, terahertz time-domain spectroscopy (THz-TDS) with strong hydrogen bonding sensitivity has been proven to be able to distinguish different types of biological solutions, which means that protein molecules in urine may have different THz spectral characteristics. In this study, we performed a preliminary clinical study investigating the terahertz spectra of 20 fresh urine samples (non-proteinuria and proteinuria). The results showed that the concentration of urine protein was positively correlated with the absorption of THz spectra at 0.5–1.2 THz. At 1.0 THz, the pH values (6, 7, 8, and 9) had no significant effect on the THz absorption spectra of urine proteins. The terahertz absorption of proteins with a high molecular weight (albumin) was greater than that of proteins with a low molecular weight (β2-microglobulin) at the same concentration. Overall, THz-TDS spectroscopy for the qualitative detection of proteinuria is not affected by pH and has the potential to discriminate between albumin and β2-microglobulin in urine.

KEYWORDS

proteinuria, terahertz time-domain spectroscopy, protein, absorption coefficient, pH

Introduction

Protein analysis of urine is an important clinical test, mainly used for diagnosis and treatment monitoring of kidney diseases, such as nephritis and renal failure. Healthy people lose less than 150 mg of protein from urine daily; therefore, a total protein excretion rate higher than 150 mg/24 h is considered proteinuria (Lamb et al., 2009). Proteinuria can be divided into glomerular proteinuria and tubular proteinuria according to the protein type. Glomerular proteinuria is dominated by albumin, whereas tubular proteinuria is dominated by β2-microglobulin (Tampe et al., 2021). At present, the protein qualitative test of urine is commonly performed using the sulfosalicylic acid method, the heated acetic acid method, and the dipstick test (Kumar and Gill, 2018). The sulfosalicylic acid method reacts with both albumin and globulin with high sensitivity (50 mg/L) and is preferred for screening tests, but strongly alkaline urine (pH > 9) or strong acid urine (pH < 3) is prone to false negative. A reaction time of more than 1 min will increase the probability of positive results, so the results need to be observed on time (Ridley, 2018). The heated acetic acid method reacts to both albumin

and globulin but is less sensitive (150 mg/L) (Rahayu and Rustiana, 2020). The dipstick test is sensitive to albumin but not to globulin, and its sensitivity (70 mg/L) is slightly lower than that of the sulfosalicylic acid method. False positives can occur when urine pH is elevated due to renal tubular acidosis, therapy of alkaline drugs, diet (vegetarian) (Carroll and Temte, 2000; Roberts, 2007; Clarkson et al., 2011). However, the dipstick test is often used to screen a large number of samples and medical emergencies duo to its simple operation, low cost. These biochemical methods require additional reagents and often rely on the naked eye to determine the results, which increases the complexity of the operation and reduces the accuracy of the results. It is necessary to develop a rapid and accurate screening method for proteinuria.

Terahertz (THz) waves are electromagnetic waves with frequencies between 0.1 and 10.0 THz, and their energy level range covers the energy levels of low-frequency motions (vibrations and rotations) of many organic macromolecules and hydrogen bonding networks in solution (9). These motions can be identified by fingerprint features in the THz transmission or absorption spectra, absorption changes, and phase changes (Zheng et al., 2014; Yan et al., 2016). Changes of biomolecules, such as change of formation, content, and state, strongly affect the THz spectral characteristics (Niehues et al., 2011; Bye et al., 2014; Klokkou et al., 2022). Recently, THz wave has been proved to have strong interactions with many biochemical molecules such as amino acids, proteins, and deoxyribonucleic acid (DNA) (Esser et al., 2018; Wu et al., 2020; Mancini et al., 2022). Moreover, THz waves have low photon energies (1 THz = 4.1 meV), which is about one million times weaker than the energy of X-ray photons, so it does not cause any harmful ionization in biological molecules (Sirkeli et al., 2018). Because of these properties, THz spectroscopy has emerged as a powerful tool for studying solvated biomolecules (Xie et al., 2014).

Blood is rich in solvated molecules, and many studies have been conducted using THz-TDS spectroscopy to detect blood components. Reid et al. found that there were significant differences in both the absorption spectra and refractive index spectra of the whole blood and thrombus, demonstrating the potential of THz spectroscopy in distinguishing different combinations of substances in human blood (Reid et al., 2013). Furthermore, Torii et al. measured the reflectance of sub-THz radiation on the concentration of glucose and albumin, and concluded that sub-THz radiation can be used to measure blood glucose and albumin (Torii et al., 2017). In addition, Chen et al. found a linear relationship between the THz absorption coefficient and blood glucose level through a quantitative analysis of 70 patients (Chen et al., 2018). Since both blood and urine are liquid biological specimens with complex compositions, and urine is essentially a product of ultra-filtered plasma, the study of THz-TDS spectroscopy for blood composition provides a theoretical basis for the use of THz-TDS spectroscopy for urine protein measurement. Therefore, we hypothesize that THz-TDS spectroscopy has the potential to detect proteins in urine samples and solve the problem of false positives and inaccuracy of the dipstick test in proteinuria screening.

In this study, we propose a new approach using THz-TDS for the qualitative detection of proteinuria. First, we compared the absorption spectra of proteinuria and non-proteinuria. Next, we investigated the effect of pH (6.0–9.0) on the analysis of proteinuria. Finally, we investigated the absorption spectra of β2-microglobulin and albumin to verify the ability of THz-TDS to distinguish different kinds of proteinuria.

Methods and materials

Experimental materials

Twenty urine samples (mean age 56 years; range 52–58 years) were provided by the department of laboratory medicine, Southwest Hospital, Chongqing. Our study was approved by Ethics Committee of the First Affiliated Hospital of Army Medical University (No.KY2020227). All the chemicals were purchased from Aladdin (Shanghai, China). Solutions were prepared with deionized water (Millipore, United States). Human Serum Albumin (HSA) (CAS No. 70024-90-7) was purchased from Solarbio (Beijing, China). Urine sample from tubular proteinuria patients which containing human β2-microglobulin was purchased from Prospec-Tany Technogene Ltd (Ness-Ziona, Israel). Urinalysis strips (H12-MA) were purchased from DiRui (Changchun, China).

For proteinuria testing, 20 samples with different protein concentrations and other parameters (pH, leukocytes, bilirubin, *etc.*) were chosen to be similar. The 20 samples were equally divided into four groups based on protein concentration: —(<0.1 g/L), + (0.3–1.0 g/L), ++ (1.0–3.0 g/L), +++ (3.0–6.0 g/L). For the test of effect of pH value on urine samples, HCl and NaOH were used to adjust the pH value of urine samples to 6.0, 7.0, 8.0, and 9.0, respectively. Normal urine sample was selected and divided into two parts, different concentrations of protein (albumin and β2-microglobulin) from 1 g/L to 10 g/L were added to observe the changes in the absorption spectrum of THz.

Urine test strip analysis

The pH and qualitative protein results contained in the urinalysis strips were reported by the fully automated UC-3500 (Sysmex, Kobe, Japan). Data are presented in the reports on an ordinal scale (as “normal,” “negative,” “positive,” or “nominal concentrations”).

Experimental equipment and sample cell

A Picometrix T-ray 5000 fiber-coupling spectrometer (Advanced Photonix, Inc., MI, United States) was used in the experiment (Figures 1A, B). The spectrometer generated and coherently detected the electric field of ultrashort THz electromagnetic pulses in the time domain using femtosecond near-infrared laser pulses and LT-InGaAs photoconductive antenna chips. The femtosecond pulse was produced by a Sapphire oscillator with a repetition rate of 100 MHz, a central wavelength of 1064 nm, and a duration of <100 fs. This pulse was

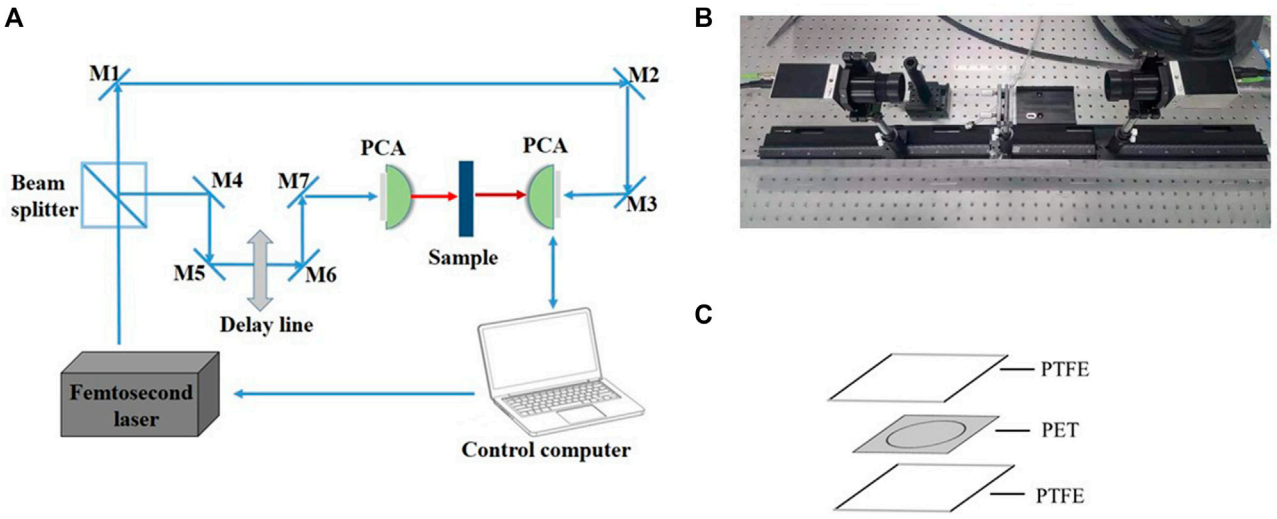

FIGURE 1
Experimental equipment **(A)** Schematics of the THz-TDS **(B)** The actual experimental setup **(C)** Schematic diagram of the sample cell.

split into two parts by a polarising beam splitter, one as a probe beam shining directly on the photoconductive antenna (PCA) and the other as pump light collected on the other PCA. The detection light was discretely sampled from the terahertz signal irradiating the second PCA to obtain a time domain waveform, which was transformed into the frequency domain using the Fast Fourier Transform. The sampling interval of the THz-TDS was 0.1 ps, and the spectral resolution was 12.5 GHz. More detailed descriptions can be found in our previous reports (Yan et al., 2016; Zang et al., 2019).

For the liquid measurement, the sample cells were prepared as follows: polyethylene glycol terephthalate (PET) double-sided tape (3M, MN, United States of America) of 0.10 mm thickness was cut into square spacers with side dimensions of 22.0 mm, in which a circle with a diameter of 15.0 mm was removed simultaneously, for accommodating the liquid sample (Figure 1C). By sealing the spacer with two polytetrafluoroethylene (PTFE) cover slips (Fisher Scientific, MA, United States) pasted together after the addition of the liquid samples, removal of excessive solution from any side of the spacer was possible to ensure that the spacer was completely filled. With a diameter of 15.0 mm and a thickness of 0.10 mm, the volume of the secure seal spacer was calculated to be ~17.7 μL, which was also the amount of sample added. The entire procedure takes less than a minute and the materials are inexpensive.

THz-TDS measurement

The THz frequency range was chosen between 0.5 and 1.2 THz to obtain the maximum signal-to-noise ratio and the most stable signal. Spectral frequency resolution of the spectrometer is 12.5 GHz. The measurement temperature was controlled at 21°C ± 0.4°C. The relative humidity was maintained at < 2.0% by nitrogen gas purging. An empty spacer was used as a reference to eliminate the background effects and each sample was measured seven times. After the sample chamber was prepared, it was sandwiched between a PTFE gasket and a neoprene gasket for measurement, and the frequency spectrum of the measured signal was obtained by using the Fourier transform.

Data analysis

The solution absorption coefficient is the energy loss of the terahertz beam in the medium. Taking into account the effect of reflection between the PTFE window and the sample, the absorption coefficient can be calculated by the improved Beer-Lambert theoretical formula as follows (Zang et al., 2019).

$$\alpha(\omega) = \frac{2}{d}\ln\left\{\frac{4n(\omega)n_q(\omega)}{\left[n(\omega)+n_q(\omega)\right]^2}\cdot\frac{\left[n_q(\omega)+1\right]^2}{4n_q(\omega)}\cdot\frac{1}{A(\omega)}\right\} \quad (1)$$

Where d is the thickness of the urine sample cell; $n_q(\omega) = 1.43$ is the refractive index of PTFE; $A(\omega)$ is the amplitude ratio of the Fourier transform of the urine sample cell (I_s) and the blank sample cell (I_{ref}); $n(\omega)$ is the refractive index of the sample.

Statistics analysis

The statistical analysis was performed using the SPSS software package, version 16.0 (SPSS, Chicago, IL, United States). The data are presented as means ± standard deviations (SDs), or medians. For comparisons, Student's t-test and the Mann–Whitney test were applied to continuous variables, while the chi-squared test was applied to categorical variables. The results of THz absorption in urine with different pH values were analyzed by one-way ANOVA and postoperative examination. The statistical differences between each group were determined by the least significant difference (LSD) test. p values <0.05 were considered significant.

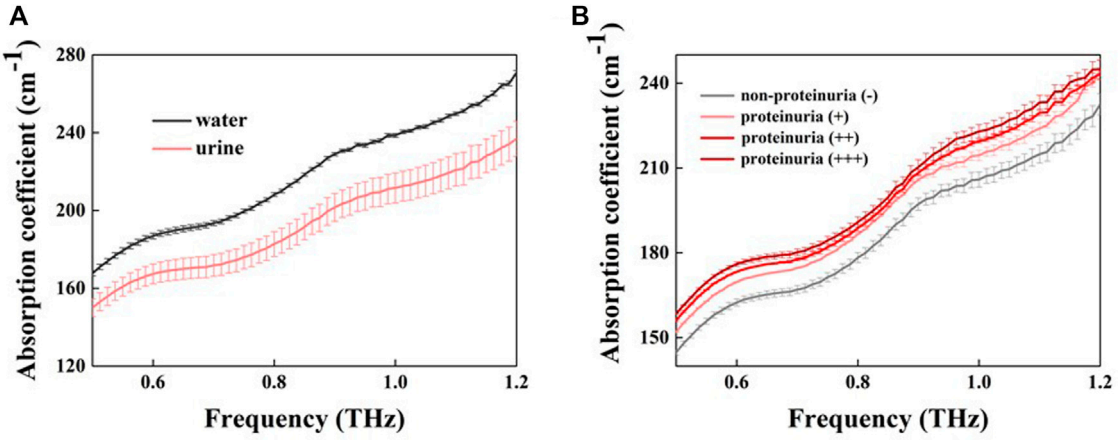

FIGURE 2
The absorption coefficient of water and urine samples **(A)** Absorption coefficients for pure water (black line) and urine (red line) **(B)** THz absorption coefficients for different concentrations of proteinuria (different red lines) and non-proteinuria (grey lines). Error bars indicate the standard deviation.

Results

Normal urine and proteinuria identification based on THz spectra

All non-smooth curves in the article are Fabry-Perot oscillations produced by thin sample pools and have no effect on the comparison of absorption coefficients between samples. Figure 2 shows the absorption coefficient of urine and pure water in the range of 0.5–1.2 THz. No significant absorption peaks were observed in the THz absorption spectra for the samples due to the disturbance and concealment of the liquid water (Xu et al., 2006). The absorption coefficient of water was higher than that of urine (Figure 2A). At 1.0 THz, the average absorption coefficient of water was 239 cm^{-1}, while that of urine was 214 cm^{-1}, with a difference of 25 cm^{-1}. The largest absorption coefficient difference between the urine samples was 14 cm^{-1} at 1.0 THz. We can observe that the largest absorption coefficient between the urine samples was comparable to the absorption coefficient difference between water and urine, which strongly indicates that THz absorption coefficient is sensitive to some contents in urine. Since the proteinuria samples were normal in other parameters, we therefore inferred protein in urine sample caused the absorption coefficient difference. Figure 2B shows the relationship between absorption coefficient and protein concentration in urinary samples. Proteinuria sample generally have a greater absorption coefficient than non-protein urine sample, moreover, the absorption coefficient increases with increasing protein concentration.

The effect of pH on urine

It is well known that alkaline urine (pH > 7.5) can cause false-positive results in the detection of urinary protein by dipstick method (Penders et al., 2002). To confirm whether the detection of protein by THz-TDS method is affected by pH, we used proteinuria samples with different pH value for detection. Here, HCl or NaOH was used to adjust the pH of urine samples to 6, 7, 8, and 9, respectively. The absorption coefficient of proteinuria (different protein concentrations) did not change significantly by different pH value at 1.0 THz ($p > 0.05$, Figure 3A). A linear increase in the absorption coefficient with increasing protein concentration was observed in the absorption coefficient profiles of urine samples with different concentration of proteins at the same pH (Figure 3B). The colorimetric profile of the urine analysis test strips was shown in Figure 3C. The protein concentration of normal urine without pH adjustment was negative with a pH around 6.5 (strip 1, Figure 3D). When this normal urine was adjusted to pH around 8.0, the protein concentration showed + ~ ++ (strip 2, Figure 3D). The above results demonstrated that the test strip method gave a false positive for protein at high pH, while the THz method was independent of pH with no significant change in absorption coefficient. In other words, the THz-TDS method seemed to be more suitable than the strip method for protein detection in alkaline urine samples.

The effect of different concentrations and types of protein on urinary absorption

The absorption spectra of β2-microglobulin and albumin with different concentrations at 1.0 THz are shown in Figure 4. The absorption coefficient of albumin was progressively greater than that of β2-microglobulin with increasing concentration, at concentrations higher than 0.5 g/L ($p < 0.05$). Although the error bars overlap at low concentration (<0.5 g/L), the curves generally show that higher molecular weight protein (albumin) has higher absorption capacity. Albumin is a single polypeptide chain consisting of 585 amino acids, and adopts a heart-shaped 3D structure with three homologous domains I-III; each domain contains two subdomains (He and Carter, 1992). The β2-microglobulin is a single-chain polypeptide composed of

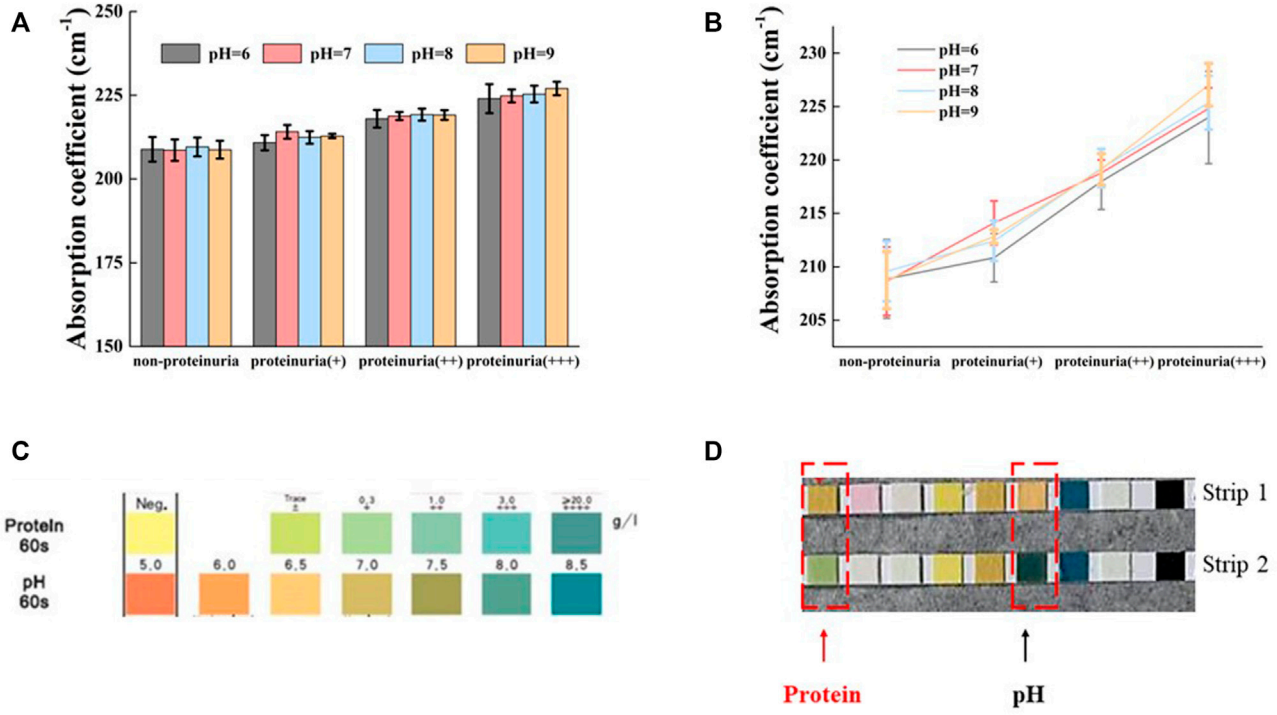

FIGURE 3
Effect of pH on the absorption of THz in different urine **(A)** Variation of urine absorption coefficient with pH for four different protein concentrations at 1.0 THz **(B)** Absorption coefficients and protein concentrations of urine with different protein concentrations at the same pH **(C)** Colorimetric mapping of urine analysis test strips **(D)** Non-proteinuria (strip 1) appears false positive after raising pH (strip 2). All data are shown as the mean ± standard deviation.

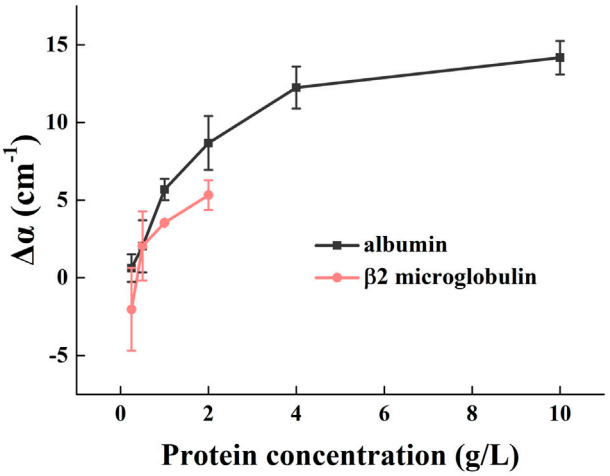

FIGURE 4
Effect of different types and concentrations of protein on urinary THz absorption. At 1.0 THz, the absorption spectra of albumin and β2 microglobulin at different concentrations. Δα = α(c) - α(urine), where α(urine) is absorption coefficient of urine before protein addition.

99 amino acids, containing a pair of disulfide bonds within the molecule and no sugars. Comparing these two proteins, albumin has a more complex conformation, which directly affects the dielectric response in the THz range and enhances THz absorption.

Discussion

In our study, the absorption coefficient increased with increasing protein concentration in the range of 0.5 THz to 1.2 THz, which can be explained exactly by the following theory. We consider the collected urine samples to have the same concentration of all components except for the protein concentration, which can be approximated by defining the samples as different concentrations of protein solutions. When aqueous solutions of various substances were studied, which could not be simply described as a two-component system; a third component was needed. Logically, the component was assumed as a hydrated shell (Penkov et al., 2018). For solvated protein, the total absorption could be decomposed into three components, the volume weighted average of the solute, the solvation water, and the bulk water, defined as follows (Ebbinghaus et al., 2007)

$$\alpha = \left(\alpha_{protein} V_{protein}\right)/V + \left(\alpha_{shell} V_{shell}\right)/V + \alpha_{protein}\left[1 - \left(V_{protein} + V_{shell}\right)/V\right] \quad (2)$$

When protein was added, the solute molecules had a lower frequency mode than the solvent, and the protein solution had a linear decrease in terahertz absorption compared to pure water. In addition, the concentrations of protein in the urine samples collected in this study were all below 0.5 mM, the absorption of solute water molecules in the broader (>10 Å) solute shell layer was enhanced, resulting in a linear increase in the absorption coefficient of the protein solution with concentration (Ebbinghaus et al., 2008).

When we discuss the effect of pH on the terahertz absorption of protein urine, we focused on the analysis of albumin, the main component of urinary protein. Global perturbations of the protein hydration shell caused by pH and local perturbations caused by charge dependent mutations at surface sites can alter the hydration dynamics, producing significant changes in the terahertz absorption spectrum of the protein solution (Ebbinghaus et al., 2008; Born and Havenith, 2009). During the transition from weakly acidic (pH 6.0) to alkaline (pH 9.0), albumin undergoes transitions, including normal type (N) and alkaline type (B) (Qin et al., 2016). The N-B transition undergoes a very subtle change with almost no loss of secondary structure (Leonard et al., 1963), which implies that the protein retains most of its heterogeneity and is chemically identical in the B and N conformations (Babcock and Brancaleon, 2013). Nevertheless, the protein still undergoes de-folding, extending from a tiny spherical structure to a loose chain with no specific spatial structure. This process alters the absorption rate and thickness of the extended hydration shell, which lead to a decrease in absorption (Heyden and Havenith, 2010). However, unfolded proteins have a high density of vibrational modes between 0 and 2.0 THz, leading to an increase in THz absorption (Castro-Camus and Johnston, 2008). The two effects cancel each other out so that pH has no significant effect on the absorption coefficient of the protein solution.

We demonstrated that there were differences in THz absorption of two different types of proteins, which could help distinguish between tubular proteinuria and glomerular proteinuria, the most common type of proteinuria in the clinic. Proteins with a molecular weight less than 20.0 kDa pass the glomerular capillary wall easily (Larson, 1994). Conversely, albumin, with a molecular weight of 65.0 kDa and negative charge, is restricted under normal conditions. The low molecular weight proteins are largely reabsorbed at the proximal tubule, only few amounts are excreted. Thus, tubular proteinuria is dominated by low molecular weight proteins, such as β2-microglobulin (11.7 kDa), and the total amount of the tubular proteins is very small in urine. β2-microglobulin tends to accumulate in the blood and urine of chronic renal failure patients (Winchester et al., 2003). On the other hand, glomerular proteinuria has a large amount of protein and its composition is dominated by albumin. Albuminuria is generally regarded as an excellent marker for assessing early renal damage in diabetes and hypertension (Nah et al., 2017). Distinguishing these two proteins is instructive in diagnosing of proteinuria.

We have initially demonstrated the feasibility of THz in the detection of urinary protein. However, future studies could benefit from the application of data processing algorithms based on the Principal Component Analysis or Karhunen–Loève Transform (KLT) to classify different concentrations of proteinuria (Zaharov et al., 2014; Shao et al., 2022).

Conclusion

The screening methods of urine samples should clearly separate samples without any indication for renal or genitourinary tract disorders from those samples which need further examination. In our study, a significantly different in absorption coefficient was found between proteinuria and non-proteinuria by THz-TDS method. Further analysis found that urinary protein and solvent water played a key role in this difference. At the same time, we investigated the effect of pH value (6.0–9.0) on urine sample and found that the absorption coefficient of urine sample did not change under different pH value by THz-TDS method. Finally, the absorption spectra of β2-microglobulin and albumin were studied, due to differences in conformation and molecular weight, these two proteins showed significant differences characteristics in absorption coefficient. Our study confirms that THz-TDS method can be used for proteinuria detection with ability to distinguish different proteinuria (renal tubular proteinuria and glomerular proteinuria). Moreover, THz spectroscopy has the potential to overcome the limitations of dipstick method by accurate detection of proteinuria even under alkaline condition. THz-TDS is a label-free method and shows great potential in the field of proteinuria detection. Further studies will establish a complete THz-TDS based system for the quantitative analysis of proteinuria.

Data availability statement

The raw data supporting the conclusions of this article will be made available by the authors, without undue reservation.

Ethics statement

The studies involving human participants were reviewed and approved by Ethics Committee of the First Affiliated Hospital of Army Medical University (No.KY2020227). The patients/participants provided their written informed consent to participate in this study.

Author contributions

CY supervised the project and revised the manuscript. ZX participated in the experimental work and writing of the manuscript. PM and PP contributed to scientific discussion and revised the manuscript. SY and ZZ contributed to some of the experimental work and data analysis.

Funding

This work was supported by the high-technology military medical cultivation project of the Third Military Medical University (Grant No. CX2019JS208); National Key R&D Program of China (No. 2016YFC0101300).

Conflict of interest

The authors declare that the research was conducted in the absence of any commercial or financial relationships that could be construed as a potential conflict of interest.

Publisher's note

References

Babcock, J. J., and Brancaleon, L. (2013). Bovine serum albumin oligomers in the E- and B-forms at low protein concentration and ionic strength. *Int. J. Biol. Macromol.* 53, 42–53. doi:10.1016/j.ijbiomac.2012.10.030

Born, B., and Havenith, M. (2009). Terahertz dance of proteins and sugars with water. *J. Infrared, Millim. Terahertz Waves* 30 (12), 1245–1254. doi:10.1007/s10762-009-9514-6

Bye, J. W., Meliga, S., Ferachou, D., Cinque, G., Zeitler, J. A., and Falconer, R. J. (2014). Analysis of the hydration water around bovine serum albumin using terahertz coherent synchrotron radiation. *J. Phys. Chem. A* 118 (1), 83–88. doi:10.1021/jp407410g

Carroll, M. F., and Temte, J. L. (2000). Proteinuria in adults: A diagnostic approach. *Am. Fam. Physician* 62 (6), 1333–1340.

Castro-Camus, E., and Johnston, M. B. (2008). Conformational changes of photoactive yellow protein monitored by terahertz spectroscopy. *Chem. Phys. Lett.* 455 (4-6), 289–292. doi:10.1016/j.cplett.2008.02.084

Chen, H., Chen, X., Ma, S., Wu, X., Yang, W., Zhang, W., et al. (2018). Quantify glucose level in freshly diabetic's blood by terahertz time-domain spectroscopy. *J. Infrared, Millim. Terahertz Waves* 39 (4), 399–408. doi:10.1007/s10762-017-0462-2

Clarkson, M. R., Magee, C. N., and Brenner, B. M. (Editors) (2011). "Chapter 2 - laboratory assessment of kidney disease," *Pocket companion to brenner and rector's the kidney*. Eighth Edition (Philadelphia: W.B. Saunders), 21–41.

Ebbinghaus, S., Kim, S. J., Heyden, M., Yu, X., Gruebele, M., Leitner, D. M., et al. (2008). Protein sequence- and pH-dependent hydration probed by terahertz spectroscopy. *J. Am. Chem. Soc.* 130 (8), 2374–2375. doi:10.1021/ja0746520

Ebbinghaus, S., Kim, S. J., Heyden, M., Yu, X., Heugen, U., Gruebele, M., et al. (2007). An extended dynamical hydration shell around proteins. *Proc. Natl. Acad. Sci. U. S. A.* 104 (52), 20749–20752. doi:10.1073/pnas.0709207104

Esser, A., Forbert, H., Sebastiani, F., Schwaab, G., Havenith, M., and Marx, D. (2018). Hydrophilic solvation dominates the terahertz fingerprint of amino acids in water. *J. Phys. Chem. B* 122 (4), 1453–1459. doi:10.1021/acs.jpcb.7b08563

He, X. M., and Carter, D. C. (1992). Atomic structure and chemistry of human serum albumin. *Nature* 358 (6383), 209–215. doi:10.1038/358209a0

Heyden, M., and Havenith, M. (2010). Combining THz spectroscopy and MD simulations to study protein-hydration coupling. *Methods* 52 (1), 74–83. doi:10.1016/j.ymeth.2010.05.007

Klokkou, N. T., Rowe, D. J., Bowden, B. M., Sessions, N. P., West, J. J., Wilkinson, J. S., et al. (2022). Structured surface wetting of a PTFE flow-cell for terahertz spectroscopy of proteins. *Sensors Actuators B Chem.* 352, 131003. doi:10.1016/j.snb.2021.131003

Kumar, V., and Gill, K. D. (2018). *To perform qualitative tests for urinary proteins. Basic concepts in clinical biochemistry: A practical guide*. Springer, 33–37.

Lamb, E. J., MacKenzie, F., and Stevens, P. E. (2009). How should proteinuria be detected and measured? *Ann. Clin. Biochem.* 46 (3), 205–217. doi:10.1258/acb.2009.009007

Larson, T. S. (1994). Evaluation of proteinuria. *Mayo Clin. Proc.* 69 (12), 1154–1158. doi:10.1016/s0025-6196(12)65767-x

Leonard, W. J., Jr., Vijai, K. K., and Foster, J. F. (1963). A structural transformation in bovine and human plasma albumins in alkaline solution as revealed by rotatory dispersion studies. *J. Biol. Chem.* 238, 1984–1988. doi:10.1016/s0021-9258(18)67930-x

Mancini, T., Mosetti, R., Marcelli, A., Petrarca, M., Lupi, S., and D'Arco, A. (2022). Terahertz spectroscopic analysis in protein dynamics: Current status. *Radiation* 2 (1), 100–123. doi:10.3390/radiation2010008

Nah, E-H., Cho, S., Kim, S., and Cho, H-I. (2017). Comparison of urine albumin-to-creatinine ratio (ACR) between ACR strip test and quantitative test in prediabetes and diabetes. *Ann. Laboratory Med.* 37, 28–33. doi:10.3343/alm.2017.37.1.28

Niehues, G., Heyden, M., Schmidt, D. A., and Havenith, M. (2011). Exploring hydrophobicity by THz absorption spectroscopy of solvated amino acids. *Faraday Discuss.* 150, 193–207. ; discussion 57-92. doi:10.1039/c0fd00007h

Penders, J., Fiers, T., and Delanghe, J. R. (2002). Quantitative evaluation of urinalysis test strips. *Clin. Chem.* 48 (12), 2236–2241. doi:10.1093/clinchem/48.12.2236

Penkov, N., Yashin, V., Fesenko, E., Jr., Manokhin, A., and Fesenko, E. (2018). A study of the effect of a protein on the structure of water in solution using terahertz time-domain spectroscopy. *Appl. Spectrosc.* 72 (2), 257–267. doi:10.1177/0003702817735551

Qin, Y., Wang, L., and Zhong, D. (2016). Dynamics and mechanism of ultrafast water-protein interactions. *Proc. Natl. Acad. Sci. U. S. A.* 113 (30), 8424–8429. doi:10.1073/pnas.1602916113

Rahayu, D., and Rustiana, T. (2020). Laboratory trial of protein determination in urine using different pH values of acetic acid and acetate buffer method. *Indonesian J. Med. Laboratory Sci. Technol.* 2 (1), 34–41. doi:10.33086/ijmlst.v2i1.1459

Reid, C. B., Reese, G., Gibson, A. P., and Wallace, V. P. (2013). Terahertz time-domain spectroscopy of human blood. *IEEE J. Biomed. Health Inf.* 17 (4), 774–778. doi:10.1109/jbhi.2013.2255306

Ridley, J. W. (2018). *Procedures for complete urinalysis/confirmation testing. Fundamentals of the study of urine and body fluids*. Springer, 203–249.

Roberts, J. R. (2007). Urine dipstick testing: Everything you need to know. *Emerg. Med. News* 29 (6), 24–27. doi:10.1097/01.eem.0000279130.93159.d9

Shao, D., Miao, S., Fan, Q., Wang, X., Liu, Z., and Ding, E. (2022). Classification method of coal and gangue using terahertz time-domain spectroscopy, cluster analysis and principal component analysis. *J. Appl. Spectrosc.* 89 (4), 719–725. doi:10.1007/s10812-022-01416-3

Sirkeli, V. P., Yilmazoglu, O., Preu, S., Küppers, F., and Hartnagel, H. L. (2018). Proposal for a monolithic broadband terahertz quantum cascade laser array tailored to detection of explosive materials. *Sens. Lett.* 16 (1), 1–7. doi:10.1166/sl.2018.3919

Sun, L., Zhao, L., and Peng, R-Y. (2021). Research progress in the effects of terahertz waves on biomacromolecules. *Mil. Med. Res.* 8 (1), 28–8. doi:10.1186/s40779-021-00321-8

Tampe, D., Korsten, P., Ströbel, P., Hakroush, S., and Tampe, B. (2021). Proteinuria indicates decreased normal glomeruli in ANCA-associated glomerulonephritis independent of systemic disease activity. *J. Clin. Med.* 10 (7), 1538. doi:10.3390/jcm10071538

Torii, T., Chiba, H., Tanabe, T., and Oyama, Y. (2017). Measurements of glucose concentration in aqueous solutions using reflected THz radiation for applications to a novel sub-THz radiation non-invasive blood sugar measurement method. *Digit. Health* 3, 205520761772953. doi:10.1177/2055207617729534

Winchester, J. F., Salsberg, J. A., and Levin, N. W. (2003). Beta-2 microglobulin in ESRD: An in-depth review. *Adv. Ren. Replacement Ther.* 10 (4), 279–309. doi:10.1053/j.arrt.2003.11.003

Wu, K., Qi, C., Zhu, Z., Wang, C., Song, B., and Chang, C. (2020). Terahertz wave accelerates DNA unwinding: A molecular dynamics simulation study. *J. Phys. Chem. Lett.* 11 (17), 7002–7008. doi:10.1021/acs.jpclett.0c01850

Xie, L., Yao, Y., and Ying, Y. (2014). The application of terahertz spectroscopy to protein detection: A review. *Appl. Spectrosc. Rev.* 49 (6), 448–461. doi:10.1080/05704928.2013.847845

Xu, J., Plaxco, K. W., and Allen, S. J. (2006). Probing the collective vibrational dynamics of a protein in liquid water by terahertz absorption spectroscopy. *Protein Sci.* 15 (5), 1175–1181. doi:10.1110/ps.062073506

Yan, S., Wei, D., Tang, M., Shi, C., Zhang, M., Yang, Z., et al. (2016). Determination of critical micelle concentrations of surfactants by terahertz time-domain spectroscopy. *IEEE Trans. Terahertz Sci. Technol.* 6 (4), 532–540. doi:10.1109/tthz.2016.2575450

Zaharov, V., Farahi, R. H., Snyder, P. J., Davison, B. H., and Passian, A. (2014). Karhunen–Loève treatment to remove noise and facilitate data analysis in sensing, spectroscopy and other applications. *Analyst* 139 (22), 5927–5935. doi:10.1039/c4an01300j

Zang, Z., Yan, S., Han, X., Wei, D., Cui, H-L., and Du, C. (2019). Temperature-and pH-dependent protein conformational changes investigated by terahertz dielectric spectroscopy. *Infrared Phys. Technol.* 98, 260–265. doi:10.1016/j.infrared.2019.03.021

Zheng, Z-P., Fan, W-H., Li, H., and Tang, J. (2014). Terahertz spectral investigation of anhydrous and monohydrated glucose using terahertz spectroscopy and solid-state theory. *J. Mol. Spectrosc.* 296, 9–13. doi:10.1016/j.jms.2013.12.002

frontiers | Frontiers in Bioengineering and Biotechnology

TYPE Original Research
PUBLISHED 13 March 2023
DOI 10.3389/fbioe.2023.1143443

OPEN ACCESS

EDITED BY
Junhong Lü,
Shanghai Advanced Research Institute (CAS), China

REVIEWED BY
Annalisa D'Arco,
National Institute of Nuclear Physics of Rome, Italy
Hongwei Zhao,
Shanghai Advanced Research Institute (CAS), China

*CORRESPONDENCE
Mingkun Zhang,
zhangmk@cigit.ac.cn
Huabin Wang,
wanghuabin@cigit.ac.cn

SPECIALTY SECTION
This article was submitted to Nanobiotechnology, a section of the journal Frontiers in Bioengineering and Biotechnology

RECEIVED 13 January 2023
ACCEPTED 02 March 2023
PUBLISHED 13 March 2023

CITATION
Fu Y, Chen T, Chen L, Guo Y, Yang Z, Mu N, Feng H, Zhang M and Wang H (2023), Terahertz time-domain attenuated total reflection spectroscopy integrated with a microfluidic chip. *Front. Bioeng. Biotechnol.* 11:1143443. doi: 10.3389/fbioe.2023.1143443

Terahertz time-domain attenuated total reflection spectroscopy integrated with a microfluidic chip

Ying Fu[1,2], Tunan Chen[3], Ligang Chen[1,2], Yuansen Guo[1,2], Zhongbo Yang[1,2], Ning Mu[3], Hua Feng[3], Mingkun Zhang[1,2]* and Huabin Wang[1,2]*

[1]Center of Super-Resolution Optics & Chongqing Engineering Research Center of High-Resolution and Three-Dimensional Dynamic Imaging Technology, Chongqing Institute of Green and Intelligent Technology, Chinese Academy of Sciences, Chongqing, China, [2]Chongqing School, University of Chinese Academy of Sciences, Chongqing, China, [3]Department of Neurosurgery and Key Laboratory of Neurotrauma, Southwest Hospital, Third Military Medical University (Army Medical University), Chongqing, China

The integration of a microfluidic chip into terahertz time-domain attenuated total reflection (THz TD-ATR) spectroscopy is highly demanded for the accurate measurement of aqueous samples. Hitherto, however little work has been reported on this regard. Here, we demonstrate a strategy of fabricating a polydimethylsiloxane microfluidic chip (M-chip) suitable for the measurement of aqueous samples, and investigate the effects of its configuration, particularly the cavity depth of the M-chip on THz spectra. By measuring pure water, we find that the Fresnel formulae of two-interface model should be applied to analyze the THz spectral data when the depth is smaller than 210 μm, but the Fresnel formula of one-interface model can be applied when the depth is no less than 210 μm. We further validate this by measuring physiological solution and protein solution. This work can help promote the application of THz TD-ATR spectroscopy in the study of aqueous biological samples.

KEYWORDS

terahertz, attenuated total reflection, microfluidic chip, evanescent field, lactate dehydrogenase

1 Introduction

Terahertz (THz) wave normally refers to the electromagnetic radiation with a frequency ranging from 0.1 THz to 10.0 THz, which is located between microwave and infrared regions (Wang et al., 2020a; Li et al., 2020; Yang et al., 2020; Meng et al., 2023). In the recent 2 decades, THz biological studies have attracted much attention among scientific communities, mainly thanks to the broad-band, label-free, and bio-sensitive features of THz wave (Zaytsev et al., 2015; Zhou et al., 2016; Sun et al., 2018; Bai et al., 2020; Chen et al., 2020; Zhu et al., 2020; Shen J. et al., 2021; Shen S. et al., 2021; Zhang et al., 2022b; Tang et al., 2022; Zhang et al., 2023). THz time-domain attenuated total reflection (THz TD-ATR) spectroscopy is an advanced THz technique, and superior to many conventional THz techniques due to its remarkable sensitivity by taking the advantage of evanescent-field detection (Arikawa et al., 2008; Wang et al., 2019; Hu et al., 2021; Liao et al., 2022). Moreover, THz TD-ATR spectroscopy enables the minimization of THz absorption by water when

measuring aqueous samples. As a result, THz TD-ATR spectroscopy is preferred by the researchers probing aqueous biological samples where high detection sensitivity and minimized water absorption are urgently required (Baxter and Guglietta, 2011; McIntosh et al., 2012; Qin et al., 2017; Peng et al., 2021). Employing this technique, various aqueous biological samples such as protein, DNA, amino acids, and saccharide have been investigated, which greatly promoted the development and application of THz TD-ATR spectroscopy in biological studies (Qin et al., 2013; Yang et al., 2016; Wang et al., 2020b; Tang et al., 2020).

THz TD-ATR spectroscopy includes two core parts, i.e., a THz TD spectroscopy system and an ATR prism incorporated into the THz optical path to allow in- and out-coupling of a THz beam. Normally, the prim is made of high-resistivity silicon, which is an almost perfectly transparent, non-dispersive and high-index material in the THz band. In a typical THz TD-ATR spectroscopy experiment, a sample is deposited onto the prism base, and the THz beam incident at a certain angle experiences total internal reflection at the prism-sample interface, producing an evanescent field attenuating exponentially inside the sample along the normal direction of the sample-prism boundary (Nagai et al., 2006; Peng et al., 2020). By detecting and analyzing the reflected detected THz beam, useful information on the measured sample is extracted. To obtain a reliable result, the sample thickness is required to be no less than the penetration depth of the evanescent field which is dependent on the THz frequency and the sample refractive index (Averett et al., 2008; Gotz et al., 2020; Mendoza-Galvan et al., 2021). To meet this requirement, a common practice in the study of aqueous sample is depositing a large amount of sample solution directly onto the ATR prism base or into an open liquid cell situated on the ATR prism base to guarantee the ATR reflection surface to be completely submerged and the thickness of the solution is high enough to prevent the penetration of THz evanescent field (Gu et al., 2019). Although this operation may work in some cases, it has at least two issues: 1) the inevitable solvent evaporation causes changes in the sample concentration, which compromises the accuracy of results; and 2) it needs relatively a large amount of sample, which is not allowed for rare or precious samples. The integration of a microfluidic chip (M-chip) into THz TD-ATR spectroscopy is a promising approach for tackling the above-mentioned issues, simultaneously (Karabudak, 2013). Although a few groups reported the application of M-chips in transmission mode THz spectroscopy (Xu et al., 2017; Gong et al., 2019), little work has been conducted to fabricate suitable M-chips for THz TD-ATR spectroscopy. Usually, M-chips used for transmission mode THz spectroscopy are not applicable for THz TD-ATR spectroscopy, and the mechanisms underlying the interactions between THz wave and M-chips are different for the 2 THz techniques.

In the present work, we fabricate a polydimethylsiloxane (PDMS) M-chip, integrate it into THz TD-ATR spectroscopy to form a THz TD-ATR microfluidic system, and investigate the configuration, particularly the influence of the depth of M-chip cavity on THz spectra. By measuring pure water, we find that the Fresnel formula of two-interface model should be used to extract aqueous sample properties when the cavity depth is smaller than 210 μm, but a simple Fresnel formula of one-interface model can be applied when the cavity depth is no less than 210 μm. This observation is further confirmed by measuring physiological solution and protein solution. Collectively, we demonstrate that the THz-TD ATR microfluidic system can serve as a useful platform for the study of aqueous biological samples.

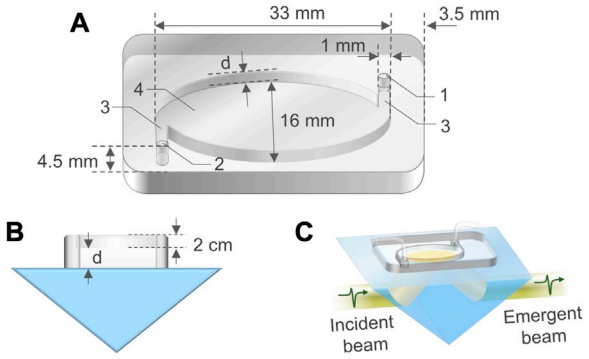

FIGURE 1
Configuration of a M-chip. **(A)** A 3D schematic view of a M-chip, in which the inlet "1" and outlet "2" holes, channels "3", and cavity "4" are connected. The diameter of the holes is 1 mm. The cavity is in a shape of elliptic cylinder, with a major axis length of 33 mm, and a minor axis length of 16 mm. The distances between the holes and the chip outside edges are 3.5 mm along the major axis direction and 4.5 mm along the minor axis direction of the cavity, respectively. **(B)** Side view of a M-chip situated on an ATR prism. The depth of channels is the same as the cavity depth (*d*), which is a variable. The depth of the holes is the summation of the cavity depth and the thickness (2 cm) of the upper wall. **(C)** A 3D schematic view of the ATR apparatus integrated with a M-chip. A *p*-polarized THz beam is incident horizontally to the left slanted side of the ATR prism, an isosceles triangulated column, then refracted and incident to the prism base at which the attenuated total internal reflection occurs. The emergent beam is detected for analysis.

2 Results and discussion

2.1 Configuration of microfluidic chips

PDMS is a popular material for fabricating microfluidic devices due to its advantages such as highly biocompatible, chemical inert, impermeable to water, inexpensive, flexible, and easy to be fabricated and bonded to other surfaces. PDMS M-chips were fabricated *via* injection molding (Sia and Whitesides, 2003) (Notes S1 and S2 of the Supplementary Material). Figure 1A is a three-dimensional (3D) schematic view of a fabricated M-chip, including an inlet, an outlet, a cavity with an elliptic cylinder shape, and two channels tangential to the wall of the cavity. The M-chip has upper wall and side wall, but no bottom (Figure 1B). This design ensures an aqueous sample in the cavity to contact with the ATR prism base without any barriers, enabling the sample to be directly probed with the evanescent filed generated by the total internal reflection occurring at the sample-prism interface (Figure 1C). Before a THz TD-ATR measurement, the M-chip was aligned carefully to make the cavity to fully cover the elliptical THz beam spot, and securely attached and sealed on the prism base by applying an even loading. A syringe or pump was employed to infuse a sample solution through a soft tube into the inlet by a pressure-driven mechanism, and the solution passed through the channel connected with the inlet to fill the cavity.

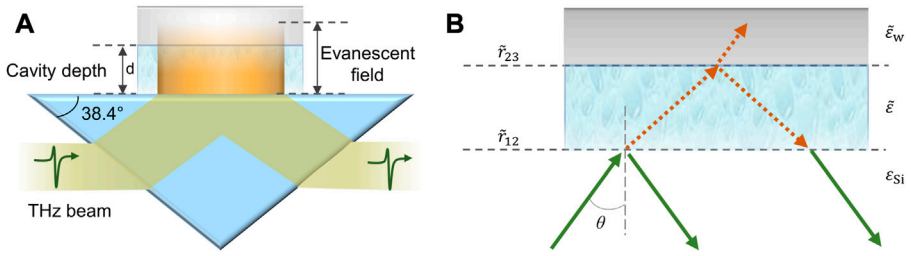

FIGURE 2
Schematic illustration of the interaction mechanism between the THz evanescent field and sample and M-chip. **(A)** THz evanescent field (in orange color) occurs at the prism-substance interface, penetrates the cavity, and enters the upper wall of the M-chip. The angle of ATR prism slant side is 38.4°. The substance in the cavity of the M-chip can be either air (i.e., reference) or aqueous sample. A prism-substance interface and a substance-PDMS upper-wall interface are formed. As the side wall of the M-chip does not influence the analysis in our case, it is not shown for simplicity. **(B)** $\tilde{r}_{12}$ and $\tilde{r}_{23}$ are the Fresnel's reflection coefficients of prism-substance interface and the substance-PDMS upper-wall interface, respectively. $\tilde{\varepsilon}_w$, $\tilde{\varepsilon}$, ε_{Si} denote the complex dielectric constants of the PDMS, substance in the cavity, and silicon prism, respectively. $\tilde{E}_{in}$ and $\tilde{E}_{out}$ are the incident and emergent beams, respectively, and $\tilde{r}$ is the ultimate Fresnel's reflection coefficient of the two-interface system. θ is the incident angle of the THz beam in the prism.

The excess sample solution and air bubbles were drained out through the outlet.

2.2 Analytical models for THz TD-ATR spectroscopy integrated with a M-chip

For proper application of the THz TD-ATR spectroscopy integrated with a PDMS M-chip, namely, the THz TD-ATR microfluidics system, we have to carefully consider the possible influence of the configuration of the M-chip on THz spectra. It is a non-trivial work to extract the true THz spectra of an aqueous sample filled in the cavity if the side wall of the M-chip interacts with the evanescent field. Fortunately, for a certain THz TD system, the cross section of the evanescent filed at the sample-prism interface can be estimated. In our case, the diameter of the THz beam is about 12 mm, yielding an elliptical beam spot on the prism base with major axis length of ~31 mm ($12/\sin^2 38.4^\circ$) and minor axis length of ~12 mm. Thus, we designed a M-chip with a cavity cross section larger than that of the evanescent field. With proper alignment of the M-chip, we ensured only the cavity region overlaid on the evanescent field, by which the influence of the side wall was avoided (Figure 2A). Although the effects of the side wall can be eliminated with this design, the influence of the upper wall of the M-chip has to be taken into account, i.e., the THz reflection occurred at the interface formed by the sample and PDMS upper wall needs to be considered, in order to extract reliable THz spectral data of the sample measured by the THz TD-ATR microfluidics system.

The sample complex dielectric constant is key for analyzing the sample properties. For our THz TD-ATR microfluidic system, the Fresnel's formulae for two-interface model are used to extract the complex dielectric constant of the sample for general cases (Møller et al., 2007),

$$\tilde{r}_{12} = \frac{\sqrt{\varepsilon_{Si}}\sqrt{1-\left(\varepsilon_{Si}/\tilde{\varepsilon}\right)\sin^2\theta} - \sqrt{\tilde{\varepsilon}}\cos\theta}{\sqrt{\varepsilon_{Si}}\sqrt{1-\left(\varepsilon_{Si}/\tilde{\varepsilon}\right)\sin^2\theta} + \sqrt{\tilde{\varepsilon}}\cos\theta} \quad (1)$$

$$\tilde{r}_{23} = \frac{\sqrt{\tilde{\varepsilon}}\sqrt{1-\left(\varepsilon_{Si}/\tilde{\varepsilon}_w\right)\sin^2\theta} - \sqrt{\tilde{\varepsilon}_w}\sqrt{1-\left(\varepsilon_{Si}/\tilde{\varepsilon}\right)\sin^2\theta}}{\sqrt{\tilde{\varepsilon}}\sqrt{1-\left(\varepsilon_{Si}/\tilde{\varepsilon}_w\right)\sin^2\theta} + \sqrt{\tilde{\varepsilon}_w}\sqrt{1-\left(\varepsilon_{Si}/\tilde{\varepsilon}\right)\sin^2\theta}} \quad (2)$$

where $\tilde{r}_{12}$ and $\tilde{r}_{23}$ are the Fresnel's reflection coefficients of prism-substance interface and the substance-PDMS upper-wall interface, respectively; $\tilde{\varepsilon}_w$, $\tilde{\varepsilon}$, and ε_{Si} are the complex dielectric constants of the PDMS, substance filled in the cavity and silicon prism, respectively; and θ is the incident angle of the THz beam in the prism.

For a cavity with a depth of d and an incident wave with a wavelength of λ, the ultimate Fresnel's reflection coefficient ($\tilde{r}$) that contains the information of the substance in the cavity and PDMS upper-wall due to their interactions with the evanescent wave is calculated by (McIntyre and Aspnes, 1971)

$$\tilde{r} = \frac{\tilde{r}_{12} + \tilde{r}_{23}\exp\left(i\frac{4\pi d}{\lambda}\sqrt{\tilde{\varepsilon} - \varepsilon_{Si}\sin^2\theta}\right)}{1 + \tilde{r}_{12}\tilde{r}_{23}\exp\left(i\frac{4\pi d}{\lambda}\sqrt{\tilde{\varepsilon} - \varepsilon_{Si}\sin^2\theta}\right)} \quad (3)$$

It needs to point out that if the evanescent field cannot penetrate the cavity to reach the upper wall of the M-chip, $\tilde{r}_{23}$ is zero, thus $\tilde{r}_{12}$ is equal to $\tilde{r}$. In this case, the two-interface model is degenerated to the one-interface model.

In the experiments, the M-chip without and with an aqueous sample was measured in tandem to obtain the information of the reference (i.e., air) and the sample, respectively. The above three equations are applicable to both the reference and the sample. By substituting Eqs 1, 2 into Eq. 3, the ultimate Fresnel's reflection coefficients of the reference ($\tilde{r}_{ref}$) and the sample ($\tilde{r}_{sam}$) were obtained, respectively. Furthermore, the relationship between the ultimate reflected electromagnetic field amplitudes of the sample ($\tilde{E}_{sam}$) and reference ($\tilde{E}_{ref}$) from the prism-substance interface and their corresponding reflection coefficients can be described by Eq. 4,

$$\frac{\tilde{E}_{sam}}{\tilde{E}_{ref}} = \frac{\tilde{r}_{sam}}{\tilde{r}_{ref}} \quad (4)$$

In the above equations, ε_{Si} (3.42), d; λ, θ (51.6°) and the dielectric constant of air (1) are all known, and $\tilde{\varepsilon}_w$ was measured using the THz TD spectroscopy in transmission mode (Supplementary Figure

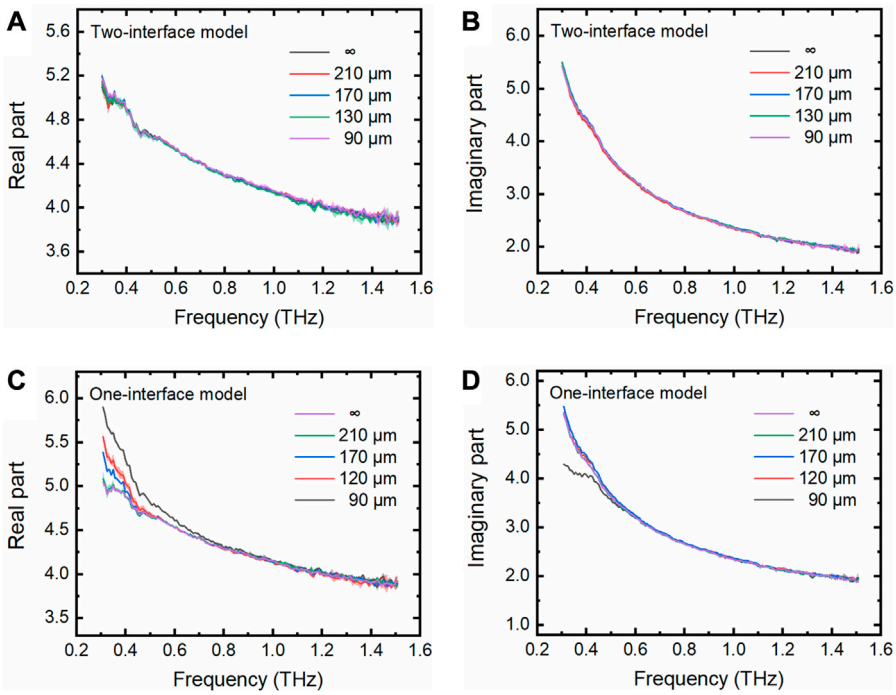

FIGURE 3
THz spectra of pure water measured using the THz TD-ATR microfluidic system. **(A–B)** Real and imaginary parts of the complex dielectric constants of pure water filled in the M-chips with various depths (90, 130, 170, and 210 μm) and the infinite thickness relative to the penetration depth of the evanescent waves, denoted by "∞", which were extracted by the two-interface model. **(C–D)** These parameters were extracted by the one-interface model. The semitransparent homochromic shadows around the lines represent the standard deviation (SD) of three independent measurements.

S3). With the above information, the complex dielectric constant of the measured sample can be calculated.

THz absorption coefficient (α) is also often used to describe the properties of samples, which is calculated according to the following equations (Jepsen et al., 2011; Zhang et al., 2022a),

$$\tilde{\varepsilon}(\nu) = \varepsilon'(\nu) - i\varepsilon''(\nu) \tag{5}$$

$$\varepsilon'(\nu) = n^2(\nu) - k^2(\nu) \tag{6}$$

$$\varepsilon''(\nu) = 2n(\nu)k(\nu) \tag{7}$$

$$\alpha(\nu) = \frac{4\pi\nu k(\nu)}{c} \tag{8}$$

where ε' and ε'' are the real and imaginary part of $\tilde{\varepsilon}$, respectively; ν is the frequency; n and k are the refractive index and extinction coefficient, respectively; and c is the speed of light in vacuum.

2.3 Dielectric measurement of pure water using the THz TD-ATR microfluidic system

Pure water is commonly used as the solvent for many biological samples. Therefore, we measured the THz spectra of pure water (Milli-Q water, 18.2 MΩ cm) using our fabricated M-chips with various cavity depths. By applying the two-interface model, we can see that the complex dielectric constants of pure water measured in the M-chips of various depths are highly consistent with each other (Figures 3A,B). They are also highly consistent with those measured without using the M-chips, for pure bulk water through which the THz evanescent field cannot penetrate. The results tell us that the two-interface model is accurately enough to be used to extract the THz properties of pure water in the cavity of M-Chips.

In contrast, the complex dielectric constants are not necessarily consistent with each other when the one-interface model was applied to analyze the data. Although the complex dielectric constant of pure water measured in the cavity with a depth of 210 μm is consistent with that of pure bulk water, the parameters extracted for the pure water in the cavities with depths of 90, 130, and 170 μm deviate from those of pure bulk water at the lower THz frequency range (Figures 3C,D). These observations indicate that the evanescent field penetrated the pure water with a thickness less than 210 μm, and reached the upper wall of the PDMS M-chip. Obviously, it is inappropriate to apply the one-interface model when the cavity depth is less than 210 μm because the one interface model is only suitable for the situation where the evanescent field does not penetrate the pure water. The influence of the cavity depth on the detected THz wave was further explored by analyzing the depth-related term contained in Eq. 3 for the two-interface model, as shown below,

$$\tilde{\Phi} = \tilde{r}_{23}\exp\left(i\frac{4\pi d}{\lambda}\sqrt{\tilde{\varepsilon} - \varepsilon_{Si}\sin^2\theta}\right) \tag{9}$$

This term is associated with the cavity depth when the evanescent wave reaches the upper wall of the PDMS M-chip. However, this term is zero, so the two-interface is degenerated to

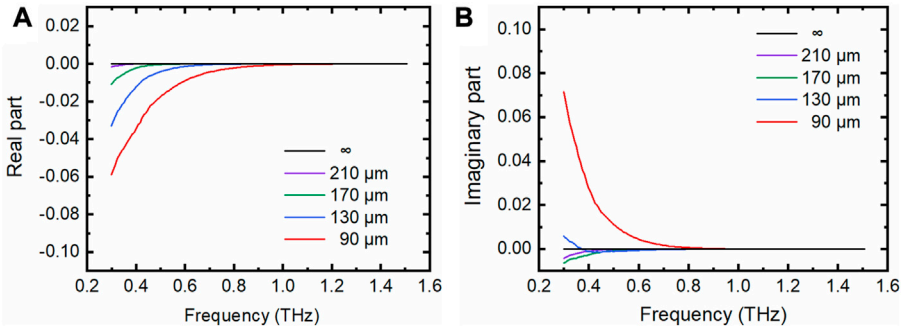

FIGURE 4
The real parts and imaginary parts of the depth-related term. **(A)** Real parts of the depth-related term $\tilde{\Phi}$. **(B)** Imaginary parts of $\tilde{\Phi}$. The cavity depth (pure water thickness) includes 90, 130, 170, and 210 μm "∞" indicates the thickness of pure bulk water, for which either the real part or the imaginary part of $\tilde{\Phi}$ is zero for the frequency range investigated.

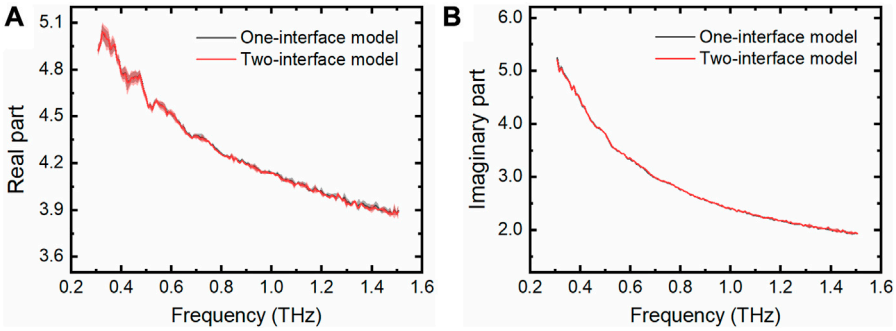

FIGURE 5
THz spectra of PBS measured by the THz TD-ATR microfluidic system. Real parts **(A)** and imaginary parts **(B)** of the complex dielectric constants of PBS were extracted by employing the one-interface model and the two-interface model, respectively. Translucent areas around each line indicate the standard deviation from three independent tests.

the one-interface model when the evanescent wave cannot penetrate through the aqueous sample in the cavity to reach the upper wall of the PDMS M-chip.

Experimentally, indeed, we observed that both the real and imaginary parts of $\tilde{\Phi}$ show a cavity-depth and frequency dependent character, particularly for the lower frequency range (Figures 4A,B). Interestingly, it is found that both the real and imaginary parts of $\tilde{\Phi}$ for the pure water with a thickness of 210 μm are nearly the same as those of the pure bulk water for the frequency is higher than 0.3 THz. The result verifies that the two-interface model can be degenerated to the one-interface model when the pure water thickness is no less than 210 μm, and that the two-interface model should be applied for pure water with the thickness less than 210 μm. These observations well explain the phenomena observed for the dielectric complex constants in Figure 3. For a commonly used THz TD-ATR spectroscopy system, the THz signal below 0.3 THz is very noisy and often not included in the data analysis. Thus, we recommend to use a M-chip with a cavity depth no less than 210 μm in THz TD-ATR microfluidic system, by which one can employ the simple one-interface model to analyze the data with enough reliability while avoid the complexity of the two-interface model. Specifically, the one-interface model is also applicable for M-chips with cavity depths of 90 μm and above when only the frequency beyond ~1.0 THz is considered in data analysis (Figure 4).

2.4 Dielectric measurement of physiological solution using the THz TD-ATR microfluidic system

From the above results we know that the THz TD-ATR spectroscopy integrated with a M-chip with a cavity depth no less than 210 μm can be reliably applied to measure pure water by simply using the one-interface model in the data analysis. To test the wide applicability of the THz TD-ATR system of the above configuration, we measured the THz spectra of phosphate buffered saline (PBS) solution, which is a physiological solution widely used to dissolve biological samples. It is evident that the extracted complex dielectric constants obtained by the one-interface model are well superimposed on those retrieved by the two-interface model (Figure 5).

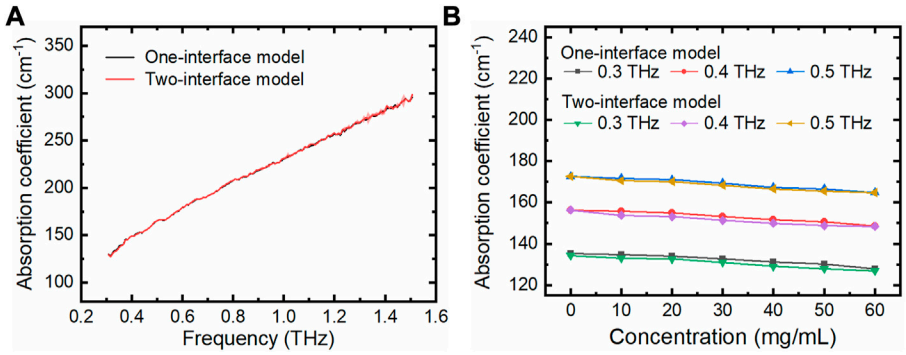

FIGURE 6
LDH solutions measured using the THz TD-ATR microfluidic system. **(A)** THz absorption coefficients of LDH solution (60 mg/mL) are plotted against the THz frequency, which were extracted using the two-interface model and one-interface model, respectively. **(B)** THz absorption coefficients of LDH solutions at specific THz frequencies are plotted against the LDH concentrations. The solution with a LDH concentration of 0 mg/mL is PBS solution. The error bars for the three independent experiments are too small to be clearly observed.

2.5 THz absorption measurement of protein solutions using the THz TD-ATR microfluidic system

One of our major purposes is to integrate a suitable M-chip into THz TD-ATR spectroscopy to study biological samples. Thus, we further measured lactic dehydrogenase (LDH) solutions with different concentrations using the PDMS M-chip with a cavity depth of 210 μm, and extracted their THz absorption coefficients which are widely used to assess the character of biological solutions. The THz coefficients were obtained by both the two-interface model and the one-interface model. For example, the THz coefficient of LDH solution with a concentration of 60 mg/mL plotted against a wide-band frequency was shown in Figure 6A. It is clear that for this M-chip configuration, the one-interface model is as accurate as the two-interface model for the measurement of LDH solutions. In addition, we also checked the THz absorption coefficients against the LDH concentrations at certain frequencies (e.g., 0.3, 0.4, and 0.5 THz; Figure 6B). Again, it confirms that there are no observable differences when applying the two models to analyze protein solutions measured by our THz TD-ATR microfluidic system. The THz absorption coefficient decreases with the increase of LDH concentration observed here is consistent with previous studies (Bye et al., 2014), which is very likely due to the solute (LDH) induced dilution and static depolarization effects (Penkov et al., 2017).

3 Conclusion

In this work, we demonstrated a simple and low-cost method of fabricating a M-chip for the measurement of a liquid phase sample with the THz TD-ATR. With the integration of the M-chip into the THz TD-ATR, the sample volume could be reduced to an unprecedentedly small volume as less as 40 μL. We also rationalized the application of theoretical models for analyzing the data obtained by the THz TD-ATR microfluidic system, which is critical for the proper application of the system. By measuring pure water, we found that the one-interface model can be safely applied in the data analysis when the cavity depth of M-chips is no less than 210 μm, but the two-interface model should be applied when the depth is less than 210 μm. Based on these results, we propose to use PDMS M-chips with a cavity depth of at least 210 μm in a THz TD-ATR microfluidic system when measuring readily available or cheap aqueous sample solutions to avoid the complexity of using the two-interface model in data analysis. Instead, PDMS M-chips with a cavity depth smaller than 210 μm and the two-interface model are suggested to be applied when measuring precious or expensive aqueous sample solutions in order to save the samples while keep the experimental reliability. With such a system, we successfully detected physiological (PBS) and protein (LDH) solutions. We also note that the theories shown here also hold for other solutions as far as the solutions are inert to PDMS, and that the threshold value of the cavity depth for applying the one-interface model may change, dependent on the performance of the THz TD-ATR and the refractive index of the measured solution (Liu et al., 2017). Collectively, the work presented here is helpful for researchers who exploit THz TD-ATR spectroscopy to investigate aqueous biological samples in a reliable and economical way.

4 Methods

4.1 Chemicals

Lactic dehydrogenase powder was purchased from Beijing Solarbio Science & Technology Co., Ltd. (Beijing, China), and dissolved in phosphate buffer saline (PBS, pH 7.4, Shanghai Branch of Thermo Fisher Scientific Inc. Shanghai, China) and diluted to desired concentrations with PBS. The prepolymer and the crosslinker of PDMS were ordered from the Shanghai Branch of Dow Corning Corp. (Shanghai, China).

4.2 Experimental setup

The THz-TD ATR spectroscopy system was established by incorporating an ATR apparatus (BATOP GmbH, Jena, Germany) into the optical path of a commercial THz-TDS system (Tera K15, Menlo Systems GmbH, Münich, Germany). A femtosecond laser with a

center wavelength of 1,560 nm, a repetition rate of 100 MHz, and a pulse width less than 90 fs was split into the pump beam and the probe beam. The THz radiation was emitted from a biased photoconductive antenna irradiated by the pump beam, and detected by another photoconductive antenna with the aid of the probe beam. Before experiments, the microfluidic chip fabricated by us was integrated into the system for the measurement of aqueous samples. The whole system was located in a clean room maintained at a temperature of 22°C ± 1.0°C. In experiments, the apparatus including the THz emitter, ATR prism integrated with microfluidic chip and THz detector were enclosed in a sealed container filled with pure nitrogen and kept the humidity to less than 4% to minimize the vapor absorption of THz wave. A *p*-polarized pulsed THz beam was horizontally incident on the left slanted side of the prism, and the refracted beam was detected from the right side of the prism. The ATR prism and PDMS chip can be re-used after cleaning by ethanol and distilled water in order. Either a milliliter medical syringe (Minkang Medical Materials Co., Ltd. Changsha, China) or a pressure-based flow controller (MFCS-EZ, Fluigent, Paris, France) was used to infuse sample solution into an M-chip.

4.3 Data analysis

Time-domain spectra were measured and converted to frequency-domain data by the fast Fourier transform algorithm, from which the electric field amplitude at different frequencies can be obtained. Then the complex dielectric constant and absorption coefficient can be calculated according to Eqs 1–8. The data for each sample represents the average value obtained from three independent measurements.

4.4 Fabrication of the microfluidic chip

Microfluidic chips with different cavity depths were fabricated by using a standard protocol, and the details were described in the Supplementary Material.

Data availability statement

The original contributions presented in the study are included in the article/Supplementary Material, further inquiries can be directed to the corresponding authors.

Author contributions

MZ and HW conceived the academic idea, HW guided the experiments, YF, TC, LC, NM, YG, and MZ performed the experiments, YF, MZ, ZY, and HW analyzed the data, YF completed the drawing work, TC contributed with helpful discussions, YF and HW wrote the manuscript with revisions by all.

Funding

This work is supported by the National Natural Science Foundation of China (62175238), the National Key Research and Development Program of China (2021YFA1301503), the University of Chinese Academy of Sciences Supported Program for Tackling Key Problems in Science and Technology (E029610601), Natural Science Foundation of Chongqing (cstc2019jcyj-msxmX0051), and Youth Innovation Promotion Association CAS (2022390).

Conflict of interest

The authors declare that the research was conducted in the absence of any commercial or financial relationships that could be construed as a potential conflict of interest.

Publisher's note

Supplementary material

The Supplementary Material for this article can be found online at: https://www.frontiersin.org/articles/10.3389/fbioe.2023.1143443/full#supplementary-material

References

Arikawa, T., Nagai, M., and Tanaka, K. (2008). Characterizing hydration state in solution using terahertz time-domain attenuated total reflection spectroscopy. *Chem. Phys. Lett.* 457 (1), 12–17. doi:10.1016/j.cplett.2008.03.062

Averett, L. A., Griffiths, P. R., and Nishikida, K. (2008). Effective path length in attenuated total reflection spectroscopy. *Anal. Chem.* 80 (8), 3045–3049. doi:10.1021/ac7025892

Bai, Z., Liu, Y., Kong, R., Nie, T., Wen, L., Li, H., et al. (2020). Near-field terahertz sensing of Hela cells and pseudomonas based on monolithic integrated metamaterials with a spintronic terahertz emitter. *ACS Appl. Mater. Interfaces* 12 (32), 35895–35902. doi:10.1021/acsami.0c08543

Baxter, J. B., and Guglietta, G. W. (2011). Terahertz spectroscopy. *Anal. Chem.* 83 (12), 4342–4368. doi:10.1021/ac200907z

Bye, J. W., Meliga, S., Ferachou, D., Cinque, G., Zeitler, J. A., and Falconer, R. J. (2014). Analysis of the hydration water around bovine serum albumin using terahertz coherent synchrotron radiation. *J. Phys. Chem. A* 118 (1), 83–88. doi:10.1021/jp407410g

Chen, L., Ren, G., Liu, L., Guo, P., Wang, E., Zhou, L., et al. (2020). Terahertz signatures of hydrate formation in alkali halide solutions. *J. Phys. Chem. Lett.* 11 (17), 7146–7152. doi:10.1021/acs.jpclett.0c02046

Gong, A., Qiu, Y., Chen, X., Zhao, Z., Xia, L., and Shao, Y. (2019). Biomedical applications of terahertz technology. *Appl. Spectrosc. Rev.* 55 (5), 418–438. doi:10.1080/05704928.2019.1670202

Gotz, A., Nikzad-Langerodi, R., Staedler, Y., Bellaire, A., and Saukel, J. (2020). Apparent penetration depth in attenuated total reflection Fourier-transform infrared

(ATR-FTIR) spectroscopy of Allium cepa L. epidermis and cuticle. *Spectrochim. Acta A* 224, 117460. doi:10.1016/j.saa.2019.117460

Gu, Y., Li, S., Xu, Y., Han, J., Gu, M., Cai, Z., et al. (2019). The effect of magnetic field on the hydration of cation in solution revealed by THz spectroscopy and MDs. *Colloid Surf. a-physicochem. Eng. Asp.* 582, 123822. doi:10.1016/j.colsurfa.2019.123822

Hu, M., Tang, M., Wang, H., Zhang, M., Zhu, S., Yang, Z., et al. (2021). Terahertz, infrared and Raman absorption spectra of tyrosine enantiomers and racemic compound. *Spectrochim. Acta A* 254, 119611. doi:10.1016/j.saa.2021.119611

Jepsen, P. U., Cooke, D. G., and Koch, M. (2011). Terahertz spectroscopy and imaging - modern techniques and applications. *Laser Photonics Rev.* 5 (1), 124–166. doi:10.1002/lpor.201000011

Karabudak, E. (2013). Micromachined silicon attenuated total reflectance infrared spectroscopy: An emerging detection method in micro/nanofluidics. *Electrophoresis* 35 (2-3), 236–244. doi:10.1002/elps.201300248

Li, Z., Yan, S., Zang, Z., Geng, G., Yang, Z., Li, J., et al. (2020). Single cell imaging with near-field terahertz scanning microscopy. *Cell Prolif.* 53 (4), e12788. doi:10.1111/cpr.12788

Liao, Y., Zhang, M., Tang, M., Chen, L., Li, X., Liu, Z., et al. (2022). Label-free study on the effect of a bioactive constituent on glioma cells *in vitro* using terahertz ATR spectroscopy. *Biomed. Opt. Exp.* 13 (4), 2380–2392. doi:10.1364/boe.452952

Liu, H., Wang, Y., Xu, D., Wu, L., Yan, C., Yan, D., et al. (2017). High-sensitivity attenuated total internal reflection continuous-wave terahertz imaging. *J. Phys. D. Appl. Phys.* 50 (37), 375103. doi:10.1088/1361-6463/aa7d9a

McIntosh, A. I., Yang, B., Goldup, S. M., Watkinson, M., and Donnan, R. S. (2012). Terahertz spectroscopy: A powerful new tool for the chemical sciences? *Chem. Soc. Rev.* 41 (6), 2072–2082. doi:10.1039/c1cs15277g

McIntyre, J. D. E., and Aspnes, D. E. (1971). Differential reflection spectroscopy of very thin surface films. *Surf. Sci.* 24 (2), 417–434. doi:10.1016/0039-6028(71)90272-X

Mendoza-Galvan, A., Mendez-Lara, J. G., Mauricio-Sanchez, R. A., Jarrendahl, K., and Arwin, H. (2021). Effective absorption coefficient and effective thickness in attenuated total reflection spectroscopy. *Opt. Lett.* 46 (4), 872–875. doi:10.1364/ol.418277

Meng, Q., Wang, X., Zhang, B., Qian, S., Peng, B., Zhou, H., et al. (2023). Magnetic induced terahertz modulation characteristics based on ferromagnetic nematic liquid crystals. *Spectrochim. Acta A* 289, 122232. doi:10.1016/j.saa.2022.122232

Møller, U., Merbold, H., Folkenberg, J. R., and Jepsen, P. U. (2007). Determination of alcohol concentration in aqueous solutions and food analysis using reflection terahertz time-domain spectroscopy. *OSA Tech. Dig. Ser. (CD)* 2007, MB2. doi:10.1364/OTST.2007.MB2

Nagai, M., Yada, H., Arikawa, T., and Tanaka, K. (2006). Terahertz time-domain attenuated total reflection spectroscopy in water and biological solution. *Int. J. Infrared. Milli. Waves* 27 (4), 505–515. doi:10.1007/s10762-006-9098-3

Peng, W., Chen, S., Kong, D., Zhou, X., Lu, X., and Chang, C. (2021). Grade diagnosis of human glioma using Fourier transform infrared microscopy and artificial neural network. *Spectrochim. Acta A* 260, 119946. doi:10.1016/j.saa.2021.119946

Peng, Y., Shi, C., Zhu, Y., Gu, M., and Zhuang, S. (2020). Terahertz spectroscopy in biomedical field: A review on signal-to-noise ratio improvement. *PhotoniX* 1 (1), 12. doi:10.1186/s43074-020-00011-z

Penkov, N., Yashin, V., Fesenko, E., Manokhin, A., and Fesenko, E. (2017). A study of the effect of a protein on the structure of water in solution using terahertz time-domain spectroscopy. *Appl. Spectrosc.* 72 (2), 257–267. doi:10.1177/0003702817735551

Qin, J., Xie, L., and Ying, Y. (2017). Rapid analysis of tetracycline hydrochloride solution by attenuated total reflection terahertz time-domain spectroscopy. *Food Chem.* 224, 262–269. doi:10.1016/j.foodchem.2016.12.064

Qin, J., Ying, Y., and Xie, L. (2013). The detection of agricultural products and food using terahertz spectroscopy: A review. *Appl. Spectrosc. Rev.* 48 (6), 439–457. doi:10.1080/05704928.2012.745418

Shen, J., Zhu, Z., Zhang, Z., Guo, C., Zhang, J., Ren, G., et al. (2021a). Ultra-broadband terahertz fingerprint spectrum of melatonin with vibrational mode analysis. *Spectrochim. Acta A* 247, 119141. doi:10.1016/j.saa.2020.119141

Shen, S., Liu, X., Shen, Y., Qu, J., Pickwell-MacPherson, E., Wei, X., et al. (2021b). Recent advances in the development of materials for terahertz metamaterial sensing. *Adv. Opt. Mater.* 10 (1), 2101008. doi:10.1002/adom.202101008

Sia, S. K., and Whitesides, G. M. (2003). Microfluidic devices fabricated in poly (dimethylsiloxane) for biological studies. *Electrophoresis* 24 (21), 3563–3576. doi:10.1002/elps.200305584

Sun, Y., Du, P., Lu, X., Xie, P., Qian, Z., Fan, S., et al. (2018). Quantitative characterization of bovine serum albumin thin-films using terahertz spectroscopy and machine learning methods. *Biomed. Opt. Exp.* 9 (7), 2917–2929. doi:10.1364/boe.9.002917

Tang, C., Wang, Y., Cheng, J., Chang, C., Hu, J., and Lu, J. (2022). Probing terahertz dynamics of multidomain protein in cell-like confinement. *Spectrochim. Acta A* 275, 121173. doi:10.1016/j.saa.2022.121173

Tang, M., Zhang, M., Xia, L., Yang, Z., Yan, S., Wang, H., et al. (2020). Detection of single-base mutation of DNA oligonucleotides with different lengths by terahertz attenuated total reflection microfluidic cell. *Biomed. Opt. Exp.* 11 (9), 5362–5372. doi:10.1364/boe.400487

Wang, Y., Cui, Z., Zhang, X., Zhang, X., Hu, H., Chen, S., et al. (2020a). Excitation of surface plasmon resonance onmultiwalled carbon nanotube metasurfaces for pesticide sensors. *ACS Appl. Mater. Interfaces* 12 (46), 52082–52088. doi:10.1021/acsami.0c10943

Wang, Y., Jiang, Z., Xu, D., Chen, T., Chen, B., Wang, S., et al. (2019). Study of the dielectric characteristics of living glial-like cells using terahertz ATR spectroscopy. *Biomed. Opt. Exp.* 10 (10), 5351–5361. doi:10.1364/boe.10.005351

Wang, Y., Wang, G., Xu, D., Jiang, B., Ge, M., Wu, L., et al. (2020b). Terahertz spectroscopic diagnosis of early blast-induced traumatic brain injury in rats. *Biomed. Opt. Exp.* 11 (8), 4085–4098. doi:10.1364/boe.395432

Xu, W., Xie, L., and Ying, Y. (2017). Mechanisms and applications of terahertz metamaterial sensing: A review. *Nanoscale* 9 (37), 13864–13878. doi:10.1039/c7nr03824k

Yang, X., Zhao, X., Yang, K., Liu, Y., Liu, Y., Fu, W., et al. (2016). Biomedical applications of terahertz spectroscopy and imaging. *Trends Biotechnol.* 34 (10), 810–824. doi:10.1016/j.tibtech.2016.04.008

Yang, Z., Tang, D., Hu, J., Tang, M., Zhang, M., Cui, H., et al. (2020). Near-field nanoscopic terahertz imaging of single proteins. *Small* 17 (3), 2005814. doi:10.1002/smll.202005814

Zaytsev, K. I., Kudrin, K. G., Karasik, V. E., Reshetov, I. V., and Yurchenko, S. O. (2015). *In vivo* terahertz spectroscopy of pigmentary skin nevi: Pilot study of non-invasive early diagnosis of dysplasia. *Appl. Phys. Lett.* 106 (5), 053702. doi:10.1063/1.4907350

Zhang, G., Wang, Y., Qian, J., Wang, Y., Li, X., and Lü, J. (2023). Terahertz refractive phenotype of living cells. *Front. Bioeng. Biotechnol.* 10, 1105249. doi:10.3389/fbioe.2022.1105249

Zhang, Z., Li, Y., Xiang, Z., Huang, Y., Wang, R., and Chang, C. (2022a). Dielectric dispersion characteristics of the phospholipid bilayer with subnanometer resolution from terahertz to mid-infrared. *Front. Bioeng. Biotechnol.* 10, 984880. doi:10.3389/fbioe.2022.984880

Zhang, Z., Zhang, T., Fan, F., Ji, Y., and Chang, S. (2022b). Terahertz polarization sensing of bovine serum albumin proteolysis on curved flexible metasurface. *Sens. Actuators A Phys.* 338, 113499. doi:10.1016/j.sna.2022.113499

Zhou, S., Valchev, D. G., Dinovitser, A., Chappell, J. M., Iqbal, A., Ng, B. W. H., et al. (2016). Terahertz signal classification based on geometric algebra. *IEEE Trans. Terahertz Sci. Technol.* 6 (6), 793–802. doi:10.1109/tthz.2016.2610759

Zhu, Z., Zhang, J., Song, Y., Chang, C., Ren, G., Shen, J., et al. (2020). Broadband terahertz signatures and vibrations of dopamine. *Analyst* 145 (18), 6006–6013. doi:10.1039/d0an00771d

frontiers | Frontiers in Bioengineering and Biotechnology

TYPE Original Research
PUBLISHED 23 March 2023
DOI 10.3389/fbioe.2023.1170218

OPEN ACCESS

EDITED BY
Sai Kumar Tammina,
Kyung Hee University, Republic of Korea

REVIEWED BY
Han Wang,
Applied Materials, United States
Saranya Packialakshmi Jeyakumar,
Kyung Hee University, Republic of Korea

*CORRESPONDENCE
Wei Shi,
swshi@mail.xaut.edu.cn

SPECIALTY SECTION
This article was submitted to Biosensors and Biomolecular Electronics, a section of the journal Frontiers in Bioengineering and Biotechnology

RECEIVED 20 February 2023
ACCEPTED 13 March 2023
PUBLISHED 23 March 2023

CITATION
Wang H, Shi W, Hou L, Li C, Zhang Y, Yang L and Cao J (2023), Detection of the minimum concentrations of α-lactose solution using high-power THz-ATR spectroscopy.
Front. Bioeng. Biotechnol. 11:1170218.
doi: 10.3389/fbioe.2023.1170218

Detection of the minimum concentrations of α-lactose solution using high-power THz-ATR spectroscopy

Haiqing Wang[1,2], Wei Shi[1]*, Lei Hou[1], Chunhui Li[1], Yusong Zhang[1], Lei Yang[1] and Juncheng Cao[3]

[1]Key Laboratory of Ultrafast Photoelectric Technology and Terahertz Science in Shaanxi, Xi'an University of Technology, Xi'an, China, [2]School of Physics and Opto-Electronic Technology, Baoji Key Laboratory of Micro-Nano Optoelectronics and Terahertz Technology, Baoji University of Arts and Sciences, Baoji, Shaanxi, China, [3]Country the Key Laboratory of Terahertz Solid-State Technology, Shanghai Institute of Microsystem and Information Technology, Chinese Academy of Sciences, Shanghai, China

Terahertz (THz) technology has emerged as a promising tool for the qualitative and quantitative identification of markers containing major diseases, enabling early diagnosis and staged treatment of diseases. Nevertheless, the detection of water-containing biological samples is facing significant challenges due to limitations in high-power THz radiation sources and high-sensitivity detection devices. In this paper, we present a designed and constructed set of Terahertz-Attenuated Total Reflection (THz-ATR) spectrometer for high-sensitivity detection of liquid biological samples, which can dynamically maintain the signal-to-noise ratio (SNR) of THz detection signal of liquid biological samples at 40–60 dB. Our high-power THz-ATR spectroscopy can identify and quantitatively detect α-lactose aqueous solution with a minimum concentration of 0.292 mol/L. Moreover, we observed that the rate of change in the absorption peak position varied greatly between high and low concentration samples. Our high-power, high-sensitivity THz-ATR spectroscopy detection provides a rapid, accurate, and low-cost method for detecting disease markers such as blood and urine indicators. Additionally, this approach offers new perspectives for the refinement and in-depth detection of biomedical samples.

KEYWORDS

high-power THz-ATR spectroscopy, α-lactose solution, signal-to-noise ratio (SNR), LT-GaAs PCA, high-energy LiNbO3

1 Introduction

Terahertz (THz) spectroscopy has shown great potential in the biomedical field for qualitative and quantitative identification of key substances, such as early detection of cancer and blood indicator detection (Torii et al., 2017; Wang et al., 2020; Shi et al., 2021; Liao et al., 2022). However, the detection of characteristic spectra of target substances is often limited by the insufficient signal-to-noise ratio (SNR) of the detection system, resulting in inaccurate identification of the target substance (Naftaly, 2012; Peng et al., 2020a; Peng et al., 2020b). Factors affecting the SNR of biomedical sample detection include: 1) low SNR of the THz spectroscopy system (Alfihed et al., 2020); 2) strong absorption of THz waves by water, leading to high loss in the transmission of the sample signal (Yang et al., 2016); and 3) interference of non-target materials, leading to difficulties in resolving the target signal (Peng

et al., 2018). Therefore, improving the SNR of aqueous samples is fundamental to achieve qualitative and quantitative detection of biomedical samples.

Currently, there are three main technical means to improve the SNR of water-containing samples. The first is system optimization, which involves developing a THz radiation source with high radiated power and good stability. Strong field THz radiation technology includes the use of femtosecond laser and non-linear crystal interaction, high-intensity THz pulse obtained using the tilted pulse-front technique, and the high-power crystal radiation source represented by LiNbO3 crystal, which has been used in experimental detection work (Moriguchi et al., 2018; Yang et al., 2020). Although the interaction of ultrafast and ultra-strong laser and plasma, as well as the new mechanism of strong laser-solid-target interaction, have achieved high radiation power, they have not yet been applied to THz spectroscopy (Yardimci et al., 2017; Liao et al., 2019).

The second approach is the use of THz detection devices to enhance biological THz signals. Existing works focus on methods that utilize evanescent waves or enhance local THz field strength, such as the use of microfluidic chips, metamaterial sensors, waveguides, and THz-ATR (Liu et al., 2019; Hou et al., 2021; Yang et al., 2021; Yu et al., 2022). THz-ATR has several advantages, including high detection sensitivity, low sample requirements, and the ability to achieve qualitative and quantitative detection of samples simultaneously.

The third approach involves algorithm denoising reconstruction of data. For signals containing noise, multiple summations can be used for denoising, and data smoothing methods can be employed, including conventional methods represented by N-point averaging and special methods represented by wavelet transform denoising methods, which may sacrifice some signal information (Qiao et al., 2017; Cui et al., 2019; Takagi et al., 2020).

In this paper, we present a set of THz detection spectrometers for cells and biomolecules that can switch instantly between the low temperature grown GaAs photoconductive antenna (LT-GaAs PCA) radiation source and high-energy LiNbO3 radiation source. ATR-assisted enhancement of sample signals maximizes the detection sensitivity of aqueous samples. With improved system performance, the SNR of different concentration sample signals can be dynamically maintained at 40–60 dB, enabling the qualitative and quantitative detection.

2 Sample preparation and experiment

2.1 Sample preparation

The α-lactose monohydrate used in this study was procured from Aladdin (Shanghai) Co., Ltd. and was of analytical purity. To ensure accuracy, the sample powder was weighed using an electronic analytical balance with a precision of 0.01 mg. Quantitative addition of water was performed using a pipette gun with a range of 10–100 μl and an accuracy of 1 μl. The α-lactose monohydrate powder to be tested was placed directly into the sample cell on the ATR prism, followed by the quantitative addition of water for the test. As α-lactose monohydrate is soluble in water, the homogeneity of the sample solution was ensured. The concentrations of the prepared samples were 19.467 mol/L, 5.309 mol/L, 1.168 mol/L, 0.664 mol/L, 0.314 mol/L, and 0.292 mol/L, respectively. To prevent water from spreading to the surroundings, a sealing ring was placed on the surface of the ATR prism. During the test, the drip port was sealed with a metal foil to prevent water evaporation, thereby avoiding concentration deviations caused by the test sample.

2.2 Design of attenuating total reflection prism

The design of the attenuated total reflection spectroscopic detection system is based on the principle of total reflection of light. When a light wave is incident from a medium with a high refractive index (prism material) to a medium with a lower refractive index (air or aqueous biological samples), total reflection occurs at the interface between the two media if the angle of incidence is greater than the critical angle, also known as the Broster angle. This results in the generation of evanescent waves at the interface between the two media, where the amplitude of the evanescent wave decays exponentially with the vertical direction of the interface. The penetration depth of the incident evanescent wave into the sample can be calculated using the following formula:

$$d_p = \frac{\lambda}{2\pi\sqrt{n_1^2 \sin^2\theta - n_2^2}} \tag{1}$$

where λ represents the wavelength of the incident light wave, n1 and n2 represent the refractive indices of the two media, respectively, and they satisfy n1 > n2. θ is the angle of incidence. The attenuation of the evanescent wave at the interface allows for spectral information to be obtained from a micron or thinner layer from the interface, which can be used for the detection of trace biological samples.

In this project, molten silicon with a resistance greater than 10,000 Ω/cm is used as the basic material to fabricate the ATR prisms. The ATR prisms are made using cutting, grinding, and polishing processes to form right isosceles triangular prisms. Figures 1A,B show the schematic diagram of the design dimensions of the ATR prism and THz-ATR spectroscopic detection of aqueous samples, respectively. The triangular prisms have side lengths of 48 mm, 34 mm, and 34 mm, respectively, with a thickness of 21 mm. The angle of incidence θ1 is 45°, the angle of refraction θ2 is 11.8°, and the internal total reflection angle θ3 is 56.8°.

2.3 THz detection spectrometer for liquid biological samples

We have designed and constructed a THz detection spectrometer for liquid biological samples to meet the high SNR requirements of biomedical sample detection signals. The system consists of two sets of THz radiation sources that can be instantly switched by folding mirrors to meet the detection needs of various samples. Moreover, an ATR setup is employed to enhance the sample signal, ensuring that the SNR of the signal of different concentrations always stays between 40–60 dB to achieve qualitative and quantitative detection of aqueous samples.

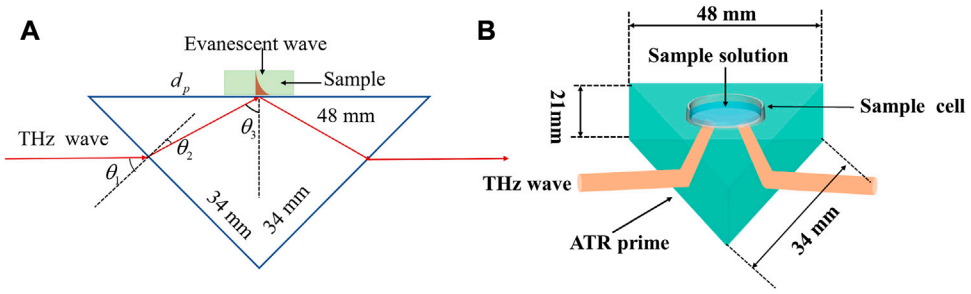

FIGURE 1
The schematic diagram of **(A)** the design dimensions of the ATR prism and **(B)** THz-ATR spectroscopic detection of aqueous samples.

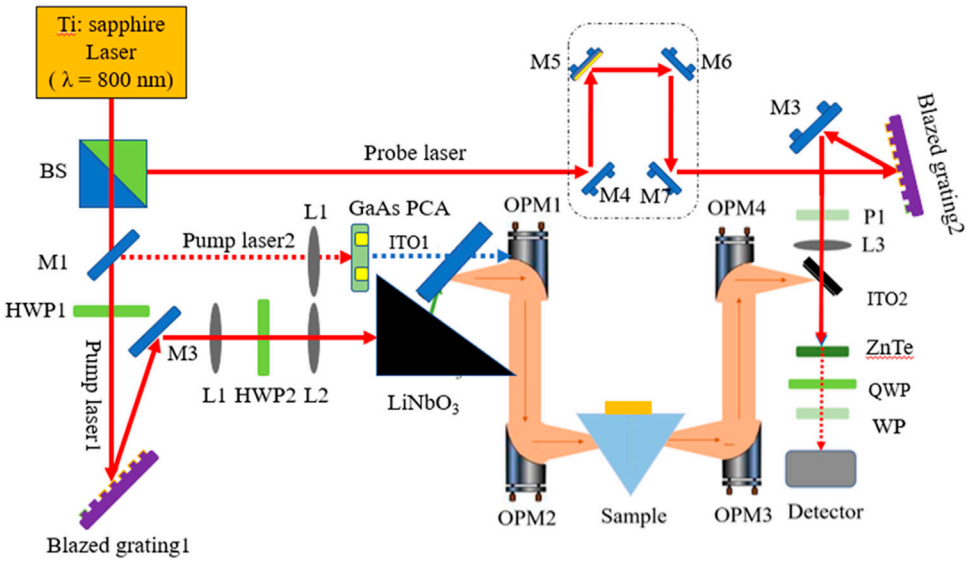

FIGURE 2
The schematic diagram of the design optical path of THz-ATR spectrometer for liquid biological samples.

The schematic diagram of the designed optical path of the THz-ATR spectrometer for liquid biological samples is presented in Figure 2. The system mainly comprises a MaiTai femtosecond laser, THz radiation sources (LT-GaAs PCA and LiNbO3 crystal), ATR prism, and THz detector. The MaiTai XF-1 titanium sapphire femtosecond laser oscillator from Spectra-Physics is used as the seed light source, with an average output power of approximately 4.5 W. The femtosecond laser is split into pump light 1 and probe light by a beam splitter, with corresponding pulse energies of 3 W and 100 mW, respectively. Pump 1 is attenuated and then passed through mirror M1 (foldback mirror) to generate pump light 2 with a pulse energy of about 300 mW.

First, the laser polarization direction of pump light 1 is adjusted to horizontal polarization through the half-wave plate HWP1 to maximize the first-stage diffraction efficiency of the blazed grating. Then, the first-stage diffraction of the shining grating creates an inclined wavefront, which is vertically polarized by adjusting the direction of laser polarization through the half-plate HWP2. Finally, pump light 1 is incident at a suitable wavefront inclination angle to a LiNbO3 crystal with a cutting angle of 63°, matching the wave velocity of the THz wave and the femtosecond laser in the exit direction of the THz wave, thus exciting a high-power THz wave. Pump light 2 is focused through the lens and incident on the LT-GaAs PCA to generate broad-spectrum THz waves. The THz pulses exiting from the radiation sources are collimated by the first off-axis parabolic mirror (OPM1) and then converged by the off-axis parabolic mirror (OPM2). The ATR sample cell is placed at the focal point of the second off-axis parabolic mirror. The reflected THz waves carrying the sample information are collected by OPM3 and OPM4 and focused on ZnTe. Finally, data acquisition is carried out by lock-in amplifier and computer. The entire system is placed in a closed box and filled with dry air to ensure that the relative humidity of the working environment is less than 3%, and the working environment temperature is maintained at 24°C.

In conclusion, we have successfully designed and constructed a THz detection spectrometer for liquid biological samples, capable of

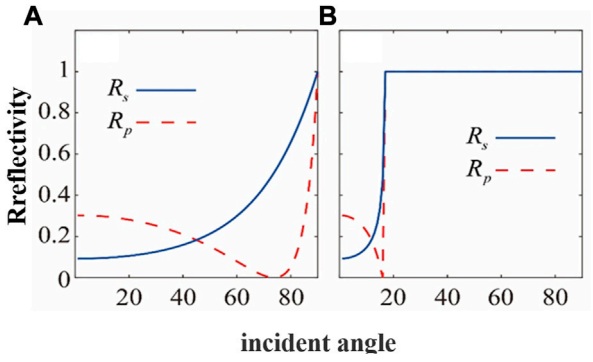

FIGURE 3
The reflectivity of S-light and P-light **(A)** incident from air to high-resistivity silicon and **(B)** incident from high-resistivity silicon to air.

achieving qualitative and quantitative detection of aqueous samples. The system's two sets of THz radiation sources and ATR setup ensure that the SNR of the signal of different concentrations is always maintained between 40–60 dB, meeting the high SNR requirements of biomedical sample detection signals. The system's construction and design, as well as its performance, have been described in detail in this paper.

3 Results and discussion

3.1 THz-ATR spectroscopy detection

In the THz band, high-resistivity silicon exhibits desirable characteristics such as a high refractive index (~3.45), small propagation loss, and minimal dispersion, making it a widely-used material in device processing for THz photonics research. The reflectivity of S and P light when air is incident on high-resistivity silicon and *vice versa* are shown in Figures 3A, B, respectively. This indicates that only the S-light incident on ATR prism can achieve total reflection of THz light and generate the evanescent wave necessary for sample detection. Furthermore, an incidence angle of 45° for S-light ensures minimal loss of high-resistance silicon to THz waves, as well as minimal outgoing sample THz signal loss. Additionally, the total internal reflection angle of 56.8° ensures almost all focused incident light will produce total reflection.

Taking these factors into account, experiments have shown that the complete time-domain spectrum of THz-ATR can be detected regardless of whether an LT-GaAs PCA or high-energy LiNbO3 radiation source is used, as shown in Figures 4A, B. Notably, the ordinates of both figures have the same magnification for detection amplitude. As the ATR prism has a path delay of 12 mm, the abscissa of the ATR signal is moved forward for ease of comparison. Comparing Figures 4A, B, it can be observed that the peak-to-peak THz signal of high-energy systems and ATR prisms is 17.42 times and 41.5 times higher than that of low-energy radiation THz, respectively. Furthermore, the effective utilization rate of the THz-ATR signal of the high-energy LiNbO3 source is about 80%, which is much higher than the effective utilization rate of the PCA source of 30%.

Two factors contribute to the utilization difference: 1) for LiNbO3 crystals characterized by low-frequency and high-power, the low-frequency signal concentrated in the range of 0.1-1 THz is very strong, and a small amount of low-frequency signal loss will not cause an insufficient SNR due to the reflection of the ATR prism; 2) for LT-GaAs PCA with low-power and wide-spectrum radiation characteristics, in the range of 0.1-3 THz, strong low-frequency signals and weak high-frequency signals are present. The ATR reflection loss will cause the loss of some high-frequency signals, resulting in decreased SNR. However, due to the different requirements of THz radiation power and spectrum for test samples, the choice of detection method should be made according to the specific advantages of each.

3.2 Detection of different concentrations of α-lactose solution using traditional THz-ATR spectroscopy

Traditional THz-ATR systems have shown potential for quantitative detection of high concentrations of α-lactose

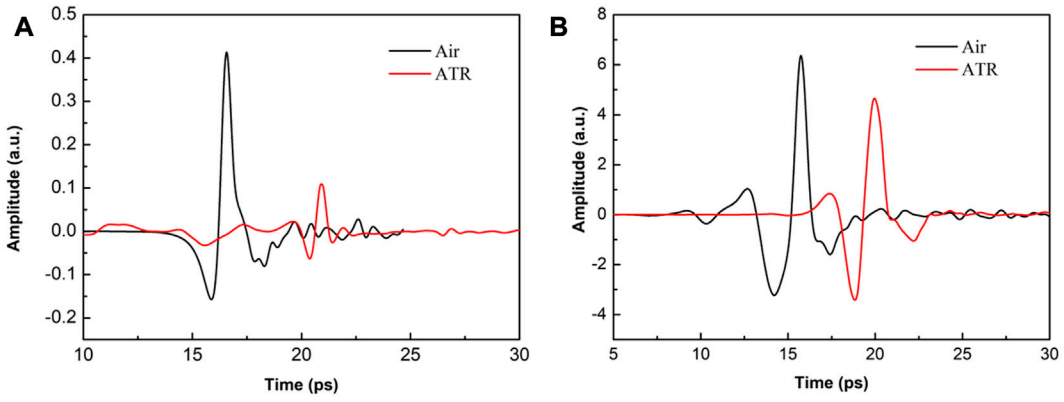

FIGURE 4
THz time-domain spectral comparison diagram of system and no-load ATR prime, when the radiation source is **(A)** LT- GaAs PCA and **(B)** high-energy LiNbO3, respectively.

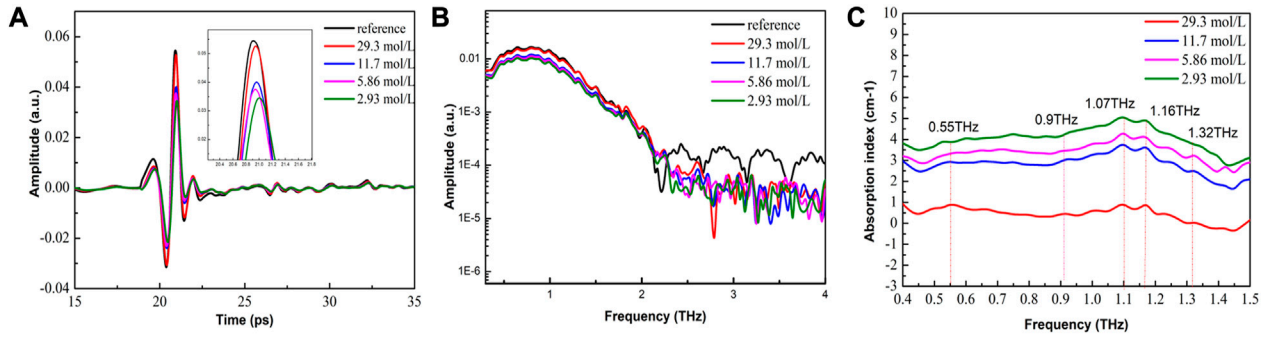

FIGURE 5
THz-ATR spectroscopy of reference (no-load ATR sample cell) and α-lactose solution with different concentrations. **(A)** Time-domain spectra (see enlarged image for details); **(B)** The corresponding frequency-domain spectra; and **(C)** Characteristic absorption spectra.

samples. However, these systems cannot distinguish between different types of α-lactose molecules due to the low SNR. In this study, we investigated the effect of water content on the THz spectra of α-lactose solutions using THz-ATR spectroscopy.

As shown in Figure 5A, the THz signal of α-lactose samples exhibits a clear time delay effect compared to the reference signal of the no-load ATR sample cell. This effect is caused by the refraction of THz waves through the sample, and becomes more pronounced as the water content in the sample increases. Moreover, as the water content increases, the signal amplitude of the sample decreases correspondingly. The frequency-domain spectra of Figure 5B show that the signal amplitude of the sample also decreases significantly in the range of 0.1-2 THz with increasing water content. By combining these observations with the characteristic absorption spectra of Figure 5C, we can distinguish between different concentrations of α-lactose solutions, but cannot distinguish the absorption peak of α-lactose.

We attribute this phenomenon to three factors. Firstly, the penetration depth of the evanescent wave incident into the sample is only tens of microns, which results in ATR spectra that provide only micron-level spectral information. Secondly, the amplitude of the sample absorption peak is determined by the superposition effect of the sample molecules absorbing THz waves, which can result in the spectral fingerprinting features of THz being weakly masked by noise due to the shallow THz penetration depth. Thirdly, ATR prisms are not specific for sample signal enhancement, which can result in the water signal being enhanced and the α-lactose sample signal being masked with a low SNR.

Notably, the strong absorption of water is extremely sensitive in the detection spectrum, which enables quantitative detection of high concentrations of α-lactose solutions based on different absorption baselines of water content. Overall, our results highlight the potential of THz-ATR spectroscopy for studying the effects of water content on the THz spectra of α-lactose solutions.

3.3 Detection of different concentrations of α-lactose solution using high-power THz-ATR spectroscopy

The detection of low-concentration aqueous biological samples is a significant challenge due to the strong absorption of water, which masks the absorption peak of the sample, making it difficult to identify and quantify the sample. However, the use of high-intensity THz radiation power has been shown to improve the SNR of the reflected signal of aqueous samples, resulting in improved detection accuracy. Furthermore, THz waves generate evanescent waves at the ATR-Sample interface, which extend into and interact with the sample, achieving highly sensitive detection of micro samples. THz-ATR spectroscopy shows higher sensitivity than ordinary THz spectroscopy, making it ideal for detecting low-concentration aqueous samples.

In this study, high-power THz-ATR time-domain spectra were obtained for α-lactose samples with different concentrations, with the minimum concentration reaching 0.292 mol/L. From Figures 6A,B, it can be found that the decrease in concentration resulted in a delay effect and amplitude reduction of the sample signal, indicating that the detection spectrum carried sample information. The SNR of the sample signal was maintained at 40 dB–60 dB for different concentrations, providing the possibility for the qualitative and quantitative detection of low-concentration aqueous samples. The frequency-domain spectra were smooth, with minimal noise impact on the sample signal. This is because the power of the THz wave passing through the sample is relatively high, and ATR enhances the sample signal, greatly improving the sensitivity of sample detection. A significant drop point was observed in the spectra of the reference and samples at the frequency position of 0.55 THz, while only the sample spectra had a particularly small drop point at 0.53 THz.

The characteristic absorption spectra of α-lactose aqueous solution were analyzed, enabling the identification and quantitative detection of the solution with a minimum concentration of 0.292 mol/L, which is presented in Figure 6C. A normal absorption peak was observed at 0.53 THz, while a concave peak was observed at 0.55 THz, with the concave peak decreasing with the decrease in concentration. The absorption baseline of the entire absorption spectra became higher overall as the concentration decreased. The peak of 0.53 THz was identified as the absorption peak of α-lactose molecules, while the peak at 0.55 THz may have

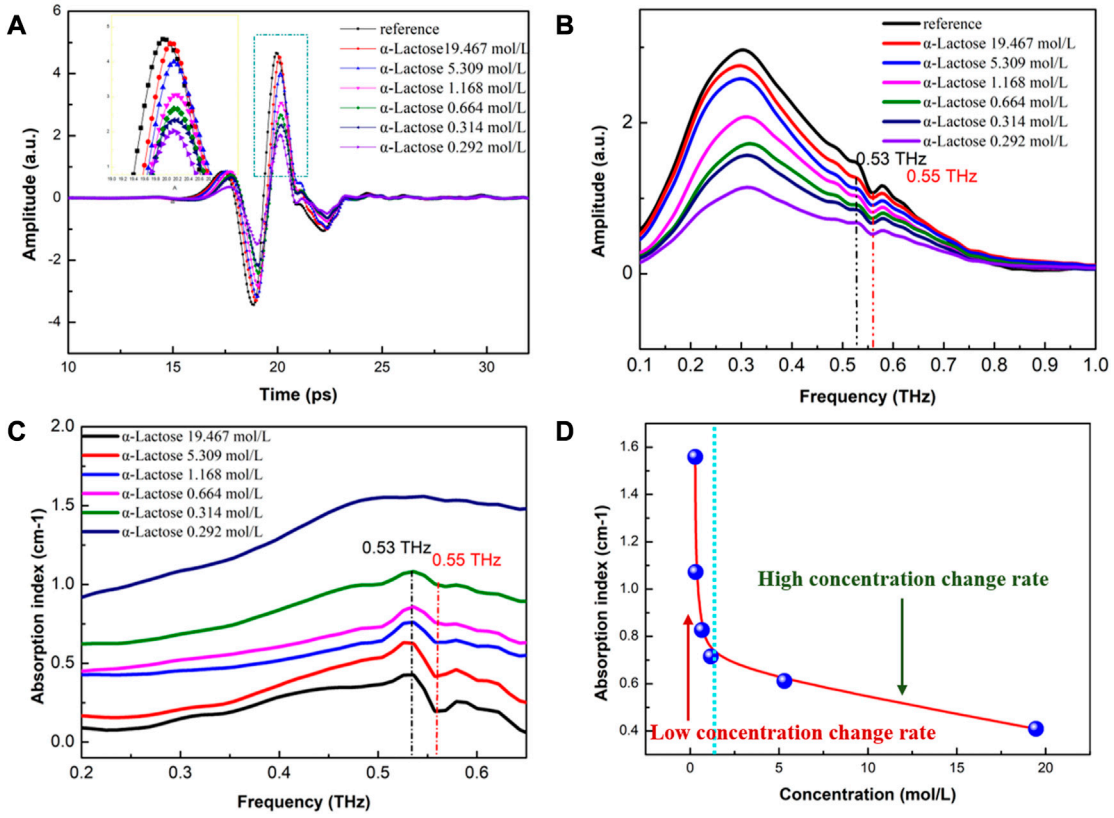

FIGURE 6
High-power THz-ATR spectra of α-lactose samples with different concentrations **(A)** Time-domain spectra (see enlarged image for details); **(B)** The corresponding frequency-domain spectra; and **(C)** Characteristic absorption spectra; and **(D)** The change rate of absorption peak position with different concentrations of α-lactose solution.

been caused by water vapor. However, the test environment was dry air with humidity lower than 3%, and previous high-power THz detections based on the sample cell had no interference of water vapor (Wang et al., 2023). Therefore, it is speculated that the observed phenomenon was caused by the enhancement effect of ATR on the sample signal, and ATR is more sensitive than the sample cell. As shown in Figure 6D, the change rate of the absorption peak position with different concentrations of α-lactose solution was analyzed, revealing a linear inverse relationship between the absorption peak position and the decrease in sample concentration at high concentrations. However, at low concentrations, the absorption peak position showed a non-linear inverse relationship with the decrease in sample concentration. The rate of change in the absorption peak position varied greatly between high and low concentration samples, possibly due to the increasing contribution of water to the absorption rate and the gradual weakening of the contribution of samples.

In conclusion, the use of high-power THz-ATR spectroscopy can improve the detection sensitivity and SNR of aqueous samples, making it an ideal tool for the qualitative and quantitative detection of low-concentration aqueous samples. The observed characteristics in the spectra provide insights into the molecular interactions of aqueous biological samples, facilitating further studies in the field of biomedical research.

4 Conclusion

In this paper, we present the design and construction of a set of THz-ATR spectrometers for highly sensitive detection of liquid biological samples. The system is capable of switching between two types of THz radiation sources, namely, traditional LT-GaAs PCA and high-energy LiNbO3, to meet the detection requirements of different samples. Our experimental results demonstrate that traditional THz-ATR spectroscopy can be employed for the quantitative detection of high concentrations of α-lactose samples, while high-power THz-ATR spectroscopy is effective for the qualitative identification and quantitative detection of α-lactose aqueous solutions with a minimum concentration of 0.292 mol/L.

Moreover, we observe that the absorption peak position changes linearly with the decrease of sample concentration at high concentrations; at low concentrations, the absorption peak position showed a non-linear inverse relationship with the decrease in sample concentration. Furthermore, the change rate of absorption peak position varies significantly between high and low concentration samples. Through the use of high-power THz-ATR technology, we have achieved qualitative identification and quantitative detection of low-concentration α-lactose solutions, which provides a novel approach for THz spectroscopic detection of biomedical samples. In the future, it is anticipated that the qualitative and quantitative identification of low-power and broad-spectrum THz-ATR can be accomplished through effective data denoising technology. Overall, our work contributes to the

advancement of THz-ATR spectroscopy and its potential applications in the field of biomedical research.

Data availability statement

The raw data supporting the conclusions of this article will be made available by the authors, without undue reservation.

Author contributions

All authors listed have made a substantial, direct, and intellectual contribution to the work and approved it for publication.

Funding

This work was supported by the National Key Research and Development Program of China (Grant No. 2017YFA0701005), and the National Natural Science Foundation of China (Grant No. 51807161, 62075179).

Acknowledgments

The authors thank Prof. Han Jiaguang and Dr. Xu Quan for their contributions to the design and production of ATR.

Conflict of interest

The authors declare that the research was conducted in the absence of any commercial or financial relationships that could be construed as a potential conflict of interest.

Publisher's note

References

Alfihed, S., Holzman, J. F., and Foulds, I. G. (2020). Developments in the integration and application of terahertz spectroscopy with microfluidics. *Biosens. Bioelectron.* 165, 112393. doi:10.1016/j.bios.2020.112393

Cui, G., Peng, W., Liu, Y., and Chang, C. (2019). "A denoising algorithm for terahertz time domain spectrum based on lifting wavelet transform," in *Second symposium on novel technology of X-ray imaging* (Hefei, China: SPIE), 11068, 254–258.

Hou, L., Shi, W., Dong, C., Yang, L., Wang, Y., Wang, H., et al. (2021). Probing trace α-lactose from aqueous solutions by terahertz time-domain spectroscopy. *Spectrochimi. Acta A* 246, 119044. doi:10.1016/j.saa.2020.119044

Liao, G., Li, Y., Liu, H., Scott, G. G., Neely, D., Zhang, Y., et al. (2019). "Multimillijoule coherent terahertz bursts from picosecond laser-irradiated metal foils," in Proceedings of the National Academy of Sciences 116 (10), 3994–3999. doi:10.1073/pnas.1815256116

Liao, Y., Zhang, M., Tang, M., Chen, L., Li, X., Liu, Z., et al. (2022). Label-free study on the effect of a bioactive constituent on glioma cells *in vitro* using terahertz ATR spectroscopy. *Biomed. Opt. Express* 13 (4), 2380–2392. doi:10.1364/BOE.452952

Liu, G. Z., Chang, C., Qiao, Z., Wu, K., Zhu, Z., Cui, G., et al. (2019). Myelin sheath as a dielectric waveguide for signal propagation in the mid-infrared to terahertz spectral range. *Adv. Funct. Mater.* 29, 1807862. doi:10.1002/adfm.201807862

Moriguchi, Y., Tokizane, Y., Takida, Y., Nawata, K., Eno, T., Nagano, S., et al. (2018). High-average and high-peak output-power terahertz-wave generation by optical parametric down-conversion in MgO: LiNbO3. *Appl. Phys. Lett.* 113 (12), 121103. doi:10.1063/1.5046126

Naftaly, M. (2012). Metrology issues and solutions in THz time-domain spectroscopy: Noise, errors, calibration. *IEEE Sensors J.* 13 (1), 8–17. doi:10.1109/JSEN.2012.2208624

Peng, Y., Shi, C., Wu, X., Zhu, Y., and Zhuang, S. (2020). Terahertz imaging and spectroscopy in cancer diagnostics: A technical review. *BME Front.* 2020. doi:10.34133/2020/2547609

Peng, Y., Shi, C., Xu, M., Kou, T., Wu, X., Song, B., et al. (2018). Qualitative and quantitative identification of components in mixture by terahertz spectroscopy. *IEEE Trans. Terahertz Sci. Technol.* 8 (6), 696–701. doi:10.1109/TTHZ.2018.2867816

Peng, Y., Shi, C., Zhu, Y., Gu, M., and Zhuang, S. (2020). Terahertz spectroscopy in biomedical field: A review on signal-to-noise ratio improvement. *PhotoniX* 1, 12–18. doi:10.1186/s43074-020-00011-z

Qiao, X., Zhang, X., Ren, J., Zhang, D., Cao, G., and Li, L. (2017). Mean estimation empirical mode decomposition method for terahertz time-domain spectroscopy de-noising. *Appl. Opt.* 56 (25), 7138–7145. doi:10.1364/AO.56.007138

Shi, W., Wang, Y., Hou, L., Ma, C., Yang, L., Dong, C., et al. (2021). Detection of living cervical cancer cells by transient terahertz spectroscopy. *J. Biophot.* 14 (1), e202000237. doi:10.1002/jbio.202000237

Takagi, S., Takahashi, S., Takeya, K., and Tripathi, S. R. (2020). Influence of delay stage positioning error on signal-to-noise ratio, dynamic range, and bandwidth of terahertz time-domain spectroscopy. *Appl. Opt.* 59 (3), 841–845. doi:10.1364/AO.378756

Torii, T., Chiba, H., Tanabe, T., and Oyama, Y. (2017). Measurements of glucose concentration in aqueous solutions using reflected THz radiation for applications to a novel sub-THz radiation non-invasive blood sugar measurement method. *Digit. health* 3, 205520761772953. doi:10.1177/2055207617729534

Wang, H., Shi, W., Hou, L., Li, C., Wang, Z., Yang, L., et al. (2023). Quantitative analysis of aqueous biomolecular mixtures by THz spectroscopy based on high-power LiNbO3 radiation source. *Spectrochimica Acta Part A Mol. Biomol. Spectrosc.* 287, 122075. doi:10.1016/j.saa.2022.122075

Wang, L., Wu, X., Peng, Y., Yang, Q., Chen, X., Wu, W., et al. (2020). Quantitative analysis of homocysteine in liquid by terahertz spectroscopy. *Biomed. Opt. Express* 11 (5), 2570–2577. doi:10.1364/BOE.391894

Yang, K., Li, J., de la Chapelle, M. L., Huang, G., Wang, Y., Zhang, J., et al. (2021). A terahertz metamaterial biosensor for sensitive detection of microRNAs based on gold-nanoparticles and strand displacement amplification. *Biosens. Bioelectron.* 175, 112874. doi:10.1016/j.bios.2020.112874

Yang, L., Hou, L., Dong, C., and Shi, W. (2020). Single-shot measurement of thz pulses. *Chin. Phys. B* 29 (5), 057803. doi:10.1088/1674-1056/ab821f

Yang, X., Yang, K., Luo, Y., and Fu, W. (2016). Terahertz spectroscopy for bacterial detection: Opportunities and challenges. *Appl. Microbiol. Biotechnol.* 100 (12), 5289–5299. doi:10.1007/s00253-016-7569-6

Yardimci, N. T., Cakmakyapan, S., Hemmati, S., and Jarrahi, M. (2017). "Highly efficient photoconductive terahertz generation through photon trapping," in *CLEO: Science and innovati*ons (San Jose, CA: Optica Publishing Group), SM1J-4.

Yu, W., Shi, J., Huang, G., Zhou, J., Zhan, X., Guo, Z., et al. (2022). THz-ATR spectroscopy integrated with species recognition based on multi-classifier voting for automated clinical microbial identification. *Biosensors* 12, 378. doi:10.3390/bios12060378

frontiers | Frontiers in Bioengineering and Biotechnology

TYPE Original Research
PUBLISHED 26 April 2023
DOI 10.3389/fbioe.2023.1147684

OPEN ACCESS

EDITED BY
Junhong Lü,
Chinese Academy of Sciences (CAS), China

REVIEWED BY
Ali Passian,
Oak Ridge National Laboratory (DOE), United States
Hongwei Zhao,
Chinese Academy of Sciences (CAS), China

*CORRESPONDENCE
Lu Chengbiao,
113066@xxmu.edu.cn
Li Xiaoli,
xiaoli@bnu.edu.cn
Li Yingwei,
lyw@ysu.edu.cn

RECEIVED 19 January 2023
ACCEPTED 03 April 2023
PUBLISHED 26 April 2023

CITATION
Shaoqing M, Zhiwei L, Shixiang G, Chengbiao L, Xiaoli L and Yingwei L (2023), The laws and effects of terahertz wave interactions with neurons. *Front. Bioeng. Biotechnol.* 11:1147684. doi: 10.3389/fbioe.2023.1147684

The laws and effects of terahertz wave interactions with neurons

Ma Shaoqing[1,2], Li Zhiwei[3], Gong Shixiang[1,2], Lu Chengbiao[4]*, Li Xiaoli[5]* and Li Yingwei[1,2]*

[1]School of Information Science and Engineering, Yanshan University, Qinhuangdao, China, [2]Hebei Key Laboratory of Information Transmission and Signal Processing, Qinhuangdao, China, [3]Institute of Electrical Engineering, Yanshan University, Qinhuangdao, China, [4]Henan International Key Laboratory for Noninvasive Neuromodulation, Xinxiang Medical University, Xinxiang, China, [5]State Key Laboratory of Cognitive Neuroscience and Learning, Beijing Normal University, Beijing, China

Introduction: Terahertz waves lie within the energy range of hydrogen bonding and van der Waals forces. They can couple directly with proteins to excite non-linear resonance effects in proteins, and thus affect the structure of neurons. However, it remains unclear which terahertz radiation protocols modulate the structure of neurons. Furthermore, guidelines and methods for selecting terahertz radiation parameters are lacking.

Methods: In this study, the propagation and thermal effects of 0.3–3 THz wave interactions with neurons were modelled, and the field strength and temperature variations were used as evaluation criteria. On this basis, we experimentally investigated the effects of cumulative radiation from terahertz waves on neuron structure.

Results: The results show that the frequency and power of terahertz waves are the main factors influencing field strength and temperature in neurons, and that there is a positive correlation between them. Appropriate reductions in radiation power can mitigate the rise in temperature in the neurons, and can also be used in the form of pulsed waves, limiting the duration of a single radiation to the millisecond level. Short bursts of cumulative radiation can also be used. Broadband trace terahertz (0.1–2 THz, maximum radiated power 100 μW) with short duration cumulative radiation (3 min/day, 3 days) does not cause neuronal death. This radiation protocol can also promote the growth of neuronal cytosomes and protrusions.

Discussion: This paper provides guidelines and methods for terahertz radiation parameter selection in the study of terahertz neurobiological effects. Additionally, it verifies that the short-duration cumulative radiation can modulate the structure of neurons.

KEYWORDS

terahertz waves, neurons, dynamic growth, cumulative radiation, thermal effect

Introduction

Terahertz waves are electromagnetic waves located between microwave and far infrared with a frequency range between 0.1–10 THz. Terahertz waves are in the energy range for hydrogen bonding, charge transfer reactions, and van der Waals forces, suggesting that many of the rotational, oscillatory, torsional, and other energy levels of biological macromolecules (proteins, DNA, RNA) are only in the terahertz band (Alexandrovet et al., 2009; Cherkasova et al., 2009; Wang et al., 2018; Sun et al., 2021). Thus, terahertz waves of specific frequencies and energies can be coupled directly to proteins to induce coherent excitation to produce

non-thermal effects (Bo et al., 2021; Peng and Zhou, 2021). For example, terahertz radiation interacts with hydrogen bonds in proteins (Fischer et al., 2002), causing low-frequency molecular vibrations that lead to changes in the conformation and functional characteristics of the protein (Cherkasova et al., 2009). It can also cause non-thermal structural changes in protein crystals (Lundholm et al., 2015). Some algorithms can also be used to improve the spectral quality when performing spectral analysis, such as the KLT transform as described by Zaharov et al. (2014). Through computer simulation modeling research, Alexandrov et al. (2009) found that terahertz radiation may interfere with the naturally occurring local strand separation kinetics of double-stranded DNA, thereby affecting the function of the DNA. The study points out that the main effect of terahertz radiation is that resonance affects the dynamical stability of the dsDNA system. It has also been shown that terahertz radiation can precisely control the proton transfer process in the hydrogen bonding of base pairs, and can control DNA demethylation (Cheon et al., 2019a; Cheon et al., 2019b; Wang et al., 2020). These studies suggest that terahertz waves can mediate changes in cell structure and function by exciting non-linear resonance effects in proteins and DNA. Based on this mechanism, terahertz waves of specific frequencies and energies affect the structure and function of neurons.

Currently, many scholars are beginning to focus on neurons' response to terahertz waves, but it is important to consider the safety of terahertz radiation protocols. Although terahertz waves are low in energy and do not ionize matter, this does not mean that they are safe (Yang et al., 2016; Mancini et al., 2022). Several studies have shown that terahertz waves' effects on neurons are two-fold. For example, terahertz radiation (3.68 THz, 10–20 mW/cm^2, 60 min) causes neuronal growth disorders (Olshevskaya et al., 2009). When the terahertz radiation power was further increased (2.1 THz, 30 mW/cm^2, 1 min), it resulted in a decrease in neuronal membrane potential with morphological disturbances and death after 2 h of radiation (Olshevskaya et al., 2010). When the radiation power was reduced to 3 mw/cm^2, neuron death occurred 3 h after radiation. Continuous wave terahertz radiation (0.12–0.18 THz, 3.2 mw/cm^2, 1–5 min) also leads to increased neuronal mortality (Borovkova et al., 2016). The above studies show that high power, continuous waves and prolonged radiation have many negative effects on neurons. However, several studies have shown that terahertz radiation has positive effects on the structure and function of neurons. The growth of neuronal protrusions was promoted when neurons were radiated using broadband micro-terahertz (0.05–2 THz, 50 uW/cm^2, 3 min). This promotion persisted when the power was reduced to 0.5 uW/cm^2 (Tsurkan et al., 2012). Additionally, narrowband trace terahertz (0.06 THz, 40–840 nW, 1 min) increased the neurons' firing rate (Pikov et al., 2010). It has also been noted that terahertz radiation has no significant effect on either neuronal activity or survival (Sun et al., 2021; Zhao et al., 2021). These phenomena indicate the non-linearity of terahertz neurobiological effects. The reason for these phenomena is associated with the total power radiated to the neuron by the terahertz, where the total power is related to the terahertz wave's frequency, energy and radiation time (Bo et al., 2021; Chen et al., 2022).

Terahertz radiation safety parameters should both ensure sufficient power radiation to the neuron and reduce the temperature effect on the neuron. This is a dilemma, and choosing the appropriate terahertz radiation parameters can mitigate the negative effects of terahertz waves on neurons (Hu et al., 2021). However, there is still a lack of guidelines and methods for selecting terahertz radiation parameters. Current research has identified positive effects of terahertz radiation on neuronal structure and function. For example, terahertz radiation can alter neuronal growth and development-related gene expression kinetics, and promote the growth of neuronal protrusions (Sun et al., 2021; Zhao et al., 2021). However, neuronal growth and development is a dynamic, ongoing process, and there are no studies which point to the short- and long-term effects of terahertz radiation on dynamic neuronal growth.

In this study, the propagation and thermal effects of terahertz wave interactions with neurons were modelled to analyze the main parameters affecting the field strength and temperature changes of terahertz waves in neurons. The field strength and temperature variations are used as evaluation criteria to select the appropriate terahertz radiation parameters. On this basis, we experimentally investigated the effect of cumulative radiation from Terahertz waves on neuronal structures. First, we built a broadband micro terahertz radiation system (0.1–2 THz, maximum radiation power 100 μW) and measured the absorption of terahertz waves by neuronal culture dishes and culture fluid. Secondly, we cultured SD rat primary cortical neurons *in vitro* and recorded the dynamic growth of neurons using broadband micro terahertz waves to focus radiation on cortical neurons for a short period. Finally, we analyzed the effect pattern of broadband trace terahertz radiation on neuronal cytosol and protrusion.

Materials and methods

The geometry of a neuronal electromagnetic-thermal coupled multiphysics field model

We first constructed the geometry of the neuronal electromagnetic-thermal coupled multiphysics field. The entire simulation area is a cuboid, containing terahertz sources, the perfect matching layer (PML), neurons, and cerebrospinal fluid (Figure 1A). The size of the model is shown in Table 1. Depending on the frequency range of the simulation, we use the RF module to simulate a terahertz source. The incident port of the terahertz wave is shown in the blue area in Figure 1A. Terahertz waves first enter the cerebrospinal fluid. After they have travelled a distance of approximately 10 um in the cerebrospinal fluid, they enter the neuron. Finally the terahertz waves are absorbed in their entirety by the PML layer.

Neurons are the most basic structural and functional units in neural networks. They contain the protrusions and cytosol (Ajenikoko et al., 2023). The cell body consists of the nucleus, the cell membrane and the cytoplasm, while the protrusions are divided into dendrites and axons. The morphology of a neuron affects the way it receives and transmits information, and varies according to its function (Ma et al., 2023). Common neuronal cytosol morphologies include star-shaped, conical, ellipsoidal and round, and the number of protrusions on the cytosol varies (Yu et al., 2023). This is due to the wide variety of neurons and the difficulty of measuring the dielectric constants of individual neurons. Therefore, for this paper, we have simplified the structure of the neurons, and established a circular neuron model with a three-layer

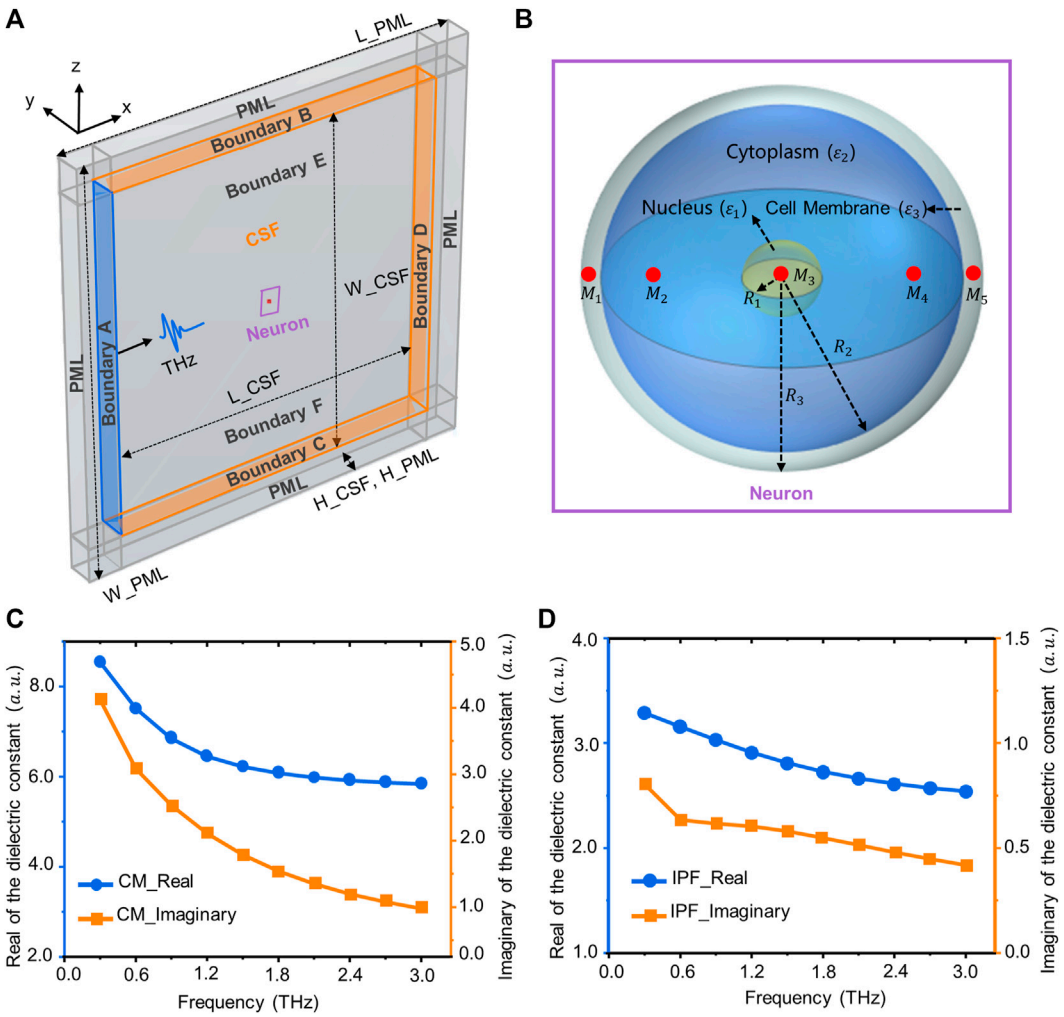

FIGURE 1
Simulation model and dielectric constant of biological tissue. **(A)** Terahertz wave transport and thermal effect model in the neuron, including neurons, terahertz sources, cerebrospinal fluid, and PML layers. **(B)** A three-dimensional neuronal model consisting of a nucleus, cell membrane (CM) and cytoplasm. The red area is the location of the sampling point (M_1–M_4). **(C)** The real and imaginary parts of the relative permittivity of the CM (3–3 THz). **(D)** The real and imaginary parts of the relative permittivity of the intracellular physiological fluid (IPF).

structure containing the cell membrane, cytoplasm and nucleus (Figure 1B). The red areas in the figure are the locations of sampling points, which are used to analyze the distribution of terahertz waves in different regions of neurons. The dimensions of the neuron geometry are shown in Table 1.

Neurons' relative dielectric constants

The neuronal membrane consists of a phospholipid bilayer that forms the basic cytoskeleton, with a variety of receptors and ion channels capable of receiving and transmitting excitation (Di Cristo and Chattopadhyaya, 2020). Due to the complexity of the membranes and the difficulty of ensuring their intact structure during extraction, the relative permittivity of phospholipids was used to characterize the relative permittivity of neuronal membranes. The relative permittivity of phospholipids in the terahertz band can be obtained from the literature (Paparo et al., 2009). After fitting through the second order Debye model, the Debye parameters are shown in Table 2. The fitted parameters were brought into Eq. 1 (Guo et al., 2021) to obtain the relationship between the relative permittivity of the neuronal membrane and frequency (Figure 1C).

$$\hat{\varepsilon}(\omega) = \varepsilon_{\infty} + \frac{\varepsilon_s - \varepsilon_2}{1 + i\omega\tau_1} + \frac{\varepsilon_2 - \varepsilon_{\infty}}{1 + i\omega\tau_2} \tag{1}$$

where ω is angular frequency; ε_{∞} is high frequency limit relative dielectric constant; ε_s is static relative dielectric constant; ε_2 is the median value; τ_1 and τ_2 are relaxation times. The slow relaxation time τ_1 is related primarily to hydrogen bonding, which reflects the change from ε_s to ε_2. The fast relaxation time τ_2 is related to the reorientation of individual molecules, which reflects the change from ε_2 to ε_{∞}.

The solvent molecules in the nucleus are the same as those in the cytoplasm. Therefore, the intracellular physiological fluid's relative permittivity is used to represent the nucleus' relative permittivity. In addition, the radius of the organelles such as mitochondria is about

TABLE 1 Dimensions of the simulation domain geometry.

Region	Description	Parameter	Value
CSF	The length of the CSF domain	L_CSF	2.5 mm
	The width of the CSF domain	W_CSF	2.5 mm
	The height of the CSF domain	H_CSF	0.15 mm
Neuron	The nuclear radius of the neuron	R_1	1.0 um
	The thickness of neuron's cytoplasm	R_2–R_1	8.0 um
	The thickness of neuron's cell membrane	R_3–R_2	1.0 um
PML	The length of the PML domain	L_PML	3.0 mm
	The width of the PML domain	W_PML	3.0 mm
	The height of the PML domain	H_PML	0.15 mm

TABLE 2 Results of fitting the parameters of the second-order Debye model for cell membrane and intracellular physiological fluid.

Type	ε_∞	ε_S	ε_2	τ_1/ps	τ_2/ps
Cell membrane	2.37	11.77	3.28	7.19	0.11
Intracellular physiological fluid	5.69	77.34	8.99	12.60	0.24

1 um, much smaller than the terahertz wavelengths examined for this paper (100–1 mm). Thus, tiny organelles exhibit only diffraction and bypassing behavior, and therefore their effects are also neglected in the calculations. The relative permittivity of the physiological fluids within neurons can be obtained from the literature (Guo et al., 2021). After fitting through the second-order Debye model, the Debye parameters are shown in Table 2. The relationship between the relative dielectric constants of physiological fluids and frequency are shown in Figure 1D.

Calculation method for the transmission characteristics for terahertz waves in neurons

In the simulation, we use the finite element method to solve the system of Maxwell's equations in full wave form, where the partial differential form of Maxwell's equations is:

$$\begin{cases} \nabla \cdot \mathrm{D} = \rho \\ \nabla \times \mathrm{E} = -\dfrac{\partial B}{\partial t} \\ \nabla \cdot \mathrm{B} = 0 \\ \nabla \times \mathrm{H} = \mathrm{J} + \dfrac{\partial D}{\partial t} \end{cases} \tag{2}$$

In the formula, E is the strength of the electric field (V/m); H is the magnetic field strength (A/m); D is the electric flux density (C/m^2); B is the magnetic flux density (Wb/m^2); J is the current density (A/m^2).

In each isotropic medium, the intrinsic relations of the electromagnetic field are:

$$\begin{cases} D = \varepsilon E \\ B = \mu H \\ J = \sigma E \end{cases} \tag{3}$$

where ε is the dielectric constant (F/m); μ is the magnetic permeability (H/m); σ is the electrical conductivity (S/m). In the solution process, it is assumed that the angular frequency is known: $\omega = 2\pi f$. The speed of light in a vacuum is c_0. The electromagnetic field varies sinusoidally with time, and all properties of the materials are linear with respect to the field strength. Then the steady-state form of the three-dimensional Maxwell control equations can be simplified as:

$$\nabla \times \left(\mu_r^{-1} \nabla \times E\right) - k_0^2 \left(\varepsilon_r - \frac{j\sigma}{\omega \varepsilon_0}\right) E = 0 \tag{4}$$

$$k_0 = \frac{\omega}{c_0} \tag{5}$$

where μ_r is the relative magnetic permeability; ε_r is the relative dielectric constant; σ is the electrical conductivity. For steady state analysis, we solved the above equations for the electric field $E = E(x, y, z)$ over the entire simulation area, where E is a vector and its weight is $E = E(E_x, E_y, E_z)$. All other physical quantities, including the magnetic field, current and power, can be deduced from the electric field.

In solving Maxwell's steady state equations along three dimensions, the boundary B-F is set to a scattering boundary condition (Figure 1A). In addition, we add PML layers to the outermost layer of the simulation domain to absorb electromagnetic waves (Figure 1A). Setting the boundary A as a terahertz source produces a terahertz wave in sinusoidal form which propagates along the x-axis (Figure 1A). The output parameters of the terahertz source, the initial conditions for solving the equations, and the properties of the materials are shown in Table 3.

Calculation method for the thermal effects of terahertz wave interactions with neurons

When terahertz waves radiate a neuron, the neuron absorbs a certain amount of terahertz wave energy and converts it into joule heat,

TABLE 3 The initial conditions for solving the equations and the properties of the materials.

Type	Description	Value	References
Terahertz source	Frequency	$f = 0.3THz$	
	Power	$P = 1mW$	
Initial temperature	Temperature	$T_0 = 298.15\,K$	
Neuron membrane	Relative dielectric constant	3.28 + 0.801i *a.u.*	Paparo et al. (2009)
	Relative permeability	1 *a.u.*	
	Specific conductance	0 S/m	
Neuron Intracellular physiological fluid	Relative dielectric constant	8.53 + 4.12i *a.u.*	Guo et al. (2021)
	Relative permeability	1 *a.u.*	
	Specific conductance	0 S/m	
Neuronal thermal parameter	Thermal conductivity	$k = 0.49\,W/(m \cdot K)$	ITIS (2023)
	Density	$\rho = 1075\,kg/m^3$	
	Constant pressure specific heat capacity	$C_p = 3613\,J/(kg \cdot K)$	
cerebrospinal fluid (CSF)	Relative dielectric constant	5.34 *a.u.*	ITIS (2023)
	Relative permeability	1 *a.u.*	
	Specific conductance	92.7 S/m	
	Thermal conductivity	$k = 0.57\,W/(m \cdot K)$	ITIS (2023)
	Density	$\rho = 1007\,kg/m^3$	
	Constant pressure specific heat capacity	$C_p = 4096\,J/(kg \cdot K)$	

which in turn exerts an effect on the structure and function of the neuron. Wilmink et al. (2011) investigated the thermal response of human skin dermal fibroblasts under terahertz irradiation and showed that the thermal effects of terahertz can be predicted by conventional bio-thermal methods. This provides a basis for modelling the thermal effects in neurons. Pennes (1948) built on this by considering the parameters of blood perfusion rate and metabolically-generated heat in biological tissues, and proposed the bio-thermal transfer equation:

$$\rho C_p \frac{\partial T}{\partial t} + \nabla \cdot (-k\nabla T) = \rho_b C_b w_b (T_b - T) + Q_{met} + Q_{ext} \tag{6}$$

where ρ is the biological tissue density, C_p is the thermal capacity of the biological tissue, T is the temperature distribution function, and k is the thermal conductivity of the biological tissue. The transfer term $Q_{pref} = \rho_b C_b w_b (T_b - T)$ represents convective cooling of the blood perfusion; ρ_b is the blood density; C_b is the specific heat capacity of the blood; w_b is the blood perfusion rate; and T_b is the temperature of the arterial blood. Q_{met} is the power density generated by metabolism, which can be neglected in the calculation considering its small quantity in the neuron. Q_{ext} is an external heat source. In the case of electromagnetic-thermal coupling, the heat generated by the electromagnetic wave in the neuron is Q_{ext}. Q_{ext} is transferred to the bio-thermal model during the simulation. In addition, little blood flows through the neurons, and the heat generated by metabolism is much less than that generated by electromagnetic waves. Thus, over the course of the calculation, the blood perfusion rate is neglected, and heat sources due to metabolism are ignored. The biological heat transfer equation can be simplified as:

$$\rho C_p \frac{\partial T}{\partial t} + \nabla \cdot (-k\nabla T) = Q_{ext} \tag{7}$$

$$Q_{ext} = Q_{rh} + Q_{ml} \tag{8}$$

$$Q_{rh} = \frac{1}{2} Re(J \cdot E) \tag{9}$$

$$Q_{ml} = \frac{1}{2} Re(i\omega B \cdot H) \tag{10}$$

In solving the bioheat equation, the boundaries E and F are set to be thermally insulated, and the effect of heat dissipation from the cerebrospinal fluid is ignored. Considering that boundaries B, C, and D are distant from the light source region, we assume that the initial temperature is constant at the boundaries. The output parameters of the terahertz source, the initial conditions for solving the equations and the properties of the materials, are shown in Table 3.

Fiber-coupled terahertz radiation platform and experimental protocol

The fiber-coupled terahertz radiation system used in the experiments was the TERA K15 from Menlo Systems, Germany, based on which the transmission optical path for terahertz has been improved. The effective frequency range of the terahertz system output is 0.1–2 THz, and the maximum output power is 100 μW. The system is transmitted through a fiber-optic connector to a fiber-coupled terahertz transmitter (TERA 15-TX-FC Fe: InGaAs) which generates terahertz waves under a bias voltage. The transmitter generates terahertz waves

and can then focus the terahertz beam into a narrow space through four lenses (L1, L2, L3, L4). Since the terahertz waves generated by the transmitter diverges, the terahertz beam is first collimated by a plano-convex lens (L1); the longer the focal length of L1, the wider the beam's diameter. The terahertz wave is then focused using a convex flat lens (L2) while placing the sample at its focal point. The plano-convex lens (L3) is used to collect any terahertz waves passing through the sample and collimate the terahertz beam, and the convex plane lens (L4) focuses the terahertz waves onto the detector to detect any terahertz waves passing through the sample.

To further investigate the pattern of terahertz wave interactions with neurons, we cultured neurons *in vitro*. Fetal mouse cortical neurons were first extracted and cultured for 2 days to allow cortical neurons to adapt to their environment and grow against the wall. To mitigate the absorption of terahertz waves by the culture medium, cortical neurons were radiated from the bottom of the Petri dish. Neurons cultured *in vitro* can be divided into 5 stages, with each stage measured in days. Therefore, the neurons were radiated using terahertz cumulative radiation, and to mitigate the thermal effect of terahertz radiation, the neurons were radiated for 3 min per day for 3 days.

Experimental materials

SPF SD (Specific Pathogen Free Sprague Dawley) pregnant rats, at 12–15 days of gestation, were purchased from Beijing Vital River Laboratory Animal Technology Co., Ltd. The main experimental reagents used for cortical primary neuron culture were: Dulbecco's Modified Eagle Medium (Gibco, 11965092), Neurobasal (Gibco, 21103049), B-27 (Gibco, 17504044), Fetal Bovine Serum (Gibco, 10099141C), Trypsin 0.25% (Gibco, 15050057), Penicillin-Streptomycin (Gibco, 15140163), Glutamine (Gibco, 35050061), Poly-L-lysine (Sigma, P4832), HBSS (Beynotime, C0218) and HEPES (Beynotime, ST090). After 4 h, the growing medium was replaced with a maintenance medium containing 97% Neurobasal, 2% B27% and 1% Glutamine. Two days later, the neurons were irradiated with terahertz for 3 min/day for 3 days.

Primary neuron cultures

Primary neuronal culture was based on Guo et al. (2013) method, with slight modifications using SPF SD (Specific Pathogen Free Sprague Dawley) pregnant rats, 12–15 days of gestation, and bodyweight of 300–350 g. The fetal rats' cerebral cortexes were extracted in a sterile bench, cut up, and added to Trypsin 0.25%, and then digested in an incubator for 15 min, and removed every 3 min. Slowly and gently, we blew the neuron with a flame-passivated pasteurized dropper. The cell suspension was grown in 10% fetal bovine serum diluted in 90% Dulbecco's modified eagle medium and adjusted to a concentration of 1×10^4 cells in 1 mL.

Neuron structure parameter extraction and analysis method

Firstly, we ensured that each neuron recorded had been radiated by terahertz, and that we could find the same neuron quickly and efficiently. Two marker lines were drawn on the Petri dish, and the intersection of the two lines was at the center of the Petri dish. The neuronal growth and development was photographed in the four quadrants with the center of the Petri dish as a right-angle coordinate system. Next, images with a clear background and low neuronal density (where the cell bodies and protrusions of individual neurons can be observed and are not connected to other neurons) were selected. Then, we used ImageView to open the optical microscope to take pictures, and used any connection curve in the "Measure" menu to measure the neurite protrusion length, and any polygon to measure the neurite cell area. The total neuronal protrusion length growth value and the cell body area growth value were calculated as follows:

$$\Delta Neurites_i^j = \frac{\sum_{k=1}^{n} Neurites_i^j(k) - Neurites_i^0(k)}{n} \tag{11}$$

$$\Delta Soma_i^j = \frac{\sum_{k=1}^{n} Soma_i^j(k) - Soma}{n} \tag{12}$$

where $\Delta Neurites_i^j$ denotes the average growth value of the total length of neuronal protrusions in the *i*th culture dish after the *j*th day of terahertz radiation. $Neurites_i^j(k)$ denotes the total length of the k neuronal protrusion in the *i*th petri dish after the *j*th day of terahertz radiation. $Neurites_i^0(k)$ denotes the total length of the k neuronal protrusion in the *i*th petri dish before terahertz radiation. Similarly, Soma denotes the area of the neuron's cytosol. The neuronal developmental state was recorded before terahertz radiation, and the neuronal cytosolic area and total protrusion length at this point were used as initial values. The total length of the neuronal cell area and the protrusion after 24 h of the first terahertz radiation was recorded and subtracted from the initial value as the growth of neuronal cell area and protrusion on the first day after terahertz radiation. The growth values of the neuronal cytosolic area and total protrusion length after the second and third day after terahertz radiation were calculated in the same way, respectively. Finally, the neuronal parameters measured in the same culture dish were averaged to represent the cellular condition of the entire dish, and used as a sample value.

Quantification and statistical analysis

All data are expressed as mean ± standard error of the mean (SEM), with specific cases noted separately. Firstly, the samples are tested for normality. Secondly, significance analysis of the results of the experimental and control groups was performed using an independent samples *t*-test. Statistical analysis was done by MATLAB, and results were considered significantly different when $p < 0.05$.

Results

The propagation law of terahertz waves in neurons

The neuron size and terahertz wave wavelength are both in the micrometer range and have the conditions for an interaction.

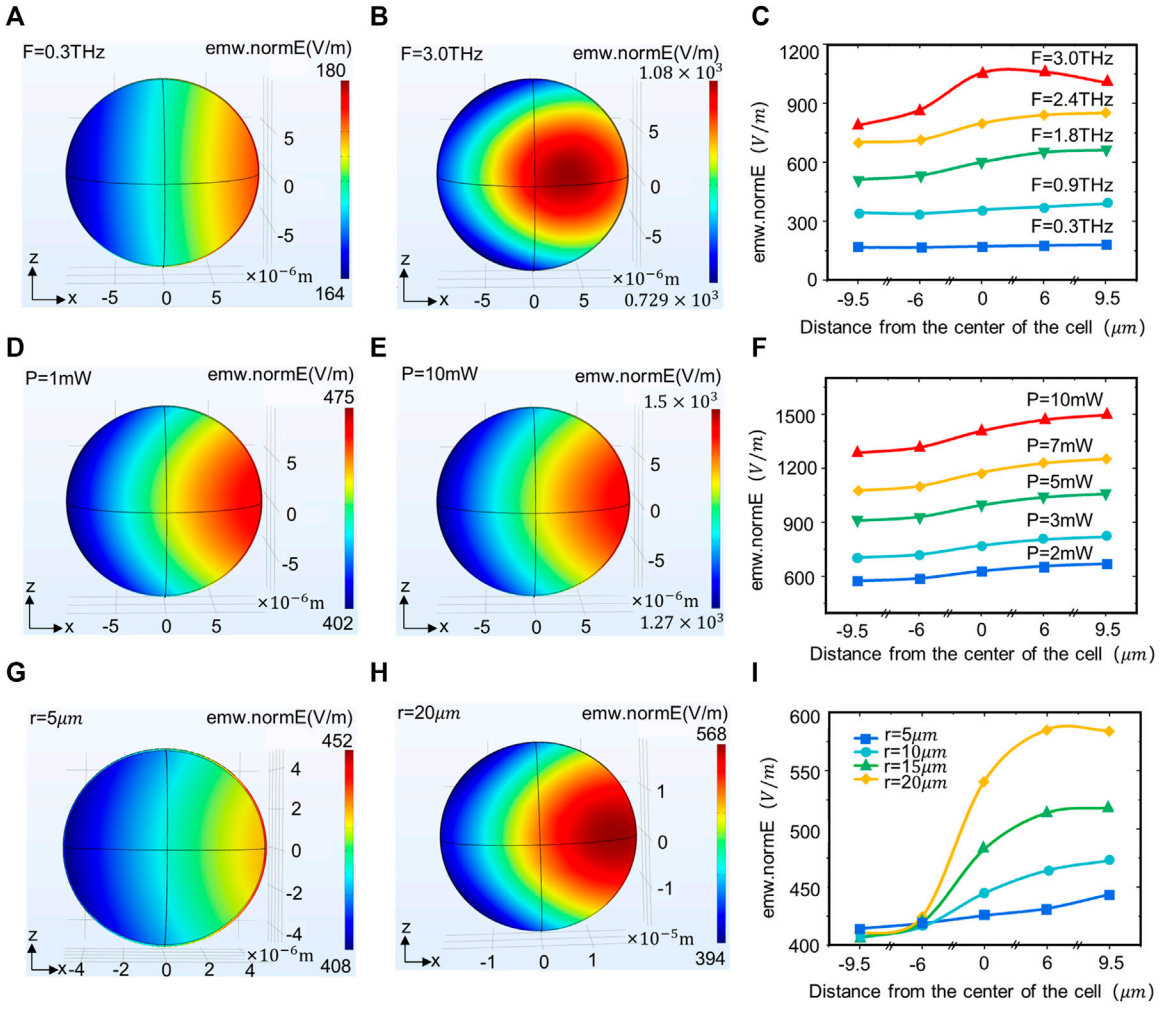

FIGURE 2
Terahertz wave propagation in neurons with different terahertz radiation parameters and neuron size. **(A, B)** Propagation law of terahertz waves with frequencies of 0.3 and 3 THz in the XZ plane of neurons. **(C)** Propagation law of terahertz waves with different powers in neurons (simulation time: steady state, initial temperature: 293.0 k, r = 10 um, F = 0.3, 0.9, 1.8, 2.4, 3.0 THz, p = 1 mW). **(D, E)** Propagation law of terahertz waves with Power of 1 and 10 mW in the XZ plane of neurons. **(F)** Propagation law of terahertz waves with different powers in neurons (simulation time: Steady state, initial temperature: 293.0 k, r = 10 um, F = 1.2 THz, p = 2, 3, 5, 7, 10 mW). **(G, H)** The propagation law of terahertz waves in different neuron sizes (radii 5 and 10 um) in the XZ plane. **(I)** Propagation law of terahertz waves in neurons of different sizes (simulation time: Steady state, initial temperature: 293.0 k, r = 5, 10, 15, 20 um, F = 1.2 THz, p = 1 mW).

Therefore, we investigated the correlation between different terahertz radiation parameters and cell size with the field strength distribution in neurons. The results show that when terahertz is radiated to the neuron, the energy is lower on the left side (the side where the terahertz enters the neuron) and gradually increases along the axis (Figures 2A, B). As the frequency of the terahertz waves increases, the energy at the same location in the neuron continues to rise. Meanwhile, the location of the energy maximum in the neuron gravitates towards the center of the neuron (Figure 2C). When the terahertz radiation power changed, the energy distribution in the neuron did not change significantly (Figures 2D, E), but the energy in the same location in the neuron kept rising (Figure 2F). There is also variation in neuron size across functions and regions of an organism, and we found that as neuron size increases, the energy in the center and to the right of the neuron continues to rise (Figures 2G–I).

Thermal effects patterns in terahertz wave interactions with neurons

The thermal effect of terahertz waves is due primarily to the absorption of terahertz waves by neurons and their conversion into thermal energy (Liu GZ. et al., 2019). The absorption properties of terahertz waves by neurons are associated primarily with water molecules and biomolecules. But high temperatures can exert some negative effects on neurons, and thus we investigated the correlation between terahertz radiation parameters and changes in neuronal temperature (Li et al., 2021). The results show that the

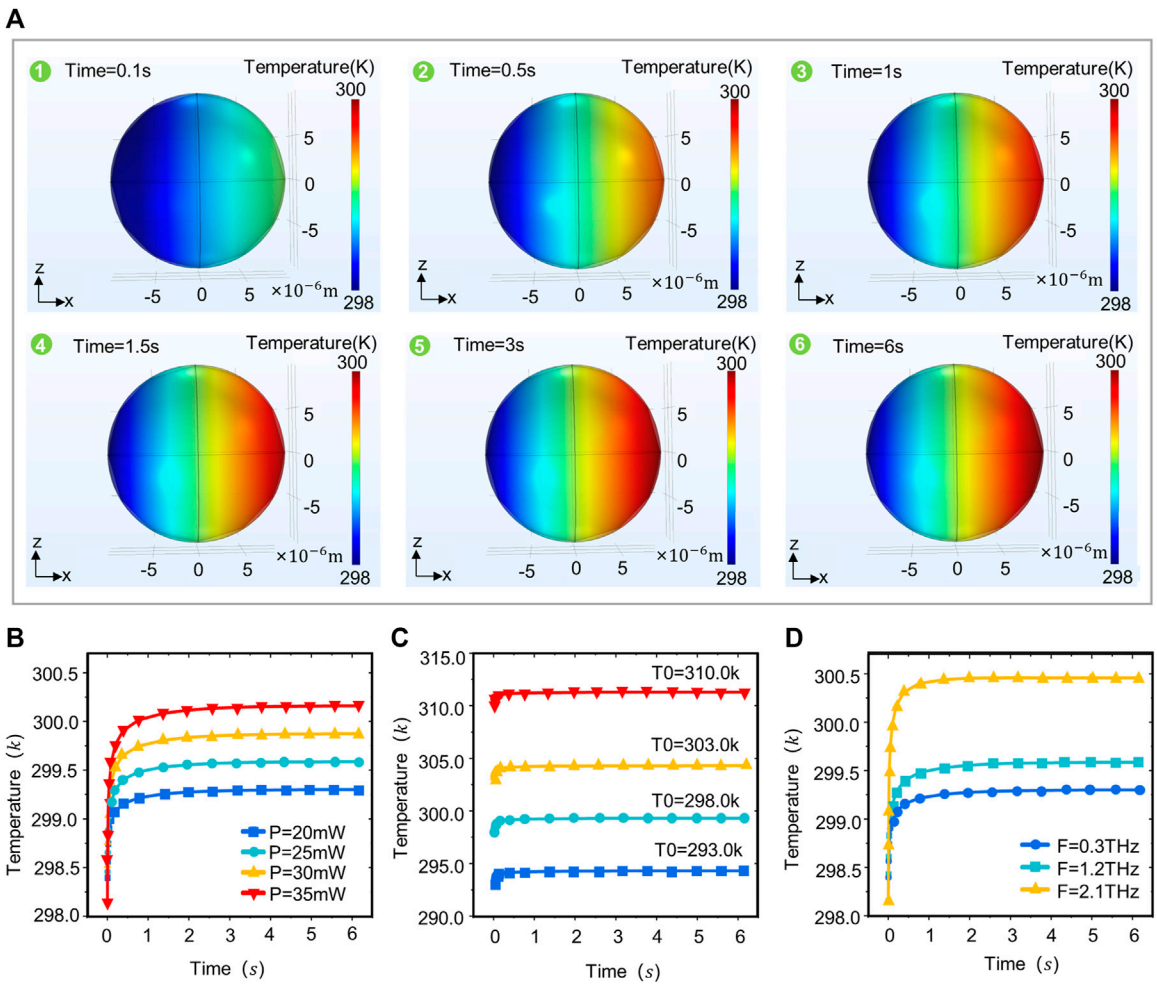

FIGURE 3
Temperature distribution patterns in neurons under different terahertz radiation parameters. **(A)** The XZ plane temperature of neurons varies with terahertz radiation time (Simulation time: 6 s, Initial temperature: 293.0 k, r = 10 um, F = 1.2 THz, *p* = 20 mW). **(B)** Variation of temperature in neurons with time at different terahertz radiation powers (simulation time: 6 s, initial temperature: 293.0 k, r = 10 um, F = 1.2 THz, *p* = 20, 25, 30, 35 mW). **(C)** Variation of temperature in neurons with time at different initial temperatures (simulation time: 6 s, initial temperature: 293.0, 298.0, 303.0, 310.0 k, r = 10 um, F = 1.2 THz, *p* = 20 mW). **(D)** Temperature variation in neurons with time at different terahertz radiation frequencies (simulation time: 6 s, initial temperature: 293.0 k, r = 10 um, F = 0.3, 1.2, 2.1 THz, *p* = 20 mW).

temperature distribution pattern in the neuron is similar to the field strength distribution pattern (Figure 3A), with lower temperatures on the left side of the neuron (the side where the terahertz wave enters the neuron). The temperature in the neuron increases continuously along the axis, peaking on the right side of the neuron (the side through which the terahertz wave passes). The temperature in the neuron rapidly stabilizes within 1 s, and spikes within 0–0.5 s. The time to reach temperature stability in the neuron is independent of the initial temperature, terahertz radiation power and frequency (Figure 3B). As the power of the terahertz radiation increases, the temperature in the neuron continues to increase (Figure 3B). The temperature in the neuron varies with the time of terahertz radiation in the same pattern for different initial temperatures (Figure 3C). The frequency of terahertz waves is also a major influence on the temperature in the neurons, which is positively correlated with the terahertz wave frequency (Figure 3D).

Terahertz radiation promotes neuronal cytosol and protrusion growth

At the beginning of the study, due to the large absorption of terahertz waves by the cell culture medium, the time and frequency domain signals of the terahertz waves after penetrating the empty culture dish and culture medium were measured in order to estimate the energy of the terahertz radiation to neurons and the frequency band range. Terahertz radiation system and radiation protocol are shown in Figures 4A, B. The results show that the terahertz waves can penetrate the culture dish and the culture fluid; the frequency range of the transmitted waves is 0.1–2 THz; and the main energy is concentrated in 0.3–1 THz (Figures 4C, D). At the same time, the absorption of terahertz by the culture fluid is large, and the energy of the transmitted wave is negatively correlated with the volume of the culture fluid.

To investigate the effect of terahertz radiation on neuronal growth and development, the neuronal cytosolic area and total

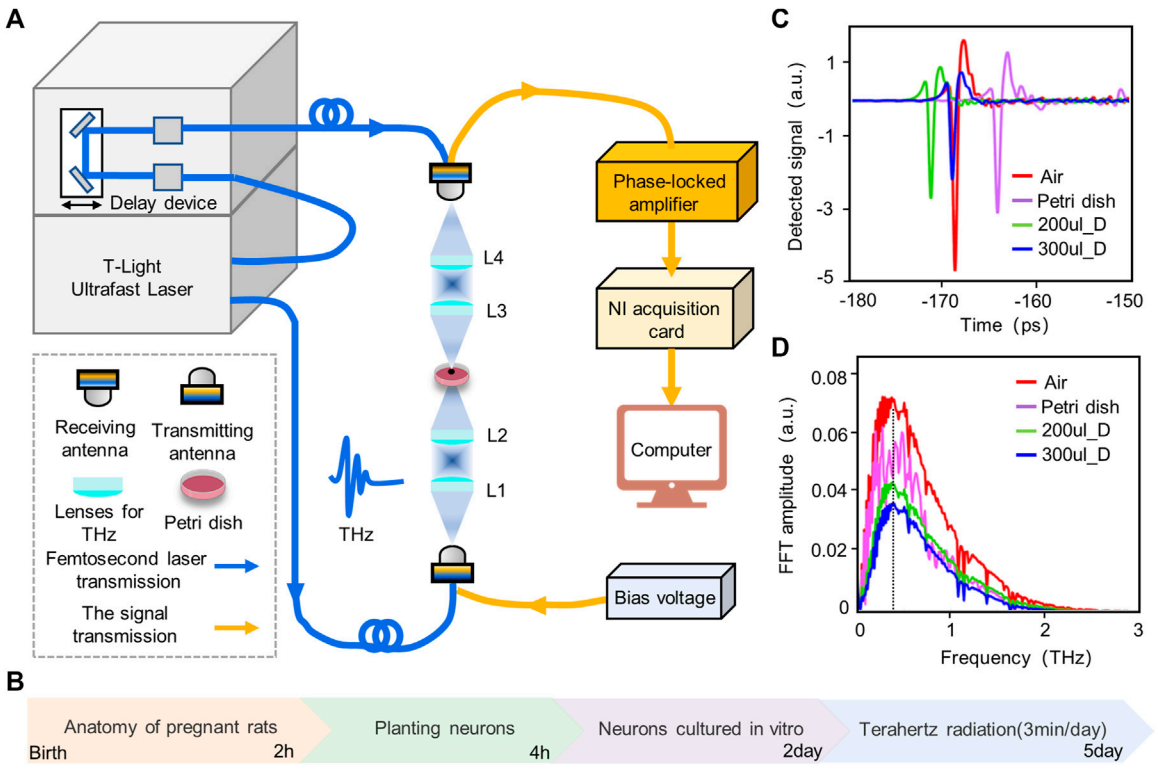

FIGURE 4
Experimental platform, protocol and terahertz wave attenuation test. **(A)** Experimental platform for wide-band terahertz radiation of cortical neurons. We radiated neurons from the bottom of a petri dish and measured the amplitude and frequency of the terahertz waves passing through the dish in real time. **(B)** Experimental protocol for terahertz radiating neurons. The experiment lasted for 5 days, with neurons being planted and cultured for the first 2 days, followed by the accumulation of radiated neurons for 3 consecutive days. **(C)** Time domain diagram of terahertz after penetrating air, petri dish, 200 ul Dulbecco's modified eagle medium (200 ul_D) and 300 ul Dulbecco's modified eagle medium (300 ul_D). **(D)** Frequency domain map of terahertz after penetrating air, petri dish, 200 ul_D and 300 ul_D.

protrusion length were used as statistical analysis quantities. Neuronal protrusions in the control and terahertz groups began to grow after 1 day of terahertz radiation, and subsequently showed neuronal properties that remained well-developed after the end of terahertz radiation (Figure 5A). The neuronal cytosol is the center of neuronal metabolism and nutrition, and is associated with neuronal survival and development (Abrahamsson et al., 2017; Yang et al., 2017). We found that the growth value of the neuronal cytosolic area in the control group increased as number of days increased, and the same phenomenon was found in the terahertz group. We further statistically analyzed the effect of terahertz radiation on neuronal cytosolic growth. The growth value of the neuronal cell area was significantly higher in the terahertz group (22.6 ± 1.6 μm^2) than in the control group (8.9 ± 1.5 μm^2) on Day 1 (Figure 5B). The terahertz group was higher than the control group on Days 2 and 3, but the statistical results were not significant (Figures 5C, D).

The protrusions of neurons are the basis for information communication between neurons, and are the key to the formation of neural networks (Moore et al., 2020). In the control group, the growth value of the total neuronal protrusion length showed a positive correlation with the number of days, and the same phenomenon was present in the terahertz group. The value of total neuronal protrusion length growth was significantly higher in the terahertz group (74.2 ± 10.0 μm) than in the control group (30.6 ± 10.9 μm) on Day 1 of terahertz radiation (Figure 5B). Additionally, the terahertz group (138.1 ± 16.0 μm, 197.8 ± 19.0 μm) was significantly higher than the control group (67.7 ± 10.1 μm, 79.5 ± 20.1 μm) on Days 2 and 3 of terahertz radiation (Figures 5C, D). In addition, we have analyzed the relationship between the radiation days in THZ_CBA (Terahertz radiation_Cell Body Area) minus CON_CBA (Control_Cell Body Area) and THZ_NP (Terahertz radiation_Neurite Protrusion) minus CON_NP (Control_Neurite Protrusion). We found that THZ_NP minus CON_NP is positively correlated with the number of days of radiation, but THZ_CBA minus CON_CBA is non-linear with the number of days of radiation (Figure 5E).

Discussion

Neuron sizes and terahertz wave wavelengths are on the order of microns and can interact with each other. Due to the disparity in relative permittivity between the cell membrane and the cytoplasm, a large amount of reflected signal is generated when terahertz waves enter the cell membrane from the cytoplasm. The reflected signals are superimposed on each other near the boundary of the two substances, resulting in a standing wave effect (Liu WQ. et al., 2019).

10.3389/fbioe.2023.1147684

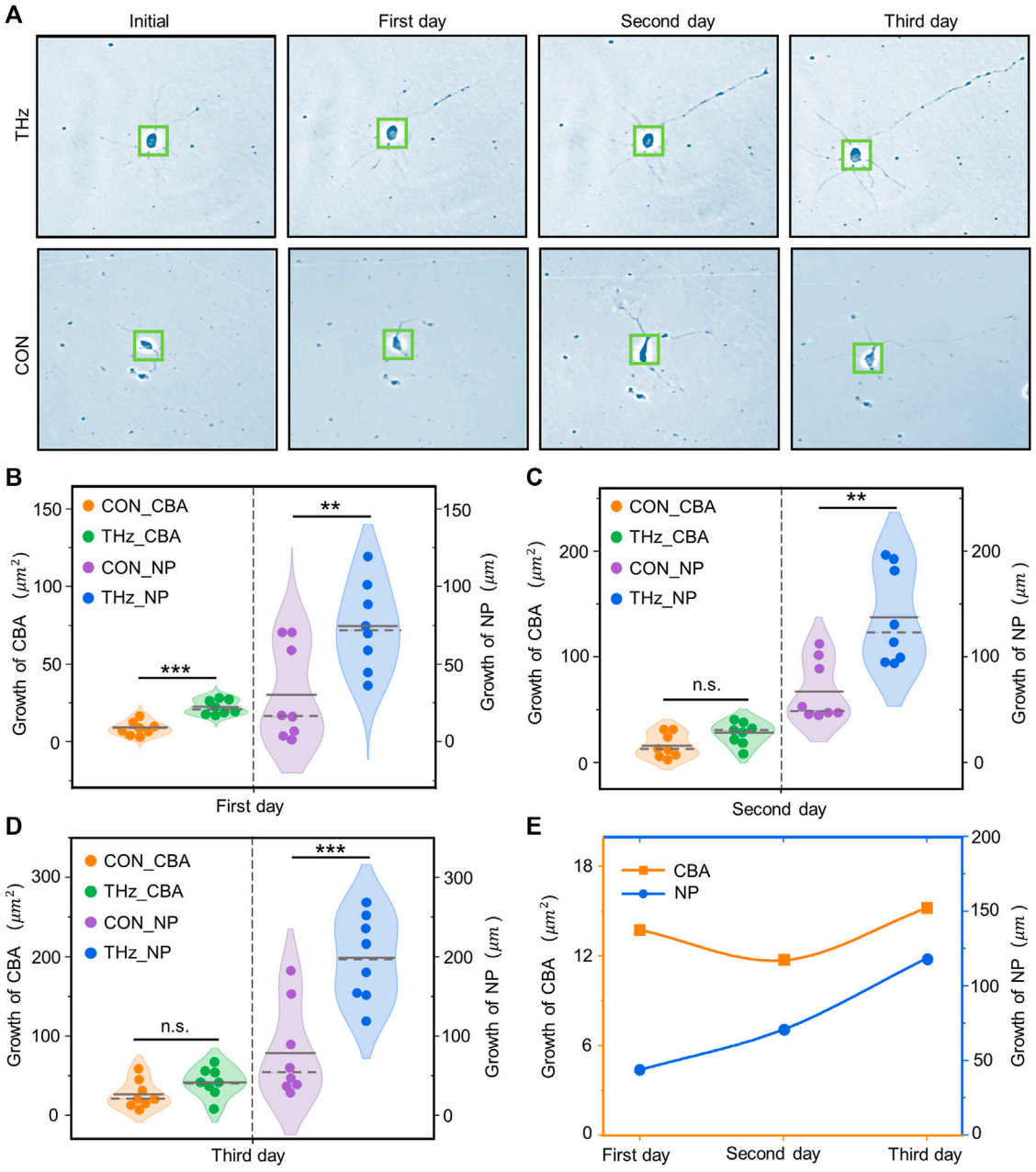

FIGURE 5
Broadband terahertz radiation promotes the dynamic growth and development of cortical neurons. **(A)** Representative performance maps of neuronal developmental status in the Terahertz (THz) and Control (CON) groups. **(B–D)** Significance analysis of the difference between THz and CON in terahertz cumulative radiation neurons for 3 days. On the first day, neurite protrusion (NP) and cell body area (CBA) were significantly higher than the CON. On the second day NP was significantly higher than the CON, but CBA showed no significant difference. On the third day, there was no significant difference between CBA and CON, but NP was significantly higher than the CON. Data are mean ± SEM (n = 8 independent experiments). **, $p < 0.01$). ***, $p < 0.001$ compared with CON, independent samples t-test. **(E)** Relationship between the radiation days in THZ_CBA minus CON_CBA and THZ_NP minus CON_NP.

Thus, the field strength and temperature in the neuron show up as low on the left side (the side where the terahertz wave enters the neuron) and high on the right side (the side where the terahertz wave transmits out of the neuron). This phenomenon is influenced by the wavelength of the terahertz wave and the size of the neuron, and does not occur when the neuron size is either much smaller or much larger than the terahertz wavelength. In addition, the field strength and temperature in the neuron are positively correlated with the frequency and power of the terahertz wave. This phenomenon is related to the relative dielectric constant of the cytoplasm. The main component of the cytoplasm is water, which can be regarded as a polar fluid, and most of its losses are polarized losses (Generalov et al., 2020). As the terahertz frequency increases, the cytoplasm's polarization loss attenuates and the neuron's internal field strength and temperature increase.

Individual terahertz photons have energies as low as meV (milli-electron volts), and do not have a direct ionizing damaging effect similar to that of x-rays (Xiang et al., 2019). However, as the terahertz beam intensity increases, terahertz waves cause a range of biological effects on neurons. The thermal effect of terahertz waves is mainly due to the absorption of terahertz waves by neurons and their conversion into thermal energy. The absorption properties of terahertz waves by neurons are associated primarily with water molecules and biomolecules. Since neurons contain much more water than biomolecules, and are the main chromophore in the terahertz band in neurons, the thermal effect produced is due primarily to water. Water has many unique properties in that its molecules can form hydrogen bonds with neighboring water molecules, creating a dynamic hydrogen bonding network (Yada et al., 2008). The intermolecular stretching and bending of vibrational modes of this network are in the terahertz band (strong resonance frequency of 1.5 THz). When a neuron is exposed to terahertz wave radiation, the vibrational modes of the hydrogen bonds in it are excited, thus triggering resonance (Duan et al., 2021). The dynamic equilibrium of the water molecular network structure is broken, resulting in strong absorption of terahertz waves by the water (Kristensen et al., 2016). The absorbed terahertz wave energy is converted into kinetic energy for the water molecules' own irregular motion, and the frequency of mutual collisions increases. This generates heat energy (Heshmat, et al., 2017; Balos et al., 2022). In the absence of photochemical processes and phase changes, this will lead directly to an increase in neuronal temperature as heat collects.

The thermal effect of terahertz radiation on neurons leads to changes in neuron structure and function (Zhang et al., 2021). This change has two primary causes: The magnitude of the neuronal temperature increase and the duration of the high temperature. When neurons are exposed to high temperatures for long periods, this can lead to disturbed neuronal growth, dehydration effects, neuronal morphological damage, neuronal stress responses, and more seriously, structural protein degeneration and neuronal death (Samsonov and Popov, 2013). Moreover, when high temperatures in neurons persist at the millisecond level, they have reversible effects on neurons (affecting intra-neuronal calcium homeostasis, inducing action potentials in neurons, and affecting neuronal synaptic transmission and neuronal firing rates) (Albert et al., 2012; Fribance, et al., 2016).

When studying terahertz neurobiological effects, it is first necessary to consider the safety of the terahertz radiation protocol. Safe terahertz radiation parameters ensure both that sufficient power is radiated to the neuron and that the temperature effect on the neuron is mitigated. Thus, field strength and temperature in neurons can characterize (to an extent) the terahertz radiation parameters' safety. From a physical point of view, the biological effects of terahertz wave radiation on neurons are derived from the thermal and non-thermal effects of terahertz waves (Peng and Zhou, 2021). Therefore, the temperature variation in neurons needs to be reduced when selecting terahertz radiation parameters to facilitate distinguishing whether the neuronal response is caused by thermal or non-thermal effects. Usually, we are looking at the non-thermal effects of terahertz waves, so the parameters are chosen by first determining the range of permissible temperature increases in the neurons. This temperature range ensures that there is no effect on the structure and function of the neurons. The non-thermal effect arises mainly from the non-linear resonance effect of biological macromolecules in neurons excited by terahertz waves (Peng and Zhou, 2021). The choice of frequency for terahertz waves is crucial because of the different resonance peaks between biological macromolecules. The terahertz wave frequency can be determined based on the modulating substance's properties. The terahertz radiation's power is then determined, and an appropriate reduction in power will mitigate the rise in temperature in the neurons. When we need to use more radiation power, we can use pulsed waves, and controlling the duration of a single round of radiation to milliseconds can also mitigate the rise in temperature in the neurons. When the temperature in the neurons cannot be mitigated by regulating the terahertz radiation protocol, the biological sample can be placed in an automatic temperature control system (Zhao et al., 2021). The effects of temperature changes on neurons can also be mitigated if the temperature control system's accuracy and adjustment time are sufficient. Alternatively, we could use short periods of cumulative radiation.

On this basis, we have investigated the effects of Terahertz wave cumulative radiation on neuronal structures. To mitigate the thermal effects of terahertz radiation on neurons, broadband trace amounts of terahertz served as the radiation source (frequency band 0.1–2 THz, maximum radiation power 100 μW), and short periods of cumulative radiation were used (3 min/day, 3 days). We found that this radiation protocol causes no significant negative effects on the neurons. Additionally, we found significantly higher neuronal cell area growth values after the first day of terahertz radiation, compared to the control group. However, there were no significant differences on either the second or the third days. We also found that the total length of the neuronal protrusions had increased by 94.6% on Day 1, 76.0% on Day 2, and 100.0% on Day 3, compared to the control group. These results were all statistically significant. The reasons for these phenomena may be related to the developmental cycle of cultured neurons *in vitro*. It has been shown that there is a "latency period" after inoculation of neurons in *in vitro* cultures, during which cells adhere to the wall and adapt to their environment, with slow cell growth. At the end of the incubation period, the cells enter a rapid growth phase in which the cytosol and protrusions grow rapidly, a phenomenon that generally occurs between Days 2 and 5 of cell inoculation. The protrusions rapidly (within 5–7 days of cell inoculation) develop into dendrites, while the axons maintain rapid growth as well (Sulatsky, et al., 2014; Cha, 2016). The first day of terahertz radiation coincided with the third day of neuronal inoculation, when the cells were in a period of rapid growth, and the neuronal cytosolic growth rate was significantly higher after terahertz radiation than in the control group. At the same time, neuronal protrusions remained in a rapid growth phase during the 3 days of terahertz radiation. Thus, the neuronal protrusions' growth rate was significantly higher after these 3 days of terahertz radiation than in the control group. These findings suggest that terahertz radiation-promoted neuronal growth only occurs during periods of intrinsic neuronal growth.

Conclusion

In this study, the propagation and thermal effects of terahertz waves' interactions with neurons were modelled to analyze the main parameters affecting the field strength and temperature variation in terahertz waves in neurons. The field strength and temperature variations are used as evaluation criteria to select the appropriate

terahertz radiation parameters. On this basis, we experimentally investigated the effects of cumulative radiation from terahertz waves on the structure of neurons. 1) The frequency and power of terahertz waves are the main factors affecting field strength and temperature in neurons, and there is a positive correlation between them, a phenomenon that is correlated with the relative dielectric constant of the cytoplasm. 2) When choosing terahertz radiation parameters, the frequency can be determined according to the properties of the modulating substance, and an appropriate reduction in radiation power can mitigate the rise in temperature in the neuron. It is also possible to use pulsed waves to keep the duration of a single round of radiation, as well as short bursts of cumulative radiation, to the millisecond level. 3) On this basis, we found that broadband trace terahertz (0.1–2 THz, maximum radiated power 100 μW), short duration cumulative radiation (3 min/day, 3 days) does not cause neuronal death. This radiation protocol can also promote the growth of neuronal cytosomes and protrusions. This paper provides a set of guidelines and methodology for selecting terahertz radiation parameters in the study of terahertz neurobiological effects. Furthermore, it provides verification that the structure of neurons can be modulated using short duration cumulative radiation.

Data availability statement

The raw data supporting the conclusion of this article will be made available by the authors, without undue reservation.

Ethics statement

The animal study was reviewed and approved by Animal Ethics Committee of Yanshan University.

Author contributions

LY, LX, and LC designed the research and revised the manuscript. MS conducted the research and wrote the manuscript. MS, LZ, and GS analyzed the experimental data. All authors contributed to the article and approved the submitted version.

Funding

This work was supported by the National Natural Science Foundation of China (Grant No. 61827811), Hebei Key Laboratory Project, China (Grant No. 202250701010046), Hebei Provincial Natural Science Foundation of China (Grant No. F2020203099), Hebei Province Funding Project for the Introduction of Overseas Students (Grant No. C20200364).

Conflict of interest

The authors declare that the research was conducted in the absence of any commercial or financial relationships that could be construed as a potential conflict of interest.

Publisher's note

All claims expressed in this article are solely those of the authors and do not necessarily represent those of their affiliated organizations, or those of the publisher, the editors and the reviewers. Any product that may be evaluated in this article, or claim that may be made by its manufacturer, is not guaranteed or endorsed by the publisher.

References

Abrahamsson, T., Chou, C. Y. C., Li, S. Y., Mancino, A., Costa, R. P., Brock, J. A., et al. (2017). Differential regulation of evoked and spontaneous release by presynaptic NMDA receptors. *NEURON* 96 (4), 839–855.e5. doi:10.1016/j.neuron.2017.09.030

Ajenikoko, M. K., Ajagbe, A. O., Onigbinde, O. A., Okesina, A. A., and Tijani, A. A. (2023). Review of Alzheimer's disease drugs and their relationship with neuron-glia interaction. *IBRO Neurosci. Rep.* 14, 64–76. doi:10.1016/j.ibneur.2022.11.005

Albert, E. S., Bec, J. M., Desmadryl, G., Chekroud, K., Travo, C., Gaboyard, S., et al. (2012). TRPV4 channels mediate the infrared laser-evoked response in sensory neurons. *J. Neurophysiol.* 107 (12), 3227–3234. doi:10.1152/jn.00424.2011

Alexandrov, B. S., Gelev, V., Bishop, A. R., Usheva, A., and Rasmussen, K. O. (2009). DNA breathing dynamics in the presence of a terahertz field. *Phys. Lett. A* 374 (10), 1214–1217. doi:10.1016/j.physleta.2009.12.077

Balos, V., Kaliannan, N. K., Elgabarty, H., Wolf, M., Kühne, T. D., and Sajadi, M. (2022). Time-resolved terahertz-Raman spectroscopy reveals that cations and anions distinctly modify intermolecular interactions of water. *Nat. Chem.* 14 (9), 1031–1037. doi:10.1038/s41557-022-00977-2

Bo, W. F., Che, R., Kong, L., Zhang, M. J., and Zhang, X. B. (2021). Research progress of biological effects of cell membrane under infrared and terahertz irradiation. *ACTA Phys. SIN-CH Ed.* 70 (24), 248707. doi:10.7498/aps.70.20212030

Borovkova, M., Serebriakova, M., Fedorov, V., Sedykh, E., Vaks, V., Lichutin, A., et al. (2016). Investigation of terahertz radiation influence on rat glial cells. *Biomed. Opt. Express* 8 (1), 273–280. doi:10.1364/BOE.8.000273

Cha, C. X. (2016). *CRMP2 and CRMP4 regulate the axonal development of hippocampal neurons*. Doctoral's thesis]. Guangzhou: University of Jinan.

Chen, X. Q., Lindley-Hatcher, H., Stantchev, I., Wang, J. R., Li, K. D., Serrano, A. H., et al. (2022). Terahertz (THz) biophotonics technology: Instrumentation, techniques, and biomedical applications. *Chem. Phys. Rev.* 3, 011311. doi:10.1063/5.0068979

Cheon, H., Paik, J. H., Choi, M., Yang, H. J., and Son, J. H. (2019b). Detection and manipulation of methylation in blood cancer DNA using terahertz radiation. *Sci. Rep.* 9 (1), 6413. doi:10.1038/s41598-019-42855-x

Cheon, H., Yang, H. J., Choi, M., and Son, J. H. (2019a). Effective demethylation of melanoma cells using terahertz radiation. *Biomed. Opt. Express* 10 (10), 4931–4941. doi:10.1364/BOE.10.004931

Cherkasova, O. P., Fedorov, V. I., Nemova, E. F., and Pogodin, A. S. (2009). Influence of terahertz laser radiation on the spectral characteristics and functional properties of albumin. *Opt. Spectrosc.* 107, 534–537. doi:10.1134/S0030400X09100063

Di Cristo, G., and Chattopadhyaya, B. (2020). Development of neuronal circuits: From synaptogenesis to synapse plasticity. *Handb. Clin. Neurol.* 173, 43–53. doi:10.1016/B978-0-444-64150-2.00005-8

Duan, T., Yan, S., Zhao, Y., Sun, T., Li, Y., Li, K. D., et al. (2021). Relationship between hydrogen bond network dynamics of water and its terahertz spectrum. *ACTA Phys. SIN-CH* 70 (24), 248702. doi:10.7498/aps.70.2021173170

Fischer, B. M., Walther, M., and ZhaoUhd Jepsen, P. (2002). Far-infrared vibrational modes of DNA components studied by terahertz time-domain spectroscopy. *Phys. Med. Biol.* 47 (21), 3807–3814. doi:10.1088/0031-9155/47/21/319

Fribance, S., Wang, J., Roppolo, J. R., de Groat, W. C., and Tai, C. (2016). Axonal model for temperature stimulation. *J. Comput. Neurosci.* 41 (2), 185–192. doi:10.1007/s10827-016-0612-x

Generalov, V., Safatov, A., Kruchinina, M., Gromov, A., Buryak, G., Generalov, K., et al. (2020). Dielectric properties of the human red blood cell. *Meas. Tech.* 63 (7), 580–586. doi:10.1007/s11018-020-01826-9

Guo, L. H., Wang, S. M., Yang, L. X., Wang, K. C., Ma, J. L., Zhou, J., et al. (2021). Weak resonance effects of THz wave transimission in nerve cell. *ACTA Phys. SIN-CH Ed.* 70 (24), 240301. doi:10.7498/aps.70.20211677

Guo, Z. Y., Li, C. Z., Li, X. J., Wang, Y. L., Mattson, M. P., and Lu, C. B. (2013). The developmental regulation of glutamate receptor-mediated calcium signaling in primary cultured rat hippocampal neurons. *NEUROREPORT* 24 (9), 492–497. doi:10.1097/WNR.0b013e32836206b5

Heshmat, B., Andrews, G. M., Naranjo-Montoya, O. A., Castro-Camus, E., Ciceri, D., Sanchez, A. R., et al. (2017). Terahertz scattering and water absorption for porosimetry. *Opt. Express* 25 (22), 27370–27385. doi:10.1364/OE.25.027370

Hu, C. C., Zuo, H. Y., and Li, Y. (2021). Effects of radiofrequency electromagnetic radiation on neurotransmitters in the brain. *Front. Public Health* 9, 691880. doi:10.3389/fpubh.2021.691880

Information Technologies in Society (ITIS) Foundation (2023). *Tissue frequency chart*. Available at: https://itis.swiss/virtual-population/tissue-properties/database/tissue-frequency-chart/ (Accessed March 1, 2023).

Kristensen, T. T., Withayachumnankul, W., Jepsen, P. U., and Abbott, D. (2016). Modeling terahertz heating effects on water. *Opt. Express* 18 (5), 4727–4739. doi:10.1364/OE.18.004727

Li, Y., Chang, C., Zhu, Z., Sun, L., and Fan, C. (2021). Terahertz wave enhances permeability of the voltage-gated calcium channel. *J. Am. Chem. Soc.* 143 (11), 4311–4318. doi:10.1021/jacs.0c09401

Liu, G. Z., Chang, C., Qiao, Z., Wu, K. J., Zhu, Z., Gui, G. Q., et al. (2019a). Myelin sheath as a dielectric waveguide for signal propagation in the mid-infrared to terahertz spectral range. *Adv. Funct. Mater.* 29 (7), 1807862. doi:10.1002/adfm.201807862

Liu, W. Q., Lu, Y. F., She, R. B., Wei, G. L., Jiao, G. H., Lv, G. C., et al. (2019b). Thermal analysis of cornea heated with terahertz radiation. *Appl. Sci.* 9, 917.doi :doi:10.3390/app9050917

Lundholm, I. V., Rodilla, H., Wahlgren, W. Y., Duelli, A., Bourenkov, G., Vukusic, J., et al. (2015). Terahertz radiation induces non-thermal structural changes associated with Frohlich condensation in a protein crystal. *Struct. Dyn.* 2 (5), 054702. doi:10.1063/1.4931825

Ma, Z. X., Liu, Z., Xiong, H. H., Zhou, Z. P., Ouyang, L. S., Xie, F. K., et al. (2023). MicroRNAs: Protective regulators for neuron growth and development. *NEURAL Regen. Res.* 18 (4), 734–745. doi:10.4103/1673-5374.353481

Mancini, T., Mosetti, R., Marcelli, A., Petrarca, M., Luqi, S., and D'Arco, A. (2022). Terahertz spectroscopic analysis in protein dynamics:current status. *Radiation* 2, 100–123. doi:10.3390/radiation2010008

Moore, R. E., Clarke, J., and Alexandre, P. (2020). Protrusion-Mediated signaling regulates patterning of the developing nervous system. *Front. Cell Dev. Biol.* 8, 579073. doi:10.3389/fcell.2020.579073

Olshevskaya, J. S., Kozlov, A. S., Petrov, A. K., Zapara, T. A., and Ratushnyak, A. S. (2010). Influence of terahertz (submillimeter) laser radiation on cell membrane permeability. *Ser. Phys.* 5 (4), 177–181. Vestnik Novosibirsk State University.

Olshevskaya, J. S., Kozlov, A. S., Petrov, A. K., Zapara, T. A., and Ratushnyak, A. S. (2009). Influence of terahertz (Submillimeter)Laser radiation on neurons *in vitro*. *J.Higher Nerv. Act.* 59, 353.

Paparo, D., Tielrooij, K., Bakker, H., and Bonn, M. (2009). TeraHertz dielectric relaxation of biological water confined in model membranes made of lyotropic phospholipids. *Mol. Cryst. Liq. Cryst.* 500 (1), 108–117. doi:10.1080/15421400802713769

Peng, X. Y., and Zhou, H. (2021). Biological effects of terahertz waves. *Acta Phys. Sin.* 70, 240701. doi:10.7498/aps.70.20211996

Pennes, H. H. (1948). Analysis of tissue and arterial blood temperatures in the resting human forearm. *J. Appl. Physiol.* 1 (2), 93–122. doi:10.1152/jappl.1948.1.2.93

Pikov, V., Arakaki, X., Harrington, M., Fraser, S. E., and Siegel, P. H. (2010). Modulation of neuronal activity and plasma membrane properties with low-power millimeter waves in organotypic cortical slices. *J. NEURAL Eng.* 7 (4), 0045003. doi:10.1088/1741-2560/7/4/045003

Samsonov, A., and Popov, S. V. (2013). The effect of a 94 GHz electromagnetic field on neuronal microtubules. *BIOELECTROMAGNETICS* 34 (2), 133–144. doi:10.1002/bem.21760

Sulatsky, M. I., Duka, M. V., and Smolyanskaya, O. A. (2014). Stimulation of neurite growth under broadband pulsed THz radiation. *Phy Wave Phenom.* 22, 197–201. doi:10.3103/S1541308X14030066

Sun, L., Zhao, L., and Peng, R. Y. (2021). Research progress in the effects of terahertz waves on biomacromolecules. *Mil. Med. Res.* 8 (1), 28. doi:10.1186/s40779-021-00321-8

Tsurkan, M. V., Smolyanskaya, O. A., Bespalov, V. G., Penniyainen, V. A., Kipenko, A. V., Lopatina, E. V., et al. (2012). Changing growth of neurites of sensory ganglion by terahertz radiation. *Proc. SPIE.* 8261, 82610.

Wang, K., Tang, S. Y., Meng, L., Li, X., Wen, X. X., Chen, S. H., et al. (2018). Effect of 1.8 GHz radiofrequency electromagnetic radiation on novel object associative recognition memory in mice. *Sci. Rep.* 7, 44521. doi:10.1038/srep44521

Wang, K., Yang, L., Wang, S., Guo, L., Ma, J., Tang, J., et al. (2020). Transient proton transfer of base pair hydrogen bonds induced by intense terahertz radiation. *Phys. Chem. Chem. Phys.* 22 (17), 9316–9321. doi:10.1039/d0cp01247e

Wilmink, G. J., Rivest, B. D., Roth, C. C., Ibey, B. L., Payne, J. A., Cundin, L. X., et al. (2011). *In vitro* investigation of the biological effects associated with human dermal fibroblasts exposed to 2.52 THz radiation. *LASER Surg. Med.* 43 (2), 152–163. doi:10.1002/lsm.20960

Xiang, Z. X., Tang, C. X., Chang, C., and Liu, G. Z. (2019). A primary model of THz and far-infrared signal generation and conduction in neuron systems based on the hypothesis of the ordered phase of water molecules on the neuron surface I: Signal characteristics. *Sci. Bull.* 65 (4), 308–317. doi:10.1016/j.scib.2019.12.004

Yada, H., Nagai, M., and Tanaka, K. (2008). Origin of the fast relaxation component of water and heavy water revealed by terahertz time-domain attenuated total reflection spectroscopy. *Chem. Phys. Lett.* 464 (4-6), 166–170. doi:10.1016/j.cplett.2008.09.015

Yang, Q., Ke, Y. N., Luo, J. H., and Tang, Y. (2017). Protocol for culturing low density pure rat hippocampal neurons supported by mature mixed neuron cultures. *J. Neurosci. METH* 277, 38–45. doi:10.1016/j.jneumeth.2016.12.002

Yang, X., Zhao, X., Yang, K., Liu, Y. P., Liu, Y., Fu, W. L., et al. (2016). Biomedical applications of terahertz spectroscopy and imaging. *TRENDS Biotechnol.* 34 (10), 810–824. doi:10.1016/j.tibtech.2016.04.008

Yu, X. B., Ton, A. N., Niu, Z. J., Morales, B. M., Chen, J. D., Braz, J., et al. (2023). ACVR1-activating mutation causes neuropathic pain and sensory neuron hyperexcitability in humans. *PAIN* 164 (1), 43–58. doi:10.1097/j.pain.0000000000002656

Zaharov, V. V., Farahi, R. H., Snyder, P. J., Davison, B. H., and Passian, A. (2014). Karhunen-Loève treatment to remove noise and facilitate data analysis in sensing, spectroscopy and other applications. *ANALYST* 139 (22), 5927–5935. doi:10.1039/c4an01300j

Zhang, J., Li, S, A., and Le, W. D, A. (2021). Advances of terahertz technology in neuroscience: Current status and a future perspective. *iScience* 24 (12), 103548. doi:10.1016/j.isci.2021.103548

Zhao, X. H., Zhang, M., Liu, Y. M., Liu, H. Y., Ren, K. K., Xue, Q., et al. (2021). Terahertz exposure enhances neuronal synaptic transmission and oligodendrocyte differentiation *in vitro*. *iScience* 24 (12), 103485. doi:10.1016/j.isci.2021.103485

frontiers | Frontiers in Bioengineering and Biotechnology

TYPE Original Research
PUBLISHED 13 July 2023
DOI 10.3389/fbioe.2023.1218927

OPEN ACCESS

EDITED BY
Olga P. Cherkasova,
Institute of Laser Physics (RAS), Russia

REVIEWED BY
Lei Hou,
Xi'an University of Technology, China
Xiaonan Yang,
Zhengzhou University, China
Ilya Ozheredov,
Lomonosov Moscow State University, Russia

*CORRESPONDENCE
Ai Peng,
pengai@tongji.edu.cn
Yongni Shao,
ynshao@usst.edu.cn

RECEIVED 08 May 2023
ACCEPTED 03 July 2023
PUBLISHED 13 July 2023

CITATION
Li H, Zhou Y, Wu Y, Jiang Y, Bao H, Peng A and Shao Y (2023), Real-time and accurate calibration detection of gout stones based on terahertz and Raman spectroscopy.
Front. Bioeng. Biotechnol. 11:1218927.
doi: 10.3389/fbioe.2023.1218927

Real-time and accurate calibration detection of gout stones based on terahertz and Raman spectroscopy

Han Li[1,2], Yuxin Zhou[3], Yi Wu[4], Yanfang Jiang[4], Hui Bao[4], Ai Peng[4]* and Yongni Shao[3,2]*

[1]The First Rehabilitation Hospital of Shanghai, School of Medicine, Tongji University, Shanghai, China, [2]Shanghai Institute of Intelligent Science and Technology, Tongji University, Shanghai, China, [3]Terahertz Technology Innovation Research Institute, Terahertz Spectrum and Imaging Technology Cooperative Innovation Center, Shanghai Key Lab of Modern Optical System, University of Shanghai for Science and Technology, Shanghai, China, [4]Shanghai Tenth People's Hospital, Tongji University School of Medicine, Shanghai, China

Gout is a metabolic disease that can result in the formation of gout stones. It is essential to promptly identify and confirm the type of gout stone to alleviate pain and inflammation in patients and prevent complications associated with gout stones. Traditional detection methods, such as X-ray, ultrasound, CT scanning, and blood uric acid measurement, have limitations in early diagnosis. Therefore, this article aims to explore the use of micro Raman spectroscopy, Fourier transform infrared spectroscopy, and Terahertz time-domain spectroscopy systems to detect gout stone samples. Through comparative analysis, Terahertz technology and Raman spectroscopy have been found to provide chemical composition and molecular structure information of different wavebands of samples. By combining these two technologies, faster and more comprehensive analysis and characterization of samples can be achieved. In the future, handheld portable integrated testing instruments will be developed to improve the efficiency and accuracy of testing. Furthermore, this article proposes establishing a spectral database of gout stones and urinary stones by combining Raman spectroscopy and Terahertz spectroscopy. This database would provide accurate and comprehensive technical support for the rapid diagnosis of gout in clinical practice.

KEYWORDS

gout stones, spectral techniques, terahertz technique, Raman spectroscopy, handheld instruments

1 Introduction

Gout stone, also known as urate crystal deposition disease, is a metabolic disorder that occurs due to the inability of the body to discharge uric acid normally, resulting in the accumulation of urate crystals in various parts of the body, including joints, soft tissues, kidneys, and the urinary tract. These crystals can trigger inflammatory reactions and cause pain (Parthasarathy and Vivekanandan, 2018). The formation of gout stones is common in joints and surrounding soft tissues such as ligaments and tendons, with the most frequently affected joint being the big toe joint. It can lead to joint inflammation, swelling, and damage, with the potential for joint deformation, distortion, or destruction, particularly in smaller

joints such as the toes (Perez-Ruiz et al., 2015). Additionally, gout stones can also develop in various external joint positions and conventional areas, such as the cardiovascular, renal, and spinal regions, leading to systemic diseases, such as urinary tract stones, chronic urate nephropathy, and cardiovascular and cerebrovascular diseases (Ahmad et al., 2021).

Currently, medical imaging techniques such as X-ray, ultrasound, computed tomography (CT), and magnetic resonance imaging (MRI), as well as blood uric acid measurement methods, are commonly used to detect gout stones. X-ray was the first technique used to detect gout stones, as it can display the distribution, shape, quantity, and size of gout stones around joints and soft tissues and identify their connection with bones. However, X-rays cannot detect gout stones smaller than 1 mm or located deep within the tissues, and they cannot detect early gout stone deposits (Fernandes et al., 2017). Ultrasound is a non-invasive detection method that can detect early symptoms of gout, such as swelling and inflammation of soft tissues around joints, and it can detect gout stones smaller than 1 mm. However, the accuracy of an ultrasound examination is affected by hypertrophic soft tissues and cannot detect deep gout stones, and different operators may produce varying results (Kaeley et al., 2020). CT scanning is a high-resolution imaging technique that is more accurate than an X-ray in diagnosing gout stones located in deep tissues and skeletal structures, particularly when X-ray examination is unclear. In addition, CT scanning can also be employed for detecting uric acid deposition of gout stones in the kidneys. However, it has higher costs and radiation compared to other imaging examination methods, which may pose certain health risks to patients and is not suitable for long-term monitoring (Dalbeth et al., 2019). Magnetic resonance imaging (MRI) provides high-resolution images and performs well in detecting small gouty stones within joints. Furthermore, it provides detailed information about joint soft tissues and bones, which can be utilized to diagnose complications of gout. However, MRI examinations require high costs in terms of time and money. Additionally, MRI has limitations, such as the inability of patients with pacemakers, metal implants, or pregnant women to undergo MRI examinations (Davies et al., 2019). In addition to imaging examinations, measuring blood uric acid levels can serve as an auxiliary means for the early diagnosis of gout and monitoring and evaluating gout treatment, but changes in blood uric acid levels are influenced by various factors, such as diet, weight, medication, *etc.*, and therefore have certain limitations (Reginato et al., 2012). However, these methods cannot distinguish gout stones from other types of crystals, and the detection and time costs are relatively high. Different detection method pairs are shown in Table 1.

In recent years, due to its high sensitivity and a non-destructive testing process that is simple and fast, optical technology has been widely used in various types of testing. Compared with traditional detection techniques, the primary focus of optical technology in the detection of gout stones is on analyzing the physical and chemical properties of gout stones. By studying the chemical composition, structure, morphology, and other aspects of gout stones, we aim to understand the etiology and pathogenesis, and develop prevention and treatment plans for gout. Among the various optical technologies, near-infrared technology is the most widely used for detecting the physical and chemical properties of gout stones. Compared to traditional detection techniques, near-infrared spectroscopy can quickly and accurately detect uric acid salts, proteins, and other components in gout stones. Additionally, the composition and chemical structure of the molecule can be analyzed based on its vibration frequency and absorption characteristics (Czarnecki et al., 2015; Sakudo, 2016). However, the resolution and accuracy of near-infrared imaging are relatively low, which may overlook some essential pathological features, especially for the detection of gout stones with complex composition or small structural changes (Jamrógiewicz, 2012). Therefore, researchers have begun exploring the application of other spectral techniques in detecting gout stones. Raman spectroscopy and Terahertz spectroscopy have become two widely studied technologies that can improve the accuracy and precision of gout detection.

Raman spectroscopy is a type of molecular spectroscopy that reflects molecular vibrations and rotations. It characterizes the interaction between molecules and photons, which leads to the characteristic frequency shift of molecular vibrations and rotational energy level differences. The differences in vibration amplitude and rotational energy levels among different substances result in distinct Raman frequency shifts. Raman technology can obtain molecular vibration and chemical structure information of substances by measuring Raman scattering spectral lines in the sample scattering spectrum (Jones et al., 2019). Raman technology has been widely used in analyzing and identifying the characteristic Raman spectral lines of different organic compounds in samples. For example, it has been used to detect organic compounds, such as additives, pigments, and preservatives in food, as well as in water quality testing, environmental monitoring, and medical fields (Auner et al., 2018). Tamosaityte et al. applied Raman spectroscopy technology to detect and analyze different types of urinary stones, and the results showed that Raman technology can accurately identify different types of urinary stones and achieve a quantitative analysis of their chemical components with high accuracy and reliability (Sandra et al., 2022). Zhu et al. (2022) used a portable Raman system to analyze urine stone samples obtained from 300 patients and demonstrated that Raman spectroscopy can be applied to portable automated analysis systems, which have the characteristics of simple operation, easy automation, and rapid detection in on-site clinical environments. Niessink et al. (2023) measured the crystals in joint synovial fluid using Raman spectroscopy, which indicated that Raman technology could be used to evaluate disease conditions or predict the formation of stones. These studies demonstrate that Raman spectroscopy technology provides a fast and convenient method for medical detection.

Terahertz refers to electromagnetic waves with a frequency range between the infrared and microwave regions, specifically ranging from 0.1–10 THz, corresponding to a wavelength range of 30 μm-3 mm (Gowen et al., 2012). Terahertz waves exhibit low photon energy (approximately 0.4–30 meV) and strong penetration, without causing damage or photoionization to the sample. This characteristic enables the use of Terahertz waves for non-contact and non-destructive testing of samples (Guo et al., 2022). Moreover, the Terahertz frequency range covers the intermolecular vibration and rotational energy levels of various organic/biological macromolecules. This ability enables the detection of intermolecular interactions between organic molecules, including hydrogen bonds, van der Waals forces, and others, which are important characteristics of organic molecules in

TABLE 1 Comparison of traditional medical detection methods.

Test method	Advantages	Disadvantages	Reference
X-ray	Detects early gout stones	High radiation level, unable to detect gout stones less than 1 mm or located deep, unable to detect early gout stone deposits	Fernandes et al. (2017)
ultrasonic	Detects early symptoms of gout	Highly affected by hypertrophic soft tissue and abdominal gas, unable to detect deep gout stones	Kaeley et al. (2020)
CT scanning	More accurate diagnosis when X-ray examination is unclear	High cost and high radioactivity, not suitable for long-term monitoring	Dalbeth et al. (2019)
MRI	Diagnoseable complications of gout	The testing cost is relatively high, and there are limitations such as patients carrying pacemakers or metal implants, or pregnant women not being able be checked	Davies et al. (2019)
Blood uric acid measurement	Detects the main pathological feature of gout	Blood uric acid levels are influenced by various factors, such as diet, weight, and medication, making it less reliable as a standalone measurement	Reginato et al. (2012)
Near-infrared	Detects physical and chemical properties of gout stones	Low resolution and sensitivity, small structural changes and complex composition may overlook pathological features	Jamrógiewicz (2012)

fields such as biology, chemistry, and drug research (Zhang et al., 2022). Jung et al. (2012) employed Terahertz time-domain spectroscopy to detect the distribution of water in human articular cartilage. Their study revealed that Terahertz time-domain spectroscopy technology can non-destructively detect small changes in water content in cartilage, offering a possibility for early diagnosis and treatment of bone and joint diseases. Gilad et al. (2017) utilized Terahertz imaging technology to compare and scan the feet of 30 patients with diabetic foot. The results demonstrated that Terahertz could precisely detect the pathological changes in diabetic foot patients through parameters such as tissue density of the foot and bone density of the foot bottom, and identify possible early pathological changes. This technique provides a new method for real-time and painless detection of the development process of gout foot disease. Zhao Yi employed Terahertz time-domain spectroscopy to detect the components of kidney stones. The study discovered that Terahertz spectroscopy can quickly and accurately detect and differentiate different types of kidney stones (Zhang, 2013; Wu et al., 2016). Additionally, Terahertz time-domain spectroscopy (THz-TDS) can provide spectral information on intramolecular and intermolecular vibrations, which enhances the characterization ability of the substance under test (Shen et al., 2020). In Terahertz spectroscopy experiments, Fourier transform infrared spectroscopy (FTIR) is usually combined to analyze the optical properties of the sample. This is because FTIR technology can achieve high-resolution and high-sensitivity Terahertz spectroscopy measurement in the Terahertz band, and at the same time, time-domain signal measurement can be achieved through Terahertz time-domain spectroscopy technology to analyze and process Terahertz waveforms. These measurement results can be used to determine the physical and chemical properties of the sample, such as the composition, structure, morphology, etc. of the material. Therefore, FTIR technology can serve as a complementary spectral technique to Terahertz time domain spectroscopy system (THz-TDS) and is a suitable tool for studying low-frequency Terahertz spectra of materials. It can provide more comprehensive and in-depth information for Terahertz band analysis and exhibits high accuracy and reliability (Lepodise, 2020; Chamorro-Posada et al., 2016).

Uric acid stones are common in the urinary system and are the only stones that can be dissolved by drugs. It is crucial to have a deep understanding of the pathogenesis of uric acid stones in order to identify, treat, and prevent them effectively. However, many patients with urinary stones are unaware of the properties and causes of their stones, and the composition of stones cannot be determined in hospitals. Therefore, analyzing the components of urinary tract stones is essential for accurate diagnosis and early prevention of gout stones. The extensive use of spectral technology in medical detection has led researchers to recognize its immense potential in disease prevention and detection. In this study, Raman and Terahertz spectroscopy techniques are combined to achieve real-time and precise calibration detection of stone samples. Compared to traditional gout diagnosis methods, these techniques offer several advantages, including non-invasiveness, absence of labeling, simple sample processing, ease of operation, fast detection speed, and acquisition of rich information. The use of non-ionizing radiation also mitigates potential health risks. Compared with methods such as blood uric acid measurement, Raman and Terahertz detection can directly identify the composition of gout stones, without the need for indirect measurement methods to infer results, resulting in higher accuracy and reliability. Furthermore, the development of handheld Raman and Terahertz spectroscopic instruments offers the possibility of detecting samples in clinical settings, facilitating the early diagnosis and treatment of medical conditions such as gout. This study presents novel ideas and techniques for detecting metabolic diseases like gout and provides robust technical support to enable convenient clinical detection of diseases.

2 Materials and methods

2.1.1 Fourier transform infrared spectrometer (FTIR)

The Bruker IFS66v/s Fourier transform infrared spectrometer, produced by BRUKER in Germany, is a high-performance spectrometer used for infrared spectral analysis. The spectrometer includes an incoherent high-pressure mercury lamp, a far-infrared beam splitter, far-infrared focusing and collimating components, a

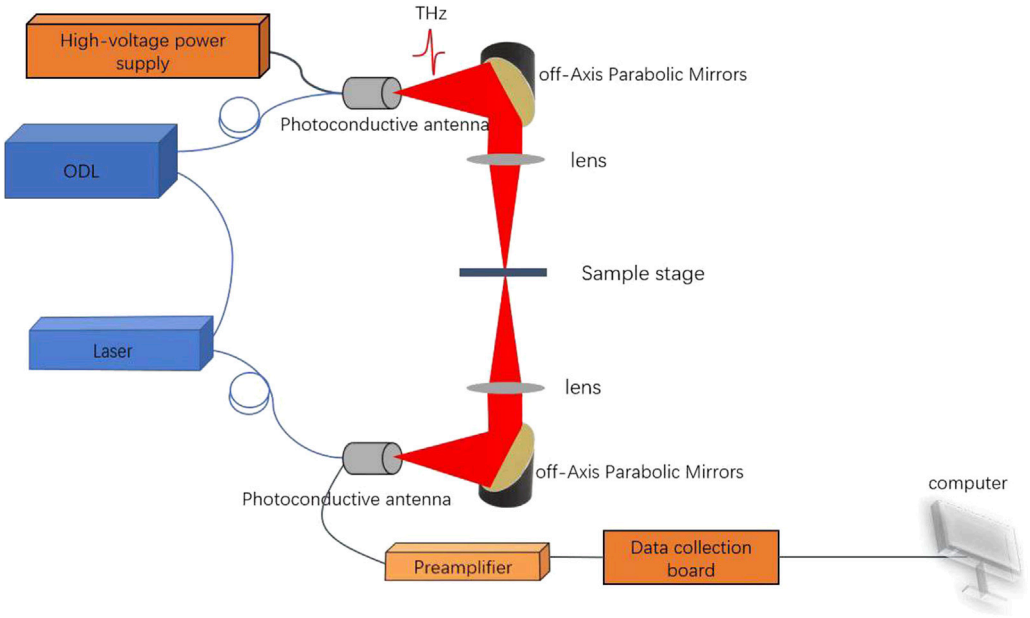

FIGURE 1
Composition of Terahertz time-domain spectroscopy system.

nonthermal detector, an electric delay line, and sample, filter, and data acquisition systems. The Terahertz spectral region studied in this experiment effectively covers 30–680 cm^{-1}, with a signal-to-noise ratio (SNR) better than 10000:1. When starting up, it is necessary to first turn on the water circulation and wait for half an hour for the system to stabilize before conducting experimental testing. In the experiment, parameters with a resolution of 4 cm^{-1}, 128 scans, and a scanning speed of 5 kHz were used for spectral collection, resulting in a spectral frequency range of 0.9–20 THz. These parameters can ensure the high quality and accuracy of the experiment and are used for the detection and analysis of Terahertz spectroscopy.

2.1.2 Terahertz time domain spectroscopy system (THz-TDS)

A Terahertz time-domain spectroscopy (THz-TDS) system designed by the Terahertz laboratory of the University of Shanghai for Science and Technology consists of a fiber femtosecond laser (1550 nm,<65 fs), optical delay line, collection board, amplifier, and Terahertz photoconductive transceiver antenna, the photoconductive antenna is fabricated using Indium Gallium Arsenide (InGaAs), as depicted in Figure 1. The main performance parameters of the system include a scanning speed of 0.1s per spectrum, an SNR exceeding 90dB, a spectrum width greater than 3THz, and a compact volume measuring 40 cm × 30 cm × 18 cm. The interior adopts a fully coupled optical path design with stable and reliable performance. In this experiment, the scanning range was 66ps, the scanning frequency was 512, and the scanning speed was 1440 mm/s. Firstly, air scanning is used as a reference signal, followed by testing the sample. Finally, the obtained data is processed and analyzed for spectral data.

2.1.3 Laser confocal micro Raman spectrometer

The LabRAM HR Evolution, a micro Raman spectrometer produced by Horiba Scientific in France, is a powerful spectrometer that can be used for both micro and large sample measurements and has advanced 2D and 3D confocal imaging performance. The spectrometer is mainly composed of an open microscope/inverted microscope, high-precision three-dimensional platform, fiber optic probe, polarization attachment, transmission testing module, and other modules. It provides convenient analysis modules and can be widely used in Raman analysis, photoluminescence (PL), needle-enhanced Raman scattering (TERS), and other combined technologies. The LabRAM HR Evolution micro Raman spectrometer has high flexibility, can be extended to the full wavelength range (200 nm–2100 nm), and achieves automatic switching of all wavelengths. In this experiment, the analysis conditions for gout stones were as follows: laser light source wavelength 633nm, grating size 600gr/mm, measurement under a ×50 objective lens, exposure time 10s, scanning intensity 100%, and spectral collection range 200 cm^{-1}–800 cm^{-1}. The selection of these parameters can ensure high-quality spectral measurement and accurate analysis of the experiment, which is used for Raman spectroscopy analysis of gout stone samples.

2.2 Chemical reagents

Polyethylene was purchased from Sigma as a solid powder with particle diameters of 40–48 μm. The CAS number is 9002-88-4. Gout stones are a characteristic clinical manifestation of gout, which can easily deposit around the auricle and joints. But it is difficult to obtain. In this study, different types of urinary stones were selected to compare the analysis of gout stones and other stones, and the advantages of different detection schemes were analyzed. In the future, handheld

portable comprehensive testing instruments will be developed to improve the efficiency and accuracy of testing.

All stone samples are sourced from the urinary calculi center of Shanghai Tenth People's Hospital. The study protocol was approved by The Shanghai Tenth People's Hospital's Institutional Ethics Committee and was performed in accordance with the Helsinki Declaration.

2.3 Sample preparation and spectral collection

Before testing the sample of gout stone, it should be cleaned using distilled water and allowed to dry naturally. Subsequently, the sample should be placed in an oven and dried at a temperature of 40°C. To ensure proper particle size, the fully dried gout stone sample should be ground. This can be achieved by placing a 2 mm diameter steel ball along with the gout stone in a grinding tube and grinding them for 190 s using a grinder. The grinder parameters should be set to a frequency of 70 Hz and a time of 190 s. The grinding process aims to achieve a powder diameter of less than 2 μm. Different instruments used in the experiment require specific sample processing methods. For Terahertz spectral analysis, take 40 mg of gout stone and 10 mg of polyethylene (PE) and place them in a clean agate mortar. Thoroughly mix the materials using a grinding bowl and mortar, and grind them finely to obtain a mixture suitable for analysis. The mixed powder should then be placed into a mold. To obtain a uniform and particle-free thin sheet with a thickness of approximately 1 mm, a professional tablet press should be adjusted to apply a pressure of 3 tons. The pressing process should be continuous and uniform for 2 min, ensuring that the experimental quality loss is limited to within 1%. To prevent contamination, it is essential to clean the agate mortar and tablet mold thoroughly with pure non-woven fabric before preparing new samples each time. Additionally, it is necessary to suppress 40 mg of polyethylene as the background during the analysis. During the spectrum collection process for each sample, 3 points should be collected, and each point should be collected 3 times to obtain an average value.

2.4 Data processing and model establishment

Analyze the data using UnscramblerX 10.1 and Origin2018 to eliminate background interference, flatten the baseline, and perform correction processing on the data.

3 Results

3.1 Raman data processing and model establishment

A small amount of ground test sample was spread on a microscope slide and subjected to Raman spectroscopy. The tested samples were numbered sequentially as S_1-S_{21}, among which the Raman spectrum of uric acid (UA) is shown in Figure 2. The Raman peak at 1,476 cm^{-1} in (a) was due to the symmetric stretching vibration of C-O in calcium oxalate dihydrate (COD); the Raman peak at 1,463 cm^{-1} in (b) was due to the C=O vibration of calcium oxalate monohydrate (COM); the Raman peaks at 1,458 cm^{-1} and 1,490 cm^{-1} in (c) were both due to the C=O vibration of COM; the Raman peaks at 626 cm^{-1} in (d), (e), and (f) were due to the ring breathing vibration of the UA molecule; the peaks at 997 cm^{-1} and 1,037 cm^{-1} were due to the highly mixed vibration of UA; the Raman peak at 1,648 cm^{-1} in (e) was due to the C=O stretching vibration of UA; the Raman peak at 1,476 cm^{-1} in (f) was due to the symmetric stretching of C-O-O in COD; the Raman peak at 896 cm^{-1} in (g) was due to the C-C stretching of COM, and the Raman peak at 1,630 cm^{-1} in S_{19} was due to the symmetric stretching vibration of C-O in COM; the Raman peak at 910 cm^{-1} in (h) was due to the C-C shift stretching of COD (Sandra et al., 2022; Selvaraju et al., 2013; Cui et al., 2018).

In most Asian countries, the most common type of stone is calcium oxalate (75%–90%), specifically COM and COD, with UA (5%–20%) ranking as the second most common type (Fisang et al., 2015). Several studies have investigated the formation of calcium oxalate stones, revealing that COD crystals are the typical form of oxalate metabolism, while the presence of COM crystals may be an indication of increased risk for stone formation. Initially, calcium oxalate stones tend to crystallize in the form of COD rather than COM. This suggests that the transition from COD to COM occurs in the body, as COM is a relatively more stable form of the calcium oxalate compound (Costa-Bauzá et al., 2007). The application of Raman spectroscopy technology to identify and classify kidney stones can provide effective data for identifying and classifying stones at a molecular level without damaging the samples.

Among the samples of stones analyzed, it was found that the composition of stones in 21 patients was predominantly composed of calcium oxalate, accounting for 76.19%, with COM accounting for 47.62% and COD accounting for 28.57%. The proportion of UA was 23.81%, and mixed stones accounted for 4.76%, consistent with the literature (Fisang, Anding, Müller, Latz, and Laube, 2015). Raman spectroscopy measures the frequency shift and intensity changes of scattered light in the sample by irradiating it with a laser, providing vibration information of the sample and enabling the screening of different types of stones from mixed stones. Particularly for the identification of two types of gout stones, COM and COD, which have minor differences in their molecular structure and chemical composition, these differences can be captured and distinguished through the high resolution of Raman spectroscopy. This is important for the treatment of stones, as current clinical methods cannot clearly identify the two types. Research has demonstrated the feasibility of using Raman spectroscopy technology for identifying and classifying stones, thereby creating a novel approach for screening and diagnosing clinical stone types, with long-term research value. Although there are not many specimens, the proportion of pure uric acid stones is close to 25%. Early diagnosis and treatment of gout is very important.

3.2 Terahertz data processing and model establishment

3.2.1 Fourier transform infrared spectrometer (FTIR)

FTIR and Raman spectroscopy are complementary technologies used for detecting basic molecular vibrations. However, FTIR is based on the absorption of light energy and the subsequent change in the dipole moment in the molecule, while Raman spectroscopy is

10.3389/fbioe.2023.1218927

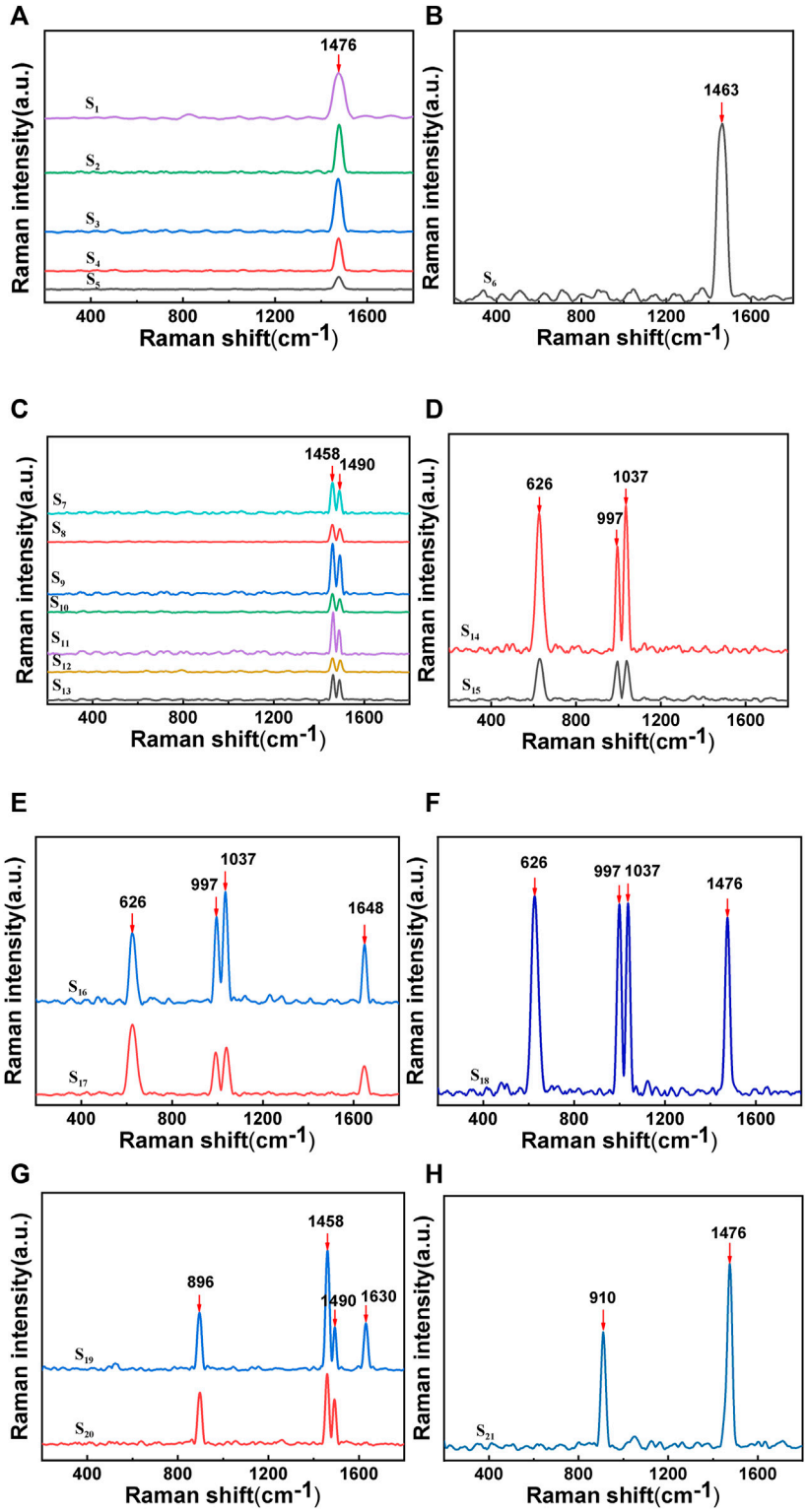

FIGURE 2
Raman spectra of stones:**(A)** and **(H)** show the Raman characteristic peak of calcium oxalate dihydrate;**(B)**, **(C)**, **(F)**, and **(G)** show the Raman characteristic peak of calcium oxalate monohydrate; **(D)**, **(E)**, and **(F)** show the Raman characteristic peak of uric acid.

generated due to the comprehensive scattering effect of light that occurs after the irradiation of monochromatic light, which causes the vibration of the change of polarizability in the molecule. Some molecules may have weaker vibrations in Raman spectroscopy but stronger vibrations in infrared spectroscopy (Paraskevaidi et al., 2021).

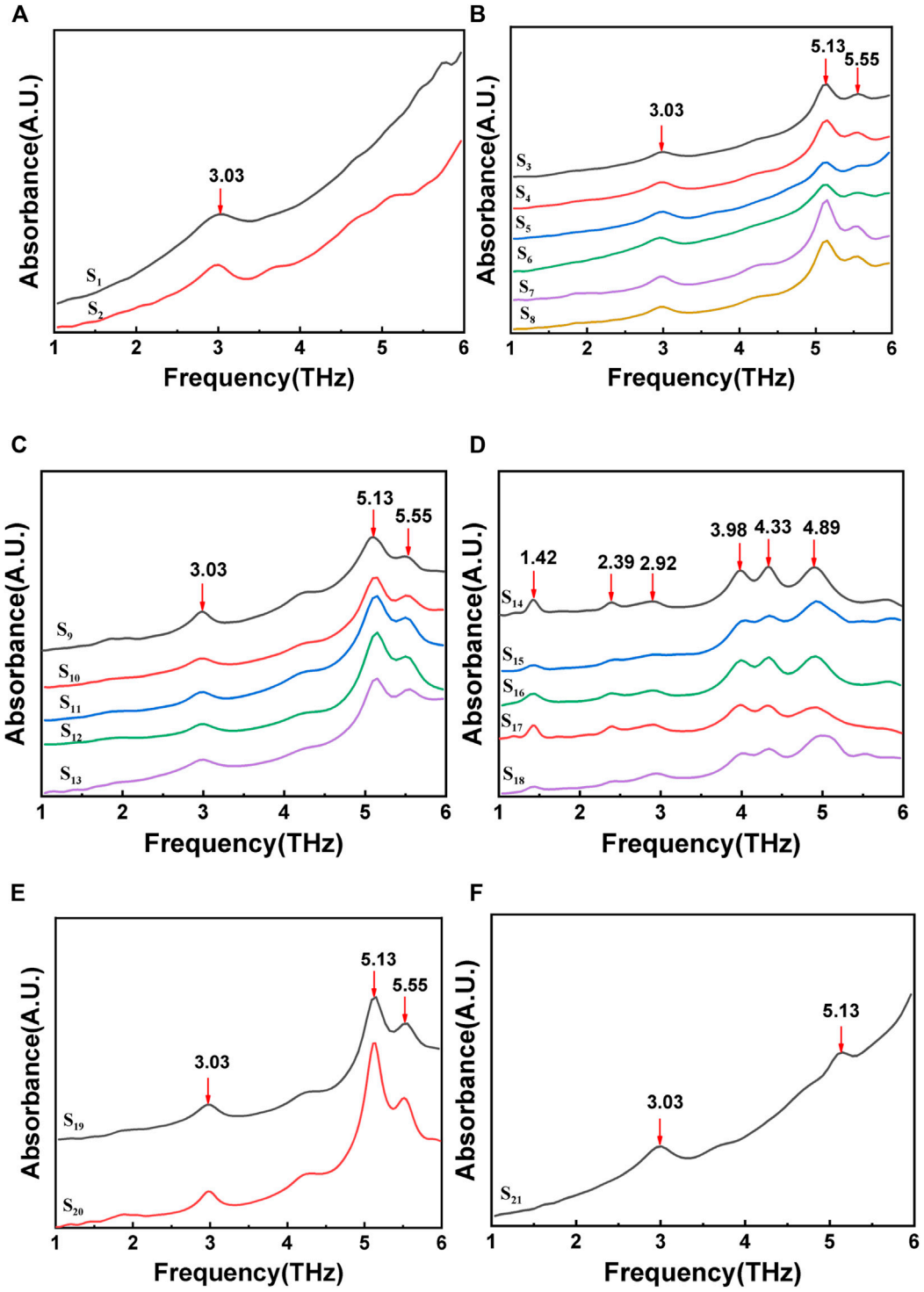

FIGURE 3
FTIR spectrum of gout stones:**(A)**, **(B)**, **(C)**, **(E)**,and **(F)** show the terahertz characteristic peak of calcium oxalate; **(D)** shows the terahertz characteristic peak of uric acid.

The compressed stone sample is placed under the laser, and the absorption spectrum in the 1-6 THz frequency band is measured using a Fourier transform infrared spectrometer. Figure 3 shows the FTIR spectra of gout stones. The characteristic absorption peak frequencies of 3.03 THz, 5.13 THz, and 5.55 THz for samples (a), (b), (c), (e), and (f) are compared to those in reference (Zhang, 2013; Wu et al., 2016). The stone component in these cases is CO, as shown in Figure 3D. Samples S_{14} to S_{18} exhibit significant Terahertz absorption peaks at 1.42 THz,2.39 THz, and 2.92 THz, indicating that the component of these stones is UA, based on a comparison of

characteristic absorption peak frequencies in the literature (Zhang, 2013; Wu et al., 2016).

After conducting FTIR spectroscopy detection, it was determined that CO and UA are the primary components of stones in 21 patients, accounting for 76.19% and 23.81%, respectively. These findings are consistent with Raman measurements and indicate the feasibility of utilizing Terahertz spectroscopy for gout stone component detection. However, upon comparison with Raman results, it was discovered that the Terahertz detection could not differentiate between COM and COD, which may be due to the sample processing method. Terahertz detection operates on the stretching and rotational energies of functional groups in the low-frequency range. Prior to detection, the sample undergoes compression processing, which involves mixing the sample with polyethylene (PE) and pressing it into a sheet. This processing method may alter the structure and composition of the sample, consequently affecting the accuracy of Terahertz spectrum measurements.

3.2.2 Terahertz time domain spectroscopy system (THz-TDS)

Fourier transform infrared spectroscopy and Raman spectroscopy are both analytical techniques used to detect information regarding molecular skeleton vibration and rotation, while X-ray diffraction is utilized to detect microstructural information of materials. In comparison, THz-TDS technology combines the benefits of the above three techniques, allowing for the precise analysis and identification of subtle changes in sample composition. THz-TDS technology captures low-frequency vibration information of molecular groups in the low-frequency Terahertz band with high time and frequency resolution, enabling fast and accurate analysis (Manceau et al., 2008). The data analysis and processing method of the THz-TDS system is consistent with that of the Fourier transform infrared spectrometer. Both methods use the fast Fourier transform (FFT) algorithm to convert time-domain information into frequency-domain information.

The absorption spectrum of gout stones in the 1-4 THz frequency band was measured using THz-TDS by placing the compressed sample under a self-built laser. Figure 4 displays the resulting spectrum, revealing several Terahertz absorption peaks. A comparison of the characteristic absorption peak frequencies from the literature (Zhang, 2013; Wu et al., 2016) at 3.00 THz (a), (b), and (c) indicates that the gout stone component is CO. The Terahertz characteristic peak of CO was found to be 3.00 THz, as shown in Figure 4, which agrees with the FTIR-measured peak of calcium oxalate in Figure 3, indicating the accuracy of the measured data and the feasibility of instrument validation for gout composition. Furthermore, the analysis of the THz-TDS spectrum revealed additional Terahertz absorption peaks at 1.19, 1.42, 2.39, and 2.92 THz in the gout stone, which are characteristic peaks of UA (Chen et al., 2020). Thus, the main component of the gout stone was identified as UA. This additional peak at 1.19 THz, not detected by FTIR, suggests that the self-built THz-TDS system can achieve high-frequency resolution in detecting low-frequency vibration information of molecules in the low-frequency Terahertz band, which is crucial for the development of handheld portable Terahertz detection instruments. However, there are certain differences in the spectra of CO samples due to the lower signal-to-noise ratio of FTIR Terahertz detection compared to THz-TDS. The unstable laser light source or subtle noise signals can impact the measurement. Additionally, the wide spectrum of FTIR measurement leads to a larger frequency interval between each two scanning points within similar scanning times, which can easily affect the measurement results, especially for low Terahertz test results. Therefore, an error of 0.03 THz in the data analysis process can be considered under allowable error conditions.

Moreover, in Figure 4C, some samples exhibited relatively consistent waveforms before 3.00 THz.To investigate this further, multiple samples were measured, and the same sample was measured multiple times in the experiment. The resulting measurement results were compared, revealing similar peak positions at the same frequency that remained relatively stable within the measurement range. Therefore, it is likely that these peak positions represent the natural frequencies of the instrument rather than the characteristic frequency analysis of the samples.

4 Discussion

Gout is a metabolic disorder characterized by abnormal metabolism of uric acid, which results in increased blood uric acid levels and the formation of urate salts in joints and soft tissues, leading to the formation of gout stones. Gout stones can cause serious health problems such as arthritis, joint pain, and kidney disease. Current diagnostic methods for gout mainly rely on blood uric acid level tests, arthritis symptoms, and X-rays, but these have certain limitations in the early diagnosis and treatment of gout stones. In this study, 21 gout stone samples were analyzed using three different instruments: laser confocal micro raman spectrometer, FTIR, and THz-TDS. The results indicate that the main components of gout stones can be determined by their characteristic absorption peaks with relatively small errors. Different detection method pairs are shown in Table 2. Compared with commonly used medical examination methods, THz-TDS detection can non-destructively detect the internal structure and physical properties of samples, which fills the gap in the mechanism of low-energy band interactions with substances that cannot be covered by the stretching and rotating energy of functional groups in the infrared range, such as hydrogen bonds, intermolecular van der Waals forces, and detecting small changes and defects. Raman spectroscopy technology can provide more detailed and accurate chemical information, analyze the molecular composition and structure of samples, and can be used for chemical analysis and material research. In terms of gout stone detection, Raman spectroscopy has high sensitivity and resolution, which means that even at low concentrations of gout stone samples, detailed identification of different chemical components and structures of gout stone samples can be carried out. A deep understanding of the characteristics and properties of gout stones is helpful for early diagnosis and treatment. Therefore, in clinical medicine, Terahertz and Raman spectroscopy techniques can complement each other to form more comprehensive analysis results.

From a clinical perspective, Terahertz and Raman spectroscopy are non-ionizing radiation detection techniques that do not pose any health risks to the human body, making them suitable for long-term disease tracking. In contrast, other imaging methods such as X-ray and CT scanning generate radiation and may cause potential health

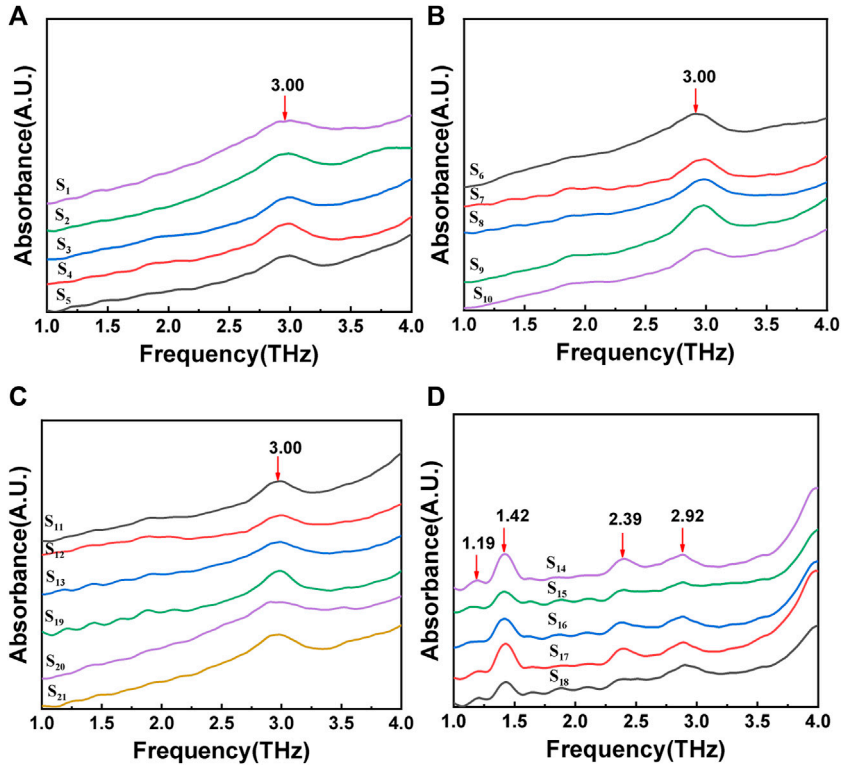

FIGURE 4
THz-TDS spectrum of gout stones:**(A)**, **(B)**, and **(C)** show the terahertz characteristic peak of calcium oxalate; **(D)** show the terahertz characteristic peak of uric acid.

TABLE 2 Comparison of optical testing methods.

Test method	Advantages	Application scope	Reference
Laser Confocal Micro Raman Spectrometer	Non-invasive Real-time	It has molecular specificity and provides high-resolution information at the cellular level for studying molecular composition and microstructure	Movasaghi et al. (2007)
Fourier Transform Infrared Spectrometer (FTIR)	High resolution	A wider spectral range is used to analyze more types of molecules, which can be used to study histology and chemical composition	Jamrógiewicz (2012)
Terahertz Time Domain Spectroscopy System (THz-TDS)	Diversity Information	Extremely high Spectral resolution and time resolution can be used to study physical properties, dynamics, and thermodynamic properties	Castro-Camus et al. (2021)

hazards (Esmonde-White et al., 2017; Demir and Severcan, 2016; Ajito, 2015; Kawase et al., 2003). Moreover, each component in gout stones has a distinct Raman or Terahertz spectrum, which can be used for spectral analysis. The unique "fingerprint spectrum" is used to conduct spectral tests on samples with known components to establish a corresponding spectral database. By comparing the spectral spectra in the database, it is possible to quickly identify and classify samples of unknown components, achieve automated analysis, improve analysis speed and efficiency, and reduce dependence on experimental personnel. Establishing a sample database not only provides more comprehensive data support for research but also promotes application and accelerates the development and popularization of technology. Raman and Terahertz spectroscopy technology is user-friendly and simple to use. Combining Raman-Terahertz spectroscopy technology with computer simulation methods has enabled quick and accurate detection of defects in organic and inorganic crystals and has provided detailed atomic structure and electronic property information (Nishizawa et al., 2006). Handheld devices are also available to detect samples with the same accuracy as traditional laboratory analysis methods (Vargas Jentzsch et al., 2016; Molter et al., 2011; Molter et al., 2011). The development of handheld portable integrated testing instruments has emerged as a solution to circumvent the requirements of specialized laboratory conditions and laborious preprocessing procedures. It effectively mitigates the cost and time inefficiencies associated with various laboratory analysis methods, while streamlining the diagnostic process. Early identification of gout stone types and prompt initiation of treatment facilitate inflammation reduction and prevent complications. Therefore, the establishment of a Raman-Terahertz spectrum library in clinical medicine assumes paramount importance. Through this study, we aim to construct a comprehensive stone composition database for *in vitro* detection of urinary system stones. In future endeavors, our

objective is to achieve early detection and diagnosis of urinary system stones and perform gout stone composition analysis using portable instruments, facilitated by urine centrifugation sediment and freeze-drying grinding of solid residue. This approach promises precise and comprehensive diagnoses, along with the exploration of novel clinical applications, thereby enhancing the provision of superior medical services to patients.

Data availability statement

The raw data supporting the conclusions of this article will be made available by the authors, without undue reservation.

Ethics statement

All stone samples are sourced from urinary calculi center of Shanghai Tenth People's Hospital The study protocol was approved by The Shanghai Tenth People's Hospital's Institutional Ethics Committee and was performed in accordance with the Helsinki Declaration.

Author contributions

HL: investigation, collecting samples, writing the original draft. YZ: investigation, processing samples, data processing, writing the original draft. YW: investigation, software. YJ: writing—review and editing. HB: investigation. AP: writing—review and editing. YS: writing—review and editing. All authors contributed to the article and approved the submitted version.

Funding

This research was funded by the National Natural Science Foundation of China (61801329), "Good Physician" Training Program of Yangpu (YP202056), the Natural Fund Project of Shanghai (21ZR1444700), Cross Innovation Science and Education Integration Fund of Shanghai, NSFC grant no. 61988102.

Conflict of interest

The authors declare that the research was conducted in the absence of any commercial or financial relationships that could be construed as a potential conflict of interest.

Publisher's note

All claims expressed in this article are solely those of the authors and do not necessarily represent those of their affiliated organizations, or those of the publisher, the editors and the reviewers. Any product that may be evaluated in this article, or claim that may be made by its manufacturer, is not guaranteed or endorsed by the publisher.

References

Ahmad, M. I., Masood, S., Furlanetto, D. M., and Nicolaou, S. (2021). Urate crystals; beyond joints. *Beyond Joints* 8, 649505. doi:10.3389/fmed.2021.649505

Ajito, K. (2015). Non-destructive terahertz imaging of illicit drugs using spectral fingerprints. *Opt. Express* 5, 2549–1145. doi:10.1364/oe.11.002549

Auner, G. W., Koya, S. K., Huang, C., Broadbent, B., Trexler, M., Auner, Z., et al. (2018). Applications of Raman spectroscopy in cancer diagnosis. *Cancer Metastasis Rev.* 37, 691–717. doi:10.1007/s10555-018-9770-9

Castro-Camus, E., Koch, M., and Mittleman, D. M. (2021). Recent advances in terahertz imaging: 1999 to 2021. *Appl. Phys. B* 128, 12. doi:10.1007/s00340-021-07732-4

Chamorro-Posada, P., Silva-Castro, I., Vázquez-Cabo, J., Martín-Ramos, P., López-Santos, J. M., and Martín-Gil, J. (2016). A study of the far infrared spectrum of N-acetyl-d-glucosamine using THz-TDS, FTIR, and semiempirical quantum chemistry methods. *J. Spectrosc.* 2016, 1–7. doi:10.1155/2016/4058478

Chen, T., Zhang, Q., Li, Z., and Hu, F. (2020). Intermolecular weak interactions of crystalline purine and uric acid investigated by terahertz spectroscopy and theoretical calculation. *J. Luminescence* 223, 117198. doi:10.1016/j.jlumin.2020.117198

Costa-Bauzá, A., Ramis, M., Montesinos, V., Grases, F., Conte, A., Pizá, P., et al. (2007). Type of renal calculi: Variation with age and sex. *World J. Urology* 25, 415–421. doi:10.1007/s00345-007-0177-4

Cui, X., Zhao, Z., Zhang, G., Chen, S., Zhao, Y., and Lu, J. (2018). Analysis and classification of kidney stones based on Raman spectroscopy. *Biomed. Opt. Express* 9, 4175–4183. doi:10.1364/BOE.9.004175

Czarnecki, M. A., Morisawa, Y., Futami, Y., and Ozaki, Y. (2015). Advances in molecular structure and interaction studies using near-infrared spectroscopy. *Chem. Rev.* 115, 9707–9744. doi:10.1021/cr500013u

Dalbeth, N., Frampton, C., Fung, M., Baumgartner, S., Nicolaou, S., and Choi, H. K. (2019). Concurrent validity of provisional remission criteria for gout: A dual-energy CT study. *Arthritis Res. Ther.* 21, 150. doi:10.1186/s13075-019-1941-8

Davies, J., Riede, P., van Langevelde, K., and Teh, J. (2019). Recent developments in advanced imaging in gout. *Ther. Adv. Musculoskelet. Dis.* 11, 1759720X1984442. doi:10.1177/1759720X19844429

Demir, P., and Severcan, F. (2016). Monitoring radiation induced alterations in biological systems, from molecules to tissues, through infrared spectroscopy. *Appl. Spectrosc. Rev.* 51, 839–863. doi:10.1080/05704928.2016.1193813

Esmonde-White, K. A., Cuellar, M., Uerpmann, C., Lenain, B., and Lewis, I. R. (2017). Raman spectroscopy as a process analytical technology for pharmaceutical manufacturing and bioprocessing. *Anal. Bioanal. Chem.* 409, 637–649. doi:10.1007/s00216-016-9824-1

Fernandes, E. D. A., Bergamaschi, S. B., Rodrigues, T. C., Dias, G. C., Malmann, R., Ramos, G. M., et al. (2017). Aspectos relevantes do diagnóstico e seguimento por imagem na gota. *Rev. Bras. Reumatol.* 57, 64–72. doi:10.1016/j.rbr.2016.03.006

Fisang, C., Anding, R., Müller, S. C., Latz, S., and Laube, N. (2015). Urolithiasis-an interdisciplinary diagnostic, therapeutic and secondary preventive challenge. *Dtsch. Arztebl Int.* 112, 83–91. doi:10.3238/arztebl.2015.0083

Gilad, R., Williams, J. C., Usman, K. D., Holland, R., Golan, S., Tor, R., et al. (2017). Interpreting the results of chemical stone analysis in the era of modern stone analysis techniques. *J. Nephrol.* 30, 135–140. doi:10.1007/s40620-016-0274-9

Gowen, A. A., O'Sullivan, C., and O'Donnell, C. P. (2012). Terahertz time domain spectroscopy and imaging: Emerging techniques for food process monitoring and quality control. *Trends Food Sci. Technol.* 25, 40–46. doi:10.1016/j.tifs.2011.12.006

Guo, C., Xu, W., Cai, M., Duan, S., Fu, J., and Zhang, X. (2022). A review: Application of terahertz nondestructive testing technology in electrical insulation materials. *IEEE Access* 10, 121547–121560. doi:10.1109/ACCESS.2022.3222860

Jamrógiewicz, M. (2012). Application of the near-infrared spectroscopy in the pharmaceutical technology. *J. Pharm. Biomed. Analysis* 66, 1–10. doi:10.1016/j.jpba.2012.03.009

Jones, R. R., Hooper, D. C., Zhang, L., Wolverson, D., and Valev, V. K. (2019). Raman techniques: Fundamentals and Frontiers. *Nanoscale Res. Lett.* 14, 231. doi:10.1186/s11671-019-3039-2

Jung, E., Choi, H. J., Lim, M., Kang, H., Park, H., Han, H., et al. (2012). Quantitative analysis of water distribution in human articular cartilage using terahertz time-domain spectroscopy. *Biomed. Opt. Express* 3, 1110–1115. doi:10.1364/BOE.3.001110

Kaeley, G. S., Bakewell, C., and Deodhar, A. (2020). The importance of ultrasound in identifying and differentiating patients with early inflammatory arthritis: A narrative review. *Arthritis Res. Ther.* 22, 1. doi:10.1186/s13075-019-2050-4

Kawase, K., Ogawa, Y., Watanabe, Y., and Inoue, H. (2003). Non-destructive terahertz imaging of illicit drugs using spectral fingerprints. *Opt. Express* 11, 2549–2554. doi:10.1364/OE.11.002549

Lepodise, L. M. (2020). Wide temperature range studies of the low frequency THz spectrum of benzoic acid using FTIR spectroscopy. *Heliyon* 6, e05577. doi:10.1016/j.heliyon.2020.e05577

Manceau, J. M., Nevin, A., Fotakis, C., and Tzortzakis, S. (2008). Terahertz time domain spectroscopy for the analysis of cultural heritage related materials. *Appl. Phys. B* 90, 365–368. doi:10.1007/s00340-008-2933-6

Molter, D., Torosyan, G., Klier, J., Matheis, C., Petermann, C., Duran, S., et al. (2011). Handheld miniature THz ATR module. *IRMMW-THz 2011 - 36th Int. Conf. Infrared, Millim. Terahertz Waves* 2011. doi:10.1109/irmmw-THz.2011.6104947

Molter, D., Torosyan, G., Klier, J., Matheis, C., Petermann, C., Weber, S., et al. (2011). "Handheld miniature THz ATR module," in 2011 International Conference on Infrared, Millimeter, and Terahertz Waves, Houston TX, 2-7 October 2011, 1–2.

Movasaghi, Z., Rehman, S., and Rehman, I. U. (2007). Raman spectroscopy of biological tissues. *Appl. Spectrosc. Rev.* 42, 493–541. doi:10.1080/05704920701551530

Niessink, T., Kuipers, C., de Jong, B. Z., Lenferink, A. T. M., Janssen, M., Jansen, T. L., et al. (2023). Raman hyperspectral imaging detects novel and combinations of crystals in synovial fluids of patients with a swollen joint. *J. Raman Spectrosc.* 54, 47–53. doi:10.1002/jrs.6452

Nishizawa, J.-i., Suto, K., Sasaki, T., Tanabe, T., Tanno, T., Oyama, Y., et al. (2006). GaP Raman Terahertz high accuracy spectrometer and its application to detect organic and inorganic crystalline defects. *Proc. Jpn. Acad. Ser. B* 82, 353–358. doi:10.2183/pjab.82.353

Paraskevaidi, M., Matthew, B. J., Holly, B. J., Hugh, B. J., Thulya, C. P. V., Loren, C., et al. (2021). Clinical applications of infrared and Raman spectroscopy in the fields of cancer and infectious diseases. *Appl. Spectrosc. Rev.* 56, 804–868. doi:10.1080/05704928.2021.1946076

Parthasarathy, P., and Vivekanandan, S. (2018). Urate crystal deposition, prevention and various diagnosis techniques of GOUT arthritis disease: A comprehensive review. *Health Inf. Sci. Syst.* 6, 19. doi:10.1007/s13755-018-0058-9

Perez-Ruiz, F., Dalbeth, N., and Bardin, T. (2015). A review of uric acid, crystal deposition disease, and gout. *Adv. Ther.* 32, 31–41. doi:10.1007/s12325-014-0175-z

Reginato, A. M., Mount, D. B., Yang, I., and Choi, H. K. (2012). The genetics of hyperuricaemia and gout. *Nat. Rev. Rheumatol.* 8, 610–621. doi:10.1038/nrrheum.2012.144

Sakudo, A. (2016). Near-infrared spectroscopy for medical applications: Current status and future perspectives. *Clin. Chim. Acta* 455, 181–188. doi:10.1016/j.cca.2016.02.009

Sandra, T., Milda, P., Arunas, Z., Sonata, V., Vaiva, H., and Valdas, S. (2022). Raman spectroscopy as a non-destructive tool to determine the chemical composition of urinary sediments. *Comptes Rendus Chim.* 25, 73–82. doi:10.5802/crchim.121

Selvaraju, R., Raja, A., and Thiruppathi, G. (2013). Chemical composition and binary mixture of human urinary stones using FT-Raman spectroscopy method. *Spectrochimica Acta Part A Mol. Biomol. Spectrosc.* 114, 650–657. doi:10.1016/j.saa.2013.05.029

Shen, Y.-C., Yang, X.-Y., and Zhang, Z.-J. (2020). Broadband terahertz time-domain spectroscopy and fast FMCW imaging: Principle and applications. *Chin. Phys. B* 29, 078705. doi:10.1088/1674-1056/ab9296

Vargas Jentzsch, P., Torrico-Vallejos, S., Mendieta-Brito, S., Ramos, L. A., and Ciobotă, V. (2016). Detection of counterfeit stevia products using a handheld Raman spectrometer. *Vib. Spectrosc.* 83, 126–131. doi:10.1016/j.vibspec.2016.01.015

Wu, Y., Li, Z., Li, C., Lu, X., Zhang, C., Chen, C. Q., et al. (2016). Exciton–phonon interaction in $Al_{0.4}Ga_{0.6}N/Al_{0.53}Ga_{0.47}N$ multiple quantum wells. *Chin. Phys. B* 25 (8), 087801. doi:10.1088/1674-1056/25/8/087801

Zhang, M., Xiao, W., Zhang, C., and Zhang, L. (2022). Terahertz kerr effect of liquids. *Sensors (Basel)* 22, 9424. doi:10.3390/s22239424

Zhang, Y. (2013). *Detection of kidney stones componets by terahertz time domain spectroscopy*. China: Huazhong University of Science and Technology.

Zhu, W., Sun, Z., Ye, L., Zhang, X., Xing, Y., Zhu, Q., et al. (2022). Preliminary assessment of a portable Raman spectroscopy system for post-operative urinary stone analysis. *World J. Urology* 40, 229–235. doi:10.1007/s00345-021-03838-8

frontiers | Frontiers in Bioengineering and Biotechnology

TYPE Review
PUBLISHED 18 July 2023
DOI 10.3389/fbioe.2023.1219042

OPEN ACCESS

EDITED BY
Junhong Lü,
Chinese Academy of Sciences (CAS), China

REVIEWED BY
Dongshan Wei,
Chinese Academy of Sciences (CAS), China
Yue Wang,
Xi'an University of Technology, China

*CORRESPONDENCE
Jiayu Zhang,
zhangjiayu0615@163.com

†These authors have contributed equally to this work and share first authorship

RECEIVED 08 May 2023
ACCEPTED 12 June 2023
PUBLISHED 18 July 2023

CITATION
Huang S, Deng H, Wei X and Zhang J (2023), Progress in application of terahertz time-domain spectroscopy for pharmaceutical analyses.
Front. Bioeng. Biotechnol. 11:1219042.
doi: 10.3389/fbioe.2023.1219042

Progress in application of terahertz time-domain spectroscopy for pharmaceutical analyses

Shuteng Huang[1†], Hanxiu Deng[1†], Xia Wei[2] and Jiayu Zhang[1*]

[1]School of Pharmacy, Binzhou Medical University, Yantai, China, [2]Shandong Institute for Food and Drug Control, Jinan, China

Terahertz time-domain spectroscopy is an analytical method using terahertz time-domain pulses to study the physical and chemical properties of substances. It has strong potential for application in pharmaceutical analyses as an original non-destructive, efficient and convenient technology for spectral detection. This review briefly introduces the working principle of terahertz time-domain spectroscopy technology, focuses on the research achievements of this technology in analyses of chemical drugs, traditional Chinese medicine and biological drugs in the past decade. We also reveal the scientific feasibility of practical application of terahertz time-domain spectroscopy for pharmaceutical detection. Finally, we discuss the problems in practical application of terahertz time-domain spectroscopy technology, and the prospect of further development of this technology in pharmaceutical analyses. We hope that this review can provide a reference for application of terahertz time-domain spectroscopy technology in pharmaceutical analyses in the future.

KEYWORDS

terahertz time-domain spectroscopy, pharmaceutical analysis, chemical drugs, traditional Chinese medicine, biological drugs, progress in application

1 Introduction

A "terahertz (THz) wave" is a general term for an electromagnetic wave located in the 0.1–10 THz band of the electromagnetic spectrum (Zhang and Xu, 2010). In this band, the corresponding THz wavelength range is 30–3,000 μm, and the corresponding wavenumber range is 3.33–333 cm^{-1}. A THz wave is between a microwave and an infrared wave. The band adjacent to a microwave is called a "submillimeter wave". The band near an infrared wave is called the "far infrared radiation wave" (Zhang and Xu, 2010; He et al., 2006).

THz waves were discovered as early as the 19th century. However, due to the lack of scientific means to generate and detect THz waves, understanding of the THz band was very limited, so the so-called "THz gap" was formed. The generation and detection of THz waves became possible with the emergence of ultrafast laser technology and the development of semiconductor technology. Subsequently, the research, exploration and application of THz waves began. With deepening of understanding of the THz wave, many of its characteristics were revealed. The first characteristic is security. The unit electron energy carried by a THz wave is very low, about 4 meV, which accounts for only 10^{-6} of an X-ray. Thus, a THz wave will not cause damage by ionization if it interacts with substances (Zhang and Xu, 2010). The second characteristic is transience. The pulse width of a THz wave is of the order of picosecond with high temporal resolution, which can be used to study the time-resolved

spectrum of substances (Juliano and Korter, 2013; Pal et al., 2002). The third characteristic is penetrability. A THz wave has excellent penetrability of dielectric materials, such as plastic, cloth and other non-metallic, weakly polar materials (Tao et al., 2020; Nüßler and Jonuscheit, 2020). Hence, a THz wave can be applied in online monitoring of drug quality. The fourth characteristic is coherent measurement. Usually, a THz wave is generated by coherent laser pulses using nonlinear optical effects or dipole oscillations driven by coherent currents. Hence, a THz wave is coherent and can be used to measure the amplitude and phase information of an electric field directly (Zhang and Xu, 2010). The fifth characteristic is fingerprinting. The THz range contains many types of energy levels, such as weak intermolecular interactions (e.g., hydrogen bonds and van der Waals forces), skeleton vibrations of biological macromolecules, rotation and vibrational transitions of dipoles and low-frequency phonon vibrations of lattices. These physical processes endow matter with unique vibration characteristics in the THz band (Qu et al., 2018; Zheng et al., 2012a). With these excellent characteristics, THz technology has been used widely in pharmaceutical analyses (Zheng et al., 2012a), biomedicine (Zheng et al., 2012b) (Yang X. et al., 2016) and other fields.

The common forms of THz spectroscopy technology are divided into terahertz time-domain spectroscopy (THz-TDS) (Zhang and Xu, 2010), time-resolved terahertz spectroscopy (Dressel et al., 2008) and terahertz emission spectroscopy (Kiwa et al., 2003). THz-TDS technology is the most widely studied, and has shown a good prospect of application in pharmaceutical research. This review discusses the application of THz-TDS in analyses of chemical drugs, traditional Chinese medicine (TCM) and biological drugs.

2 THz-TDS technology

THz-TDS technology was first proposed in the 1980s by Auston and colleagues of Bell Laboratory, and was called "coherent far infrared spectroscopy" (Auston et al., 1984). Later, Grischkowky of T.J. Watson Research Center of International Business Machines (IBM) Corporation and others developed this technology, and called it "THz-TDS technology" (Exter et al., 1989a; Exter et al., 1989b).

A typical THz-TDS system consists of four main parts: femtosecond laser, THz emitter, THz detector and the control system for time delay (Figures 1A, B). Different modes of THz-TDS detection can be used for different samples and test requirements, such as transmission type, reflection type and attenuated total reflection type. Transmission THz-TDS is the earliest and most widely used THz-TDS technology among them, and its basic working principle is interesting. Briefly, the femtosecond laser transmitter generates a beam, which is divided into a pump light and probe light through a beam splitter. The pump beam excites a THz emitter to generate a THz time-domain pulse, which is collimated and focused on the sample by a parabolic mirror. Then, the THz pulse carrying the sample information is collimated and refocused onto the THz detector. The probe beam collinear with the THz beam is used to gate the detector and measure the instantaneous THz electric field. A delay stage is used to adjust

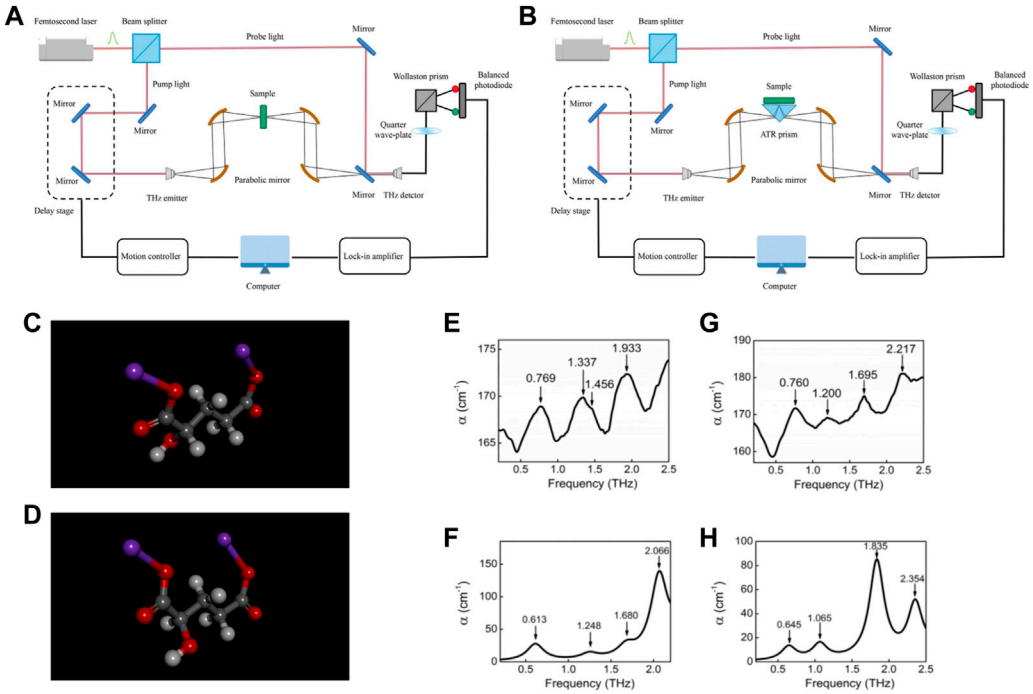

FIGURE 1
Schematics of **(A)** a typical transmission type and **(B)** a typical reflection typeTHz-TDS system. The molecular structure of **(C)** L-2HG and **(D)** D-2HG. White, gray, red, and purple atoms represent H, C, O, Na atoms, respectively. The **(E)** experimental and **(F)** theoretical spectra of L-2HG. The **(G)** experimental and **(H)** theoretical spectra of D-2HG (Chen et al., 2017).

the time delay between the pump beam and probe beam, and allows the THz temporal profile to be sampled iteratively. The time-domain waveform of the THz pulse is obtained by scanning the time delay. Afterwards, the time-domain waveform is amplified by a lock-in amplifier and processed by a computer. After Fourier transform of the waveform, the frequency spectrum of the measured sample can be obtained. Optical parameters (e.g., absorption coefficient, refractive index, and dielectric constant) can be obtained by comparing the changes in the frequency spectrum before and after sample placement.

In most cases, measurement modes for transmission and reflection differ only in that the former receives transmitted pulses, whereas the latter receives reflected pulses. Transmission spectroscopy is limited by the maximum dynamic range, especially if the sample absorbs THz radiation strongly, thereby resulting in a lower depth of penetration. In contrast, reflection spectroscopy is determined by the signal phase and amplitude accuracy rather than the sample. The maximum absorption is dependent upon the signal-to-noise ratio. Thus, transmission type THz-TDS is, in general, used as a conventional method for analyses, whereas the absorbing material is more suitable for detection with reflective THz-TDS. Combination of the advantages of a traditional THz reflection spectrum and attenuated total reflection spectrum (ATR) led to a new detection method to be obtained: attenuated total reflection terahertz time-domain spectroscopy (ATR THz-TDS). This system is constructed by addition of the corresponding lens group and ATR prism module to the THz-TDS system. ATR THz-TDS is used widely for the detection of liquid, powder and film samples, which solves the problem of a polar liquid not being conducive to direct detection of a THz wave due to its strong absorption in the THz band.

3 Application in analyses of chemical drugs

3.1 Qualitative analyses

3.1.1 Analyses of chiral drugs

"Chiral drugs" refer to one pair of enantiomers that have a mirror relationship to each other after introduction of a chiral center into the molecular structure of a drug. Each pair of chemically pure enantiomers has different physical and chemical properties (reflected not only in optical activity), and can be named as "R-type" or "S-type", "D-type" or "L-type", "left-handed" or "right-handed" according to different naming rules. Often, only one is effective, and the other is ineffective (or even toxic) in the two isomers of a drug. For instance, in 1961, thalidomide was recalled due to its intense teratogenic effect. Research showed that, for the thalidomide molecule, the R configuration had a good sedative effect, whereas the S configuration had a strong teratogenic effect. The latter made healthy infants become "seal babies", with deformed limbs, cleft palate, deafness or visceral malformations. The thalidomide incident brought great misfortune to countless families, and the chirality of chemical drugs has aroused wide attention in the pharmaceutical industry.

Several methods are available for analyses of chiral drugs, each of which having superiorities and limitations. Polarimetry is the most commonly used method for the detection of chiral molecules, with the advantages of simple operation and low cost of detection. However, several factors can affect the results of detection: temperature, wavelength of the detection light, and sample impurities. Single-crystal X-ray diffraction (SCXRD) is the most direct and effective method for the analysis of chiral drugs. However, this method requires a large sample size, and high-quality crystals must be cultivated before it can be applied. Often, the cultivation of single crystals is difficult in many practical situations. Chiral Raman spectroscopy has been proposed to identify chiral centers derived by deuterium atoms, fluorine atoms and methyl atoms (Simmen et al., 2012), but the high intensity of the Raman laser can damage (or even denature) the sample. High-performance liquid chromatography (HPLC) is a commonly method for analyzing compounds. Nevertheless, in general it is not used for the identification of chiral drugs because the specificity of this technology is not sufficiently high, and only the retention time can be used to identify the substance. Electronic circular dichroism requires samples only at a microgram level to determine its chiral structure, but also necessitates chiral compounds to contain at least one chromophore. Therefore, exploration of a rapid, nondestructive and efficient method for the detection of chiral drugs is needed.

The chemical bonds and functional groups in chiral compounds are identical, but the rotation direction and corresponding vibration rotation frequency are different. THz wave is sensitive to this difference, so it can be used to identify chiral compounds accurately. For instance, 2-Hydroxyglutaric acid disodium salt (2HG) is a unique biomarker present in gliomas (Esmaeili et al., 2013). 2HG can be used to recognize cancer development and identify the boundary between healthy tissue and cancerous tissue. However, the most efficient method of detection for 2HG is magnetic resonance spectroscopy (Zhou et al., 2011; Server et al., 2010), the testing time of which is ≥ 20 min. Chen et al. used THz-TDS technology to study the characteristic peaks of two isomers of 2-HG (L-type and D-type) in the 0.5–2.5 THz band (Figures 1C, D) (Chen et al., 2017). The characteristic peaks of these two compounds were obviously different, which were very easy to distinguish. Combining the density functional theory (DFT) (B3LYP theory and 6-311+G (*d*, *p*) basis set) function in Gaussian software, they calculated the THz absorption spectra and analyzed their corresponding relationship with molecular functional groups, which agreed well with experimental results (Figures 1E–H). According to the results of theoretical calculation, they determined the origin of these absorption peaks (Table 1). The peak at 0.769 THz of L-2HG is highly similar to 0.760 THz of D-2HG, which was caused by their highly similar vibration mode: the torsion of the whole carbon chain dominated by the butyrate group (Figures 2a1, b1). The extensional motion of the whole carbon chain, based on the to-and-fro vibration of the butyrate group, caused the formation of absorption peaks at 1.337 THz of L-2HG (Figures 2a2); the vibration modes of D-2HG at 1.200 THz were not only included the formation factors of L-2HG at 1.337 THz, but also included the aggressive torsion of the butyrate group (Figures 2b2).

Briefy, the same dominant functional groups determined their THz absorption peaks were closed to each other, while the diferent vibrational modes led to the variation in the waveform and amplitude. When the dominant functional groups were diferent,

10.3389/fbioe.2023.1219042

TABLE 1 The list of absorption peaks of L-2HG and D-2HG.

L-2HG	Simulation	D-2HG	Simulation	Experimental deviation between L-2HG and D-2HG	Analysis
Frequency (THz)					
0.769	0.613	0.760	0.645	0.009	the torsion of the whole carbon chain
1.137	1.248	1.200	1.065	0.137	Vibration and aggressively torsion of carbon chain
1.456	1.680	1.695	1.835	0.239	torsion and vibration of the ring
1.933	2.066	2.217	2.354	0.284	concertina movement of the whole ring

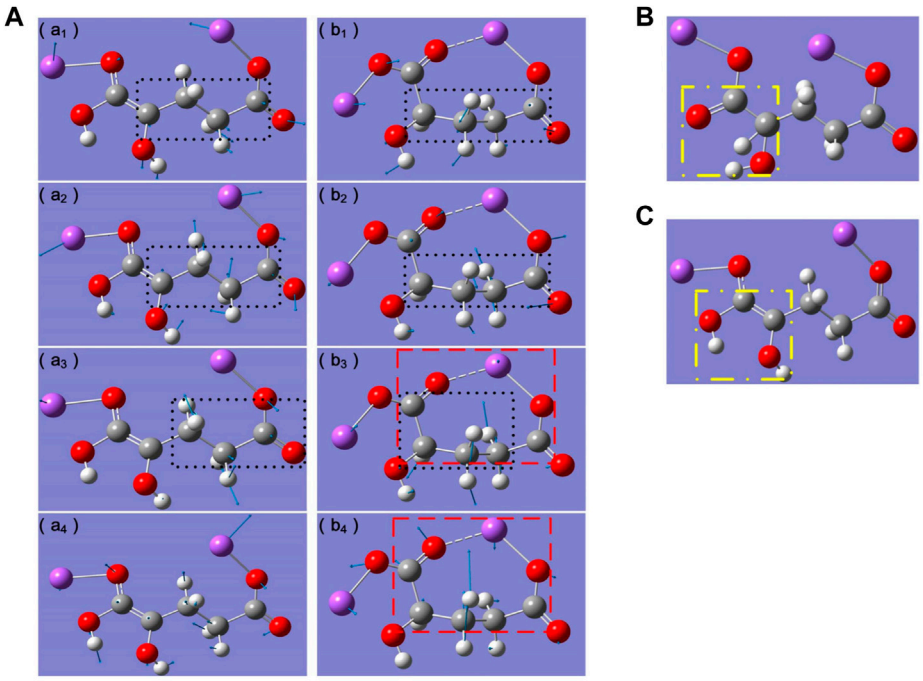

FIGURE 2
(A) Vibration modes of absorption peaks of (a1-a4) L-2HG and (b1-b4) D-2HG. (a1) 0.769 THz, (a2) 1.337 THz, (a3) 1.456 THz, (a4) 1.933 THz, (b1) 0.760 THz, (b2) 1.200 THz, (b3) 1.695 THz, (b2) 2.217 THz. White, gray, red, and purple atoms represent H, C, O, Na atoms, respectively. Blue arrows indicate the vibrational direction of atom. Black dotted boxes refer to the dominant functional groups in the vibration modes. Red dashed boxes indicate the entire molecular vibrational ring. The molecular structure of L-2HG **(B)** before and **(C)** after the structure optimization. The yellow dashed boxes indicate the transfer of the proton (hydrogen atom) (Chen et al., 2017).

the corresponding THz absorption peaks would have large differences. For example, the peak at 1.456 THz of L-2HG was caused by rotation of the propyl group (Figures 2a3), while the torsion and vibration of the ring affected by the butyrate group formed the peak at 1.695 THz (Figures 2b3). In addition, compared with the strong contractions of the whole ring resulted in the peak at 2.217 THz of D-2HG (Figures 2b4), the peak at 1.933 THz of L-2HG was completely caused by the up and down vibration of the whole carbon chain (Figures 2a4). Furthermore, based on the DFT analysis, they deduced that the differences between isomers absorption peaks originated from the proton transfer (hydrogen atom) in molecular structure (Figures 2B, C). In the case of L-2HG, during the process of molecular structure optimization, both the carbon hydrogen bond in the sodium hydroxyacetate group and the carbon oxygen double bonds were broken. As a result, two carbon atoms both had a lone pair electron, which then formed a new carbon-carbon double bond. At the same time, the hydrogen atom combined with carbonyl oxygen to form a new hydroxyl, i.e., finished the process of proton transfer. While in the case of D-2HG, the carbon chain was "sofer" than that of L-2HG, i.e., itself had a stable molecular vibrational ring, which determined no subsequent bond cleavage and the final proton transfer would happen.

In summary, the large differences of the isomer between L-2HG and D-2HG were attributed mainly to their structures: the carbon

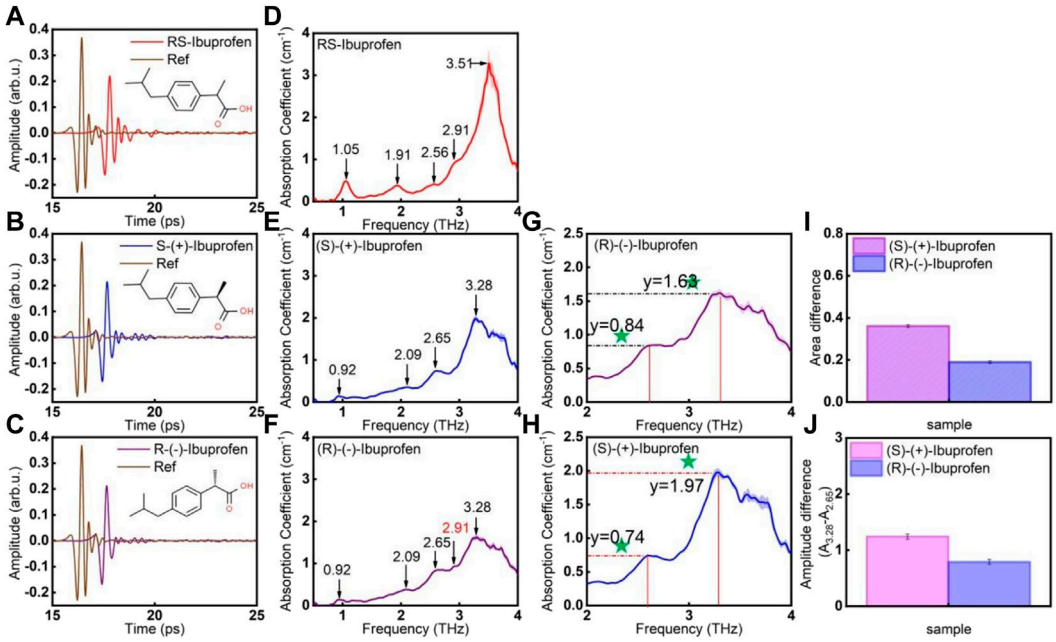

FIGURE 3
THz spectra of RS-ibuprofen, (R)-(−)-ibuprofen, (S)-(+)-ibuprofen. The THz-TDS of **(A)** RS-ibuprofen, **(B)** (R)-(−)-ibuprofen, and **(C)** (S)-(+)-ibuprofen. **(D–F)**. THz absorption spectra obtained by using **(A–C)** through fast Fourier transform. **(G,H)**. (R)-(−)-ibuprofen and (S)-(+)-ibuprofen frequency points and amplitude information graphs, **(I)**. The difference of the area under the absorption peak of 3.28 THz, **(J)**. The difference in the absorption amplitude at the absorption peak of 3.28 THz and 2.65 THz. Error bars are labelled in each figure (Wang et al., 2021).

chain of D-2HG was more flexible than L-2HG and a ring structure could be formed readily during vibration. The vibration modes of L-2HG were the torsion and swing of the carbon chain caused by proton transfer. The research stated above reflected the speed and accuracy of THz-TDS, which is crucial for the identification and analyses of drugs, as well as the further application of THz-TDS in surgery and imaging research.

Ibuprofen is a common non-steroidal anti-inflammatory drug. It has three enantiomers: RS-ibuprofen, (R)-(−)-ibuprofen and (S)-(+)-ibuprofen. Taking ibuprofen as an example, Wang et al. proposed a THz-TDS method for qualitative identification of chiral drugs from three aspects: characteristic peak frequencies, differences in peak amplitude and differences in peak area (Figure 3) (Wang et al., 2021). Here, the amplitude of the characteristic peak was determined by the highest point of the absorbance within the frequency range of the characteristic peak. The range of the area under the peak was determined by the minimum point of the first derivative of the absorbance within the frequency range of the characteristic peak. Simultaneously, to ascertain if this method was suitable for identification of other chiral substances, they also tested the THz spectra of two other chiral substances: carnitine (D-carnitine, L-carnitine) and methylbenzylamine (R-methylbenzylamine, S-methylbenzylamine). Experimental results indicated that the proposed method could distinguish the enantiomers of various drug molecules accurately.

Trehalose is a non-reducing sugar and has been shown to act against oxidative stress, heat shock and harmful chemicals. Huang et al. used THz-TDS technology and Fourier transform infrared (FTIR) spectroscopy to study three optical isomers of trehalosin: α,α-, α,β-, and β,β-trehalosin (Huang L. et al., 2020). Significant differences were observed in the THz absorption spectra between the three optical isomers of trehalose, thereby demonstrating that THz detection was a good method for distinguishing between trehalose isomers. The three isomers of trehalose were not distinguishable using infrared spectroscopy, but were distinguishable by THZ spectroscopy. For conventional infrared spectra, the chemical formula of the entire molecule is deduced mainly by testing the characteristic peaks of molecular bonds and functional groups. However, for chiral molecules, their chemical bonds and functional groups are completely consistent and cannot be identified.

Amino acids can be classified as α-, β-, γ-, and so on depending on where the amino group is attached to the carbon chain. However, the amino acids obtained by proteolysis are all α-amino acids, and there are 22 types of them, which are the basic units of proteins. Pan studied 20 chiral α-amino acids systematically using THz-TDS technology (Pan, 2017). In addition to glycine, each amino acid has three configurations (L-type, D-type and DL-racemic), and 59 different amino acids are available. Pan obtained the characteristic fingerprint spectra of these compounds in the range 0.5–4.5 THz and some amino acids to 4.75 THz. Amino acids were classified based on the different functional groups of these 20 chiral α-amino acids. The THz spectra of these amino acids with different configurations were compared systematically, which verified and supplemented the data detailed previously.

Fodostein is a typical chiral drug whose enantiomers are L-fodostein and D-fodostein. Among them, L-fodostein has

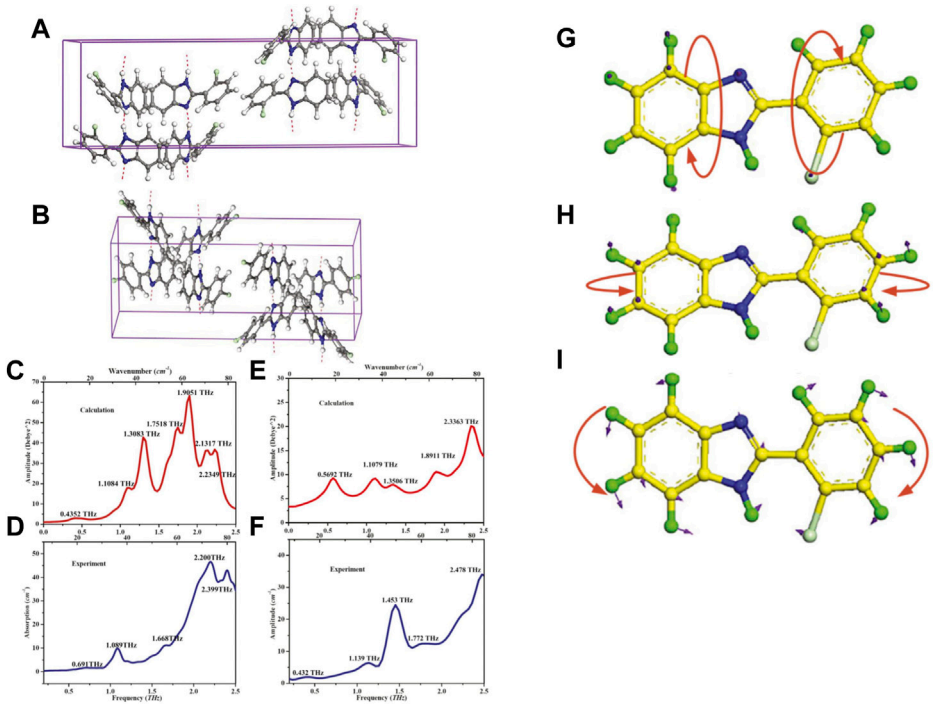

FIGURE 4
The crystal cells and the most relevant hydrogen-bonding interactions within the unit cell of **(A)** 2CPBI and **(B)** 4CPBI. The **(C)** theoretical and **(D)** experimental spectra of 2CPBI. The **(E)** theoretical and **(F)** experimental spectra of 4CPBI. The isolated-molecule motions of 2CPBI: **(G)** Out-of-plane twisting. **(H)** Out-of-plane bending. **(I)** In-plane rocking (Song et al., 2018).

pharmacological activity, whereas D-fodostein has no biological activity. The racemate DL-fodostein is one pair of enantiomers (L- and D-fodostein) that coexist in equal quantities in the lattice. Zhao et al. studied L- and DL-Fodostein by THz-TDS technology at the 0.2–2.0 THz band (Pan, 2017; Zhao et al., 2011). The absorption spectra of L- and DL-Fodostein showed significant differences in terms of the intensity and location of the absorption peaks. These experimental results indicated that THz-TDS technology could be used to identify the chiral characteristics of substances accurately, which provides a new method for the identification of chiral drugs.

3.1.2 Analyses of structural analogs

Structural analogs have the same or similar parent nucleus. Usually, the difference among these analogs is limited to the composition or location of several different branch chains. These subtle differences in structure mean that infrared spectroscopy, Raman spectroscopy and even mass spectrometry often fail to distinguish these structural analogs. However, THz wave is very sensitive to these subtle structural changes, which is an advantage of this technology for identifying structural analogs.

Benzimidazoles are an important group of heterocyclic compounds. Benzimidazole derivatives have antimicrobial (Ozkay et al., 2010), antioxidant (Gurer-Orhan et al., 2006) and antihypertensive (Rakesh et al., 2006) activities. Song et al. systematically studied the difference between 2-(2-chlorophenyl) benzimidazole (2CPBI) and 2-(4-chlorophenyl) benzimidazole (4CPBI) using THz-TDS technology (Song et al., 2018). The only difference in their molecular configurations was the arrangement of chlorine on the chlorophenyl ring. However, their THz absorption spectra had distinctive differences in the range 0.2–2.5 THz, including the amplitude and frequency position of the absorption peak. In order to confirm the experimental results and analyze the mechanism of all vibrational modes in absorption spectra, DFT calculations were performed using the programs Gaussian03 (B3LYP theory and 6-311+G (*d*, *p*) basis set). In order to gain the more accurate simulated results, isolated-molecule calculations were also performed employing the DMol3 approach. Figure 4 illustrated the crystal cells and the most relevant hydrogen-bonding interactions within the unit cell of 2CPBI and 4CPBI. The crystalline solid of 2CPBI and 4CPBI were downloaded from the Cambridge Crystallographic Data Centre (CCDC). All of vibrational modes of 2CPBI and 4CPBI were analyzed according to the combination of solid-state and isolated-molecule calculations and described in Table 2. The simulation results of DFT confirmed the validity of experimental results, and suggested that these differences originated from the different van der Waals forces and different dihedral angles of molecules within a crystal cell.

Monosaccharides can be classified as triose, tetrose, pentose, hexose and heptose according to the number of carbon atoms. Among them, pentose and hexose contain similar five-membered rings and six-membered rings, respectively, so carbohydrate compounds often have obvious structural similarity. Chen et al. measured the THz absorption spectra of two typical monosaccharides and disaccharides (D-glucose and lactose monohydrate) with similar structures at the 0.3–1.7 THz band by THz-TDS technology, and obtained their spectral data in this THz

TABLE 2 Vibrational modes of 2CPBI and 4CPBI.

Mode	Exp.	Simu.		Description
	Fre	Fre.	Int.	
2CPBI				
a	0.691	0.4352	3.204	75% optical translation along *x* axis and 20% rocking of chlorophenyl ring in plane and 5% bending of whole molecule out of plane
b	1.089	1.1084	17.983	80% twisting of whole molecule and 10% bending of benzimidazole out of plane and 10% rocking of chlorophenyl ring in plane
c	1.466	1.3083	43.041	70% bending of benzimidazole and 20% twisting of chlorophenyl ring out of plane and 10% rocking of chlorophenyl ring in plane
d	1.668	1.7518	47.959	60% bending of chlorophenyl ring and 30% twisting of benzimidazole out of plane and 10% rocking of benzimidazole in plane
e	2.048	1.9051	63.117	75% bending and 20% twisting of whole molecule out of plane and 5% rocking of benzimidazole in plane
f	2.2	2.1317	36.632	50% twisting of chlorophenyl ring and 30% bending of benzimidazole out of plane and 20% rocking of whole molecule in plane
g	2.399	2.2349	36.863	50% bending and 25% twisting of whole molecule out of plane and 25% rocking of benzimidazole in plane
4CPBI				
a	0.432	0.5692	9.136	60% optical translation along *y* axis and 30% twisting of chlorophenyl ring out of plane and 10% rocking of chlorophenyl ring in plane
b	1.139	1.1079	9.114	60% twisting of whole molecule and 10% bending of chlorophenyl ring out of plane and 30% rocking of benzimidazole in plane
c	1.453	1.3506	7.833	80% rocking of whole molecule in plane and 10% bending of benzimidazole and 10% twisting of chlorophenyl ring out of plane
d	1.772	1.8911	10.515	50% bending of benzimidazole and 10% twisting of chlorophenyl ring out of plane and 40% rocking of chlorophenyl ring in plane
e	2.478	2.3363	20.006	70% twisting of whole molecule and 20% bending of benzimidazole out of plane and 10% rocking of whole molecule in plane

frequency range (Chen et al., 2019). Although the composition of lactose contains glucose, THz wave was very sensitive to the structural changes of carbohydrate molecules, and the two substances showed different THz fingerprint absorption characteristics in the measured THz frequency band. The vibration frequencies of monomolecular and multimolecular configurations of two types of sugars in the THz band were calculated by DFT. Combination of the molecular vibration form displayed by GaussView and the potential energy distribution (PED) analytical method of decomposition of normal vibration mode enabled the contribution of the characteristic vibration mode from each group to be observed more intuitively. Reduced density gradient (RDG) analyses were undertaken using software (Multiwfn and VMD) and the position, type and intensity of the interaction between D-glucose and lactose visualized. The characteristic absorption peaks of these two substances in the THz band were shown to be derived mainly from the collective vibration mode dominated by the network of intermolecular hydrogen bonds.

Nucleosides are formed by condensation of a purine base or pyrimidine base with ribose or deoxyribose, which results in strong structural similarities between the different nucleosides. Wang et al. studied the THz spectra of four DNA nucleosides (adenosine, thymidine, cytidine and guanosine) and two guanosine derivatives (ribavirin and entecavir (reported for the first time)) experimentally in a wide spectral region of 1–10 THz (Wang F. et al., 2022). Significant spectral differences between the four DNA nucleosides were noted, as well as between ribavirin and entecavir. Their lattice energy, geometric structure and vibration spectra were analyzed theoretically by a generalized energy-based fragmentation approach under periodic boundary conditions and DFT. Experimental and calculated THz vibrational frequencies and corresponding vibrational modes for Adenosine and Thymidine were summarized in Table 3. PED and RDG methods combined with visualization software revealed all the weak interaction positions, intensities and contribution rates in the THz spectrum (Figures 5A–D). To understand the influence of structural differences on the spectrum, taking guanine, guanosine, ribavirin and entecavir as examples, the effects of substituents at different positions on THz spectra were studied. Results confirmed that through the weak interaction position, the correlation between structure and the spectrum could be judged accurately. This research could lay a foundation for crystal engineering, supramolecular chemistry, molecular recognition and self-assembly and protein–ligand interactions.

Antibiotics can be classified in many ways according to the different purposes of classification. According to a difference in chemical structure, antibiotics can be divided into quinolones, β-lactam and macrolides. Antibiotics under the same category have an identical or similar parent nucleus. As a result, the structures of some antibiotics are very similar. Xu et al. used THz-TDS technology to analyze the spectra of two groups of structural analogs (amoxicillin and penicillin sodium, cefadroxil and cefradine), and obtained their absorption spectra in the 0.2–1.7 THz band (Xu et al., 2012). The four antibiotics had obvious characteristic absorption peaks in the THz band, which could be used as the fingerprint spectrum in the THz band for identification of drug molecules. Dai et al. used THz-TDS technology to measure the spectra of six β-lactam antibiotics (penicillin sodium, cefuroxime sodium, cefotaxime sodium, ceftriaxone sodium, ceftazidime and aztreonam) in the band of 0.2–2.5 THz (Dai et al., 2013). Although these drugs had

10.3389/fbioe.2023.1219042

TABLE 3 Experimental and calculated THz vibrational frequencies and corresponding vibrational modes for Adenosine and Thymidine.

Peaks		Main vibrational modes	Description
Exp.	Cal.		
Adenosine			
1.96	1.83	Collective vibration	D (92.8%), A (2.8%), R (2.7%), L (1.7%)
2.75	2.61	Collective vibration	D (93.3%), A (2.0%), R (3.4%), L (1.3%)
3.01	2.83	Collective vibration	D (94.3%), A (4.2%), R (1.1%), L (0.4%)
3.33	3.11	Collective vibration	D (96.3%), A (1.4%), R (1.6%), L (0.7%)
4.42	4.48	Collective vibration	D (95.4%), A (2.0%), R (1.9%), L (0.7%)
5.03	5.33	Collective vibration	D (96.9%), A (2.6%), R (0.5%), L (0.0%)
6.21	6.26	Partial vibration	D (97.9%), A (1.3%), R (0.8%), L (0.0%)
6.76	6.99	Partial vibration	D (98.9%), A (1.1%), R (0.0%), L (0.0%)
	8.64	Partial vibration	D (83.5%), A (11.2%), R (5%), L (0.3%)
	9.81	Partial vibration	D (94.2%), A (5.4%), R (0.0%), L (0.4%)
Thymidine			
1.34	1.14	Collective vibration	D (96.9%), A (1.3%), R (0.9%), L (0.9%)
1.66	1.66	Collective vibration	D (98.0%), A (0.0%), R (2.0%), L (0.0%)
2.16	2.13	Collective vibration	D (92.7%), A (2.0%), R (3.9%), L (1.4%)
2.54			
3.07	3.01	Collective vibration	D (97.4%), A (0.8%), R (0.8%), L (1.0%)
3.66	3.36	Collective vibration	D (94.4%), A (0.4%), R (4.1%), L (1.1%)
4.65	4.36	Collective vibration	D (95.4%), A (0.6%), R (2.9%), L (1.1%)
5.12	4.95	Collective vibration	D (93.5%), A (1.5%), R (5.0%), L (0.0%)
5.53	5.27	Collective vibration	D (86.2%), A (5.6%), R (6.6%), L (1.6%)
6.08	5.85	Collective vibration	D (96.6%), A (1.1%), R (1.8%), L (0.5%)
8.18	7.94	Partial vibration	D (92.6%), A (5.1%), R (2.3%), L (0.0%)
	8.43	Partial vibration	D (97.1%), A (1.1%), R (1.8%), L (0.0%)
	8.87	Partial vibration	D (92.0%), A (6.5%), R (1.5%), L (0.0%)
	9.31	Partial vibration	D (94.8%), A (4.1%), R (0.8%), L (0.3%)

D, Out-of-plane bending; A, In-plane bending; R, In-plane stretching; L, Deformation vibration.

similar molecular structures, their THz spectra had significantly different characteristics.

Usually, drugs of the same parent type of nucleus have similar pharmacological effects. For example, vudine drugs are, in general, used to treat diseases caused by retrovirus. Zhao et al. analyzed two vudine drugs (zidovudine and stavudine) in the band of 0.2–1.8 THz by THz-TDS technology (Zhao et al., 2014). The hybrid density function B3LYP and Gaussian-type basis set 6-311G (*d*, *p*) were chosen to perform all the theoretical simulations of their unimolecule structures and crystal structures. Although these two vudine drugs had similar molecular structures, there were differences in their absorption spectra (especially in the location and height of the absorption peaks). The unimolecule structural simulation predicted partial experimental characteristic peaks, while the crystal structural simulation predicted all the experimental characteristic peaks within 0.2–1.8 THz which was clearly better than the results of the unimolecule simulation.

3.1.3 Analyses of drugs with crystal forms

The solid (crystal) form of a drug affects the physical and chemical properties of the active pharmaceutical ingredient (API) to some extent, such as stability, solubility and bioavailability, and then influences the efficacy and quality of the drug (Qiao et al., 2011). In addition, different solid forms of drugs have different particle properties, and these properties also have a certain impact on the quality of drugs (Chen et al., 2011). Therefore, the crystal form of the drug has become an important factor in drug development (Cho et al., 2010).

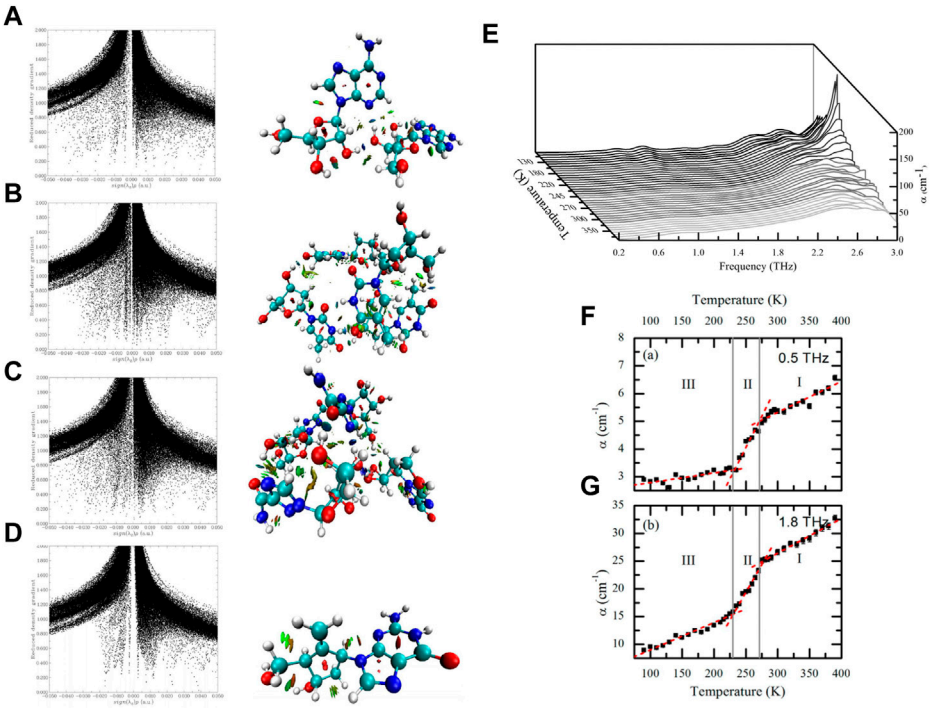

FIGURE 5
The scatter diagram of RDG *versus* sign (λ2)*ρ and RDG isosurface map corresponded to **(A)** Adenosine, **(B)** Thymidine, **(C)** Ribavirin, **(D)** Entecavir, respectively (Wang F. et al., 2022). **(E)** Waterfall plot showing terahertz absorption spectra of simvastatin from 90 to 390 K. The temperature increment between spectra is 10 K from 80 to 210 K and 290–390 K, and 5 K from 210 to 290 K. **(F)** Absorption coefficient at 0.5 THz, **(G)** absorption coefficient at 1.8 THz. Red dashed lines represent best fit linear plots. Gray vertical lines indicate the DSC derived phase transition temperatures of 230.9 and 270.7 K and separate the different polymorphic forms indicated by III, II, and I. Error bars represent standard errors reflecting both the uncertainty in sample thickness and the noise estimate based on the averaging data obtained from measurements of three samples, with 120 waveforms obtained at each temperature point per sample (Tan and Zeitler, 2015).

The main methods used to detect the crystal form of drugs are SCXRD, infrared (IR) spectroscopy, Raman spectroscopy, solid-state nuclear magnetic resonance spectroscopy, differential scanning calorimetry (DSC), and thermogravimetric analysis (TGA). However, each individual technology has its limitations. SCXRD technology is a time-consuming process that requires complex preparation of samples, so it cannot be monitored online readily or directly. In Raman spectra, compounds carry the risk of phase transitions and unwanted photochemical reactions due to the need for high-energy laser irradiation. DSC and TGA technologies require high temperatures to destroy samples and cannot be used to obtain information about sample structure. Therefore, a more convenient, accurate and non-destructive detection method for identification of the crystal form of drug is needed.

Given the high sensitivity of THz-TDS technology to intermolecular interactions, it can be used to study vibrational motions within crystal lattices, which include lattice phonon vibrations and intramolecular vibrations. These vibrational motions are heavily influenced by the arrangements and orientations of individual molecules within the crystal lattice. Hence, THz-TDS has demonstrated great utility in the study of polymorphs, being able to differentiate polymorphs arising from changes in lattice packing (Strachan et al., 2004; Zeitler et al., 2007), as well as changes in molecular conformation (Delaney et al., 2012a) (Delaney et al., 2012b). The solid drug forms mainly include polymorphism, hydrate and co-crystal (Gao et al., 2010). This type of research usually combines X-ray diffraction (XRD), nuclear magnetic resonance spectroscopy and other methods to determine the crystal form of the raw material in the experiment.

3.1.3.1 Polymorphism

Under the influence of different physical and chemical environments, the order of arrangement in the drug lattice will be different, resulting in the phenomenon of different crystal structures, which is called "polymorphism" (Ferrari et al., 2003). Approximately 40% of drugs in clinical use have polymorphic forms (Wang, 2005), and various forms of drugs, in general, have different physical and chemical properties (Zhou et al., 2010). Polymorphism affects drugs in terms of the dissolution rate, side-effects and bioavailability, so the detection and control of API polymorphism has become an important part of the development, production and storage of drugs (Rodríguez-Molina et al., 2013).

Simvastatin is a major member of the statin family that is used widely to treat hypercholesterolemia (Stancu and Sima, 2001). Simvastatin is sold as a generic after patents expired in 2006, and is listed on the list of essential medicines set by the World Health Organization. Tan et al. utilized THz-TDS technology to characterize each of the polymorphs of

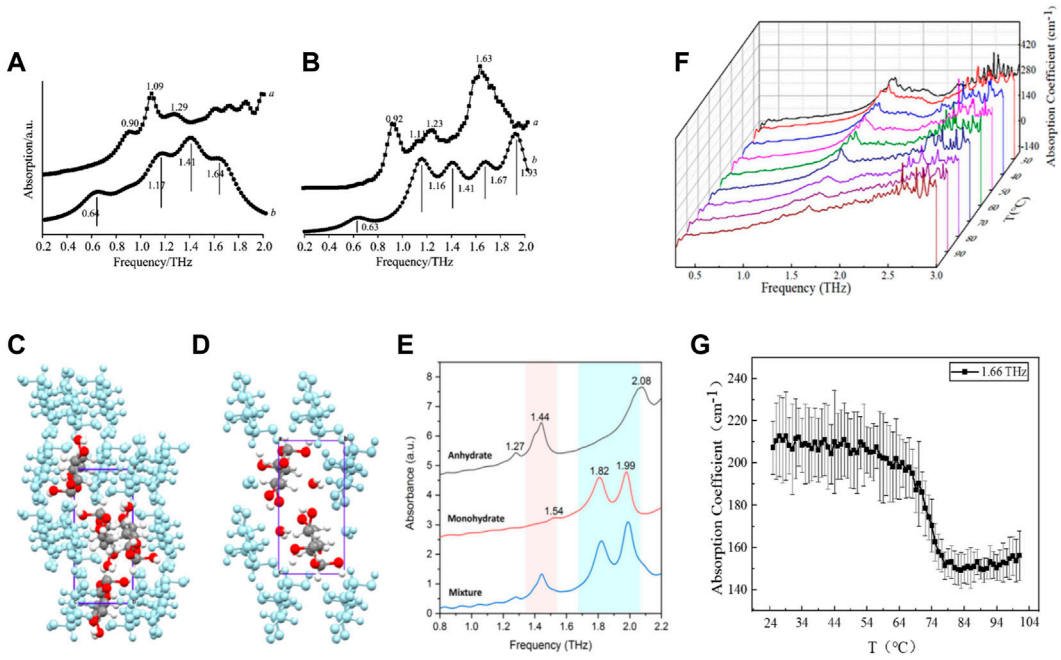

FIGURE 6
(A) Comparison of **(A)** experimental and **(B)** theoretical THz spectra of form I of chlorpropamide. **(B)** Comparison of **(A)** experimental and **(B)** theoretical THz spectra of form III of chlorpropamide (Fang et al., 2016). Molecular packing of **(C)** glucose anhydrate and **(D)** glucose monohydrate. **(E)** THz signatures of glucose anhydrate, monohydrate and their mixture in 0.8–2.2 THz (Yan et al., 2021). **(F)** Waterfall plot of THz absorption spectra of LC tetrahydrate at 25°C–100°C. **(G)** Variation of absorption coefficient of LC tetrahydrate with temperature at 1.66 THz (Gao et al., 2022).

TABLE 4 Comparison and assignment of major bands of terahertz spectra of theoretical spectrum and experimental spectrum of chlorpropamide polymorphs.

No	Peaks		Deviation	Description
	Exp.	Cal.		
I-a	0.90	1.17	0.27	δR-S-N-C-N-C-C-C
I-b	1.09	1.41	0.32	ωC-C-C
I-c	1.29	1.64	0.35	ωR; ωC-C-C
III-a	0.92	1.16	0.24	δR-S-N-C-N-C-C-C
III-b	1.11	1.41	0.30	ωR; ωC-C-C
III-c	1.23	1.67	0.44	ωR; ωN-C=O; ωC-C-C; τSO_2
III-d	1.63	1.93	0.30	δN-C-N-C-C; τR-S-C=O

δ, scissor; ω, out-of-plane bending; τ, twisting, def-torsion.

simvastatin and probe its phase transitions in the range 0.2–3.0 THz and for temperatures ranging from 90 K to 390 K (Figures 5E–G) (Tan and Zeitler, 2015). They found that the degree of rotational freedom of the ester tail increased with increasing temperature; changes in the rotational freedom of the ester tail governed the polymorphism of simvastatin. That study benefited from the advantages of THz-TDS technology, such as non-destruction of the sample and sensitivity to temperature changes, which can be used to measure a single sample over a wide range of temperatures.

Chlorpropamide is used mainly in the treatment of mild and moderate maturity-onset diabetes mellitus as a promoter of insulin secretion. Fang et al. used THz-TDS technology to characterize form I and form III of chloropropemide in the 0.2–1.8 THz band at room temperature (Fang et al., 2016). Form I had characteristic peaks at 0.90, 1.09 and 1.29 THz, whereas form III had characteristic peaks at 0.92, 1.11, 1.23 and 1.63 THz, with the strong peak at 1.63 THz being obviously different from peaks seen in form I. DFT was used to calculate the two forms of chlorpropamide, and the results of calculation were in good agreement with experimental data (Figures 6A, B). Table 4 summarized the assignment of major bands of THz spectra of theoretical spectrum and experimental spectrum of chlorpropamide form I and form III. Calculation results showed that the multimolecular vibration modes of form I and form III at 0.9 THz and 1.1 THz were identical, which could provide a reference for the attribution of THz absorption peaks of chlorpropamide in other forms.

Sulfamethoxazole (SMX) is a well-known, efficacious and tolerable antibacterial agent. It is used widely to treat infections of the urinary tract, respiratory system and intestine caused by sensitive bacteria. Du et al. measured the spectra of two polymorphic forms of SMX at room temperature and in the range of 0.2–1.5 THz by THz-TDS technology (Du et al., 2014). Form I had absorption peaks at 0.74, 1.02 and 1.25 THz, which were consistent with the absorption peaks of raw SMX. Form II had absorption peaks at 1.04 and 1.44 THz. Hence, the raw materials used in this medicine were usually present in polymorphic form I.

Maleic hydrazide (MH), also known as 3,6-Pyridazine diol, is used primarily as a selective herbicide and temporary inhibitor of plant growth. Zheng et al. used the THz-TDS system to test the

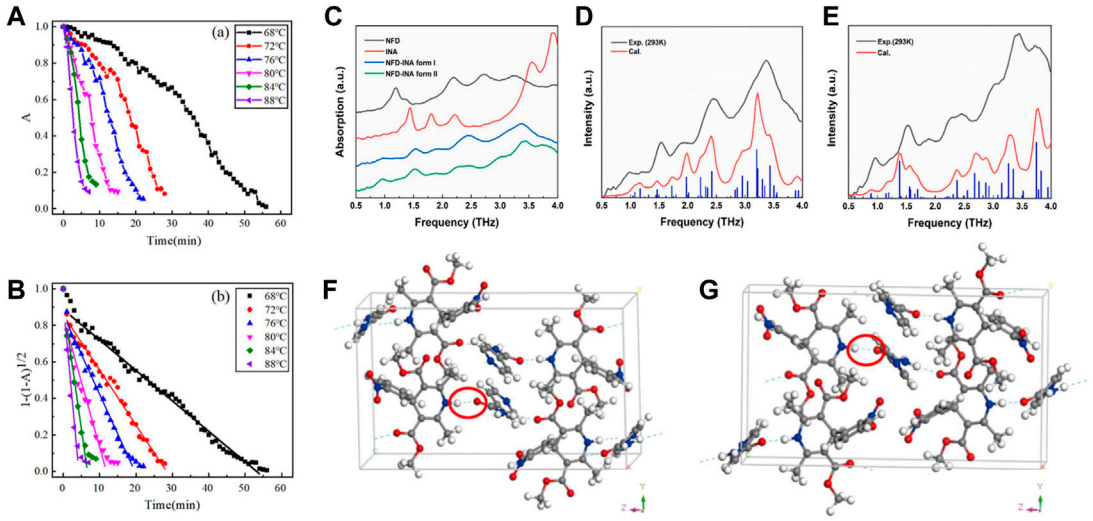

FIGURE 7
(A) Variation of the normalized THz absorption peak area with the heating time at different temperatures. **(B)** Plot and fitting curves according to the contraction area equation (Gao et al., 2022). **(C)** The THz spectra of NFD-INA cocrystal form I (blue line), form II (green line) and their parent constituents, NFD (black line) and INA (red line) in the frequency range of 0.5–4.0 THz. The experimental (black curve) and calculated (red curve) THz spectra of **(D)** form I and **(E)** form II of NFD-INA cocrystal in the frequency range of 0.5–4.0 THz. The hydrogen bond networks (blue dash lines) of **(F)** form I and **(G)** form II for NFD-INA cocrystal (Wang P. F. et al., 2022).

absorption spectra of the polymorphic forms of MH (MH2 and MH3) in the range 0.25–2.25 THz at room temperature (Zheng et al., 2022). The THz-fingerprint information of the two polymorphisms was completely different. MH2 had three characteristic absorption peaks, which were located at 0.34, 1.41 and 1.76 THz, respectively. MH3 had two characteristic absorption peaks, located at 0.75 and 1.86 THz, respectively. Results confirmed that the polymorphisms of MH could be distinguished by THz-TDS technology. They ascertained the THz spectrum of the commercial drug MH, and found that its absorption peak matched the characteristic peak of MH3, which indicated that its main component was MH3. Those studies indicated that research of the THz spectra of drugs with polymorphisms had practical importance for the identification of polymorphic drugs and revelation of the biochemical functions of drugs.

3.1.3.2 Hydrate

"Hydrate" refers to the new crystal form formed by water molecules entering the internal structure of the crystal form of a drug and forming hydrogen bonds with the molecules of the original crystal form. Hydrates may elicit different properties, and usually the physical and chemical properties of different crystal forms of the same hydrate are different. The most typical case is the carbamazepine incident in 1993. Carbamazepine in tablets was converted from anhydrous to hydrate due to becoming damp during storage, which resulted in a significant reduction in its efficacy and, eventually, the drug was withdrawn from the market. Therefore, the formation of hydrate is a focus of the monitoring of drug quality.

Glucose is a commonly used drug in clinical practice. Low-concentration glucose can be used as a medium for intravenous infusion of many drugs. High-concentration glucose can be used for the treatment of hyperkalemia and hypoglycemia. Yan et al. studied the characteristic absorption peaks of anhydrous glucose and monohydrate glucose in the 0.8–2.2 THz band by THz-TDS technology (Figures 6C–E) (Yan et al., 2021). Anhydrous glucose had a weak absorption peak at 1.27 THz, a strong absorption peak at 1.44 and 2.08 THz and a shoulder peak at 1.42 THz, which was almost coincident with 1.44 THz. These features originated from interactions of glucose molecules, behaved as absorbance of collective vibrational modes. Particularly, further calculation based on solid-state DFT implied that the peak at 1.82 THz primarily came from the intermolecular actions of water–glucose molecules. Glucose monohydrate had a negligible weak absorption peak at 1.54 THz, and strong absorption peaks of equivalent intensity at 1.82 and 1.99 THz. These results could be used for qualitative analyses of the anhydrous and monohydrate forms of glucose.

Nitrofurantoin is used commonly to treat acute simple infection of the lower urinary tract caused by bacteria sensitive to it (Orr et al., 1958), such as *Escherichia coli*, enterococci and *Staphylococcus* species. Nitrofurantoin can also be used for the prevention of urinary-tract infection. Zhang et al. studied the characteristic absorption peaks of nitrofurantoin and its hydrate form in the 0.2–1.8 THz band by THz-TDS technology (Zhang, 2016). Nitrofurantoin had absorption peaks at 1.26 and 1.60 THz, whereas its hydrate form had absorption peaks at 0.67, 1.05 and 1.60 THz. They concluded that the nitrofurantoin used in the experiment belonged to the stable crystal form β and the hydrate belonged to hydrated form II.

Usually, lithium citrate (LC) is employed as a drug for bipolar disorder and depression (Roberts, 1950). It was first studied in 1949 by the Australian physician John Cade as a drug used for psychiatric disorders (Bourgeois, 2014). Gao et al. used THz-TDS

technology to study the characteristic absorption peaks of the anhydrate and tetrahydrate forms of LC in the band of 0.5–3.0 THz (Gao et al., 2022). LC tetrahydrate at room temperature had a significant absorption peak near 1.66 THz, whereas LC anhydrate had no absorption peak in this band. With increasing temperature, the intensity or the area of the absorption peak decreased continuously. The dehydration kinetics of the LC tetrahydrate were monitored by variation in the THz absorption spectra with the heating time and heating temperature (Figures 6F, G; Figures 7A, B). The activation energy was predicted according to the Arrhenius formula to be 495.1 ± 17.8 J/g with a deviation of ~3.7% from the test result of DSC. These results indicated that THz-TDS could be used as a new technical method for the identification of drug hydrates and investigation of dehydration kinetics.

Methylene blue (MB) is an important dye. It is also a component of a frequently prescribed urinary analgesic, anti-infective and antispasmodic agents. Yan et al. used THz-TDS technology to study the characteristic absorption peaks of the pentahydrate, dihydrate and anhydrate forms in the THz band of 0.2–2.0 (Yan et al., 2017). The pentahydrate form had absorption peaks at 0.36, 0.54, 0.84 and 1.68 THz, and the latter two peaks were much stronger than the first two. The dihydrate form had a broad and weak peak at 0.89 THz, and the other weak peaks were at 0.31 THz and 1.50 THz. For the anhydrate form, there was no obvious absorption peak in the measured frequency range. The dehydration kinetics of MB hydrates were investigated according to the variation of one of the main THz characteristic absorption peaks of MB pentahydrate with the heating time at different heating temperatures. The relationship between the dehydration rate and heating temperature could be fitted closely by the Arrhenius equation. The fitted activation energy of 64.5 kJ/mol was quite consistent with the enthalpy change due to the transformation of MB pentahydrate to MB anhydrate reported in a previous study. In comparison with THz-TDS technology, the detection capability of IR spectroscopy and Raman spectroscopy was limited because MB hydrate (pentahydrate and dihydrate) have identical functional groups. XRD and TGA methods could also have been used to detect the crystal state of hydrate in that study, but the former requires complex crystal preparation, whereas the latter destroys the structure of crystal hydrate during heating. Therefore, THz-TDS technology is endowed with advantages for investigating the crystalline states of materials in simple and nondestructive ways, and may help to monitor the manufacturing process, storage stability and bioavailability of medicinal substances.

3.1.3.3 Co-crystal

The “co-crystal” of a drug refers to the crystal formed by the combination of API and co-crystal former according to a certain stoichiometric ratio under the action of non-covalent bonds (mostly hydrogen bond and π–π) (Shete et al., 2015) The co-crystal does not destroy the activity of the API, but also can improve the stability, solubility and dissolution rate of the API (Zhang et al., 2015). Therefore, co-crystal technology has a huge commercial market, and is one of the important aspects often considered in the research and development of drugs.

γ-aminobutyric acid (GABA) is an important inhibitory neurotransmitter in the central nervous system. GABA is used mainly in the treatment of stroke sequelae, cerebral arteriosclerosis and brain-trauma sequelae. In addition, intake of a certain amount of GABA can improve the quality of sleep and lower blood pressure. Zhang et al. characterized GABA, benzoic acid (BA) and their grinding and solvent co-crystal in 0.2–1.6 THz band by THz-TDS technology at room temperature (Zhang Q. et al., 2017). The absorption peaks of GABA-BA grinding and solvent co-crystal at 0.93, 1.33 and 1.97 THz were obviously different from those of raw materials. To ascertain the crystal structure of the GABA-BA co-crystal, they undertook FTIR spectroscopy and FT-Raman spectroscopy. They sought to understand the effect of the pH of the solvent on the formation conditions of the GABA-BA co-crystal. They discovered that the solvent condition for stable formation of the co-crystal was 2.00≤ pH ≤ 7.20 by means of THz-TDS and FT-Raman spectroscopy.

Nifedipine (NFD) belongs to the family of dihydropyridine calcium channel blocker (CCB), and is widely recognized as an important and effective antihypertensive pharmaceutical (Seoane-Viaño et al., 2021). Isonicotinamide (INA) is used as a common CCF in many cases with high bio-safety (Dubey and Desiraju, 2014). Wang et al. selected the cocrystal of NFD and INA to study its polymorphic behavior (form Ⅰ and form Ⅱ) by THz spectroscopy (Figures 7C–G) (Wang P. F. et al., 2022). Temperature-dependent THz spectra displayed distinguished frequency shifts of each fingerprint. Combined with solid-state DFT calculations, the experimental fingerprints and their distinct responses to temperature were elucidated by specific collective vibrational modes (Figures 8A–D). Table 5 summarized comparison of the absorption peak positions between the experimental and calculated THz spectra and vibrational modes for NFD-INA form I and form II. The vibrations of hydrogen bonding between dihydropyridine ring of NFD and INA were generally distributed below 1.5 THz, which played important roles in stabilizing cocrystal and prevented the oxidation of NFD. The rotations of methyl group in NFD were widely distributed in the range of 1.5–4.0 THz, which helped the steric recognition.

Nicotinamide (also known as 3-pyridine formamide) is used mainly in the prevention and treatment of pellagra, stomatitis, glossitis, coronary heart disease, viral myocarditis and other diseases (Revollo et al., 2007). Xiao et al. studied the characteristic absorption peaks of nicotinamide-heptanedioic acid co-crystal in the range of 0.2–2.2 THz at room temperature by THz-TDS technology (Xiao et al., 2019). They documented obvious differences between the two characteristic absorption peaks. Crystal form I had characteristic absorption peaks at 1.51, 1.73, 1.94, 2.01 and 2.17 THz, among which the peaks at 1.94, 2.01 and 2.17 THz were the peaks with higher absorption intensity. However, crystal form Ⅱ had characteristic absorption peaks at 1.66, 1.74, 1.88, 2.02 and 2.16 THz. Different from crystal form Ⅰ, crystal form Ⅱ had strong absorption peaks at 2.02 and 2.16 THz. Those studies showed that THz-TDS technology could be used to distinguish the different forms of a co-crystal.

Mesaconic acid, an endogenous anti-inflammatory molecule, is expected to serve as a candidate drug molecule to help develop the treatment of shock caused by blood poisoning and autoimmune diseases without the presence of currently used Side effects of anti-inflammatory drugs (He et al., 2022). Nguyen et al. applied THz-TDS technology to monitor a dynamic process involving two molecular crystals: mesaconic acid (mes) and phenazine (phen)

10.3389/fbioe.2023.1219042

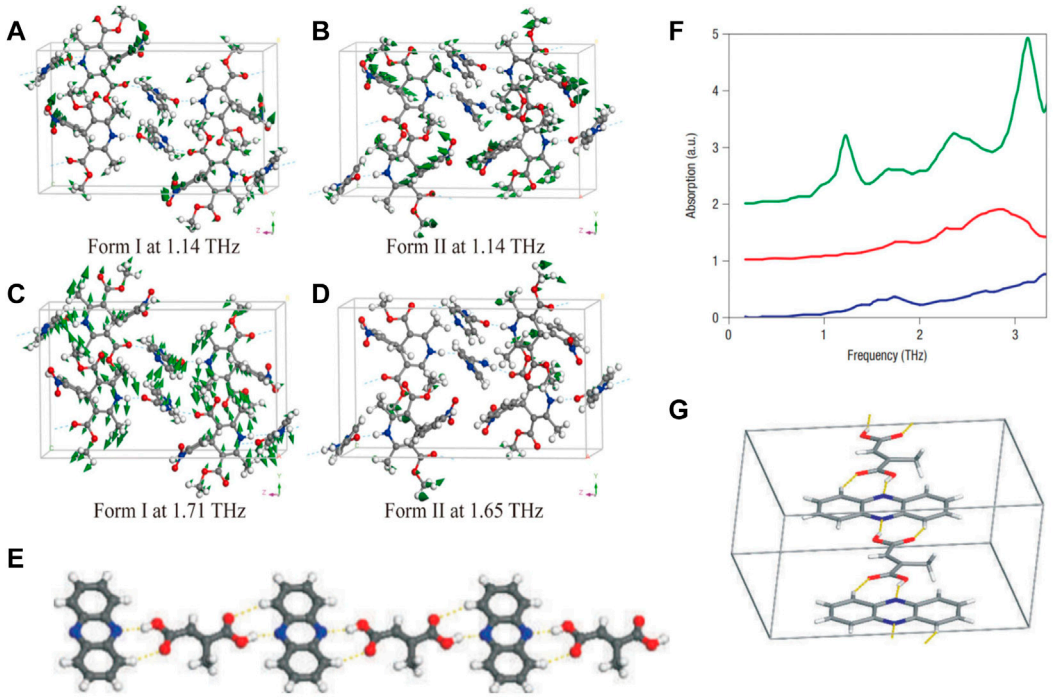

FIGURE 8
The calculated vibrational modes of **(A)** form I at 1.14 THz, **(B)** form II at 1.14 THz, **(C)** form I at 1.71 THz and **(D)** form II at 1.65 THz (Wang P. F. et al., 2022). **(E)** A ball-and-stick representation of a fragment of (phen)-(mes) cocrystal, demonstrating the presence of O–H···N and C–H···O bonds. **(F)** Spectra of phen (blue), mes (red) and (phen)-(mes) (green), following background slope subtraction. **(G)** The distortion of the hydrogen-bonded chain in (phen)-(mes) that results in the absorption peak at 1.2 THz is a combination of wagging motions of mes and phen components in each chain. The axes and directions of wagging motions are indicated. The chains propagate parallel to the crystallographic direction (Nguyen et al., 2007).

TABLE 5 Comparison of the absorption peak positions between the experimental and calculated THz spectra and vibrational modes for NFD-INA form I and form II.

	Exp./THz		Cal./THz	Vibrational mode assignment
	295 K	85 K	0 K	
Form I	0.98		1.14	Collective; *t* (NFD) + ι (INA)
	1.21		1.44	Collective; ν (Ar) + ι (INA)
	1.54	1.63	1.71	Collective; *t* (NFD) + ι (INA)
	1.94		1.99	Mainly from δ_{tw} (-CH_3)
	2.44		2.40	Collective; ν (-CH_3) + δ_{tw} (INA)
	3.37		3.21	Collective; ω (Ar) + δ_{tw} (INA)
Form II	0.97	1.02	1.14	Mainly from *t* (Ar) + *t* (-CH_3)
			1.37	Collective; *t* (NFD) + *t* (INA)
	1.52	1.59	1.65	Mainly from *t* (-CH_3)
	1.88		2.37	Collective; ν (-CH_3) + ι (INA)
	2.30		2.69	Collective; ν (-CH_3) + ι (INA)
	2.45		2.87	Collective; ι (NFD) + ι (INA)
	3.05		3.29	Collective; ν (-CH_3) + ι (INA)
	3.44		3.77	Collective; ν (-CH_3) + ι (INA)
	3.72		4.10	Collective; ι (Ar) + ι (INA)

ν, rotation; *t*, translation; ω, wagging; δ_{tw}, twisting; ι, librational; -CH3, methyl group in NFD; Ar, aromatic ring.

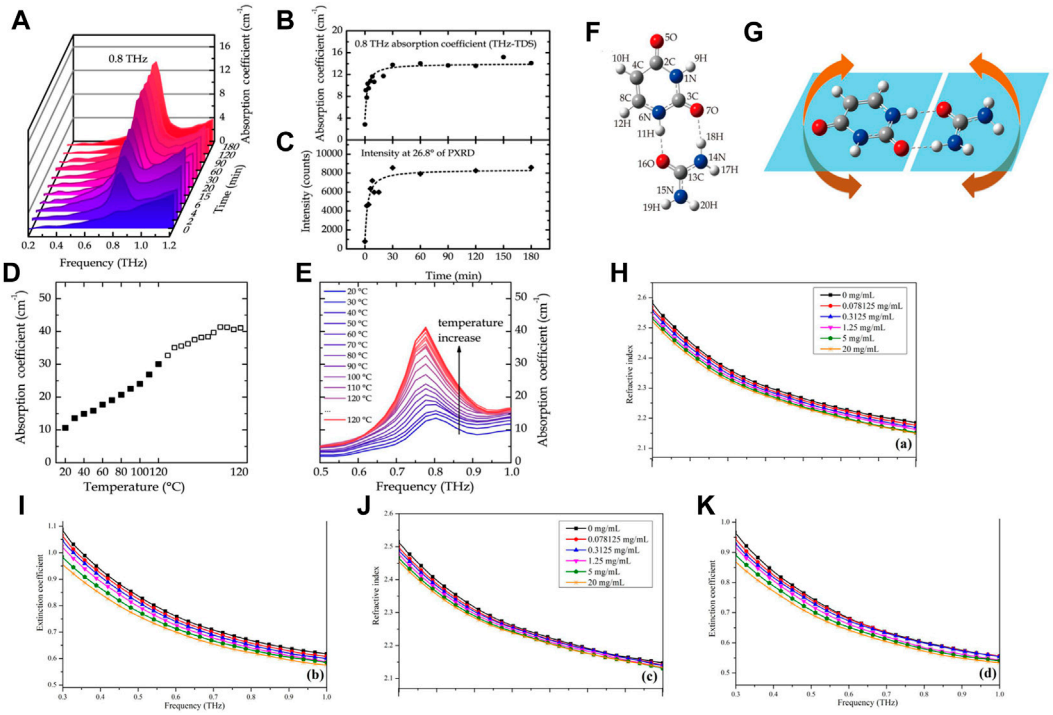

FIGURE 9
(A) THz absorption spectra of the reaction process of urea and uracil by cogrinding (0.2–1.2 THz range was taken for a clear view). **(B)** THz absorption intensity at 0.8 THz of the coground mixtures as a function of time. **(C)** Peak intensity at 26.8° of PXRD of the coground mixtures as a function of time. **(D)** THz absorption coefficient of the uracil–urea mixture around 0.8 THz varying with temperature. **(E)** THz absorption spectrum of the pellet in the frequency range from 0.5 to 1.0 THz recording the heating process from 20°C to 120°C. **(F)** Predicted representation of uracil–urea cocrystal structure based on DFT calculations. **(G)** Calculated vibration mode at 0.94 THz (Yang et al., 2014). **(H)** The refractive indices and **(I)** extinction coefficients of TCH in pure water, and **(J)** refractive indices and **(K)** extinction coefficients of TCH in pure milk in the region of 0.3–1.0 THz at 25°C (±0.1°C) (Qin et al., 2017).

(Nguyen et al., 2007). The characteristic absorption peak of cocrystal (phen)-(mes) at 1.2 THz was selected as a reference to monitor its formation. The calculated mode by lattice dynamics calculations corresponded to a combination of molecular translations and librations, which gave rised to an asymmetric stretch, with some out-of-plane twist, of the O-H···N and C-H···O hydrogen bond pairs within each (phen)-(mes) hydrogen-bonded chain (Figures 8E–G). In addition, the integration of the area under the 1.2 THz peak was seen to correlate in a linear fashion with the amount of the cocrystal, which could be used to quantitatively monitor cocrystal formation.

Use of urea as a solute probe to characterize the conformational changes in nucleic-acid processes has been suggested. The interactions of urea with heterocyclic aromatic rings and attached methyl groups are particularly favorable relative to its interactions with water (Guinn et al., 2013). Yang et al. demonstrated that urea and uracil can form a co-crystal by a solid-phase reaction in a dry environment by THz-TDS characterization, and this process was monitored (Yang et al., 2014). On the one hand, mechanical grinding and high temperature could enhance the solid-state reaction (Figures 9A–F). On the other hand, urea and uracil could recognize and interact with each other efficiently, and crystallized in the form of planar hydrogen-bonded uracil–urea without the participation of water molecules. To rationalize the observed transformation in the experiment, the cocrystallization manner was investigated using DFT calculations. One vibration mode was found at 0.94 THz, which corresponded to butterfly motion between urea and uracil through a pair of hydrogen bonds (Figure 9G). This mode could be well assigned to the prominent absorption peak at 0.8 THz in the experiment. A second one located at 1.70 THz, corresponded to the hindered rotations of uracil and urea molecules, could be assigned to the experimental 1.6 THz absorption peak.

A ternary co-crystal is a solid crystal structure formed by the combination of three different components by intermolecular forces. It is derived from a binary co-crystal, which can improve the physical and chemical properties of drugs. Simultaneously, through the addition of a third component, it can weaken or remove the side-effects of drugs, or increase the effect of pharmacology through a combination of drugs. Lamivudine (LAM) and azidothymidine (AZT), as classic antiviral drugs, have been combined to prevent mother-to-child transmission of the human immunodeficiency virus. Jin induced LAM and AZT to form a ternary co-crystal through a mixed solution of water and ethanol, and used THz spectroscopy and Raman spectroscopy as characterization methods to obtain the spectral data of LAM-AZT-H_2O (Jin, 2020). Using DFT to calculate the possible structure of the co-crystal, and by comparing experimental and theoretical spectra, the molecular structure of the ternary co-crystal was determined and each characteristic absorption peak was assigned. That study confirmed that application of THz-TDS technology was not

limited to a binary co-crystal structure, but also showed good accuracy for the detection of a ternary co-crystal with a more complex structure.

3.1.4 Analyses of other chemical drugs

THz-TDS technology can also be used to analyze other drugs, such as expired drugs. The principle is that, if a drug deteriorates because of expiration, the main chemical composition changes, and this process is often accompanied by the formation of new compounds. THz wave is extremely sensitive to changes in the structure of compounds, so it can be used to detect expired drugs. This type of research provides a new concept and method for THz-TDS technology to be used in online monitoring of drug quality. Some companies have adopted this method and put it into production service.

Xie et al. analyzed expired amoxicillin capsules as well as compound paracetamol and amantadine-hydrochloride tablets by THz-TDS technology (Xie et al., 2019). Their characteristic absorption peaks, absorption coefficients and refractive indices in the 0.2–0.9 THz band were obtained, and experimental results were compared with data reported in the literature. Both samples had absorption peaks consistent with those recorded in the literature, but the amplitude of the absorption peaks decreased and the refractive index changed. A new absorption peak near the 1.50-THz position of expired compound paracetamol and amantadine-hydrochloride tablets indicated that some of its chemical components had changed, which could be used to identify expired drugs.

Zheng et al. used THz-TDS technology to analyze the THz spectra of paracetamol tablets before and after metamorphism in the 0.3–4.5 THz band (Zheng et al., 2021). The absorption peak of the unspoiled tablet was consistent with that of the standard. However, when the tablets deteriorated, the THz characteristic absorption peak disappeared completely, which indicated that the expired drug could be distinguished by the change of its THz characteristic absorption peak.

3.2 Quantitative analyses

3.2.1 Single-component quantitative analyses

In quantitative analyses of single-component samples, the compounds to be tested are, in general, mixed with polyethylene (PE) powder or cyclic olefin copolymer (COC) powder to make different concentrations of samples. PE has no characteristic absorption in the THz band, so it is used most commonly in THz spectral analyses. COC can be highly suitable for THz spectroscopy applications due to its negligible dispersion of refractive index and negligible absorption in the THz region.

Vitamin B2 (also known as riboflavin) can promote the growth and development and cell regeneration in humans. Hu et al. mixed vitamin B2 and PE powder according to a mass ratio of 1:1, 1:3, 1:5 and 1:7, and measured their absorption spectra under different humidity conditions (4%, 15% and 70%) (Hu and Cai, 2021). In the 0.5–2.5 THz band, the position of their absorption peaks did not change with a change in material concentration, but the absorption intensity increased with increasing concentration. Also, the higher the concentration, the higher was the signal-to-noise ratio. Air humidity did not eliminate the original absorption peaks of the substance, but it introduced additional absorption peaks. The higher the humidity, the more burrs (noise), and the more difficult was the identification. This was because water is strongly absorbed in the THz region. To smoothen and de-noise spectral data, the sample was processed by a Savitzky–Golay (S–G) filter (Liu et al., 2018). Filtered data could retain the peak value of the signal and other important features, improve the smoothness of the spectrum while reducing noise interference and make the processed spectral features more obvious.

Because of the strong absorption of water in the THz region, measurement of liquid samples using THz-TDS technology has been difficult. Qin et al. used ATR THz-TDS to study the spectral differences of tetracycline hydrochloride (TCH) of different concentrations in pure water and pure milk (Qin et al., 2017). They determined the complex refractive indices of TCH in pure water and pure milk at 0.3–2.0 THz. The shape of the complex refractive index curve of pure milk was similar to that of pure water. However, a reduction in the complex refractive index of pure milk was observed at the same frequency (Figures 9H–K). A simple linear regression (SLR) method was used to establish a fitting model to determine the concentration of the TCH solution. All of these models were excellent as indicated by the high values of the correlation coefficient (R^2; 0.95–0.98), low values of root mean squared error (RMSE; 0.61–0.99 mg/mL), and the limit of detection was 0.45–1.29 mg/mL. Reflection type THz-TDS is a method for measuring liquid samples, but extracting information about the solute from the reflection data is difficult because of the extremely short interaction length. Qin et al. demonstrated experimentally that ATR THz-TDS technology could be used to determine the complex refractive index of a liquid sample with high accuracy, a goal that is difficult to achieve with conventional THz-TDS in transmission or reflection type, and expanded the application range of THz-TDS technology.

Quinolones are a class of broad-spectrum antibiotics often used to treat or prevent infections caused by bacteria (Li S. W. et al., 2013). However, the overuse of antibiotics leads to antibiotics remaining in humans or animals and an increased risk of bacterial resistance. Detection of antibiotic residues is crucial when evaluating the safe use of drugs. Taking norfloxacin as the research object, Bai et al. used large gradients (concentration series and concentration intervals >104 μg/mL (i.e. 1%)) and small gradients (concentration series and concentration intervals <0.01% (i.e., 0.01%)) of norfloxacin to detect norfloxacin in samples based on THz-TDS technology (Bai et al., 2021). The detection and analyses of norfloxacin samples with a large gradient revealed absorption peaks at 0.816 and 1.205 THz in samples of pure norfloxacin. Stepwise linear regression and a successive projections algorithm (SPA) were used to select variables for multiple linear regression analysis. The correlation coefficient of the prediction set (R_p) was 0.962 and the root mean square error of prediction (RMSEP) was 2.74%. Detection and analyses of the small gradient showed that the multiple linear regression of selected variables achieved the best effect of the model, with R_p = 0.728 and RMSEP = 18.79 μg/mL, but the prediction ability of this model was significantly lower than that of large-gradient norfloxacin. Those results showed that THz-TDS technology could not be employed to predict the content of norfloxacin with a small gradient, and it was necessary to continue to look for ways to improve it. In general, THz-TDS technology could be employed to

accurately predict norfloxacin with a large gradient, and it also showed potential in the prediction of norfloxacin with a small gradient, but the accuracy needs to be improved.

The nitroimidazole antibiotic metronidazole is used against trichomonas and amoeba, but has also been used widely against anaerobes in recent years (Gui et al., 2011; Doron et al., 2017). Li et al. recorded the THz spectra of analytically pure metronidazole and oral solutions of metronidazole with different mass fractions (20%, 30%, 40% and 50%), and obtained their absorption characteristic peaks in the 0.2–2.0 THz band (Li G. L. et al., 2020). Characteristic absorption peaks at 1.36 and 1.67 THz were noted, and there was an obvious linear relationship between the absorption intensity and mass fraction of metronidazole. Two metronidazole samples were also tested by HPLC: the principal components of an oral solution of metronidazole were consistent with those of metronidazole. The test results of THz-TDS and HPLC were in good agreement, which further confirmed the feasibility of using THz-TDS technology for rapid identification of metronidazole and other antibiotic residues.

3.2.2 Multicomponent quantitative analyses

Tuberculosis is a chronic infectious disease caused by *Mycobacterium tuberculosis* infection. Before the emergence of coronavirus disease-2019, tuberculosis was the most deadly disease caused by a single pathogen in the world. The widely used antitubercular drugs in the clinic are pyrazinamide, isoniazid and rifampicin. A combination of these drugs can improve the curative effect, and also avoid the rapid production of drug resistance of *M. tuberculosis* due to the use of an anti-tuberculosis drug alone. Zhang et al. used THz-TDS technology to collect the spectra of pyrazinamide, isoniazid and their mixture (Zhang et al., 2016). Pyrazinamide had absorption peaks at 0.52, 0.72 and 1.42 THz. Isoniazid had absorption peaks at 1.17 and 1.42 THz. With an increasing mass of pyrazinamide in the mixture, the absorption coefficient and refractive index of the sample showed a linear relationship. The models of pyrazinamide content, absorption coefficient and refractive index in mixed drugs were established by SLR and partial least square regression (PLSR) and their limit of detection were obtained. The prediction result of PLSR was better, and its limit of detection was only 1/10 that of SLR. Those results indicated that THz-TDS technology had good application in quantitative analyses of combined drugs.

Theophylline is a commonly used drug for the treatment of respiratory diseases. Acetaminophen is a widely used antipyretic analgesic in the clinic. Excipients and additives are used in the production and formulation of drugs. Pharmaceutical excipients, in addition to aiding shaping, acting as carriers and improving stability, have important functions such as solubilization, sustained release and controlled release. Hence, pharmaceutical excipients are important ingredients that can affect the quality, safety and efficacy of drugs. In addition to the API, detection of the content of pharmaceutical excipients is an indispensable part of drug-quality monitoring. Chen et al. used THz-TDS technology combined with chemometrics to quantitatively study the content of the API and medicinal excipients in multicomponent drug mixtures (Chen et al., 2013). First, the THz absorption spectra of ternary mixtures of anhydrous theophylline, lactose monohydrate and magnesium stearate, as well as quaternary mixtures of paracetamol, lactose monohydrate, microcrystalline cellulose and soluble starch, were measured by a THz-TDS system. Then, the quantitative regression models of the THz absorption spectrum and content of each component in the multicomponent mixture were established by principal component regression (PCR) and PLSR, respectively, and the contents of the API and pharmaceutical excipients in the mixture were obtained. PLSR achieved better results. The content of magnesium stearate in the ternary mixture was fixed. The correction and prediction correlation coefficient (R^2) of the PLSR quantitative model for the content of the other two components were >0.98. Correction of the PLSR quantitative model and R^2 of paracetamol, lactose monohydrate, microcrystalline cellulose and soluble starch in quaternary mixtures were higher than 0.93, 0.98, 0.63 and 0.86, respectively. That study showed that the quantitative-analyses model established by THz-TDS technology, combined with chemometrics, could enable non-destructive and rapid quantitative analysis of the content of the API and pharmaceutical excipients in drugs, and monitor the quality of drugs conveniently.

The detection of antibiotic residues has garnered considerable attention in recent years. In addition to the quantitative study of a single component of antibiotics, detection of multiple components of antibiotics should be considered. Cao et al. used THz-TDS technology to quantitatively study pefloxacin and fleroxacin in a fishmeal matrix (Figures 10A–D) (Cao et al., 2022). Samples of pefloxacin, fleroxacin, PE and fishmeal, as well as binary mixtures of pefloxacin-fishmeal and fleroxacin-fishmeal of different concentrations, were prepared, and THz spectra of all samples were measured and analyzed. SPA was used to reduce the dimension of high-dimensional data. Then, the absorption coefficient at a characteristic frequency was used to establish quantitative prediction models of PLSR, back propagation neural network (BPNN) and multiple linear regression (MLR) to predict the two binary mixtures quantitatively. Spectral measurements revealed obvious absorption peaks of pure pefloxacin at 0.775 and 0.988 THz, obvious absorption peaks of pure fleroxacin at 0.919 and 1.088 THz, no absorption peak of fish meal, and no absorption of the THz wave by PE. The absorption peaks of two antibiotics mixed with fishmeal appeared near the absorption peaks of pure antibiotics. Upon quantitative regression analyses, the SPA-BPNN model was the best to predict pefloxacin-fishmeal: R_p and RMSEP were 0.9849 and 0.0095, respectively. The SPA-MLR model was the best model for predicting fleroxacin-fishmeal: R_p and RMSEP were 0.9827 and 0.0406, respectively. Those results showed that THz-TDS technology was feasible for quantitative detection of pefloxacin and fleroxacin in a fishmeal matrix, and could provide support for the detection of antibiotic residues in multicomponent antibiotics.

4 Application for TCM analyses

Chinese herbs with medicinal properties are contained within TCM. TCM theory is used for the prevention, treatment and diagnosis of diseases. TCM has attracted attention worldwide thanks to its abundant resources, remarkable curative effects and few side-effects. Because of the complex chemical composition and the abundance of secondary metabolites, developing effective methods for the quality control of TCM is crucial. The

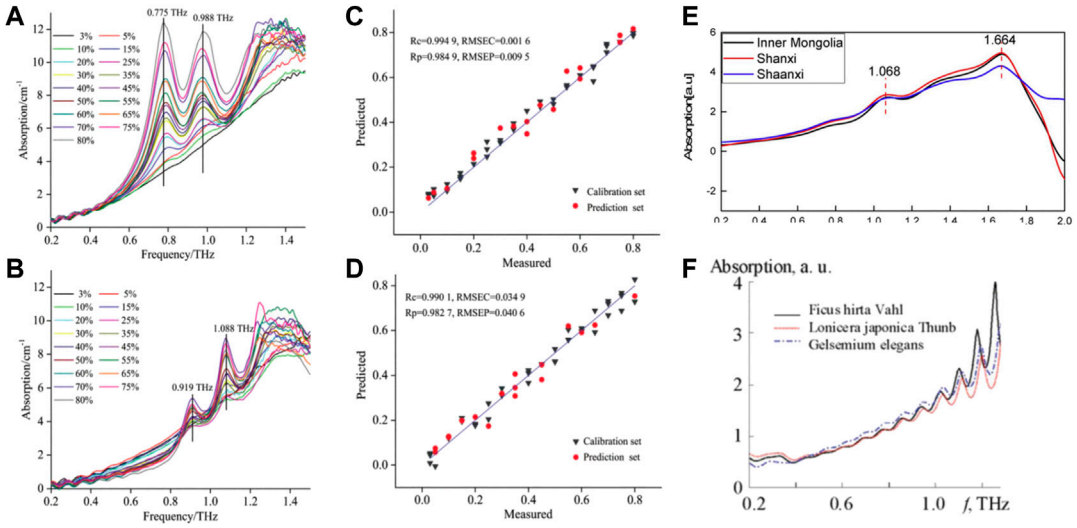

FIGURE 10
Absorption coefficient of binary mixture **(A)** Pefloxacin fishmealfeeds, **(B)** Fleroxaxin fishmealfeeds. The best prediction model requires and predictions the concentration scatterdiagram **(C)** Pefloxacin fishmealfeeds, **(D)** Fleroxaxin fishmealfeeds (Cao et al., 2022). **(E)** THz absorption spectra of Scutellaria baicalensis of different origins (Liang et al., 2018). **(F)** THz absorbance spectra of the herbs (Zhang et al., 2018).

development of identification methods for ingredients in TCM has yielded traditional and modern approaches. The traditional identification methods of TCM are mainly by looking, touching, smelling and water-testing. These methods are simple, rapid and inexpensive. These are the most basic and commonly used identification methods for ingredients in TCM. However, modern identification methods must be used for Chinese patent medicines with a complex source, obscure shape or if they have been crushed. Chromatography, spectroscopy, DNA markers and fingerprinting have been used widely for the identification of TCM ingredients (Yin and Sun, 2018). In recent years, several theoretical and experimental studies have shown that the low-frequency vibration and rotation modes of chemical components and some secondary metabolites in TCM are mostly in the THz band. Hence, THz-TDS technology provides a new method for the identification and quality control of TCM (Zhang, 2008).

4.1 Qualitative analyses

4.1.1 Identification of the origin of TCM

Identification of the origin and raw materials of TCM is the basis of inheritance, research, production, development and utilization of TCM. The method for identification of the origin or raw materials of TCM involves applying the knowledge of materia medica, TCM theory, plant/animal/mineral morphology and taxonomy. This strategy enables determination of the correct scientific name of the TCM origin and compatibility of the decoction pieces of its preparations, so as to ensure the accuracy of the varieties of TCM in application (Zhang and Wang, 2011). For example, Liang et al. studied the THz absorption spectra of Scutellaria baicalensis collected from its main growth areas in China (Inner Mongolia, Shanxi, Shaanxi and other major producing areas) using THz-TDS technology (Liang et al., 2018). Distinct absorption peaks centered on 1.068 and 1.664 THz were observed (i.e., samples from different sources had the same absorption peak) (Figure 10E). Such spectral features alone cannot be used directly to identify samples with different origins. To distinguish the absorption spectra of samples from different sources, THz-TDS combined with the support vector machine with particle swarm optimization (PSO-SVM) model could achieve identification of the different origins of S. baicalensis in 95.56% of samples. The proposed approach improved the identification accuracy of different origins of S. baicalensis, and could be used for other Chinese herbal medicines. Thus, a new approach is expected to be widely applicable in the quality control of TCM based on accurate determination of its origin.

Rao et al. used THz-TDS technology combined with chemometric methods to classify and identify the geoherbalism and origin of four types of Curcuma species (Rao et al., 2021). The slope loss multi-class support vector machine (Ramp Loss K-SVC) method, random forests (RFs) and an extreme learning machine algorithm were constructed to distinguish Curcuma species with four different origins in the range 0.5–2 THz. Use of the Ramp Loss K-SVC method and optimization of model parameters enabled identification of the four types of Curcuma species to be identified 93% of the time. Hence, an efficient and convenient method for the identification of four readily confused origins was created.

4.1.2 Identification of the authenticity of TCM

The quality of a TCM is affected by fake or substandard ingredients. This scenario affects the efficacy of the TCM, but can also have toxic side-effects, thereby leading to deterioration of the patient's condition. Therefore, the authenticity of TCM is crucial for the treatment of diseases.

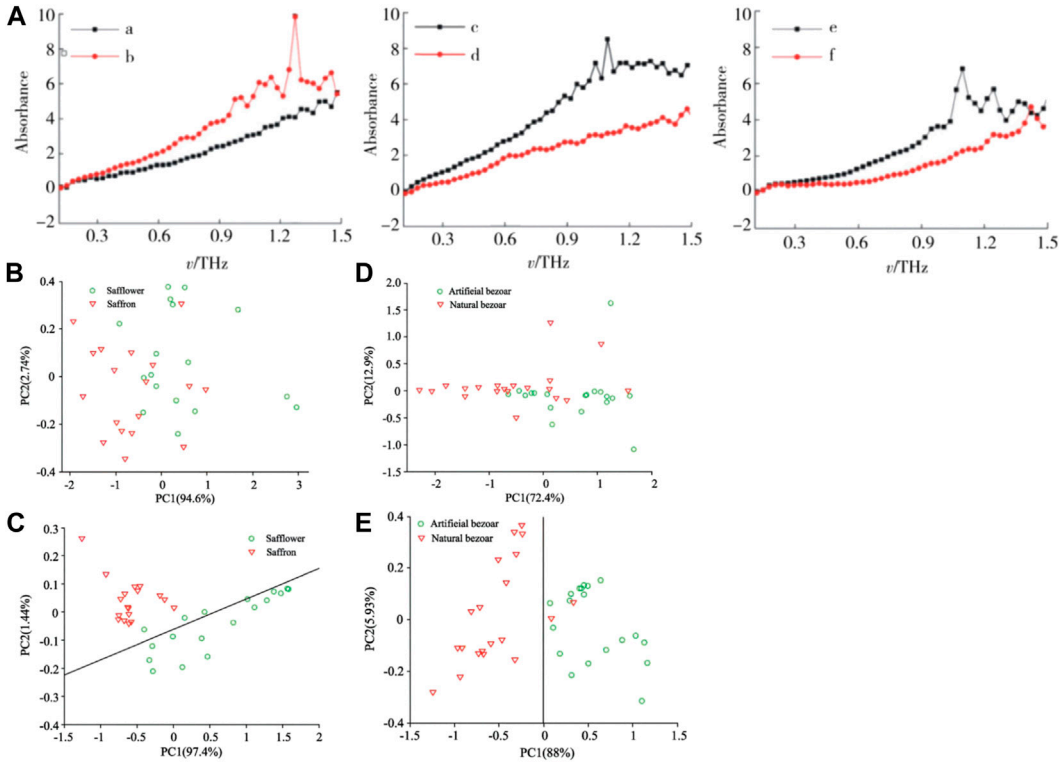

FIGURE 11
(A) Terahertz absorption map of three groups of Chinese herbal medicines. a. authentic Morinda officinalis How; b. fake Morinda officinalis How; c. authentic Stephania tetrandra S. Moore; d. fake Stephania tetrandra S. Moore; e. authentic Polyporus umbellatus Fr; f. fake Polyporus umbellatus Fr (Li R. K. et al., 2020). **(B)** Scattered scores plots PCA1 *vs.* PCA2 for the saffron and safflower data without S-G smooth. **(C)** Scattered scores plots PCA1 *vs.* PCA2 for the saffron and safflower data with S-G smooth. **(D)** Scattered scores plots PCA1 *vs.* PCA2 for two kinds of bezoar data without S-G smooth. **(E)** Scattered scores plots PCAl *vs.* PCA2 for two kinds of bezoar data with S-G smooth (Yang et al., 2019).

THz-TDS has been used widely for the authenticity identification of TCM. Wang et al. used THz-TDS technology combined with partial least squares (PLS) analyses for the identification of 41 official and unofficial rhubarb samples (Wang et al., 2016). First, the THz-TDS spectra of rhubarb samples were collected and pre-processed using chemometrics methods rather than being transformed to absorption spectra. Then, an identification model was established based on the processed THz time-domain spectra. The spectral pre-processing methods included S–G first derivatives, detrending, standard normal transformation, autoscaling and mean centering. An identification accuracy of 90% was accomplished using appropriate pretreatment methods, which was higher than the accuracy of 80% achieved without any pre-processing for the time-domain spectra. The proposed method based on the combination of THz-TDS and chemometrics proved to be rapid, simple, non-polluting and solvent-free, and was suitable for development for the quality control of many other Chinese herbal medicines. Li et al. used THz-TDS technology to identify four samples of authentic Cordyceps sinensis and three samples of counterfeit *C. sinensis* (Li C. et al., 2019). They found that the sample of authentic *C. sinensis* had characteristic absorption peaks at 1.01 and 1.13 THz. By analyzing the characteristic absorption peaks and refractive indices of several samples of authentic and counterfeit *C. sinensis* in the THz band, the common characteristics and typical differences of THz spectra between authentic and counterfeit *C. sinensis* could be evaluated, which provides technical support for the authenticity identification of valuable TCM containing *C. sinensis*. Li et al. used THz-TDS technology combined with PCA and a K-means clustering algorithm to investigate the spectral data of three groups of authentic and counterfeit Chinese herbal medicines (Morinda officinalis How, Stephania tetrandra S. Moore, Polyporus umbellatus Fr.) were compared and analyzed (Li R. K. et al., 2020). As shown in Figure 11A, the absorption spectra of three groups of Chinese herbal medicines showed distinct absorption coefficients and refractive indices in the range 0.2–1.5 THz. Spectral absorbance data were subjected to dimensionality reduction and applied to the K-means clustering algorithm. The score map of three sets of authentic Chinese herbal medicines obtained by PCA reached up to 100%. This method improved the accuracy and scientific nature of identification of the authenticity of herbal medicines. Yang et al. used THz-TDS technology combined with PCA to realize the qualitative classification and discrimination of saffron and its counterfeit safflower, as well as natural bezoar and artificial bezoar (Yang et al., 2019). Comparison of the PCA score map before and after S–G filtering revealed that the classification effect had improved significantly: the classification accuracy of saffron and safflower samples was 100%, whereas that of artificial bezoar and natural bezoar was 100% and 90%, respectively (Figures 11B–E). Hence, a new means of detection and theoretical basis for the quality monitoring of these types of herbal medicines were obtained.

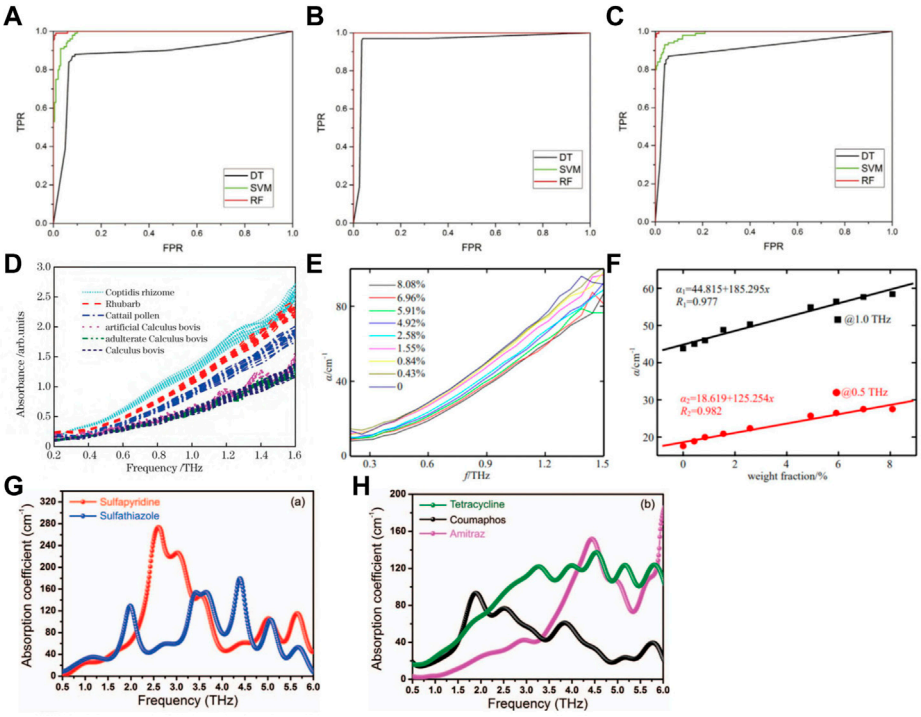

FIGURE 12
ROC curves of the three herbal medicines: **(A)** Herba Solani Lyrati; **(B)** Herba Solani Nigri; **(C)** Herba Aristolochiae Mollissimae (Zhang H. et al., 2017). **(D)** THz absorption spectra of six kinds of samples (Zhang et al., 2020). **(E)** Absorption coefficient of different moisture contents. **(F)** Linear correlation between absorption coefficient and moisture content at 0.5 THz and 1.0 THz (Ma and Yang, 2017). Spectral features of **(G)** sulfapyridine and sulfathiazole and **(H)** tetracycline, coumaphos, and amitraz, in the THz frequency range 0.5–6.0 THz, as extracted from the THz transmission measurements performed using a 100 lm-thick GaP crystal in the EO detection (Massaouti et al., 2013).

Sulfur fumigation is a method to treat a TCM by heating sulfur, which can help in deworming, whitening and stopping corrosion. However, excessive fumigate sulfur leads to a sharp increase in the sulfur content of medicinal materials, and long-term use of these medicinal materials will cause serious damage to the human body. Tian et al. used THz-TDS technology to analyze fumigated and unfumigated Angelicae dahuricae Radix, and obtained the absorption spectra of two types of TCM samples in the 0.2–1.7 THz band (Tian et al., 2018). The two samples had no obvious absorption peak in this band, but the repeatability was good. The features were extracted by PCA, and the extracted features were classified by SVM. Identification of these two types of herbal samples was achieved 100% of the time. Hence, THz-TDS technology combined with chemometrics could be employed to clearly distinguish between fumigated and unfumigated A. dahuricae Radix. This method is important for maintaining drug safety, and bodes well for further application of this technology in the identification of TCM ingredients.

4.1.3 Identification of readily confused herbal medicines

Similar appearance, similar names or incorrect records in some pharmacopoeias can lead to misuse of TCM, thereby eliciting safety risks. TCM have a wide range of sources (plants, animals, minerals), but especially plants. Obvious differences in the appearance of the whole plant can be seen, but medicinal parts (roots, stems, leaves) have similar appearances (especially after drying). In the processing of original Chinese medicinal materials into decoctions, many medicinal materials lose their original appearance (especially if they are in powder form) (Guo S., 2012). Therefore, finding a rapid and convenient method to identify readily confusable TCM products is important. THz-TDS technology can realize efficient identification of similar looking herbs, which provides a scientific basis for the determination of varieties, creation of quality standards, and ensure the authenticity of herbal varieties as well as the safety and efficacy of drug use.

The whole plant of Gelsemium elegans is highly toxic. Its roots are very similar to those of *Lonicera japonica* Thunb, and the flower is particularly similar to Ficus Hirta Vahl, so people often mistakenly pick and eat dangerous plants. Zhang et al. obtained the THz spectra of one toxic and two non-toxic herbs (*G. elegans*, *L. japonica* Thunb, and F. Hirta Vahl) in the range 0.2–1.4 THz using THz-TDS technology (Figure 10F) (Zhang et al., 2018). THz-TDS with chemometrics methods was used to distinguish a poisonous herb from unclassified herbs. A kernel-based extreme learning machine (KELM) model was created to classify the samples of different herbs. The Cuckoo-Search (CS) algorithm was employed to optimize the parameters of the KELM model to obtain a better analytical result. The prediction accuracy of classification was >97.78%. Hence, a combination of THz-TDS technology and chemometrics algorithm was an efficient and practical method for identification of readily confusable herbs, and

provided a reference for the modeling of toxic medicinal materials. Zhang et al. used THz-TDS technology to obtain the spectra of three readily confusable herbs (Herba Solani Lyrati, Herba Solani Nigri and Herba Aristolochiae Mollissimae) in the range of 0.2–1.2 THz (Zhang H. et al., 2017). PCA was applied to reduce the dimensionality of the original spectral information. Three classification algorithms, SVM, decision tree (DT) and RFs, were used to discriminate the herbal medicines. The receiver operating characteristic (ROC) curve and area under the ROC curve (AUC) were combined with classification accuracy to evaluate the performances of the three classification algorithms (Figures 12A–C). The PCA-RF method obtained the best ROC curve and AUC, and achieved a prediction accuracy of 99%. These experimental results indicated that THz-TDS technology combined with chemometric algorithms was an effective and rapid method for the discrimination of traditional herbal medicines.

Caulis spatholobi and Caulis sargentodoxae are herbs with different medicinal effects, different origins but very similar appearance, which can lead to confusion if they are used. Xu et al. used THz-TDS technology combined with a spectral-matching algorithm to distinguish five types of C. spatholobi and C. sargentodoxae from different origins and different batches (Xu et al., 2017). Due to the complex chemical composition of TCM, different components with characteristic absorption peaks can overlap. Therefore, identifying an obvious characteristic absorption peak in the THz range can be very difficult: this was the case for C. spatholobi and C. sargentodoxae. The second-derivative method was employed to enhance the curve characteristics so that the weak absorption peaks which overlapped with each other appeared again. The classification effects of four similar algorithms on sample data were analyzed and compared. The spectral angle algorithm has a high value for spectral discrimination power, and the classification accuracy of the two samples reached 95%, which could reflect the difference between the THz spectral data of C. spatholobi and C. sargentodoxae. Therefore, THz-TDS technology combined with an algorithm based on spectral angular similarity could be applied for the rapid identification of readily confusable herbs. Liu et al. used THz-TDS technology and chemometric methods to qualitatively identify four similar Chinese medicinal materials: Fritillaria cirrhosa Don, Fritillaria ussuriensis Maxim, Fritillaria pallidiflora Schrenk and Fritillaria thunbergii (Liu et al., 2021). Through a combination of spectral pre-processing and a classification model, the overall recognition accuracy of this model was 97.49%. In conclusion, THz-TDS technology can be employed to identify different types of similar Chinese herbal medicines, and it is an efficient and practical method to identify them.

In China, ginseng is a precious medicinal material, but ginseng has different medicinal properties because of its different types, origins and processing methods. Ginseng can be divided into Ginseng Radix et Rhizoma, Ginseng Radix et Rhizoma Rubra, Codonopsis Radix, Pseudostellaria Radix and Panacis Quinquefolii Radix. Due to the different chemically active ingredients of different types of ginseng, there are differences in nutritional value and medical efficacy. Therefore, developing an efficient and accurate method to identify the features of ginseng is important. Wei et al. used THz-TDS technology combined with the K-nearest neighbor algorithm of PCA to identify five types of Ginseng Radix et Rhizoma samples (Wei et al., 2020) (Wei et al., 2016). The sensitivity of the refractive index of samples could reach 95.7%. Results showed that THz-TDS technology could be applied to the detection of different types of ginseng, and provided a simple and convenient method for the quality detection of ginseng. Zhang used THz-TDS technology and chemometrics to identify and analyze Calculus bovis and its readily confusable products (Zhang et al., 2020). They obtained the THz absorption spectra of six types of Calculus species, including C. bovis, artificial C. bovis and adulterated C. bovis. However, it was found that the overlapping phenomenon of absorption spectral lines was relatively serious and difficult to distinguish directly (Figure 12D). A RF model and three-parameter optimized SVM model were constructed, and the THz absorption spectra of the six substances classified and identified. The RF model and SVM model could achieve a classification accuracy of 95.00%, but the RF model had a faster running speed. In addition, a RF model based on Synthetic Minority Oversampling Technique (SMOTE) was proposed to solve the problem that the recognition ability of the RF model decreased due to a data imbalance. The recognition ability of the improved RF model increased from 84.17% to 94.17%, and the calculation speed was essentially unchanged. Hence, THz-TDS technology combined with chemometric methods could be employed to identify C. bovis and its readily confusable products rapidly and accurately. This method provided an important reference for the identification of other types of valuable medicinal materials.

4.1.4 Identification of processed herbs and TCM

The processing of herbs can make medicinal materials pure, alter their taste, eliminate or reduce toxic side-effects and, more importantly, it can also change their clinical efficacy. During the processing of herbs, their internal structure changes, as does the interaction between molecules. The changes in the internal structure of herbs can be analyzed by THz-TDS technology.

Aconitum (also known as “aconite”) is a genus of >250 species of flowering plants belonging to the family Ranunculaceae. Li et al. used THz-TDS technology to detect and analyze aconite samples obtained from four types of production method in a dry environment at room temperature (Li X. X. D. H. et al., 2013). The THz-TDS spectra of these four types of aconite samples could be divided into two groups, and the method had good repeatability. There were obvious differences in the THz refractive index of different samples, which could be used to identify the different preparation methods employed intuitively. The four types of aconite samples had no obvious characteristic absorption peaks in the range 0.2–1.05 THz, but the absorption coefficient was obviously different, which was consistent with the THz spectra. These data indicated that aconite from the same production area but different production methods could lead to differences in their THz spectra. Yang et al. used THz-TDS technology combined with chemometrics to identify and analyze four types of processed rhubarb (Yang S. et al., 2016). The THz spectral data of these samples were obtained, and the spectral data were distinguished according to the types of samples. Simultaneously, the components of anthraquinone and tannins led to changes in processed rhubarb according to thin-layer chromatography after different processing methods. A correlation was noted among the THz spectra of processed rhubarb according to the variation in content. Hence, THz-TDS was sensitive to the components of processed rhubarb.

This conclusion provides an important reference for the study of structural changes in materials during the processing of herbs, but also provides a reliable method for the identification of processed products.

4.2 Quantitative analyses

The lack of safe, effective and stable quality standards of herbs and has restricted the development of TCM industry to the international stage. On the one hand, some chemical components of TCM are unstable and can lose their activity readily due to environmental changes during processing and storage, thereby affecting their efficacy. On the other hand, the quality and variety of medicinal materials in different herb-producing areas is different. Adulteration of herbs and TCM has been documented, which hampers guaranteeing the quality of TCM. However, the quality of a TCM will directly affect its efficacy. Therefore, a quality-control system is needed rapidly in China (Liu and Sun, 2019) (Liu and Sun, 2019). THz-TDS technology has special advantages in the identification and quality assessment of the complex components of TCM, which will help to distinguish which herbs and TCM are safe.

4.2.1 Determination of the active substances in TCM

The efficacy and curative effect of the compounds in TCM vary according to their proportion. During preparation, often the manufacturer pursues economic interests and the content of rare medicinal materials in the TCM is insufficient, or the proportion of herb content is incorrect due to weighing errors. Therefore, to ensure the quality and therapeutic effect of a TCM, it is necessary to determine the content of its main pharmacodynamic components to improve drug safety. Zhang used THz-TDS technology and a quantitative regression model to determine the content of notoginseng in the Chinese patent medicine Zhixue Dingtong Pian (Zhang, 2018). In the regression model, partial least squares regression of two-dimensional correlation spectroscopy (2DCOS-PLS) achieved the best results, and its RMSEP was 0.1092. Results showed that THz-TDS technology combined with a quantitative regression model could be used to detect the content of notoginseng in the TCM, which could lay the foundation for further application of THz-TDS technology in TCM. Liu et al. used THz-TDS technology combined with SVM and a PLS model to quantitatively analyze a mixture containing baicalin (Liu et al., 2020). The predicted data of the two models showed good correlation with actual data, and the root mean square error was small, so the quantitative detection of baicalin could be achieved. The research detailed above provides a new method for determination of active substances in TCM, which is important for the quality detection of TCM.

Flavonoids are a large class of polyphenols distributed widely in plants in the form of free flavonoids or glycosides. Flavonoids have anti-oxidation, antibacterial, antiviral, anti-tumor-growth and other pharmacological effects. Flavonoids have high medicinal value and development prospects. Yin et al. used THz-TDS technology to study the biomolecular properties of eight common flavonoids (baicalein, quercetin, naringenin, daidzein, baicalin, puerarin, genistein and gastrodin) in the 0.2–2.5 THz band (Yin et al., 2020). These flavonoids had different characteristic absorption peaks in the THz band. The THz absorption characteristics varied with temperature in the range 78–320 K. The characteristic absorption peaks increased gradually with decreasing temperature, and the frequency position of absorption peak was blue-shifted. In addition, a PLSR model and artificial neural network (ANN) model were used to analyze flavonoids with different concentrations in starch quantitatively. Comparison of the two methods revealed the ANN model to obtain the highest prediction accuracy. The R^2 value of naringenin and daidzein in the prediction set were 0.9944 and 0.9964, and the root means square error (RMSE) was 1.9325 and 1.5441, respectively. In summary, the biomolecular properties of flavonoids were studied by THz-TDS technology. Rapid, effective and non-destructive qualitative identification and quantitative analysis of flavonoids were provided. This method has potential application value in the detection of Chinese herbal medicines.

4.2.2 Control of moisture content in TCM

The moisture content is very important for the quality control of TCM. If the moisture content is high, mildew can form. If the moisture content is low, it will affect the shaping of its dosage form and drug properties. The toluene method and gas chromatography are used widely for determination of the water content in TCM. However, the toluene method has a certain amount of toxicity, whereas gas chromatography has some limitations (high consumption of solvent, limited detection types and complicated preparation of samples). Traditional moisture-detection methods are time-consuming and inefficient. Hence, an efficient and convenient method for determination of the water content in TCM is needed urgently (Shi et al., 2011). THz waves are very sensitive to water content, so THz-TDS technology could be used to detect the moisture content of TCM. Ma et al. used THz-TDS technology to measure the moisture content of medicinal Gastrodia elata BI, and obtained its THz absorption spectrum (Ma and Yang, 2017) (Ma et al., 2017). The absorption coefficient increased with increasing frequency. At an identical frequency, the higher the moisture content, the greater was the absorption (Figure 12E). Linear fitting data at 0.5 and 1.0 THz revealed a positive linear correlation between the absorption coefficient and moisture content, and the correlation coefficient was 0.982 and 0.977, respectively (Figure 12F). The research stated above indicated that THz-TDS technology could be employed to detect the moisture content in a Chinese herbal medicine rapidly, which provides a reliable method for the quality control of TCM.

4.2.3 Monitoring of adulteration of TCM

The variety and sources of Chinese herbs, coupled with the mentality of illegal drug dealers, have made the adulteration of TCM and Chinese medicinal decoctions a major issue. This problem can aggravate illnesses and endangered the health of patients. Several researchers have used THz-TDS technology to explore the adulteration of TCM. Most of the incidents of “pearl powder” adulteration have been caused by replacing pearl powder with shell powder or adding shell powder into pearl powder. Therefore, quantitative analyses of the content of shell powder in pearl powder are important. Guo measured the most common freshwater pearl powder, shell powder and their mixtures

(Guo C. S., 2012) (Guo, 2012). They obtained the spectra of the refractive index and absorption coefficient in the range 0.2–1.5 THz. The PLS regression model of the refractive index and mass percentage of shell powder were established using the refractive-index spectrum for quantitative analyses. This method provided a reference for the quantitative detection of adulteration of pearl powder and shell powder, and was rapid and simple. Li et al. used THz-TDS technology to quantitatively detect the content of seed potato starch in kudzu (Li B. et al., 2019) (Li et al., 2019). They established quantitative detection models of kudzu powder mixed with seed potato starch by PLS and least squares support vector machine (LS-SVM), respectively. The LS-SVM model could be more accurate for the rapid and non-destructive quantitative detection of kudzu powder mixed with seed potato starch. Xu et al. used THz-TDS technology combined with chemometric methods to identify pure unibract fritillary bulb and five types of adulterated unibract fritillary bulb powder (Xu et al., 2021). Through establishment of a classification model based on partial least squares discriminant analysis (PLS-DA), correct identification of these six samples was reached 100% of the time. Hence, this method could be employed to distinguish between pure Fritillariae cirrhosae bulbus and samples containing adulterants.

Li et al. used THz-TDS technology combined with chemometric methods to detect the adulteration of similar substances in Panax notoginseng powder (Li et al., 2022). Four types of samples were prepared in their study: three kinds of adulterated samples of P. notoginseng powder were adulterated with zedoary turmeric powder; P. notoginseng powder was adulterated with wheat flour; P. notoginseng powder was adulterated with rice flour. Comparison of the spectra of identical adulterated samples at different concentrations and the spectra of different adulterated samples was undertaken. The THz spectra of samples showed significant differences for identically adulterated samples at different concentrations. The spectral information of samples with varying types of adulteration also showed significant differences. In addition, Li used the same method and technology to explore the rapid and undamaged detection of the adulteration of kudzu powder (Li et al., 2021). The absorption coefficient was analyzed through the THz spectral data obtained. They built a model and optimized it. The comparison revealed that the radial basis function of the least squares support vector machines decision analysis based on elimination of the uninformative variables prediction model for adulteration of kudzu powder was more accurate than the others. Hence, THz-TDS combined with chemometric methods could provide a rapid and accurate method for qualitative analyses of adulteration of kudzu powder.

4.2.4 Monitoring of harmful substances in TCM

The four types of hazardous substances that may be present in TCM are heavy metals, aflatoxin, pesticide residues and microorganisms (Li, 2005). In addition, during the production and processing of TCM, some residues of pollutants may be introduced. The existence of these harmful substances reduces the quality of TCM, but also affects their safety. Therefore, it is particularly important to establish a standard method for the detection of the residues of harmful substances. Zhang et al. used THz-TDS technology combined with an improved PLS method to quantitatively determine the harmful additive auramine O in the medicinal herb Pollen Typhae (Zhang and Li, 2018) (Zhang et al., 2018). A THz-TDS system was built to collect the absorbance spectra, and stacked partial least squares based on variable contribution sorting (VIP-SPLS) was used to establish a correlation between the absorbance and content of auramine O. Compared with the original PLS and SPLS, VIP-SPLS obtained a better performance. That study indicated that THz-TDS technology combined with VIP-PLSR could be employed for the rapid and non-destructive detection of residues of harmful additives. Liu et al. used THz-TDS technology to quantitatively analyze the content of benzoic acid in kudzu powder (Liu et al., 2019) (Liu et al., 2019). They compared a group without plastic packaging with a group with plastic packaging. Multivariate scattering correction, baseline correction, first derivative, second derivative and other methods were used to pre-process the original data, and the PLS method was employed to establish a prediction model for the content of benzoic acid in kudzu powder. The determination factor of the plastic bag-free sample was 0.975 and RMSEP was 1.126%. The determination factor of the plastic-bag sample was 0.976 and RMSEP was 1.356%. Those results showed that the THz pulse absorbed by the plastic packaging could be ignored, so THZ-TDS technology could be used to realize the non-destructive detection of benzoic-acid content in kudzu powder. THz-TDS technology could also be employed for the detection and analyses of three antibiotics and two acaricides in honey products (Massaouti et al., 2013). Those five chemicals had obvious absorption peaks in 0.5–6.0 THz (Figures 12G, H). Therefore, this method could be used to determine various chemical residues in honey rapidly and accurately.

5 Application in analyses of biological drugs

5.1 Qualitative analyses

Biological drugs include antitoxins, immunoglobulins and interferons. In general, they are proteins or macromolecular polypeptides. Several mature technologies are available for qualitative detection of protein or peptide biological drugs, such as peptide mapping, amino-acid analysis and electrophoresis. For antibody-based drugs, the commonly used detection methods are enzyme-linked immunosorbent assay and immunofluorescence. These methods are used widely and their sensitivity can result in detection. However, the detection process of some of these technologies is troublesome, complex, time-consuming and destructive to the sample, so repeat detection is not possible. Therefore, finding a rapid, convenient and non-destructive qualitative detection method to identify proteins, peptides or antibody-based drugs is needed.

An amino acid is the smallest unit of polypeptides and proteins. Amino acids have specific absorption peaks in the THz band, which can be used to establish fingerprints and databases for rapid qualitative identification of different types of amino acids. Li et al. measured the absorption spectrum of reduced glutathione at the 0.1–2 THz band and found that it had characteristic absorption peaks (Li et al., 2018). Kutteruf et al. studied the absorption spectra of some short-chain peptides in the THz band. They found that with an increasing of number of amino

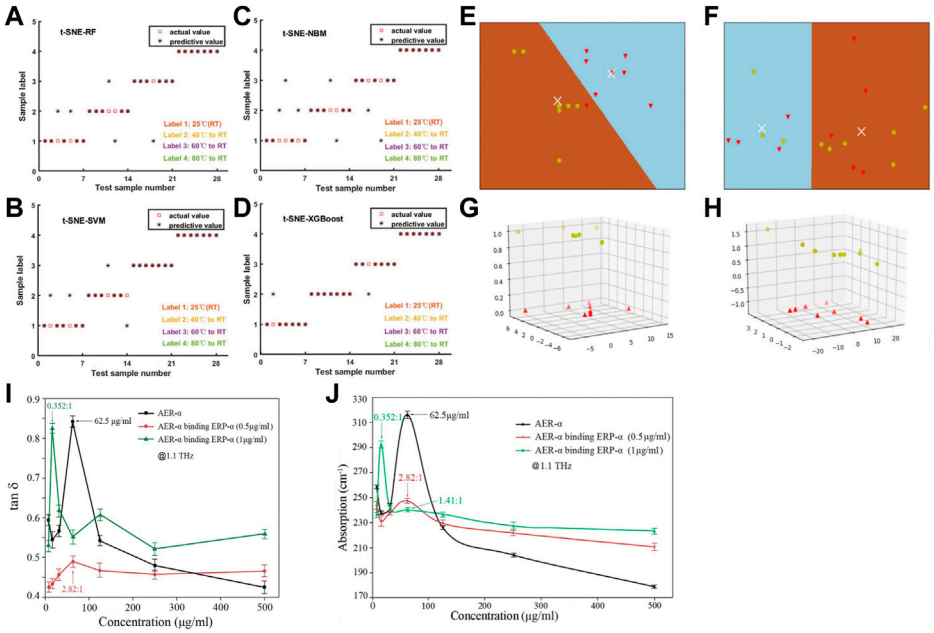

FIGURE 13
The comparison chart of test set obtained by applying **(A)** t-SNE-RF, **(B)** t-SNE-Naive Bayes model (NBM), **(C)** t-SNE-SVM and **(D)** t-SNE-XGBoost (Cao et al., 2021). Yellow point is FET and red point is ASF **(E)** 2D Feature by CMSE **(F)** 2D Feature by PCA **(G)** 3D Feature by CMSE **(H)** 3D Feature by PCA (Huang P. J. et al., 2020). **(I)** Plots of the dielectric loss tangent for AER-a, AER-a binding ERP-a (0.5 μg/ml), and AER-a binding ERP-a (1 μg/ml) at 1.1 THz. **(J)** Absorption coefficient of AER-a, AER-a binding ERP-a (0.5 μg/ml), and AER-a binding ERP-a (1 μg/ml) at 1.1 THz (Li et al., 2017).

acids that comprised the peptide chain, the corresponding absorption spectra became more complex (Kutteruf et al., 2003). Tan used THz-TDS technology to measure the absorption and refractive-index spectra of bovine serum albumin (BSA) at different temperatures (Tan, 2018). BSA had no obvious absorption peak in the 0–1.4 THz band, and only a monotonous upward curve appeared with increasing frequency. As the temperature increased, the average absorption coefficient decreased because the secondary structure of BSA molecules (e.g., α-helix) changed upon heating.

In general, solid-phase proteins have no obvious characteristic absorption peak in the THz band. Different protein samples can only be distinguished according to the difference in absorption coefficient and refractive index. The protein to be detected will, in general, dissolve in water to form a liquid phase. However, water has strong absorption in the THz band, which makes the characteristic absorption peak more difficult to measure. To solve these problems, some scholars have combined THz-TDS technology with machine learning to distinguish different proteins. For example, Cao et al. used two dimension-reduction algorithms and four machine-learning models to solve the identification problem of BSA samples with multiple conformations induced by different heating conditions (Cao et al., 2021) (Cao et al., 2020). A combination of the t-distributed stochastic neighbor embedding (t-SNE) algorithm and extreme gradient boosting (XGBoost) had the highest recognition accuracy (Figures 13A–D). Huang et al. through composite multiscale entropy (CMSE) feature extraction method to identify glycoprotein ASF and FET (Huang P. J. et al., 2020) (Huang et al., 2021). Features are clustered by the K-means algorithm. The results indicated that features extracted by the CMSE method were better than the PCA method in both specificity and sensitivity of recognition (Figures 13E–H). Meanwhile, the absorption coefficient and dielectric loss angle tangent (tan δ) were more suitable for qualitative identification.

Tan δ is a parameter in the THz dielectric spectrum. Tan δ can also be used to reflect the binding of antigen and antibody. Tan δ reveals more deeply the physical mechanism of molecular interaction, but FTIR spectroscopy and Raman spectroscopy cannot provide this information. Therefore, THz-TDS technology has a unique advantage in qualitative analyses of biological drugs. Li et al. monitored the interaction between anti-estrogen receptor-α (AER-α) and different concentrations of the polypeptide fragment of estrogen receptor-α (ERP-α) by THz dielectric spectroscopy (Figures 13I, J) (Li et al., 2017). Sun et al. used a THz-TDS system to measure the THz spectra of different concentrations of a solution of hemagglutinin protein of influenza A H9N2 and its reaction with antibody F10 (specific binding) and unrelated antibody irmAb (negative control) (Sun et al., 2015). The most sensitive optical parameters of THz in the antigen reaction system and antigen-antibody reaction system were screened by spectral pretreatment and PCA. According to the optimal comparison of clustering analysis, the dielectric loss angle tangent was the most suitable parameter for the qualitative analysis of HA-F10 interaction.

THz-TDS technology combined with “metamaterials” could also be used to qualitatively analyze antigen–antibody reactions or other proteins. The sensing mechanism of metamaterial sensors is interesting: molecules from different compounds cover their

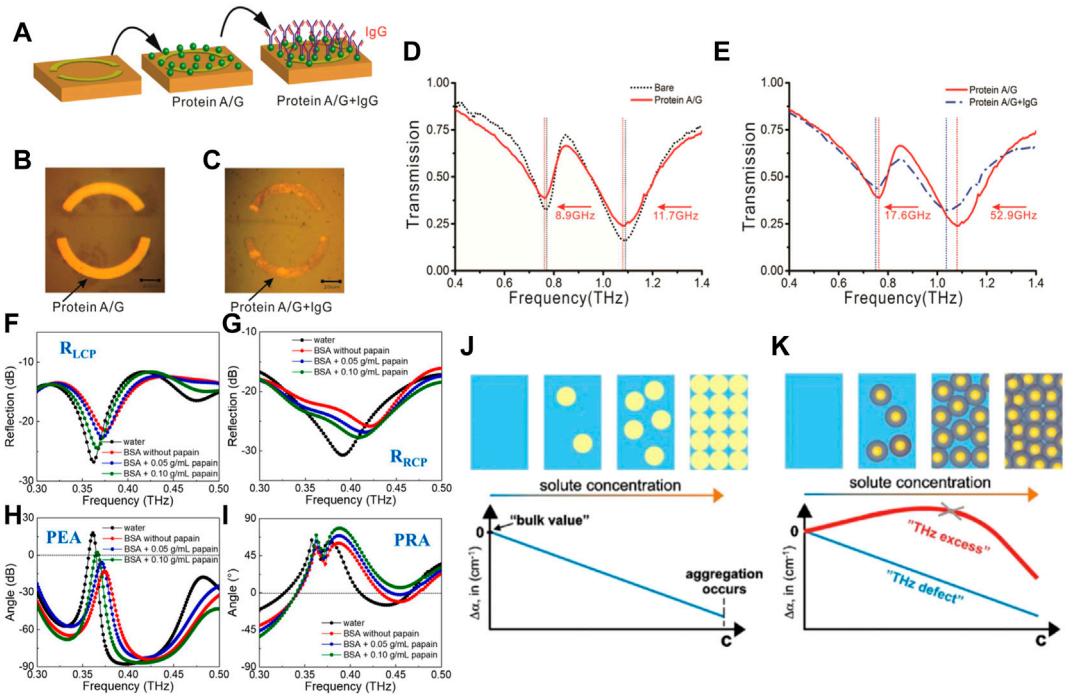

FIGURE 14
The preparation process of Protein A/G and protein A/G + IgG. **(A)** Schematic of protein A/G and protein IgG preparation process. Microscope images of samples **(B)** protein A/G and **(C)** protein A/G + IgG, respectively. The measured THz transmissions of the ASRs biosensors after **(D)** protein A/G and **(E)** protein A/G + IgG (Cheng et al., 2020). **(F)** Left characteristic polarization reflection spectra (RLCP), **(G)** Right characteristic polarization reflection spectra (RRCP), **(H)** polarization elliptical angle (PEA), and **(I)** polarization rotation angle (PRA) spectra of water, BSA solution and BSA added with 0.05 g/mL and 0.10 g/mL papain solutions, respectively (Zhang et al., 2022). Concepts of THz hydration: Shown are the concepts of THz defect **(J)** and THz excess **(K)**. The former describes linear changes of THz absorbance with increasing solute concentration for biomolecules (yellow spheres) dissolved in water (blue) with disregard to hydration. The latter displays the non-linear behaviour of the concentration dependent absorption coefficient, thereby taking into account a dynamical hydration shell (dark gray spheres) for biomolecules (orange spheres) in water (blue) (Born and Havenith, 2009).

surfaces and cause a change in resonance frequency. Niu et al. presented a toroidal metamaterial biosensor integrated with functionalized gold nanoparticles (Niu et al., 2023. Carcinoembryonic antigen biomarkers with various concentrations and four types of proteins were measured by the designed biosensor, achieved a limit of detection of 0.17 ng and high specificity. Cheng et al.used a designed hypersurface biosensor based on Fano resonance to detect the recombinant protein A/G, sheep anti-mouse immunoglobulin G (Ig G) and their specific binding with high sensitivity (Figures 14A–E) (Cheng et al., 2020). Zhang et al. proposed a THz polarization-sensing method combining a THz reflective time-domain polarization spectroscopy-sensing system and a flexible chiral hypersurface sensor to realize the proteolysis sensing of BSA in a papain reaction (Figures 14F–I) (Zhang et al., 2022). The sensor and sensing method could be used to detect changes of molecular structure during protein hydrolysis.

5.2 Quantitative analyses

The absorption coefficient of a protein solution in THz band does not show a good linear relationship with its concentration according to the Lambert–Beer law. With an increase in the solute concentration, the absorption coefficient increases initially and then decreases. The explanation proffered by Benjamin et al. for this phenomenon has been accepted widely: “THz defect” and “THz excess” (Figures 14J, K) (Born and Havenith, 2009). “THz excess” explains the nonlinear phenomenon that the THz absorption coefficient varies with concentration after the combination of biomolecules and solvents in a certain concentration range. Therefore, it is difficult to determine the exact concentration of the protein solution directly through the absorption spectrum.

Currently, there are generally two common methods for quantitative analysis of proteins: THz-TDS technology combined with metamaterials (i.e., metamaterial biosensors) and THz-TDS technology combined with machine learning. For example, Lin et al. proposed a THz metasurface immunosensor coupled with gold nanoparticles, which had good biocompatibility and high specific surface area for biomarkers (Lin et al., 2022). The detection performance of the THz immunosensor was also verified with different concentrations of CA125 and CA199. The experimental results showed that the frequency shift of the resonance peak was linearly related to the concentration of CA125 and CA199. The detection limits for both CA125 and CA199 were 0.01 U/ml, which was better than that of other common methods. Sun et al. probed BSA deposited thin-films prepared used solutions with concentrations ranging from 0.5 to 35 mg/mL by support vector regression (SVR) method (Sun et al., 2018). The learned mode accurately predicted the concentrations of the unknown test samples with a coefficient of determination of $R^2 = 0.97272$. Furthermore, the

maximal information coefficient (MIC) was applied and three most relevant frequencies to the target concentrations were identified at 1.2, 1.1, and 0.5 THz, respectively. This meant that a good prediction for BSA concentration could be achieved by using the top three relevant frequencies, and further proved the efficiency and practicability of the THz spectroscopy and machine learning methods.

6 Prospects and challenges

THz technology is an important interdisciplinary field. It provides unprecedented opportunities for promoting technological innovation, accelerating economic development and ensuring national security. A THz wave has a strong interaction with a drug molecule. The THz spectrum of drug molecules contains a lot of information on physical and chemical properties. Therefore, much attention has been paid to the application of THz-TDS technology in pharmaceutical analysis. However, some problems need to be solved jointly by scientists and engineers to promote the development of this technology in pharmaceutical analyses.

First, THz-TDS technology has two main problems: resolution and cost. Resolution is one of the most important indicators of analytical instruments. According to the working principle of the instrument, the resolution of the THz-TDS system is inversely proportional to the length of the time-domain signal. The length of the time-domain signal is related to the adjustable length of the delay line. However, the adjustable length of the delay line in the system is short, which determines the low resolution of the THz time-domain spectrometer from the structure. THz instruments are bulky and expensive, and only universities or institutions with sufficient funds can engage in this research which, to a certain extent, restricts application of this technology. Therefore, the development of portable, inexpensive, high-resolution and strong-specificity THz instruments is an important future direction.

Second, there are several problems in pharmaceutical analyses: detection environment, detection standards and databases. Water has strong absorption in the THz band. Hence, water vapor in air causes a lot of noise, resulting in poor sensitivity and a weak THz spectral signal. Air humidity will not eliminate the original absorption peak of the substance, but will introduce additional absorption peaks. The higher the humidity, the more burrs (noise), and the more difficult it is to identify the characteristic peak. Therefore, the interference wrought by water should be eliminated during sample detection, such as filling N_2 to reduce the impact of the environment on the THz spectrum and improving the spectral signal-to-noise ratio, sensitivity and stability. In addition, the accuracy of the THz instrument, sample source, measurement environment, sample pretreatment and data-processing methods are different, which results in the poor compatibility and comparability of measurement data. The next step is to establish a standardized and unified database and THz fingerprints of major drugs.

In analyses of chemical drugs, the main problem is the lack of sensitivity, especially for the detection of trace levels of drugs. The detection accuracy is poor due to the weak absorption intensity of samples in the THz band. Research teams have used metamaterials, parallel-plate metal waveguides and other methods to enhance the sensitivity and accuracy of THz technology, and achieved a good enhancement effect (Wang Y. et al., 2022) (Hou et al., 2021). In addition, there are some challenges of theoretical works by DFT calculations on the THz spectroscopy of molecules. Although the quantum chemical calculation provides us with much valuable information, there are some offset compared with the experimental results. And the following reasons may be worth considering, such as the temperature effect of experiments and simulations, humidity and pressure of environment, system error of experimental measurements etc. Furthermore, the disparity of crystals situations in actual experiments and theoretical simulations also need to take into consideration. On the one hand, the purity and pretreatment of the samples used may be different. On the other hand, the calculation is based on the perfect crystal structure, while the actual system is difficult to idealize.

There are three main problems in analyses of medicinal herbs in TCM. First, herbs have a wide range of sources, varieties, and active ingredients are diverse and complex. For substances without an obvious THz absorption peak, it is difficult to distinguish them using absorption spectroscopy, which requires further classification and identification by combining machine-learning algorithms and chemometrics. Therefore, a combination of THz-TDS technology and an effective analytical model will be the key for analyses of TCM. Second, because the chemical composition of medicinal herbs and TCM is diverse and complex, it is difficult to use DFT to directly simulate their molecular structure, so a THz characteristic absorption peak cannot be assigned. Establishment of a more effective molecular-structure model of medicinal herbs and TCM and simulation analysis for more scenarios will help to better explain the THz characteristic absorption peaks of medicinal herbs and TCM. Third, the residue of harmful substances in TCM is a key factor in the quality control of TCM, but little research on THz-TDS technology in this area has been done. Therefore, efforts should be made to promote application of THz-TDS technology in the monitoring of the residues of pesticides and harmful components to supplement and improve the quality control of TCM. In addition, THz-TDS technology can be used to monitor changes in the chemical components of TCM. When a TCM is processed into crude slices and then made into a patent medicine, the efficacy of the TCM is different at each stage. This difference arises from a series of chemical changes in the processing of the chemical components in the TCM. Monitoring the production of effective components and the decomposition of harmful components by THz-TDS technology can provide necessary data for the pharmacological research of the TCM, but can also be used for quality control in the production process of TMCFs.

In analyses of biological drugs, two main problems are prominent. First, the protein has no characteristic absorption peak in the THz band. Amino acids and short-chain peptides have characteristic absorption peaks in the THz band, and their spectra become more complex as the number of peptide chains increases. A continuous increase in molecular weight, on the one hand, enables amino acids to fold through intermolecular interaction to form a spatial structure but, on the other hand, causes the molecular-skeleton vibration to overlap. The inevitable effect on the THz spectrum is to "submerge" the characteristic absorption of each amino acid. Therefore, proteins and macromolecular peptides have no characteristic absorption peaks in the THz band.

There must be a "node" between small molecular peptides and macromolecular peptides. Before this node, the absorption peak can be used as a parameter for reference. After this node, the absorption peak is submerged and cannot be measured. The components of biological drugs are mostly proteins with very high molecular weights. Even peptide drugs, such as human insulin and human epidermal growth factor, have molecular weights of 5.8 and 6 kDa, respectively. Obviously, they are unable to distinguish different structures through changes in the frequency and intensity of characteristic absorption peaks in the terahertz band, nor can they establish a one-to-one corresponding fingerprint database like amino acids. Second, the absorption coefficient and concentration of a protein solution in the THz band do not conform to the Lambert–Beer law, which hampers spectral quantitative analysis of biological drugs. Widely used methods for quantitative analyses of proteins include immunofluorescence and enzyme-linked immunosorbent assay. Methods for qualitative analyses of proteins include peptide mapping. These methods are complex and cumbersome, but THz-TDS technology is not very mature for analyses of biological drugs, or has few advantages. Compared with test kits, the THz instrument is too expensive and inconvenient to carry. Only if THz-TDS technology shows clear advantages over other detection technologies can the disadvantages of THz instruments (expense and non-portability) be ignored. Therefore, the development of biosensors based on metamaterials will be the key to solve the problem of THz-TDS technology for biomedical analyses in the future.

Author contributions

All authors listed have made a substantial, direct, and intellectual contribution to the work and approved it for publication.

Conflict of interest

The authors declare that the research was conducted in the absence of any commercial or financial relationships that could be construed as a potential conflict of interest.

Publisher's note

All claims expressed in this article are solely those of the authors and do not necessarily represent those of their affiliated organizations, or those of the publisher, the editors and the reviewers. Any product that may be evaluated in this article, or claim that may be made by its manufacturer, is not guaranteed or endorsed by the publisher.

References

Auston, D. H., Cheung, K. P., Valdmanis, J. A., and Kleinman, D. A. (1984). Cherenkov radiation from femtosecond optical pulses in electro-optic media. *Phys. Rev. Lett.* 53 (16), 1555–1558. doi:10.1103/physrevlett.53.1555

Bai, J. P., Li, B., Zhang, S. J., and Chen, Y. M. (2021). Study on norfloxacin concentration detection based on terahertz time domain spectroscopy. *Spectrosc. Spectr. Analysis* 41 (09), 2710–2716. doi:10.3964/j.issn.1000-0593(2021)09-2710-07

Born, B., and Havenith, M. (2009). Terahertz dance of proteins and sugars with water. *J. Infrared Milli Terahz Waves* 30, 1245–1254. doi:10.1007/s10762-009-9514-6

Bourgeois, M. L. (2014). Lithium since 1950. *Ann. Médico-psychologiques* 172 (3), 170–172. doi:10.1016/j.amp.2014.02.016

Cao, C., Zhang, Z. H., Zhao, X. Y., and Zhang, T. T. (2021). Terahertz spectroscopy and machine learning algorithm for non-destructive evaluation of protein conformation. *Opt. Quantum Electron.* 52 (4), 225. doi:10.1007/s11082-020-02345-1

Cao, Y. Y., Li, X., Bai, J. P., Xu, W., Ni, Y., Zhong, H. L., et al. (2022). Study on qualitative and quantitative detection of pefloxacin and fleroxacin veterinary drugs based on THz-TDS technology. *Spectrosc. Spectr. Analysis* 42 (06), 1798–1803. doi:10.3964/j.issn.1000-0593(2022)06-1798-06

Chen, J. M., Wu, C. B., and Lu, T. B. (2011). Application of supramolecular chemistry on pharmaceutical cocrystals. *Chem. J. China Univ.* 32 (09), 1996–2009.

Chen, T., Cai, Z. H., Hu, F. R., Yin, X. H., and Xu, C. P. (2019). A study of terahertz spectra of monosaccharides and disaccharides with StructuralSimilarities. *Spectrosc. Spectr. Analysis* 39 (03), 686–692. doi:10.3964/j.issn.1000-0593(2019)03-0686-07

Chen, T., Li, Z., Mo, W., and Hu, F. R. (2013). Simultaneous quantitative determination of multicomponents in tablets based on terahertz time-domain spectroscopy. *Spectrosc. Spectr. Analysis* 33 (05), 1220–1225. doi:10.3964/j.issn.1000-0593(2013)05-1220-06

Chen, W., Peng, Y., Jiang, X., Zhao, J., Zhao, H., and Zhu, Y. (2017). Isomers identification of 2-hydroxyglutarate acid disodium salt (2HG) by terahertz time-domain spectroscopy. *Sci. Rep.* 7 (1), 12166. doi:10.1038/s41598-017-11527-z

Cheng, R. J., Xu, L., Yu, X., Zou, L. E., Shen, Y., and Deng, X. H. (2020). High-sensitivity biosensor for identification of protein based on terahertz Fano resonance metasurfaces. *Opt. Commun.* 473, 125850. doi:10.1016/j.optcom.2020.125850

Cho, E., Cho, W., Cha, K. H., Park, J., Kim, M. S., Kim, J. S., et al. (2010). Enhanced dissolution of megestrol acetate microcrystals prepared by antisolvent precipitation process using hydrophilic additives. *Int. J. Pharm.* 396 (1-2), 91–98. doi:10.1016/j.ijpharm.2010.06.016

Dai, H., Xu, K. J., Jin, B. B., Wu, K. Q., and Liu, B. (2013). Terahertz spectroscopy of β-lactam antibiotics. *Infrared Laser Eng.* 42 (01), 90–95.

Delaney, S. P., Pan, D., Galella, M., Yin, S. X., and Korter, T. M. (2012a). Understanding the origins of conformational disorder in the crystalline polymorphs of irbesartan. *Cryst. Growth & Des.* 12 (10), 5017–5024. doi:10.1021/cg300977e

Delaney, S. P., Witko, E. M., Smith, T. M., and Korter, T. M. (2012b). Investigating tautomeric polymorphism in crystalline anthranilic acid using terahertz spectroscopy and solid-state density functional theory. *J. Phys. Chem. A* 116 (30), 8051–8057. doi:10.1021/jp303961w

Doron, S. I., Beaulac, K. R., Dhand, A., and Snydman, D. R. (2017). Mechanisms of resistance in metronidazole. In D. L. Mayers, J. D. Sobel, M. Ouellette, K. S. Kaye, and D. Marchaim (Eds.) *Antimicrobial drug resistance: Mechanisms of drug resistance*, (United Kingdom; Oxford University Press).

Dressel, M., Drichko, N., Gorshunov, B., and Pimenov, A. (2008). Thz spectroscopy of superconductors. *IEEE J. Sel. Top. Quantum Electron.* 14 (2), 399–406. doi:10.1109/JSTQE.2007.910764

Du, Y., Xia, Y., Tang, W. J., and Hong, Z. (2014). Investigation of sulfamethoxazole polymorphism with terahertz time-domain spectroscopica technique. *Infrared Laser Eng.* 43 (09), 2919–2924.

Dubey, R., and Desiraju, G. R. (2014). Structural landscape of the 1 : 1 benzoic acid: Isonicotinamide cocrystal. *Chem. Commun. Camb. Engl.* 50 (10), 1181–1184. doi:10.1039/c3cc47955b

Esmaeili, M., Vettukattil, R., and Bathen, T. F. (2013). 2-hydroxyglutarate as a magnetic resonance biomarker for glioma subtyping. *Transl. Oncol.* 6 (2), 92–98. doi:10.1593/tlo.12424

Exter, M. V., Fattinger, C., and Grischkowsky, D. (1989a). High-brightness terahertz beams characterized with an ultrafast detector. *Appl. Phys. Lett.* 55 (4), 337–339. doi:10.1063/1.101901

Exter, M. V., Fattinger, C., and Grischkowsky, D. (1989b). Terahertz time-domain spectroscopy of water vapor. *Opt. Lett.* 14 (20), 1128–1130. doi:10.1364/OL.14.001128

Fang, H. X., Zhang, Q., Zhang, H. L., Hong, Z., and Du, Y. (2016). Experimental study and DFT calculation of FTIR, FT-Raman and THz-TDS spectra of Ⅰ and Ⅲ polymorphs of chlorpropamide. *Spectrosc. Spectr. Analysis* 36 (05), 1382–1388. doi:10.3964/j.issn.1000-0593(2016)05-1382-07

Ferrari, E. S., Davey, R. J., Cross, W. I., Gillon, A. L., and Towler, C. S. (2003). Crystallization in polymorphic Systems: the solution-mediated transformation of β to α Glycine. *Cryst. Growth & Des.* 3 (1), 53–60. doi:10.1021/cg025561b

Gao, J., Li, Y., Liu, J., Ling, D., Deng, X., Liu, B., et al. (2022). Terahertz spectroscopy detection of lithium citrate tetrahydrate and its dehydration kinetics. *Spectrochimica acta. Part A, Mol. Biomol. Spectrosc.* 266, 120470. doi:10.1016/j.saa.2021.120470

Gao, Y., Zu, H., and Zhang, J. J. (2010). The multiple actions of NO. *Prog. Chem.* 22 (05), 829–839. doi:10.1007/s00424-009-0773-9

Gui, Y., Ni, Y. N., and Kokot, S. (2011). Simultaneous determination of three 5-nitroimidazoles in foodstuffs by differential pulse voltammetry and chemometrics. *Chin. Chem. Lett.* 22 (05), 591–594. doi:10.1016/j.cclet.2010.12.014

Guinn, E. J., Schwinefus, J. J., Cha, H. K., Mcdevitt, J. L., Record, M. T., Ritzer, R., et al. (2013). Quantifying functional group interactions that determine urea effects on nucleic acid helix formation. *J. Am. Chem. Soc.* 135 (15), 5828–5838. doi:10.1021/ja400965n

Guo, C. S. (2012b).*Quantitative determination of pearl powder with terahertz spectroscopy*. (China: Master Dissertation, Jiliang University). https://kns.cnki.net/KCMS/detail/detail.aspx?dbname=CMFD201301&filename=1012488946.nh.

Guo, S. (2012a). *Research of traditional Chinese medicine terahertz spectroscopy and data management system*. China: Master Dissertation, Tianjin University.

Gurer-Orhan, H., Orhan, H., Suzen, S., Püsküllü, M. O., and Buyukbingol, E. (2006). Synthesis and evaluation of *in vitro* antioxidant capacities of some benzimidazole derivatives. *J. enzyme inhibition Med. Chem.* 21 (2), 241–247. doi:10.1080/14756360600586031

He, M., Azad, A. K., Ye, S., and Zhang, W. (2006). Far-infrared signature of animal tissues characterized by terahertz time-domain spectroscopy. *Opt. Commun.* 259 (1), 389–392. doi:10.1016/j.optcom.2005.08.029

He, W., Henne, A., Lauterbach, M., Geißmar, E., Nikolka, F., Kho, C., et al. (2022). Mesaconate is synthesized from itaconate and exerts immunomodulatory effects in macrophages. *Nat. Metab.* 4 (5), 524–533. doi:10.1038/s42255-022-00565-1

Hou, L., Shi, W., Dong, C. G., Yang, L., Wang, Y. Z., Wang, H. Q., et al. (2021). Probing trace lactose from aqueous solutions by terahertz timedomain spectroscopy. *Spectrochimica acta. Part A, Mol. Biomol. Spectrosc.* 246, 119044. doi:10.1016/j.saa.2020.119044

Hu, Q. F., and Cai, J. (2021). Research of terahertz time-domain spectral ldentification based on deep learning. *Spectrosc. Spectr. Analysis* 41 (01), 94–99. doi:10.3964/j.issn.1000-0593(2021)01-0094-06

Huang, L., Li, C., Li, B., Liu, M., Lian, M., and Yang, S. (2020a). Studies on qualitative and quantitative detection of trehalose purity by terahertz spectroscopy. *Food Sci. Nutr.* 8 (4), 1828–1836. doi:10.1002/fsn3.1458

Huang, P. J., Huang, Z. W., Lu, X. D., Cao, Y. Q., Yu, J., Hou, D. B., et al. (2020b). Study on glycoprotein terahertz time-domain spectroscopy based on composite multiscale entropy feature extraction method. *Spectrochimica acta. Part A, Mol. Biomol. Spectrosc.* 229, 117948. doi:10.1016/j.saa.2019.117948

Jin, S. J. (2020). *Detection and analysis about the pharmaceutical cocrystal structures of typical anti HBV drugs based on vibrational spectroscopy*. (Master Dissertation, China; Jiliang University).

Juliano, T. R., Jr, and Korter, T. M. (2013). Terahertz vibrations of crystalline acyclic and cyclic diglycine: Benchmarks for london force correction models. *J. Phys. Chem. A* 117 (40), 10504–10512. doi:10.1021/jp407112w

Kiwa, T., Tonouchi, M., Yamashita, M., and Kawase, K. (2003). Laser terahertz-emission microscope for inspecting electrical faults in integrated circuits. *Opt. Lett.* 28 (21), 2058–2060. doi:10.1364/ol.28.002058

Kutteruf, M. R., Brown, C. M., Iwaki, L. K., Campbell, M. B., Korter, T. M., and Heilweil, E. J. (2003). Terahertz spectroscopy of short-chain polypeptides. *Chem. Phys. Lett.* 375 (3-4), 337–343. doi:10.1016/S0009-2614(03)00856-X

Li, B., Du, X. Y., Liu, Y. D., and Hu, J. (2019b). Detection research of seed potato starch in kudzu using terahertz time-domain spectroscopy. *Laser & Optoelectron. Prog.* 56 (20), 322–327. doi:10.3788/LOP56.203001

Li, B., Luo, B., Liu, Y. D., and Wu, J. (2021). Detection of adulteration of kudzu powder by terahertz time-domain spectroscopy. *J. Food Meas. Charact.* 15 (5), 4380–4387. doi:10.1007/S11694-021-01023-4

Li, B., Yin, H., Yang, A. K., and Ouyang, A. G. (2022). Detection of adulteration of Panax notoginseng powder by terahertz technology. *J. Spectrosc.* 2022, 1–10. doi:10.1155/2022/7247941

Li, C., Wei, C. H., Wang, Z. Q., Huang, L. L., and Yang, S. Z. (2019a). Authenticity assessment of Cordyceps sinensis using terahertz spectroscopy. *J. Shenzhen Univ. Sci. Eng.* 36 (02), 213–220. doi:10.3724/SP.J.1249.2019.02213

Li, D. H., Song, B. B., Ji, B. B., Guo, X. S., Li, Z. X., and Zhou, W. (2018). Terahertz time-domain spectroscopy and vibration modes of reduced L-glutathione. *J. Shandong Univ. Sci. Technol. Nat. Sci.* 37 (02), 115–120. doi:10.16452/j.cnki.sdkjzk.2018.02.017

Li, G. L., Deng, H., Liu, Q. C., Guo, Z. C., Zhang, Q., and Shang, L. P. (2020a). Terahertz characteristic absorption spectral analysis of metronidazole. *Laser & Optoelectron. Prog.* 57 (17), 291–296. doi:10.3788/LOP57.173001

Li, M. L., Chang, T. Y., Wei, D. S., Tang, M. J., Yan, S. H., Du, C. L., et al. (2017). Label-free detection of anti-estrogen receptor alpha and its binding with estrogen receptor peptide alpha by terahertz spectroscopy. *RSC Adv.* 7, 24338–24344. doi:10.1039/c6ra28754a

Li, R. K., Hou, K. X., Zhang, L. N., Lou, C. G., and Liu, X. L. (2020b). Identification of three Chinese herbal medicines based on terahertz time-domain spectroscopy. *J. Hebei Univ. Nat. Sci. Ed.* 40 (04), 379–384. doi:10.3969/j.issn.10001565.2020.04.007

Li, S. F. (2005). Study on monitoring and perspective of harmful substances in traditional Chinese medicine. *Chin. Archives Traditional Chin. Med.* 23 (01), 86–87. doi:10.13193/j.archtcm.2005.01.84.lishf.040

Li, S. W., Wang, D., Liu, H. B., and Lu, T. Y. (2013a). Effects of norfloxacin on the drug metabolism enzymes of two sturgeon species (acipenser schrencki and acipenser ruthenus). *J. Appl. Ichthyology* 29 (6), 1204–1207. doi:10.1111/jai.12239

Li, X. X., D, H., Liao, H. T., Shang, L. P., and He, J. (2013b). Analysis of the terahertz spectrum of Chinese herbal medicine aconite at room temperature. *Laser & Infrared* 43 (11), 1282–1285. doi:10.3969/j.issn.1001-5078.2013.11.18

Liang, J., Guo, Q., Chang, T., Ke, L., and Cui, H. L. (2018). Reliable origin identification of scutellaria baicalensis based on terahertz time-domain spectroscopy and pattern recognition. *Optik* 174, 7–14. doi:10.1016/j.ijleo.2018.08.050

Lin, S. J., Wang, Y. L., Peng, Z. Y., Chen, Z. C., and Hu, F. R. (2022). Detection of cancer biomarkers CA125 and CA199 via terahertz metasurface immunosensor. *Talanta* 248, 123628. doi:10.1016/j.talanta.2022.123628

Liu, H., Zhang, Z., Yang, Y., Chen, T., and Zhang, C. (2018). Identification terahertz spectra for the dyestuffs based on principal component analysis and savitzky-golay filter. *Optik - Int. J. Light Electron Opt.* 172, 668–673. doi:10.1016/j.ijleo.2018.07.079

Liu, L. Y., Chang, T. Y., Li, K., Li, Y. Z., Zhang, X. S., and Xu, W. Q. (2020). Spectral analysis and quantitative detection of baicalin based on terahertz radiation. *Chin. J. Lasers* 47 (03), 313–319. doi:10.3788/CJL202047.0314001

Liu, S., and Sun, H. F. (2019). Common technology and its applicaion in the field of quality control of Traditional Chinese Medicine. *Chem. Eng.* 33 (02), 60–64. doi:10.16247/j.cnki.23-1171/tq.20190260

Liu, Y. D., Du, X. Y., Li, B., Hu, J., Wu, J., and Zheng, Y. L. (2019). Detection of benzoic acid in arrowroot by terahertz technology. *Laser & Optoelectron. Prog.* 56 (04), 123–129. doi:10.3788/LOP56.041101

Liu, Y. D., Hu, J., Li, M. P., and Cui, H. Z. (2021). Research on variety ldentification of Fritillaria based on terahertz spectroscopy. *Spectrosc. Spectr. Analysis* 41 (11), 3357–3362. doi:10.3964/j.issn.1000-0593(2021)11-3357-06

Ma, P., and Yang, Y. P. (2017). Determination of moisture content of Gastrodia elata BI by terahertz spectroscopy. *J. Terahertz Sci. Electron. Inf. Technol.* 15 (01), 26–28. doi:10.11805/TKYDA201701.0026

Massaouti, M., Daskalaki, C., Gorodetsky, A., Koulouklidis, A. D., and Tzortzakis, S. (2013). Detection of harmful residues in honey using terahertz time-domain spectroscopy. *Appl. Spectrosc.* 67 (11), 1264–1269. doi:10.1366/13-07111

Nguyen, K. L., Friscić, T., Day, G. M., Gladden, L. F., and Jones, W. (2007). Terahertz time-domain spectroscopy and the quantitative monitoring of mechanochemical cocrystal formation. *Nat. Mater.* 6 (3), 206–209. doi:10.1038/nmat1848

Niu, Q., Fu, L. L., Zhong, Y. X., Cui, B., Zhang, G. L., and Yang, Y. P. (2023). Sensitive and specific detection of carcinoembryonic antigens using toroidal metamaterial biosensors integrated with functionalized gold nanoparticles. *Anal. Chem.* 95 (2), 1123–1131. doi:10.1021/acs.analchem.2c03836

Nüßler, D., and Jonuscheit, J. (2020). Terahertz based non-destructive testing (ndt). *tm-Technisches Mess.* 88 (4), 199–210. doi:10.1515/teme-2019-0100

Orr, L. M., Daniel, W. R., Campbell, J. L., and Thomley, M. W. (1958). Effect of nitrofurantion (furadantin) on morbidity after transurethral prostatic resection. *J. Am. Med. Assoc.* 167 (12), 1455–1459. doi:10.1001/jama.1958.02990290009003

Ozkay, Y., Tunali, Y., Karaca, H., and Işikdağ, I. (2010). Antimicrobial activity and a SAR study of some novel benzimidazole derivatives bearing hydrazone moiety. *Eur. J. Med. Chem.* 45 (8), 3293–3298. doi:10.1016/j.ejmech.2010.04.012

Pal, S. K., Peon, J., Bagchi, B., and Zewail, A. H. (2002). Biological water: Femtosecond dynamics of macromolecular hydration. *J. Phys. Chem. B* 106 (48), 12376–12395. doi:10.1021/jp0213506

Pan, T. T. (2017). The application research of terahertz spectra in the molecular structures of amino acids. (Master dissertation, east China university of science and technology). https://kns.cnki.net/KCMS/detail/detail.aspx?dbname=CMFD201702&filename=1017151283.nh.

Qiao, N., Li, M., Schlindwein, W., Malek, N., Davies, A., and Trappitt, G. (2011). Pharmaceutical cocrystals: An overview. *Int. J. Pharm.* 419 (1-2), 1–11. doi:10.1016/j.ijpharm.2011.07.037

Qin, J., Xie, L., and Ying, Y. (2017). Rapid analysis of tetracycline hydrochloride solution by attenuated total reflection terahertz time-domain spectroscopy. *Food Chem.* 224, 262–269. doi:10.1016/j.foodchem.2016.12.064

Qu, F., Lin, L., He, Y., Nie, P., Cai, C., Dong, T., et al. (2018). Spectral characterization and molecular dynamics simulation of pesticides based on terahertz time-domain spectra analyses and density functional theory (DFT) calculations. *Mol. (Basel, Switz.* 23 (7), 1607. doi:10.3390/molecules23071607

Rakesh, K. J., Jat, J. L., and Pathak, D. P. (2006). Synthesis of benzimidazole derivatives: As anti-hypertensive agents. *J. Chem.* 3 (4), 278–285. doi:10.1155/2006/765712

Rao, J. Q., Chen, L. Y., Bai, P. P., Zhang, T. T., Zhao, Q. D., and Qiu, F. (2021). Identification of four origins of Curcuma based on terahertz time-domain spectroscopy. *Laser & Optoelectron. Prog.* 58 (22), 35–43. doi:10.3788/LOP202158.2200002

Revollo, J. R., Grimm, A. A., and Imai, S. (2007). The regulation of nicotinamide adenine dinucleotide biosynthesis by Nampt/PBEF/visfatin in mammals. *Curr. Opin. gastroenterology* 23 (2), 164–170. doi:10.1097/MOG.0b013e32801b3c8f

Roberts, E. L. (1950). A case of chronic mania treated with lithium citrate and terminating fatally. *Med. J. Aust.* 2 (7), 261–262. doi:10.5694/j.1326-5377.1950.tb81010.x

Rodríguez-Molina, B., Ochoa, M. E., Romero, M., Khan, S. I., Farfán, N., Santillan, R., et al. (2013). Conformational polymorphism and isomorphism of molecular rotors with fluoroaromatic rotators and mestranol stators. *Cryst. Growth & Des.* 13 (11), 5107–5115. doi:10.1021/cg4012873

Seoane-Viaño, I., Januskaite, P., Alvarez-Lorenzo, C., Basit, A. W., and Goyanes, A. (2021). Semi-solid extrusion 3D printing in drug delivery and biomedicine: Personalised solutions for healthcare challenges. *J. Control. release official J. Control. Release Soc.* 332, 367–389. doi:10.1016/j.jconrel.2021.02.027

Server, A., Josefsen, R., Kulle, B., Maehlen, J., Schellhorn, T., Gadmar, O., et al. (2010). Proton magnetic resonance spectroscopy in the distinction of high-grade cerebral gliomas from single metastatic brain tumors. *Acta Radiol.* 51 (3), 316–325. doi:10.3109/02841850903482901

Shete, A., Murthy, S., Korpale, S., Yadav, A., Sajane, S., Sakhare, S., et al. (2015). Cocrystals of itraconazole with amino acids: Screening, synthesis, solid state characterization, *in vitro* drug release and antifungal activity. *J. drug Deliv. Sci. Technol.* 28, 46–55. doi:10.1016/j.jddst.2015.05.006

Shi, H. Q., Bai, Y., Xie, C. X., Gong, H. Y., and Wang, X. (2011). Content determination of moisture in liuwei dihuang pills from different manufacturers by near-infrared spectroscopy. *Res. Explor. Laboratory* 30 (05), 38–41. doi:10.3969/j.issn.1006-7167.2011.05.012

Simmen, B., Weymuth, T., and Reiher, M. (2012). How many chiral centers can Raman optical activity spectroscopy distinguish in a molecule? *J. Phys. Chem. A* 116 (22), 5410–5419. doi:10.1021/jp303428f

Song, M., Yang, F., Liu, L., Shen, L., Hu, P., Zhang, L., et al. (2018). Research on the differences between 2-(2-Chlorophenyl)benzimidazole and 2-(4-Chlorophenyl) benzimidazole based on terahertz time domain spectroscopy. *Spectrochimica acta. Part A, Mol. Biomol. Spectrosc.* 196, 49–57. doi:10.1016/j.saa.2018.02.003

Stancu, C., and Sima, A. (2001). Statins: Mechanism of action and effects. *J. Cell. Mol. Med.* 5 (4), 378–387. doi:10.1111/j.1582-4934.2001.tb00172.x

Strachan, C. J., Rades, T., Newnham, D. A., Gordon, K. C., Pepper, M., and Taday, P. F. (2004). Using terahertz pulsed spectroscopy to study crystallinity of pharmaceutical materials. *Chem. Phys. Lett.* 390 (1-3), 20–24. doi:10.1016/j.cplett.2004.03.117

Sun, Y. W., Du, P. J., Lu, X. X., Xie, P. F., Qian, Z. F., Fan, S. T., et al. (2018). Quantitative characterization of bovine serum albumin thin-films using terahertz spectroscopy and machine learning methods. *Biomed. Opt. express* 9 (7), 2917–2929. doi:10.1364/BOE.9.002917

Sun, Y. W., Zhong, J. L., Zuo, J., Zhang, C. L., and Dan, G. (2015). Principal component analysis of terahertz spectrum on hemagglutinin protein and its antibody. *Acta Phys. Sin.* 64 (16), 448–454. doi:10.7498/aps.64.168701

Tan, H. Y. (2018). Investigation of bovine serum albumin at different temperatures by terahertz time-domain spectroscopy. *Spectrosc. Spectr. Analysis* 38 (11), 3374–3378. doi:10.3964/j.issn.1000-0593(2018)11-3374-05

Tan, N. Y., and Zeitler, J. A. (2015). Probing phase transitions in simvastatin with terahertz time-domain spectroscopy. *Mol. Pharm.* 12 (3), 810–815. doi:10.1021/mp500649q

Tao, Y. H., Fitzgerald, A. J., and Wallace, V. P. (2020). Non-contact, non-destructive testing in various industrial sectors with terahertz technology. *Sensors (Basel, Switz.* 20 (3), 712. doi:10.3390/s20030712

Tian, J. H., Zhou, J., Zheng, X. X., Jiang, G. H., and Ma, Y. Y. (2018). Study on the ldentification technology of Chinese herbal medicines based on terahertz time-domain spectrometer. *China Med. Devices* 33 (07), 9–13. doi:10.3969/j.issn.1674-1633.2018.07.002

Wang, F., Sun, X., Zan, J., Li, M., Liu, Y., and Chen, J. (2022a). Terahertz spectra and weak intermolecular interactions of nucleosides or nucleoside drugs. *Spectrochimica acta. Part A, Mol. Biomol. Spectrosc.* 265, 120344. doi:10.1016/j.saa.2021.120344

Wang, P. F., Zhao, J. T., Zhang, Y. M., Zhu, Z. J., Liu, L. Y., Zhao, H. W., et al. (2022b). The fingerprints of nifedipine/isonicotinamide cocrystal polymorph studied by terahertz time-domain spectroscopy. *Int. J. Pharm.* 620, 121759. doi:10.1016/j.ijpharm.2022.121759

Wang, R. J., Zhang, Z. Y., Zhang, Z. W., and Xiang, Y. H. (2016). Identification of official rhubarb samples by using PLS and terahertz time-domain spectroscopy. *Spectrosc. Spectr. Analysis* 36 (02), 316–321. doi:10.3964/j.issn.1000-0593(2016)02-0316-06

Wang, Y., Zhang, X., Zhang, X. J., Zhou, T., Cui, Z. J., and Zhang, K. (2022c). A novel terahertz metasurface based on a single-walled carbon nanotube film for sensing application. *J. Mater. Chem. A* 10, 1780–1787. doi:10.1039/d1ta09396g

Wang, Z., Peng, Y., Shi, C., Wang, L., Chen, X., Wu, W., et al. (2021). Qualitative and quantitative recognition of chiral drugs based on terahertz spectroscopy. *Analyst* 146 (12), 3888–3898. doi:10.1039/d1an00500f

Wang, Z. Q. (2005). Polymorphism and drug availability. *Chin. J. Pharm.* 36 (7), 442–446.

Wei, A. J., Liu, S. J., Zuo, J., and Zhang, C. L. (2020). Application of terahertz spectroscopy in different ginseng detection. *Spectrosc. Spectr. Analysis* 40 (S1), 229–230.

Woodward, R. M., Cole, B. E., Wallace, V. P., Pye, R. J., Arnone, D. D., Linfield, E. H., et al. (2002). Terahertz pulse imaging in reflection geometry of human skin cancer and skin tissue. *Phys. Med. Biol.* 47 (21), 3853–3863. doi:10.1088/0031-9155/47/21/325

Xiao, T. T., Tang, H. Q., Zhang, Z. Y., Guo, C. B., Wang, G., and Liao, Y. (2019). Terahertz spectroscopic and density functional theory lnvestigation on the polymorph ofthe cocrystals of nicotinamide and pimelic acid. *Spectrosc. Spectr. Analysis* 39 (05), 1386–1391. doi:10.3964/j.issn.1000-0593(2019)05-1386-06

Xie, W., Shang, L. P., Deng, H., and Liu, Q. C. (2019). Terahertz spectroscopic study for expired drugs. *Spectrosc. Spectr. Analysis* 39 (08), 2409–2414. doi:10.3964/j.issn.1000-0593(2019)08-2409-06

Xu, X. H., Fu, X. H., Xia, Y., Du, Y., Liu, J. J., and Hong, Z. (2012). Research on detection of antibiotic drugs based on terahertz time-domain spectroscopy. *Mod. Sci. Instrum.* 06, 42–45.

Xu, Z., He, M. X., Li, P. F., and Wang, P. F. (2017). Spectral matching algorithm applied to identify the terahertz spectrum of Caulis spatholobi and Caulis sargentodoxae. *Spectrosc. Spectr. Analysis* 37 (01), 42–47. doi:10.3964/j.issn.1000-0593(2017)01-0042-06

Xu, Z., Liu, Y. D., Hu, J., Li, M. P., Cui, H. Z., Zhan, C. H., et al. (2021). Temporal expectation driven by rhythmic cues compared to that driven by symbolic cues provides a more precise attentional focus in time. *Trans. Chin. Soc. Agric. Eng.* 37 (15), 308–314. doi:10.3758/s13414-020-02168-y

Yan, H., Fan, W., Chen, X., Liu, L., Wang, H., and Jiang, X. (2021). Terahertz signatures and quantitative analysis of glucose anhydrate and monohydrate mixture. *Spectrochimica acta. Part A, Mol. Biomol. Spectrosc.* 258, 119825. doi:10.1016/j.saa.2021.119825

Yan, S., Zhang, H., Yang, Z., Tang, M., Zhang, M., Du, C., et al. (2017). Transformation and dehydration kinetics of methylene blue hydrates detected by terahertz time-domain spectroscopy. *Rsc Adv.* 7 (66), 41667–41674. doi:10.1039/C7RA07118C

Yang, J., Li, S., Zhao, H., Song, B., Zhang, G., Zhang, J., et al. (2014). Molecular recognition and interaction between uracil and urea in solid-state studied by terahertz time-domain spectroscopy. *J. Phys. Chem. A* 118 (46), 10927–10933. doi:10.1021/jp506045q

Yang, S., Zuo, J., Liu, S. J., and Zhang, C. L. (2016b). Application of terahertz spectroscopy in the detection of Chinese medicine processed drugs of rhubarb. *Spectrosc. Spectr. Analysis* 36 (12), 3870–3874. doi:10.3964/j.issn.1000-0593(2016)12-3870-05

Yang, X., Zhao, X., Yang, K., Liu, Y., Liu, Y., Fu, W., et al. (2016a). Biomedical applications of terahertz spectroscopy and imaging. *Trends Biotechnol.* 34 (10), 810–824. doi:10.1016/j.tibtech.2016.04.008

Yang, Y. P., Zhang, C., Liu, H. S., and Zhang, Z. W. (2019). Identification of two types of safflower and bezoar by terahertz spectroscopy. *Spectrosc. Spectr. Analysis* 39, 45–49. doi:10.3964/j.issn.1000-0593

Yin, M., Wang, J. L., Huang, H. L., Huang, Q. P., Yang, M. M., Fu, Z. P., et al. (2020). Research on flavonoids based on terahertz time-domain spectroscopy. *Spectrosc. Spectr. Analysis* 40 (12), 3919–3924. doi:10.3964/j.issn.1000-0593(2020)12-3919-06

Yin, Y. J., and Sun, X. (2018). Traditional identification methods and modern identification techniques of traditional Chinese medicine. *Cardiovasc. Dis. Electron. J. Integr. Traditional Chin. West. Med.* 6 (30), 15–16. doi:10.16282/j.cnki.cn11-9336/r.2018.30.008

Zeitler, J. A., Taday, P. F., Gordon, K. C., Pepper, M., and Rades, T. (2007). Solid-state transition mechanism in carbamazepine polymorphs by time-resolved terahertz spectroscopy. *Chemphyschem a Eur. J. Chem. Phys. Phys. Chem.* 8 (13), 1924–1927. doi:10.1002/cphc.200700261

Zhang, G. J., and Wang, J. J. (2011). Science connotation on identification of Chinese materia medica origin. *Drugs & Clin.* 26 (01), 1–3. doi:10.7501/j.issn.1674-5515

Zhang, H. (2018). *Study on measurement methods of Chinese traditional medicine based on terahertz time-domain spectroscopy*. China: Doctoral Dissertation, Xi'an University of Electronic Science and Technology.

Zhang, H., and Li, Z. (2018). Terahertz spectroscopy applied to quantitative determination of harmful additives in medicinal herbs. *Optik* 156, 834–840. doi:10.1016/j.ijleo.2017.12.050

Zhang, H., Li, Z., Chen, T., and Liu, J. J. (2018). Detection of poisonous herbs by terahertz time-domain spectroscopy. *J. Appl. Spectrosc.* 85 (1), 197–202. doi:10.1007/s10812-018-0632-6

Zhang, H., Li, Z., Chen, T., and Liu, J. J. (2017b). Discrimination of traditional herbal medicines based on terahertz spectroscopy. *Optik* 138, 95–102. doi:10.1016/j.ijleo.2017.03.037

Zhang, L., Li, C., Li, T. Y., Zhang, Y., Jiang, L., and Zhang, J. (2020). Combination of lapatinib and luteolin enhances the therapeutic efficacy of lapatinib on human breast

cancer through the FOXO3a/NQO1 pathway. *Laser & Optoelectron. Prog.* 57 (23), 364–371. doi:10.1016/j.bbrc.2020.07.049

Zhang, P. (2008). Terahertz spectroscopic identification of Chinese herbs. (Master dissertation, capital normal university). https://kns.cnki.net/KCMS/detail/detail.aspx?dbname=CMFD2009&filename=2008144291.nh.

Zhang, Q. (2016). Investigation on crystal structures of nitrogen heterocyclic drugs based on characteristic spectral techniques. (Master dissertation, China jiliang university). https://kns.cnki.net/KCMS/detail/detail.aspx?dbname=CMFD201701&filename=1016292158.nh.

Zhang, Q., Fang, H. X., Qin, D., Hong, Z., Zheng, J. Q., and Du, Y. (2016). Network-based methods for identifying critical pathways of complex diseases: A survey. *Chin. J. Pharm. Analysis* 36 (06), 1082–1089. doi:10.1039/c5mb00815h

Zhang, Q., Fang, H. X., Zhang, H. L., Qin, D., Hong, Z., and Du, Y. (2017a). Vibrational spectroscopic characterization of the Co-crystal and the forming conditionbetween γ-aminobutyric acid and benzoic acid. *Spectrosc. Spectr. Analysis* 37 (12), 3786–3792. doi:10.3964/j.issn.1000-0593(2017)12-3786-07

Zhang, X. C., and Xu, J. (2010). *Introduction to THz wave photonics* springer US. doi:10.1007/978-1-4419-0978-7

Zhang, Z. H., Zhang, Q., Zhang, Q. Q., Chen, C., He, M. Y., Chen, Q., et al. (2015). From a binary salt to salt co-crystals of antibacterial agent lomefloxacin with improved solubility and bioavailability. *Acta Crystallogr. Sect. B, Struct. Sci. Cryst. Eng. Mater.* 71, 437–446. doi:10.1107/S2052520615011191

Zhang, Z. Y., Zhang, T. R., Fan, F., Ji, Y. Y., and Chang, S. J. (2022). Terahertz polarization sensing of bovine serum albumin proteolysis on curved flexible metasurface. *Sensors and actuators A: Physical* 338, 113499–113506. doi:10.1016/j.sna.2022.113499

Zhao, R. J., Du, Y., and Hong, Z. (2014). Investigation of vudine pharmaceutical compounds by terahertz spectroscopy and density functional theory. *Chin. J. Pharm. Analysis* 34 (01), 108–114. doi:10.16155/j.0254-1793.2014.01.031

Zhao, R. J., He, J. L., Li, J., Guo, C. S., Du, Y., and Hong, Z. (2011). Terahertz time-domain spectroscopy of L- and DL-fudosteine. *Acta Physico-Chimica Sin.* 27 (12), 2743–2748. doi:10.3866/PKU.WHXB20112743

Zheng, Z. P., Fan, W. H., and Hui, Y. (2012a). Terahertz absorption spectra of benzene-1,2-diol, benzene-1,3-diol and benzene-1,4-diol. *Chem. Phys. Lett.* 525-526, 140–143. doi:10.1016/j.cplett.2011.12.062

Zheng, Z. P., Fan, W. H., Yan, H., Liu, J., Yang, W. Z., and Zhu, S. L. (2012b). Terahertz and mid-infrared spectroscopy of benzene-1,2-diol. *J. Mol. Spectrosc.* 281, 13–17. doi:10.1016/j.jms.2012.09.005

Zheng, Z. P., Li, A. D., Dong, J., Zhi, Y., and Gong, J. M. (2022). Terahertz spectroscopic investigation of maleic hydrazide polymorphs. *Spectrosc. Spectr. Analysis* 42 (04), 1104–1108. doi:10.3964/j.issn.1000-0593(2022)04-1104-05

Zheng, Z. P., Li, A. D., Li, C. Y., and Dong, J. (2021). Terahertz time-domain spectral study of paracetamol. *Spectrosc. Spectr. Analysis* 41 (12), 3660–3664. doi:10.3964/j.issn.1000-0593(2021)12-3660-05

Zhou, J., Tryggestad, E., Wen, Z., Lal, B., Zhou, T., Grossman, R., et al. (2011). Differentiation between glioma and radiation necrosis using molecular magnetic resonance imaging of endogenous proteins and peptides. *Nat. Med.* 17 (1), 130–134. doi:10.1038/nm.2268

Zhou, X. Y., Liu, Z., and Feng, X. Z. (2010). Research advance of drug polymorphism. *Chem. Bioeng.* 27 (10), 1–5.

Frontiers in
Bioengineering and Biotechnology

Accelerates the development of therapies, devices, and technologies to improve our lives

A multidisciplinary journal that accelerates the development of biological therapies, devices, processes and technologies to improve our lives by bridging the gap between discoveries and their application.

Discover the latest Research Topics

See more →

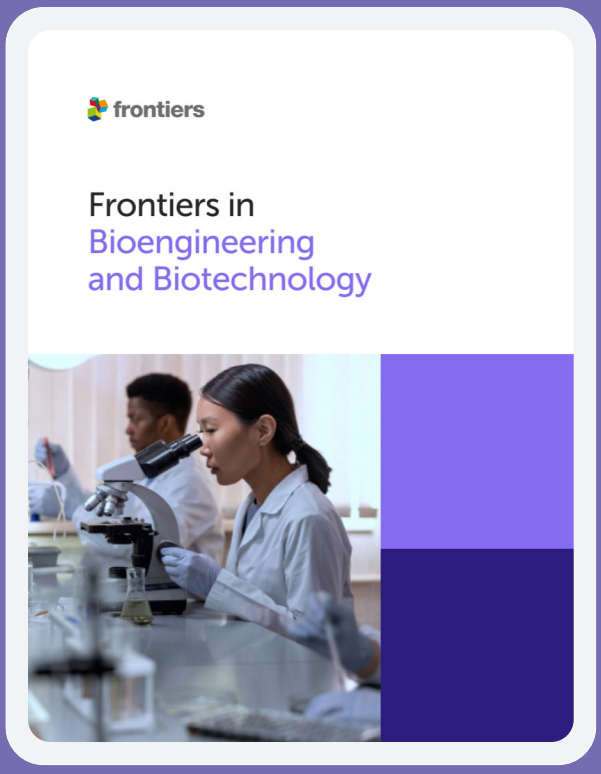

Frontiers

Avenue du Tribunal-Fédéral 34
1005 Lausanne, Switzerland
frontiersin.org

Contact us

+41 (0)21 510 17 00
frontiersin.org/about/contact